DESIGN AND FABRICATION OF NOVEL REGENERATIVE IMPLANT BASED ON POLYMERIC MATERIAL

by

SAMIA BENMERAH

A thesis submitted to

The University of Birmingham

For the degree of

DOCTOR OF PHILOSOPHY

Department of Electronic, Electrical and Systems Engineering

School of Engineering and Physical Sciences

The University of Birmingham

May,2014

UNIVERSITY OF
BIRMINGHAM

University of Birmingham Research Archive

e-theses repository

This unpublished thesis/dissertation is copyright of the author and/or third parties. The intellectual property rights of the author or third parties in respect of this work are as defined by The Copyright Designs and Patents Act 1988 or as modified by any successor legislation.

Any use made of information contained in this thesis/dissertation must be in accordance with that legislation and must be properly acknowledged. Further distribution or reproduction in any format is prohibited without the permission of the copyright holder.

ABSTRACT

This thesis presents the design and the fabrication process of a three-dimensional (3D) neural interface consisting of a bundle of parallel micro-channels with (100μmx100μm) cross-sectional area and embedded micro-electrodes. This is a regenerative implant that is able to stimulate and record extracellular neural signals in the peripheral nervous system as demonstrated by the *in vivo* experiments conducted in collaboration as part of this project. These implants have the potential to be developed into long-term neural interfaces capable of extracting neural signals from stumps of severed peripheral nerves to use as control inputs for muscles simulators or artificial limbs for amputees. The skeleton of the device is entirely made of flexible polyimide films. Gold micro-electrodes and micro-channels of photosensitive polyimide are patterned directly on polyimide substrates. After fabrication, the 2D electrode micro-channel array is rolled into a 3D structure forming concentric rolls of closed micro-channel arrays with a Swiss-roll like arrangement. Microflex Interconnection technique (MFI) was incorporated successfully into the implant. The performance of the implant microelectrodes was characterised *in-vitro* through impedance spectroscopy and *in-vivo* via implantation in animals for three months. The ability of the electrodes to stimulate and capture action potentials from regenerated tissue was also assessed.

TO MY BELOVED FAMILY

MY FATHER AND MY MOTHER

MY SISTER AND MY MANY BROTHERS

MY BELOVED HUSBAND, ADEL

MY BOYS, RAED AND AYMEN

ACKNOWLEDGEMENTS

This work could not have been completed without the help, guidance and support of many people. Only few of them I can mention here. I would like to express my deepest gratitude towards my supervisor, Dr Edward Tarte for his continuous help and great support.

My thanks should also go to my colleagues Richard Barrett and Andreas Frommhold for their immense help and support, from providing samples, to offering me guidance on the design and microfabrication of structures. Discussions and encouragement from both of my colleagues have been invaluable. I would also like to thank our technician, Donna Johnson, who maintains the clean room and lab facilities. In addition, I greatly appreciate the assistance of Dr Mao Long whose knowledge of cleanroom technologies has helped me during the course of my lab work.

Last but not least, I am thankful to my family and friends who have been there for me during the ups and downs of this Ph.D. I am ever indebted to my parents and my siblings whose love has been a mountain of constant hope and treasure for me. A special thank you to my husband's family for their continuous encouragement and immense support. To my loving, supportive, encouraging and patient husband Adel whose faithful support during the final stages of this Ph.D. is so appreciated. To my sons Raed and Aymen for being such good kids and for cheering me up when I needed it the most. Thank you, I am grateful to you all.

And above all, thank you God for being there for me and guiding me every step of the way!

TABLE OF CONTENTS

1. Introduction---- 1
   1.1. Motivation---- 2
   1.2. Overview of the thesis---- 4
2. The anatomy and the activity of neural tissue---- 7
   2.1. Introduction ---- 7
   2.2. The Nervous System---- 7
      2.2.1. Neurons ---- 8
      2.2.2. Cell membrane----10
      2.2.3. The Hodgkin Huxley membrane model----14
   2.3. The brain and the peripheral nervous system ----24
   2.4. Chapter Summary ----28
3. Review of interfacing technology----29
   3.1. Introduction ----29
   3.2. Review of peripheral nerve interfacing technology----29
      3.2.1. Interface Electrodes ----30
      3.2.2. Non-invasive Electrodes----31
      3.2.3. Invasive electrodes ----32
   3.3. Review of brain nervous system interfacing technology----43
      3.3.1. Electro-encephalography (EEG) ----44
      3.3.2. Electro-corticography (ECoG) ----44
      3.3.3. Penetrating implanted electrodes----45
   3.4. Materials used in neural interfaces ----50
   3.5. Biocompatibility----51
   3.6. Chapter summary----53
4. Micro-channels arrays as axonal amplifiers in regenerative neural implants ---55
   4.1. Introduction ----55
   4.2. Extracellular Amplification through confinement ----63
      4.2.1. Effect of varying channel cross-sectional area and axon diameter ----65
      4.2.2. Effect of varying channel length ----65

4.2.3. Radial potential distribution ----66
4.2.4. Amplitude versus axial position----67
4.3. In Vitro study of Axon outgrowth through 2D array of micro-channel ----72
4.4. 3D micro-channel structure investigation *in vivo* ----73
4.5. Chapter Summary ----78
5. Design chapter ----81
5.1. Spiral Peripheral Neural Interface- The SPNI ----81
5.2. Design overview of the SPNI implants ----82
5.3. Experimental consideration- the dimensional parameters of the implant ----88
5.4. Design of electrodes and their placement ----91
5.4.1. The importance of placing the wiring on the neutral plane ----91
5.4.2. Derivation of the stress model ----93
5.4.3. The SPNI neutral plane – The initial stress model ---- 102
5.4.4. The effect of neglecting the insulation layer ---- 108
5.4.5. The Corrected stress model ---- 113
5.5. Chapter Summary ---- 118
6. Fabrication and testing methods for the spni implants---- 120
6.1. Introduction ---- 120
6.2. Techniques used to fabricate the SPNI devices---- 120
6.2.1. Wafer preparation ---- 120
6.2.2. Spin Coating Polyimide Resins and photo-resist ---- 121
6.2.3. Softbaking of Polyimide resins and photoresist ---- 124
6.2.4. Photolithography---- 126
6.2.5. Evaporation and Fabrication of Thin Metal Features ---- 128
6.2.6. Etching and other surface treatments ---- 129
6.2.7. Dry Etching---- 131
6.2.8. Curing of the polyimide structures---- 133
6.2.9. Methods to determine the film thickness ---- 134
6.3. Techniques used to test the SPNI polyimide devices ---- 135
6.3.1. Electrochemical Impedance spectroscopy ---- 135
6.4. Chapter summary---- 138
7. Fabrication of SPNI devices ---- 139

7.1. Introduction ---- 139
7.2. Materials ---- 139
7.3. Wafer preparation and substrate adhesion ---- 141
7.3.1. Pyralin substrate adhesion ---- 142
7.4. Increasing the thickness of the substrate layer ---- 144
7.5. Metallisation layer ---- 146
7.6. Insulation layer ---- 148
7.7. Channel layer ---- 149
7.7.1. Spin coating parameters for 100 μm channel height ---- 150
7.7.2. Pre-baking regime for 100µm channel height ---- 151
7.8. Curing ---- 155
7.9. De-scum of microelectrodes ---- 157
7.10. Cutting and rolling the devices ---- 158
7.11. Connecting to the SPNI devices ---- 160
7.12. Chapter summary ---- 161
8. Optmisation of the MFI Technique for interconnection with polymeric devices -- 162
8.1. Introduction ---- 162
8.2. Current connection technique for SPNI implants ---- 164
8.3. Microflex Interconnection Technology (MFI) ---- 166
8.3.1. MFI in greater details ---- 168
8.4. Integration of MFI into SPNI fabrication process ---- 170
8.4.1. Fabrication of Pyralin test structures ---- 171
8.4.2. Investigation of sacrificial layer ---- 175
8.4.3. Fabrication of test structures based on PSPI ---- 177
8.4.4. MFI ball bonding of the test structures ---- 180
8.4.5. Varying the thickness of the SPNI ---- 181
8.4.6. Varying *Via* hole sizes ---- 183
8.4.7. Testing of the electrical conductivity of the interconnects ---- 184
8.5. Chapter Summary ---- 185
9. characterising the SPNI devices via impedance spectroscopy ---- 187
9.1. Introduction ---- 187
9.2. Modelling Overview-Extracting Model parameters from Data ---- 188

9.3. Modelling of Impedance spectra ---------- 189
9.4. Analysing the impedance measurements ---------- 194
9.5. Chapter summary ---------- 202
10. Regeneration and *in vivo* results ---------- 204
10.1. The passive SPNI implants ---------- 204
10.1.1. In vivo implantation of the passive implants ---------- 205
10.1.2. Explantation of the passive implants and preparation for histological assessment ---------- 206
10.1.3. Regeneration results through the passive SPNI implants ---------- 208
10.2. Assessment of the active SPNI implants ---------- 212
10.2.1. Implantation of the active SPNI devices ---------- 214
10.2.2. Explantation of the active SPNI implants and the experimental set up for electrophysiology ---------- 214
10.2.3. Impedance of the active SPNI devices *in vivo* ---------- 217
10.2.4. Stimulation in SPNI devices ---------- 218
10.2.5. Recording in the active SPNI devices ---------- 221
10.2.6. Histological analysis of regenerated tissue ---------- 223
10.3. Chapter Summary ---------- 225
11. Conclusion and future work ---------- 229
11.1. Future work ---------- 233
12. Appendices ---------- 237
A.1 Masks used to fabricate the SPNI devices ---------- 237
A.2 Photos for some of the chrome-on-glass masks used in the fabrication the SPNI devices ---------- 243
A.3 SPNI fabrication process- step by step summary ---------- 247
13. Bibliography ---------- 251

LIST OF FIGURES

Fig. 2.1: Nerve cell. Top-The structure of a typical neuron, Bottom: illustration of an active synapse between two neurons [14]---------- 9
Fig. 2.2: A schematic of a nerve cell membrane with ions and ion channels. Sodium (Na^+), Potassium (K^+) and chloride (Cl^-) are capable of flowing across the membrane. The concentrations of these ions on the inside and on the outside surface of the membrane are unequal. The large in size A^- anion symbolises immobile and impermeable molecules that are important for the electroneutrality but do not contribute to ionic flow[13] ----------11
Fig. 2.3: Action potential[15] ----------12
Fig. 2.4: Conduction of an action potential in an axon. (A) continuous propagation in an unmyelinated axon, (B)Saltatory conduction in a myelinated axon[13] ----------13
Fig. 2.5: Frequency coding of neural signals[15]----------14
Fig. 2.6: The equivalent circuit for a patch of neural membrane based on the Hodgkin-Huxley model----------16
Fig. 2.7: The process for determining the variation of potassium conductance during depolarisation and repolarisation in the voltage clamp mode based on the Hodgkin-Huxley model. (A) The response of n-particles to a sudden depolarisation. (B) The transfer rate coefficients response (α_n and β_n) to sudden depolarisation and repolarisation. (C) n and n^4 response to a sudden depolarisation and repolarisation (potassium conductance G_K is proportional to n^4). ----------19
Fig. 2.8: The process for determining the variation of sodium conductance during depolarisation and repolarisation in the voltage clamp mode based on the Hodgkin-Huxley model. (A) The response of m- and h-particles to a sudden depolarisation. (B) The transfer rate coefficients response ($\alpha_m, \beta_m, \alpha_h$ and β_h) to sudden depolarisation and repolarisation. (C) m, h, m^3 and m^3h response to a sudden depolarisation and repolarisation (sodium conductance G_{Na} is proportional to m^3h)[13]. ----------21
Fig. 2.9: Equivalent circuit to model to incorporate action potential conduction [13]-----22
Fig. 2.10:Action potential computations based on the Hodgkin-Huxley model. Top-computed action potential halfway a 50μm long axon based on Hodgkin-Huxley model, Bottom- gating parameters for the ion channels[5]----------23

Fig. 2.11: The brain anatomy[13] ----------25
Fig. 2.12: mapping sensory and motor functions in the human cortex[13] ----------26
Fig. 2.13: Illustration of the structure of a peripheral nerve[16]----------27
Fig. 3.1: invasiveness Vs selectivity for different types of electrodes interfacing PNS[19] ----------30
Fig. 3.2: Surfaces electrodes; Left – surface electrode, Right- Walkaid stimulator[17] ---32
Fig. 3.3: Eight channel stimulator with one Epimysial Electrode (the insert on the right)[19] ----------34
Fig. 3.4: Examples of epineurial electrode, Left- epineurial electrode (From Finetech implantable Drop foot), Right- helicoidal electrode (Cybertronics)[26] ----------35
Fig. 3.5: Book electrodes implant, Left- standard three channel book electrode (Finetech brindley), Right- Schematic of book electrode in operation[17] ----------36
Fig. 3.6:Examples of Epineurial electrodes, Top- cuff electrode, Bottom two: schematic of FINE electrodes implanted on a peripheral nerve[17] ----------38
Fig. 3.7: Schematic of LIFE electrode[19]----------40
Fig. 3.8: Examples of Sieve regenerative electrodes, Top- sieve electrode in situ, Bottom- two different sieve electrode designs (notice the fringes added on the periphery of the bottom right design; they are normally used for attachment)[19] ----------42
Fig. 3.9: three main variations of Brain Computer Interface (BCI) electrodes; EEG, ECoG and intracortical implanted electrodes [31] ----------43
Fig. 3.10:Electroencephalographic (EEG) System, Left- 256 electrode EEG system in operation, Right- Standard EEG electrode placements [33] ----------45
Fig. 3.11: An Eletro-corticogram system, Left- Selection of ECoG electrode arrays compared to a US penny for scaling, Right- x-ray of skull showing ECoG electrode array implanted bilaterally [34-35]----------46
Fig. 3.12: The Michigan Electrodes, Top left- a variety of different silicone probes placed on the back of a U.S. penny, Top right- four 64 site probes assembled into a three dimensional structure, Bottom left: Schematic of single shank Michigan probe, Bottom right- Multi-shank Michigan array [39-40] ----------47
Fig. 3.13: The Utah Array. Left- three-dimensional array features 100 silicon-based microelectrodes, each with a platinum-coated tip, Right- The slanted array has been used to stimulate fibres at different depths in the cochlear nerve [41]. ----------48

Fig. 3.14: (a) well defined wire electrode array (design concept, Fabricated device and SEM of the spike tips), (b) Microwire bundle (Scale Bar =1cm)[18] ----------49
Fig. 4.1: Local currents during depolarization of an axonal membrane[10]----------59
Fig. 4.2: Simulation geometry used in FEM analysis by Fitzgerald et el[10]. Top- 2D axisymmetric unmyelinated axon. Middle- the 2D model is swept over 360^0 to give a 3D structure. Bottom- Myelin segments added for myelinated axons in the model ----------60
Fig. 4.3: Modelled Action Potential for: Top- a $2\mu m$ diameter unmyelinated axon, and Bottom-$10\mu m$ diameter myelinated axon outside of the channel[10] ----------62
Fig. 4.4: Modelled Intracellular (V_{in}) and extracellular (V_{out}) voltages for a $10\mu m$ myelinated axon (a) before it enters the microchannel, (b) Halfway the channel, and (c) after emerging from the micro-channel[10].----------64
Fig. 4.5: The amplitude of V_{out} versus the channel cross sectional area.----------66
Fig. 4.6: The Amplitude V_{out} versus the axon diameter[10].----------66
Fig. 4.7: The Amplitude V_{out} versus the length of the channel[10] ----------67
Fig. 4.8: V_{out} amplitude versus radial distance from the centerline of a $10\mu m$ myelinated axon[10] ----------68
Fig. 4.9: (a) V_{out} amplitude versus axial position in a $1000\mu m^2$ channel for a $2\mu m$ diameter unmyelinated axon and $10\mu m$ diameter myelinated axon. (b) a close up into a 1mm section of the same $10\mu m$ diameter myelinated axon approximately 7mm before channel entry[10] ----------69
Fig. 4.10: Dorsal Root Ganglions cultured onto polymide arrays have an oblique approach, straight approach or turn away [61] ----------72
Fig. 4.11: Proportion of neurites entering channels versus channel array transparency for (a) neonatal rats and (b) adult rats. Neurites that entered the channels parallel to the channel axons were recorded as 'straight', while neurites approaching the channels at a 30^0 angle or greater were recorded as 'oblique'[61]----------73
Fig. 4.12: Optical micrographs of micro-channel implants. (a) Type 1- batch processed Short silicon implants, with a length of 0.5mm, a channel diameter range of 55μm - 100μm (scale bar: 1mm). (b) Type 2- Long silicone micro-channel implants, prepared by casting silicone over a grid of 100μm diameter nylon filaments, and pulling out the filaments once silicone had set. The implants host bundles of parallel channels over a

1.5mm diameter cross section, and 1mm to 5mm lengths. Scale bars are 0.5mm. (c) Type 3. Rolled polyimide implants prepared using standard planar micro-fabrication processes. Micro-channels shown on the right have a cross of 70μmx40μm. Rolls were held in a silicone tube of 1.5mm inner diameter matching rat sciatic nerve diameter. Scale bar: 0.5mm[62]. ----------75
Fig. 4.13: Micrographs of transverse sections of regenerated nerves through type 1 micro-channels (sieve implants). (a) Array of mini-nerves growing through a type 1 implant, at the distal end of the channels. Micro-channels are 100μm side (Scale bar: 100μm). (b-c) Typical regenerated mini-nerves (scale bar: 20μm). Micro-channels may be filled with unmyelinated and myelinated axons and blood vessels (b) or mainly with fibrous tissue (c). (d-e) TEM (Transmission Electron microscopy) images of a mini-nerve showing myelinated fibres that regenerated close to a blood vessel (d – asterisk), and Schwann cells with unmyelinated fibres (e – asterik)[62].----------76
Fig. 4.14: Effect of channel geometry on axon regeneration through type 1 micro-channel arrays. All data were obtained 30 days post-implantation. (b) Number of regenerated myelinated fibres as a function of channel size. Implant transparency was 0.49[62]. ----77
Fig. 4.15: Number of regenerated myelinated axons as a function of micro-channel length at 4 and 12 weeks post-implantation[63]----------78
Fig. 5.1: Illustration of the 3D micro-channel implant; the spiral peripheral neural interface (the SPNI) ----------82
Fig. 5.2: layer layout for the SPNI active devices . Substrate layer thickness (12 to 20 μm), Metal layer thickness (gold is 250nm thick, Chromium layer is 50nm as an adhesive layer), the insulation layer is 3to 5 μm thick with micro-electrode sites (30 μm x100 μm) and track (50 μm) and contact pads (300 μm x2000 μm), the channel layer is 100 μm x100 μm thick. ----------85
Fig. 5.3: Layer layout for passive devices (passive SPNI implants)----------86
Fig. 5.4: Top- Schematic of SPNI design, Bottom- application of silicone tube to either end of the SPNI roll [65] ----------88
Fig. 5.5: Microelectrode dimension and placement for the SPNI implants; (a) a schematic for location of the micro-electrodes in the 2D structure of the implant. This illustrates the location of the active micro-channels supplied by electrodes and passive micro-channels that contain no micro-electrodes, (b) Mask layout showing the overall device footprint

and the microelectrode distribution in the area corresponding to the two central rolls of the structure. 20 channels out of 60 channels in the central rolls (layer number 3 and 4 in the rolled structure containing 6 rolls in total) are supplied with electrodes positioned in the centre of their corresponding channel. (c) The dimensions of the microelectrodes and their location inside their corresponding micro-channel. ----------92
Fig. 5.6: the effect of bending a metal layer sandwiched between two polyimide layers; a- No strain experienced by the layers, b) Tensile Extension of the wiring plane, c) Tensile compression of the wiring plane [17]----------93
Fig. 5.7: rectangular cross-section prior and post bending; AB is the neutral plane of the structure, CD is a plane that extends the cross –section a distance y from the neutral plane. A'B' and C'D' are the planes through the rectangle post bending. θ is the angle characterising the length of the arcs ----------95
Fig. 5.8: Illustration of the incremental element ----------96
Fig. 5.9: SPNI composite structure ----------99
Fig. 5.10: illustration of Parallel axis theorem on a composite structure---------- 100
Fig. 5.11: The transformed section for the SPNI composite structure---------- 102
Fig. 5.12: the variation of the neutral plane position with different substrate thicknesses - and the variation of the distance, between the top of the substrate layer and the neutral plane (y, used in strain calculations), with the substrate thickness. The calculations are for an implant with $100\,\mu m$ x$100\,\mu m$ micro-channel cross-sectional area, 50 μm wall thickness and 5 μm insulation layer. These calculations were based on the initial stress model presented in section [5.4.3] ---------- 105
Fig. 5.13: SPNI cross-section, showing concentric rolls and their radii of curvature --- 106
Fig. 5.14: Strain experienced by the wiring at different rolls for different substrate thicknesses. These calculations were based on the initial stress model presented in section [5.4.3]. The other implant parameters included $100\,\mu m$ x$100\,\mu m$ micro-channel cross-sectional area, 50 μm wall thickness and 5 μm insulation layer. ---------- 107
Fig. 5.15: Neglecting the insulation layer of SPNI in neutral plane and strain calculations ---------- 108
Fig. 5.16: The effect of neglecting the insulation layer in the calculations of the neutral plane position for different substrate thicknesses- and the variation of the value of y with the substrate thickness (y is the distance between the top of the substrate layer and the

neutral plane; it is used in strain calculations). The plots are calculated using the initial stress model presented in section [5.4.3] and the model presented in section [5.4.4] which is similar but neglects the insulation layer thickness. The other dimensional parameters of the implant were $100\,\mu m$ x$100\,\mu m$ micro-channel cross-sectional area, $50\ \mu m$ wall thickness and $5\,\mu m$ insulation layer.---------- 110
Fig. 5.17: the effect of neglecting the insulation layer on the calculations of the Strain experienced by the wiring at different rolls for different substrate thicknesses. The calculations are for an implant with $100\,\mu m$ x$100\,\mu m$ micro-channel cross-sectional area, $50\ \mu m$ wall thickness and $5\,\mu m$ insulation layer. The plots are calculated using the initial stress model presented in section [5.4.3] and the model presented in section [5.4.4] which is similar but neglects the insulation layer thickness. ---------- 112
Fig. 5.18: the SPNI 3D structure with x,y,z axes and the bending moments for the initial stress model (Mx) and the corrected stress model (Mz) ---------- 114
Fig. 5.19: The structure used to calculated the neutral plane in the corrected model ---- 115
Fig. 5.20: The position of the neutral plane for different substrate thicknesses, and the distance between the neutral plane and the top of the substrate. These were calculated using the corrected stress model presented in section [5.4.5]. The corresponding plots calculated using the initial stress model presented in section [5.4.4] were also included for comparison purposes, ---------- 116
Fig. 5.21: variation of the strain with the substrate thickness across the concentric rolls of the implant based on the corrected stress model presented in section [5.4.5]. Strain plots based on the initial stress model presented in section [5.4.3] are also included for comparison purposes. ---------- 117
Fig. 6.1: An example of multiple coating chart[72] ---------- 123
Fig. 6.2: The photolithographic process for negative photoresist- a) film is spin coated onto the wafer, b) only selected regions of the layer are exposed to UV light using a mask, c) development removes resist in unwanted regions[17]. ---------- 124
Fig. 6.3: Polaron Thermal Evaporator ---------- 126
Fig. 6.4: Etching profiles- a) Amorphous isotropic etching, b) Perfectly anisotropic etching ---------- 130
Fig. 6.5: Full curing temperature profile for polyimide ---------- 132
Fig. 6.6: Using a ZIF and a convention PCB to access the SPNI microelectrodes ------- 135

Fig. 6.7: The experimental set-up to perform Electrochemical Impedance Spectroscopy (EIS)- Left; Positioning of SPNI and counter electrode in the electrolyte, Right; Electrodes under test connected to Network Analyser[17]. ---------- 135
Fig. 6.8: the principle of the auto-balancing bridge method [17] ---------- 137
Fig. 7.1: Process steps for fabricating the SPNA devices ---------- 140
Fig. 7.2: SEM image of 20µm thick substrate layer cross-section , fabricated using multiple spin coating with full cures in between. First a layer of PI2611 is spin coated on a 4'' wafer and then fully cured. A second layer of PI2611 is spin coated on the top of the first layer and then the whole wafer is fully cured to give a to total thickness of 20 µm. Specific spin speeds are used to obtain this thickness. The inset is a zoom into the substrate cross-section.---------- 143
Fig. 7.3: Patterned metal layer showing Micro-electrode sites (top), tracks (top) and insulated connection pads (Bottom) ---------- 146
Fig. 7.4: Top: Channel layer aligned over electrode layer. Bottom left: alignment marks, Bottom right: a zoom into the micro-electrode sites ---------- 147
Fig. 7.5: Spin profile: PSPI7020 thickness after full cure vs. spin speed ---------- 149
Fig. 7.6: effects of baking regime on the SPNI layers ---------- 150
Fig. 7.7: SEM of photosensitive polyimide (PSPI) micro-channels tilted at 30^0 -------- 151
Fig. 7.8: 100µm channel walls. The undercut observed in the channel walls can be attributed to the layer thickness and the exposure time. The photo-sensitive polyimide used to make the channels is a negative material, consequently under-exposing a thick channel layer (thickness>50 μm) through the mask can lead to an undercut feature in the channel walls during development. This can be improved by adjusting the exposure time further. ---------- 152
Fig. 7.9: Channel walls- left channel walls before cure. Right: Channel walls after full cure ---------- 153
Fig. 7.10: partially and fully cured PSPI (Before and after cure) ---------- 153
Fig. 7.11:Optical image of the SPNI device at the micro-electrode sites ---------- 155
Fig. 7.12: the de-scum process: left- Micro-electrode site requiring de-scum, Top right: Microelectrode with PSPI residues before de-scum, Bottom right: the microelectrode after de-scum---------- 156

Fig. 7.13(a) sheet of the polyimide layers peeled off and ready to be cut, (b) SEM image for a sheet of polyimide layer that has been cut and which is ready to be rolled --------- 157
Fig. 7.14: Left rolled a PSPI device, Right: A PSPI roll inserted into a silicone tube, Bottom-SPNI devices rolled and held in 3D structure with a silicone tube whist allowing access to the connection pads. ---------- 158
Fig. 7.15: SEM of cross sections of rolled PI devices with 100 μm high channel walls 159
Fig. 7.16: the SPNI device inserted into a ZIF connector to access its 20 electrode channels via dill sockets mounted on the PCB. ---------- 160
Fig. 8.1: Overview of the experimental setup to connect to the individual microelectrode channels. This the primitive setup used to gain access to the microelectrode channels individually. ---------- 164
Fig. 8.2: Overview of the Microflex ball bonding technique. Right: SEM micrograph of the contact array, all bonds aligned on the contact pad[73] ---------- 167
Fig. 8.3: Microflex process steps for a bond[74] ---------- 167
Fig. 8.4: Comparison of the relative strengths of interconnection technologies for neural implants[76]. Left; Examples of bending techniques used to conduct the tensile experiments, Right; Results of the tensile experiment[76]. ---------- 169
Fig. 8.5: Updated design of SPNI devices to incorporate Microflex Technique [17]---- 171
Fig. 8.6: Etch profile for Pyralin 2611 in oxygen plasma ---------- 172
Fig. 8.7: Ball bonds on through a Pi2611 substrate ---------- 173
Fig. 8.8: Failed release of the PSPI structures on Aluminium[17] ---------- 176
Fig. 8.9: a test sample base layer fabricated using PSPI7020 ---------- 178
Fig. 8.10: - Top Patterned S1813 layer on a gold layer for two different samples, Bottom-patterned gold/chrome layer on two different samples, S1813 layer is washed off. ----- 178
Fig. 8.11: 1 released samples placed on a gold printed substrate (underneath) ready to be ball bonded---------- 179
Fig. 8.12:The Kulicke and Soffa gold ball bonder---------- 180
Fig. 8.13: Alumina gold printed bonding targets (substrates) ---------- 181
Fig. 8.14: SEM micrograph of ball bonds through PSPSI samples, Top- ball bonds on different test sample designs, Bottom- a zoom into two ball bonds ---------- 182

Fig. 8.15: Bonding through different hole sizes, Top right – bonding through different holes sizes on PSPI samples, Bottom- SEM micrograph of a via hole in the PSPI samples (PSPI residues can be seen at the base of the hole) ---------- 183
Fig. 8.16: A PSPI sample example to test and measure the resistance of the ball bonds. 184
Fig. 9.1: Modelled impedance and spectra for a constant phase element (CPE) in series with a solution resistance. The plots show the effect of varying the surface properties of the electrode by assigning different values to the imperical constant n which is a measure for the surface roughness of the electrode [5]. The plot for the value of n=1 represents the behaviour of an ideal capacitor. As n value decreases, the slope of the frequency dependant part of the impedance plot changes and the cuff off frequency shifts to higher frequencies, whereas the phase drops from -90^0C for ideal capacitance (n=1) to lower values for decreasing values of n. ---------- 190
Fig. 9.2: Modelled impedance spectra of a simple electrode interface, showing the effect of varying charge transfer resistance on the electrode interface[5] ---------- 191
Fig. 9.3: Modelled Impedance spectra of a simple electrode interface, showing the effect of varying the Warburg impedance on the electrode interface[5] ---------- 193
Fig. 9.4: Impedance spectra for an electrode from an SPNI device belonging to batch1 before and after rolling (batch 1 contains 8 devices in total). The frequency ranges is 10Hz to100KHz as it allows electrode-electrolyte interface characterisation in addition to containing the frequency range relevant for nerve signal recordings ---------- 195
Fig. 9.5: Phase spectra for an electrode from an SPNI device belonging to batch1 before and after rolling. (batch 1 contains 8 devices in total). The frequency ranges is 10Hz to100KHz as it allows electrode-electrolyte interface characterisation in addition to containing the frequency range relevant for nerve signal recordings ---------- 195
Fig. 9.6: Impedance spectra for a rolled device from batch 1 and rolled device from batch 2. ---------- 196
Fig. 9.7: Phase spectra for a rolled device from batch 1 and rolled device from batch 2. 197
Fig. 9.8: Impedance spectra for 5 different microelectrodes from batch 2 prior rolling. 198
Fig. 9.9: Impedance spectra for 6 different microelectrodes from different SPNI devices taken from batch 2 post rolling ---------- 199
Fig. 9.10: Impedances of various electrodes from batch2 at 1Khz prior and post rolling (batch 2 contains 8 SPNI devices in total) ---------- 200

Fig. 9.11: Phase spectra for 5 different microelectrodes from batch2 prior rolling ------ 201
Fig. 9.12: Phase spectra for 6 different microelectrodes from batch2 post rolling ------- 202
Fig. 10.1: Passive SPNI and PDMS implants. Left- A cross-section of a passive SPNI implant, Right- image of stacked PDMS implants with an illustration its cross-section 204
Fig. 10.2:Explanted nerve with implants. Left- an explanted passive SPNI device with the two sciatic nerve stumps. Right- an explanted passive PDMS device with the two sciatic nerve stumps---------- 206
Fig. 10.3: Optical micrograph through the centre of a PDMS implant at 12 weeks post-implantation; Left- an optical micrograph through the centre of a PDMS device shows no axonal regeneration through the micro-channels at any time point post-implantation (4 weeks and 12 weeks). Right- a Zoom into the content of one of the PDMS micro-channels reveals absence of neural tissue; the channels are mainly filled with connective fibrous tissue.---------- 207
Fig. 10.4: An optical micrograph of regeneration through the distal end of a 2.5mm long passive SPNI implant at 4 weeks post-implantation. Regeneration through the passive implants is not significant at this time point (where only 4 out of 12 animals implanted with the 2.5mm long passive SPNI implants had axons on the distal end of the device, while no axons were seen distally to the 4mm long SPNI devices.---------- 209
Fig. 10.5: Axonal regeneration through different passive SPNI devices at 12 weeks post-implantation. (MF in the figure stands for regenerating Myelinated Fibres). All animals had regenerated axons on the distal end of the implant at 12 weeks post- implantation. The top set of images show regeneration at the distal end of 4 of the 2.5mm long passive SPNI devices (the number of myelinated fibres that have regenerated through the micro-channels of each implant is also shown. The middle row set of images show regeneration at the distal end of 4 of the 4mm long passive SPNI devices along with the number of myelinated fibres that have regenerated through micro-channels of each implant. The bottom set presents transmission electron microscopy images of transverse semi-thin sections of nerves that have regenerated through SPNI micro-channels; the blood vessels appear as white (almost) circular shapes. The images clearly show the myelinated fibres (with the dark contoured shapes) and the unmyelinated fibres ---------- 210

Fig. 10.6: average number of myelinated axons that have regenerated through a 2.5 mm long implant and 4mm long implant at 12 weeks post-implantation. The number of myelinated axons in an intact nerve is also shown for comparison purposes. ---------- 212
Fig. 10.7: (a-c) SPNI implants (a) A simplified schematic illustrating the application of the silicone tubes on either end of the rolled SPNI structure to prevent it from unravelling and to provide attachments for stitching the nerve stumps. (b) A complete device with the micro-channel rolls bearing the electrodes inserted into the silicone tube. (c) SEM of the end of the rolled channel bundle showing how each channel is roofed by the next layer of the roll. The hole down the centre of the implant was blocked using plastic plug before implantation. (d-f)Silicone implants (d) A schematic of a silicone cylinder containing 24 parallel 130 μm diameter micro-channels. (e) Nylon filaments fed through two aligned electron microscopy grids form a coherent bundle for casting in silicone. (f) Silicone cylinder with filaments pulled out, trimmed to 2.5mm length, and inserted into a silicone tube [65]. ---------- 213
Fig. 10.8: connection set up to gain access to the individual micro-electrodes of the SPNI devices. The microelectrodes are connected to external circuitry to test their ability to stimulate and record from the regenerated tissue in the micro-channels. The contact pad strip is glued onto a metal par positioned just above the wound for mechanical support and the connections with the microelectrodes are made individually with a micromanipulator controlled needle. ---------- 216
Fig. 10.9: Impedances of microelectrodes at 1 kHz *in vivo* after 3 months implantation[65] ---------- 217
Fig. 10.10: Experimental set-up to investigate the ability of the SPNI to stimulate and elicit EMG responses[65] ---------- 218
Fig. 10.11: The EMG response elicited in Tibia Anterior (*t.a.*) and its antagonist (*Gastroc.*) as the stimulation current delivered through the SPNI micro-electrode in a micro-channel innervating both muscles is increased. Four motor units in *t.a.* and three in *gastroc* were recruited. Arrows indicate the traces where new motor units are added (compare with the trace immediately above) [65] ---------- 220
Fig. 10.12: Recording through the SPNI- signals recorded through embedded microelectrodes in the SPNI following distal stimulation of afferent fibres via needle electrodes inserted into the animal's hindpaw[65] ---------- 222

Fig. 10.13: Top- Clusters of axons surrounded by connective tissue (CT) and blood vessels (V) that have regenerate and grew through the SPNI (bar 50 μm) Bottom Right-Transverse Micro-computed tomography of SPNI device showing the implant scaffold in light grey, regenerated tissue in dark grey (Osmium stained) and vascularisation (as small white circles) through the micro-channel array (bar 500 μm)[65], Bottom Left-Equivalent vertical section through the SPNI device showing the implant scaffold in light grey with regenerated tissue in dark grey (osmium stained) and blood vessels as narrow white lines (bar 500 μm)[83]. ---------- 224
Fig. 12.1: the overall SPNI photpmask layout with the overlapping layers. This layout can produce 8 SPNI devices per wafer. ---------- 238
Fig. 12.2: The photomask design for one SPNI device with its overlapping layers. ----- 238
Fig. 12.3: the photomask footprint for the metallisation layer consisting of the microelectrodes, the metal tracks and the connection pads ---------- 239
Fig. 12.4: the photomask for the insulation layer; insulating the metal tracks whilst exposing the microelectrode sites and the connection pads ---------- 239
Fig. 12.5: The photomask for the micro-channel layer, the channels in these devices have to be cut down into 4mm long micro-channels ---------- 239
Fig. 12.6: The photomask design for one SPNI device with its overlapping layers, the microchannels are designed to have the right length in this mask (4mm). Hence, the micro-channel length is defined photolithographically, eliminating the need to cut the micro-channels down to the right length. However, as the substrate is still made out of non-photo-definable pyralin 2611, I still need to cut around the foot print of the devices to separate them. Making the substrate with the photo-sensitive Durimide 7020 (as is done when incorporating the Microflex interconnection technique MFI, see next Appendix) 240
Fig. 12.7: the overall SPNI photpmask layout with the overlapping layers. This layout can produce 8 SPNI devices per wafer. ---------- 241
Fig. 12.8: The photomask design for one SPNI device with its overlapping layers. This design incorporates the Microflex interconnection technique MFI by designing the substrate to have via holes for MFI. ---------- 241
Fig. 12.9: The photomask design for the 1st layer of the photo-definable substrate with the via holes for MFI. This layer will enable ball bonding through the connection pads of the SPNI. The substrate will be made out of photo-definable Durimide7020, allowing the

device foot print to be patterned and separated into individual devices photolithographically. ---------- 242
Fig. 12.10: The photomask design for the 2nd layer of the photo-definable substrate. This layer sets the substrate thickness to the right level so that the metal layer of the SPNI device stays intact during rolling. ---------- 242
Fig. 12.11: the photomask footprint for the metallisation layer consisting of the microelectrodes, the metal tracks and the connection pads.---------- 242
Fig. 12.12: hotomask for the insulation layer; insulating the metal tracks whilst exposing the microelectrode sites and the connection pads. This layer is also shaped on the device footprint to allowing the individual device prints to be defined and separated photolithographically---------- 243
Fig. 12.13: The photomask for the micro-channel layer. The micro-channels are designed to have the right length in this mask (4mm). Hence, the micro-channel length is defined photolithographically, eliminating the need to cut the micro-channels down to the right length (4mm). The substrate will be made out of photo-definable Durimide7020, allowing the device foot print to be patterned and separated into individual devices photolithographically. ---------- 243
Fig. 12.14: the chrome-on-glass mask used in fabricating the photosensitive substrate layer of the SPNI devices---------- 244
Fig. 12.15: the chrome-on-glass mask used in fabricating the metallisation layer of the SPNI devices ---------- 245
Fig. 12.16: the chrome-on-glass mask used in fabricating the insulation layer of the SPNI devices---------- 246
Fig. 12.17: e chrome-on-glass mask used in fabricating the microchannel layer of the SPNI devices ---------- 247

LIST OF ABBREVIATIONS

Acronym	Definition
AEP	Audio/aural Evoked Potentials
AP	Action Potential
BCI	Brain Computer Interface
BION	Bionic Neuron
CMOS	Complementary Metal-Oxide Semiconductor
CNS	Central Nervous System
COMSOL	Computer and Solution (A finite element modeling and simulation software)
CPE	Constant Phase Element
DI water	De-Ionised water
EEG	Electro-encephalography
ECF	Extracellular conducting fluid
ECG	Electro-cardiography
ECoG	Electro-corticography
EIS	Electrochemical Impedance Spectroscopy
EMG	Electromyography
FES	Functional Electrical Stimulation
FINE	Flat Interface Nerve Electrodes
Gastroc.	antagonist gastrocenemius muscle
IBM	Ion beam Milling
IC	Integrated Circuit
LIFE	Longitudinally implanted intrafascicular electrodes
MEMs	Micro Electromechanical Systems
MFI	Micro-Flex Interconnection Technique
PCB	Printed Circuit Board
PI	Pyralin
PMMA	Poly-methyl-methacrylate
PNS	Peripheral Nervous System

PSPI	photosensitive polyimide
RPM	Revolutions per minute
SEM	Scanning Electron Microscopy
SPNI	Spiral Peripheral Neural Interface
t.a	tibia anterior
UV	Ultra-Violet
VEP	visually evoked potentials
ZIF	Zero Insertion Force

LIST OF PUBLICATIONS

1. S. Benmerah, S. P. Lacour, E. Tarte “Design and fabrication of neural implant with thick channels based on flexible polymeric materials”, 31st IEEE EMBS Conference Proceeding, Minneapolis, 2009.

2. S. P. Lacour, S. Benmerah, E. Tarte, J. FitzGerald, J. Serra, S. McMahon, J. Fawcett, O. Graudejus, Z. Yu, B. Morrison III “Flexible and stretchable micro-electrodes for in vitro and in vivo neural interfaces”, Journal of Medical and Biological Engineering and Computing, Jan 2010.

3. C.P. Watling, N. Lago, S. Benmerah, J.J. FitzGerald, E. Tarte, S. McMahon, S.P. Lacour, R. E. Camerona “Novel use of X-ray micro computed tomography to image rat sciatic nerve and integration into scaffold”, Journal of Neuroscience Methods, vol. 188(1), pp. 39–44, April 2010.

4. J. Fitzgerald, N. Lago, S. Benmerah, J. Serra, C. Watling, R. Cameron, e. Tarte, S. P. Lacour, S. B. MacMahon , J. Fawcett "A regenerative microchannel neural interface for recording from and stimulating peripheral nerve axons in vivo", Journal of Neural Engineering, vol. 9(1), 2012.

1. INTRODUCTION

Interfacing the nervous system with electronic devices can offer a great opportunity to improve the quality of life of many debilitated patients. When the peripheral nerve is injured, the distal part of the nerve that is disconnected from their cell body degenerates while its proximal section still connected to the cell bodies in the dorsal and ventral ganglion roots regenerates. If the gap between the two nerve endings is short, a direct tension free suture constitutes the best chance for good functional recovery [1]. However, if the gap between the nerve endings does not allow for a direct suture, an artificial bridge, in the form of hollow tube whose internal diameter matches nerve's diameter, can be used. Because of the huge number of axons in a single nerve, regenerating fibres are often misrouted to the wrong receptor cells, resulting in poor functional recovery [2]. In cases where the functional recovery post the lesion is not achieved or when there is complete amputation of the limb, finding a method for extracting neural signals and identifying the regenerating fibres would be very useful. The extracted and processed signals could then be used to drive muscle simulators or supply input signals to prosthetic limbs. The research in this thesis provides a solution to this problem in the form of a regenerative peripheral nerve implant which is not only able to act as a bridge between the two injured nerve stumps but is also able to reliably stimulate and record from the regenerated nerve fibres.

This project will present the design and the implementation of this implant. It will outline and discuss the methods used, the fabrication techniques applied and the testing of these fabricated implants. In this introductory chapter, the overall motivation and the objectives behind this research will be highlighted, in addition to a brief overview of the thesis and the individual content of each chapter.

1.1. Motivation

Neural interfaces are electronic devices that have been developed to enable communication with the nervous system. The intention is to record and analyse electrical neural signals that coordinate certain body functions. The interfaces are also used to stimulate part of the nervous system and trigger a particular biological reaction in the body. Examples of commercially available interfaces are cochlear implants and pacemakers which are widely in use. The main motivation behind such implants is to help improve the quality of life of many patients with severe impediments.

Studies have shown that muscle movement activates particular areas in the motor cortex mapping the concerned muscles [3]. Interestingly, the same regions of the motor cortex are also active during imagined movement. In other words, a paralyzed patient who is unable to move certain muscles can still activated the same regions in the motor cortex by imagining the movement. This is very important for neuro-prosthetic applications as neural interfaces can be used to monitor these cognitive activities and use them as inputs to cognitively control artificial systems. This was employed in a particular experiment where a completely paralysed patient was able to control an artificial hand by simply imagining the desired action [4]. To enable this cognitive control a neural interface, in the form of silicon chip connected to the artificial hand, was implanted into the surface of patient's brain. In another experiment[5], a neural interface was implanted to interface for whole month with the severed nerve stumps of an amputee who lost his forearm in an accident. The interface enabled the patient to carry out complex tasks such as grabbing and releasing objects or moving the artificial fingers of the prosthesis in an independent manner. This artificial limb was also equipped with tactile sensors that provided sensory feedback to the nervous system providing the patient with a sense of touch.

Significant research has been invested to develop techniques that would make achieving a durable and reliable neural interfaces a reality. Many interfaces have been developed, some of which were initially used as diagnostic tools to record neural signals giving an insight into the complex architecture and functions of the nervous system. Their potential for clinical applications was explored by developing them to be part of a neuro-prosthesis

intended to restore or support a neuro-sensory or neuro-mascular path via the simulation of neural tissue or muscles or the recording of their activity. Examples of where this is employed include the cochlear and retinal implants[6-7]. Although, a neural interface that is capable of completely replacing the lost functions has not yet been developed, technological advent is driving development in neuro-prosthetics.

Developing implants for applications in the peripheral nervous system has been the focus of recent research. Two types of interfaces designed particularly for implantation in the peripheral nerves are the cuff and the sieve implants [8-9] which will be discussed in more details in chapter 3 of this thesis. This thesis introduces a new type of regenerative peripheral neural implant aimed at recording and stimulating a proportion of nerves in the peripheral nervous system. It focuses on optimising the implant design to maximise regeneration through it and improve its ability to record neural signals. This constituted part of a collaborative project between the group at the University of Birmingham - Department of Electrical Engineering, The University of Cambridge- Department of Material science and Brain Repair Centre, and King College London- Department of Neuroscience. The main aim was to develop novel regenerative implants intended for long term use, one of which was the Spiral Peripheral Neural Interface (SPNI).

The motivation behind the SPNI implant is to boost the quality of the signals recorded from the peripheral nerves. Recording extracellular signals from myelinated axons is a challenging task as the amplitude of the recordable signal is too small (a few μV) and is heavily dependent on the proximity of the recording electrodes to the nodes of Ranvier. Accurate positioning of electrodes in such circumstances is extremely challenging as one cannot predict where the nodes of Ranvier will be located on the regenerating axons [1]. A way of solving this problem was recently reported by Fitzgerald et al. They found that confinement of axons in micro-channels removes the dependence of the recorded extracellular signal amplitude on the proximity of a node of Ranvier[10]. The micro-channels act as axonal signal amplifiers where the axons' confinement in the insulating channels increases the electrical resistance of the extracellular medium leading to an amplification of the recordable extracellular potential[1]. This means that designing an implant with micro-channels that can house regenerating axons will not only provide

mechanical guidance but will also allow axonal signals to be reliably recorded. The channel backbone carrying electrode sites in close proximity to the enclosed regenerated axons offers a potentially significant improvement in the fibre selectivity of the implant which means the ability of the implant to distinguish between signals recorded from different nerve fibres. This is advantageous for analyzing and processing the extracted signals which could then be used to drive muscle simulators or supply input signals to a prosthetic limb. This thesis presents the work done to optimize the design and the fabrication process of the SPNI implant to ultimately improve regeneration through it and enable a reliable recording of neural signals.

1.2. Overview of the thesis

To help understand the requirements of neural interfaces, chapter 2 introduces the anatomy of the nervous system briefly and sheds some light on the biological aspects governing the formation of neural signals and their propagation. The chapter starts by introducing the components of the nervous system which include the central nervous system (CNS) and the peripheral nervous system (PNS). It then presents the building block for this system (the neuron) and elaborates on how action potentials are formed and propagated based on processes taking place at the cell structure. The chapter also discusses how action potentials are used to communicate information between different neurons at various locations in the system.

Chapter 3 of the thesis gives an overview of the main neural interfaces that have been developed to interface with the peripheral and the central nervous systems. The design of each interface type is briefly explained in addition to its advantages and disadvantages. Most of the introduced interfaces were custom made to either be used in the peripheral or the central nervous system. The implants were categorized in CNS and PNS based on their posed invasiveness to the system. Examples of implants used in PNS included the cuff implants which is a sheet that wraps around the peripheral nerve like a sleeve. The inner surface of this sheet contains microelectrode sites for stimulating and recording neural signals. Another type of peripheral implant is the sieve regenerative implants.

These are thin sheets of material perforated with holes to allow the axons at the proximal end of a nerve to regenerate through it. Stimulation and recording are achieved through metal rings deposited on the periphery of the holes to come into contact with the regenerated axons.

Chapter 4 then introduces the driving concept behind the SPNI implant design which is the use of micro-channel confinement as axonal amplifiers to boost signals recorded from peripheral nerves. The term axonal amplifier implies confining the axons in a narrow space, (like a channel) to increase the extracellular resistance of medium (within the channel) resulting in amplification of the extracellular recorded signal. Enclosing the axons in such channels also removes the dependence of the recorded signal on its proximity to a node of Ranvier which poses a challenge when attempting to record from peripheral nerves. The chapter starts by presenting the results from a simulation model for myelinated and unmyelinated section of an axon confined in a channel. The changes to the extracellular signals are reported as a function of the channel and axon parameters. The chapter then summarizes findings from in vitro and in vivo studies that were carried out as part of this collaborative project. These findings will be incorporated into the SPNI implant design as will be seen later on in this thesis.

The thesis then introduces the design of the SPNI implant in chapter 5. First overview of the design concept behind the implant is given followed by a section detailing the dimensional requirements of the micro-channels based on experimental findings. The remainder of the chapter discusses the design of the electrodes and their placement in the rolled implant. This involves calculating the position of the neutral plane in the rolled structure where the strains are zero. Certain implant parameters can then be modified so that the metal layer of the implant is positioned at the neutral plane to protect it from mechanical failure posed by potential strains in the rolled structure of the device.

Chapter 6 presents the micro-fabrication techniques and methods that have been used in the fabrication and testing of the SPNI devices. The first part focuses on fabrication techniques such as spin coating, photolithography and etching methods. The control parameters for these techniques are also discussed. The final part of this chapter

introduces the electrochemical impedance spectroscopy which was used to test the SPNI devices and their performance in vitro. The fabrication process of the SPNI implants was then presented in chapter 7. The implant consisted of four layers, namely: the substrate, the metal layer, the insulation layer and the channel layer. The layers were fabricated and patterned using various photolithographic techniques. They were manually, then, peeled off and cut into individual sheets and rolled into 3D structures.

Chapter 8 of the thesis investigates ways of connecting to the SPNI implants. The Microflex interconnection Technique (MFI) was the chosen method to enable the SPNI implants to be connected to electronic circuitry, and hence enable access to the microelectrodes embedded in the micro-channels. After introducing MFI, the chapter presents the work that had been carried out to optimize the implant design and allow for the integration of this technique into the implant design. The testing of the fabricated SPNI devices with impedance spectroscopy is then presented in chapter 9. The chapter, first, presents an equivalent circuit that can be used to model the behaviour of the microelectrodes in the saline solution during impedance spectroscopy. The modelling is based on the work conducted by Andreas Frommhold [5]. The measured impedance and phase spectra for different SPNI devices prior and post rolling are then discussed and analysed.

Finally, the thesis introduces the in-vivo results from the implantation of the SPNI devices in the sciatic nerve of rats. To evaluate regeneration through the micro-channels of the SPNI, 24 passive SPNI implants (with no embedded microelectrodes) were implanted. Half of these had channel lengths of 2.5mm and other half had channels lengths of 4mm. The regeneration was then accessed at two time intervals (4 weeks and 12 weeks) post-implantation. The positive regeneration results through these passive implants led to the implantation of 6 active SPNI devices (with embedded electrodes) for three months. Stimulation and recording of neural signals through the SPNI implants was carried out in collaboration at King's college London. The results of these experiments are reported and analysed in chapter [10].

2. THE ANATOMY AND THE ACTIVITY OF NEURAL TISSUE

2.1. Introduction

In order to make progress with the research in this thesis, an understanding of the nervous system and its activity is needed. The focus of this section is to shed light on the basic constituents of the human nervous system and the biological aspect underlying neurological signals. Having an understanding of the systems and its operational principles will assist in finding potential solution for various problems or diseases associated with disruption of functionality in part of the nervous system. Most of the material in this chapter is compiled from [11]-[12-13]

2.2. The Nervous System

The nervous system is the mechanism that controls the functions of our bodies consisting of sensation, emotion, thought and motion. The basic components of this system are the nerve cells or neurons which are excitable cells that use electrical signals to communicate. The nervous system is made up of the Central Nervous system (CNS) and the Peripheral Nervous system (PNS). The CNS consists of the brain and the spinal cord containing the cell bodies of the neurons, whilst the PNS consists of the nerves which are extensions of the nerve cells that link the central nervous system to the rest of the body. The PNS provides input signals (afferent) to the CNS which then processes and interprets this information to produce an output response (efferent) which is transmitted via motor fibres to the appropriate organ. Examples of responses include contracting voluntary or involuntary muscles or trigger secretion in glands.

The nerve fibres consist of two cell types:

- The neurons (the nerve cells) which are responsible for transmitting the sensory input and motor output between the CNS and a targeted recipient in the body
- The glial cell (neuroglia) which are non-conductive cells. They are support cells that provide mechanical and physiological support to protect the neurons. In the PNS, these cells wrap around nerve extension of the nerve cell (known as an axon) to form myelin sheath.

2.2.1. Neurons

The human body contains approximately 100 billion neurons [5] which are the building blocks of the nervous systems. Fig. 2.1 presents an illustration of a single neuron. The neurons or nerve cells share three common structural elements; these are:

- The cell body (*soma*) which houses the cell nucleus containing the DNA. It also contains typical components found in cells generally to sustain their functionality. They have an approximate diameter in the range of 10 to 100 μm
- The dendrites which are short processes protruding from the cell body and branch to form a fine and complex network with dendrites from other neurons. They receive input signals from other neurons and transfer them to the cell body for processing.
- The axon which is a long, relatively thick fibre extending out from the cell body. It bi-directionally transmits signals between the cell body and other neurons or recipients in the body (afferent and efferent fibres). All neurons possess only one single axon. Axons branch out at their endings to form pre-synaptic terminals that connect to other neurons or cell to pass on relayed signals.

Neurons can be categorised based on function into three types; sensory neurons, motor neurons and inter-neurons. Sensory neurons propagate afferent signals from receptors into the central nervous system. Motor neurons propagate efferent signals from the CNS to effector organs such as muscles and glands. Inter-neurons are relay neurons which project locally to connect to nearby neurons and allow for signal distribution. They are the neurons that link sensory afferent and motor efferent neurons.

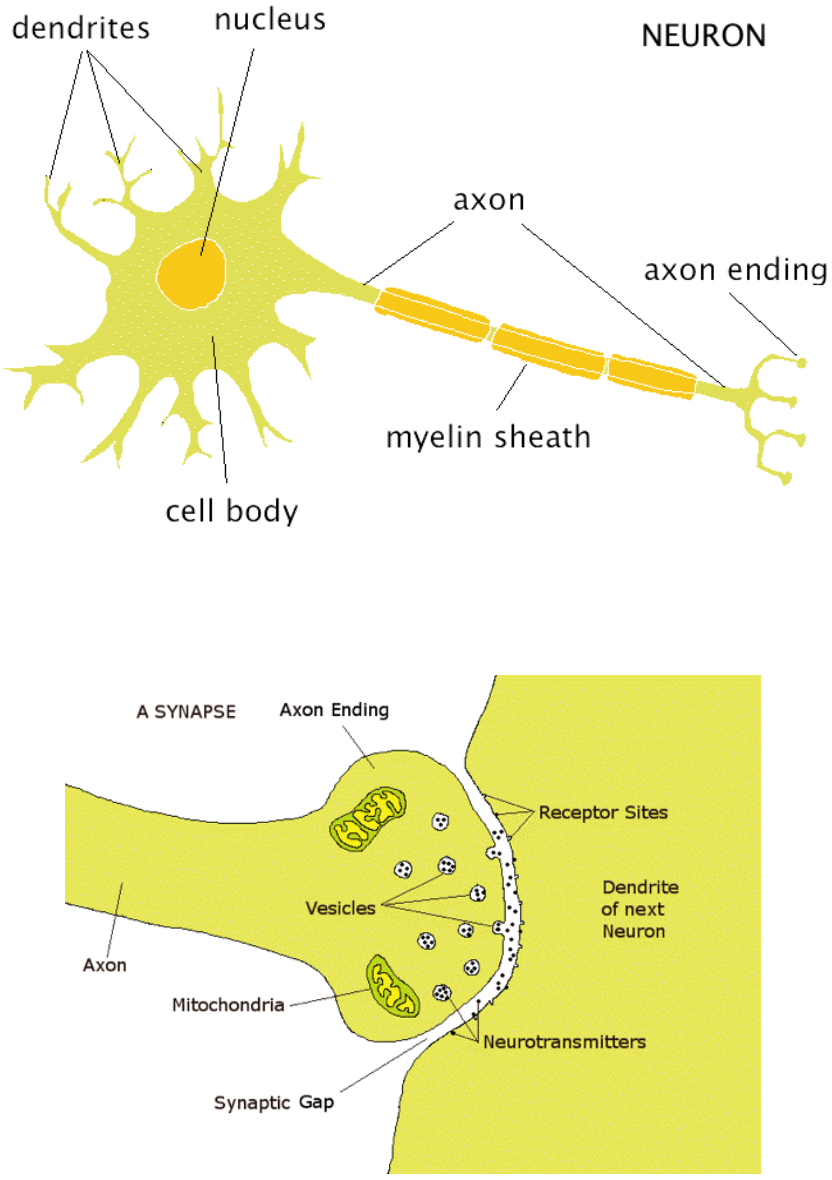


Fig. 2.1: Nerve cell. Top-The structure of a typical neuron, Bottom: illustration of an active synapse between two neurons [14]

Many neurons have axons that are encapsulated by a myelin sheath. In the peripheral nervous system, the myelin sheath is made of Schwann cells wrapped around the axon whist oligodentrocytes are responsible for forming myelin sheath in the central nervous system. Each myelinated axon is encased by many Schwann cells along its length which are separated by regular gaps called 'the nodes of Ranvier'. These nodes and the myelin sheath have substantial effect on the propagation properties of electrical signals; the

insulating characteristic of myelin forces the neural signal to jump from one node of Ranvier to the next (known as saltatory conduction) instead of propagating along the axon in a continuous fashion. Because of this, saltatory conduction has much higher conduction velocities when compared to continuous conduction. Axons have diameters in the region of 0.2 μm to 20 μm and they are normally organised into bundles called nerves.

Signals are propagated in the form of action potentials which are relayed between neurons through synapses made up of an axon terminal of one neuron and the dendrite of a nearby cell (see Fig. 2.1 Bottom). Electrical stimulation at the axon terminal elicits the release of chemical transmitters (neurotransmitters) which cross the synaptic cleft to arrive at the receptors in the post synaptic terminal of the neighbouring cell triggering a new action potential in this cell. Pre-synaptic part is located on an axon but some pre-synaptic sites are located on a dendrite or soma. Post-synaptic part can be found on a dendrite, soma but can also be found on cells like a muscle fibres evoking muscle contraction.

2.2.2. Cell membrane

The excitable membrane of nerve cells is what gives the ability to be conductive and transfer electrical signals. It consists of phospholipids which possess hydrophilic heads and hydrophobic tails causing these molecules to congregate into a bi-layer arrangement as illustrated in Fig. 2.2. In addition, the cell membrane has ion channels distributed along its length. They enable the transport or the flow of ion such as sodium, potassium, chloride and calcium through the membrane. These ion channels are made of special proteins with ion-selective properties giving them the ability to change their permeability according to the potential difference across the membrane. So these voltage-controlled ion channels enable the membrane to sustain a differential in the ion concentrations across it which translates into a trans-membrane potential v_m. This is defined as the potential difference between the inner surface of the membrane (Φ_i) and its outer surface (Φ_o), hence:

$$V_m = \Phi_i - \Phi_o \qquad \text{(Equ. 2.1)}$$

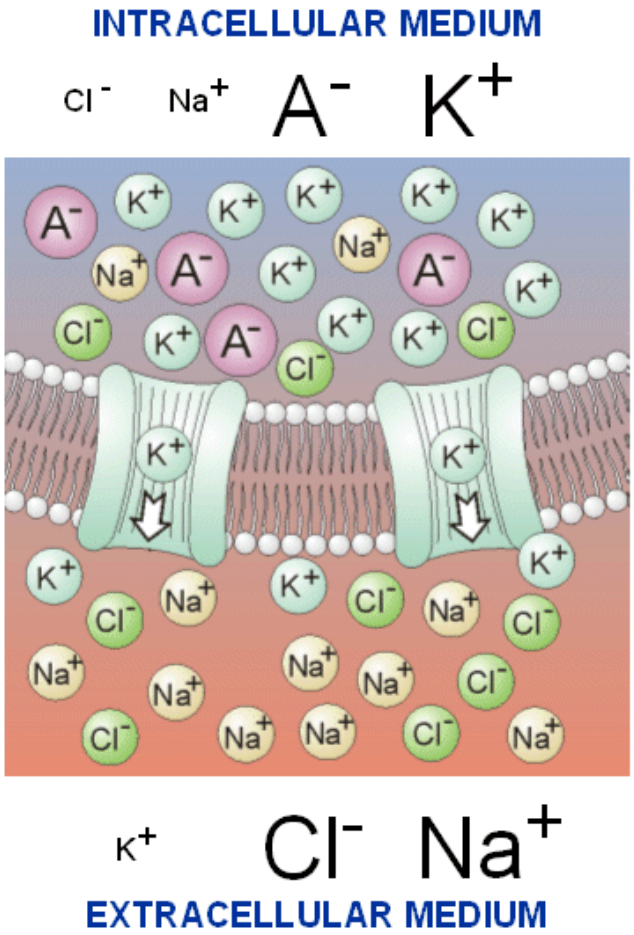


Fig. 2.2: A schematic of a nerve cell membrane with ions and ion channels. Sodium (Na^+), Potassium (K^+) and chloride (Cl^-) are capable of flowing across the membrane. The concentrations of these ions on the inside and on the outside surface of the membrane are unequal. The large in size A^- anion symbolises immobile and impermeable molecules that are important for the electroneutrality but do not contribute to ionic flow[13]

In the absence of a stimulus signal, the trans-membrane potential is at an equilibrium value of around -65mV which is often referred to the membrane resting potential. The membrane maintains this value by retaining a high concentration of sodium (Na) outside the cell and high concentration of potassium (K) inside the cell through a specialised ion channels acting as Na-K pump. Stimulation disturbs this potential balance. If the stimulus triggers a change in the trans-membrane voltage that rises above a certain threshold, a nerve pulse is generated. This increases the permeability of the membrane to sodium (through specialised Na-channels) allowing an influx of sodium into the cell which results

in the inner surface of the membrane becoming more positive. As a reaction to this, the membrane becomes more permeable to potassium ions (through specialised K-channels) allowing an efflux of potassium ions out of the cell which aims to restore the trans-membrane potential to its resting value. Consequently, the Na-K pump restores the ion concentrations inside and outside the cell to their initial values. Once activated the membrane becomes insensitive to any new stimuli regardless of its strength. This is referred to as the *absolute refractory period.* Near the end of the activation pulse, the membrane may be activated by a strong stimulus. This period is referred to as the *relative refractory period*.

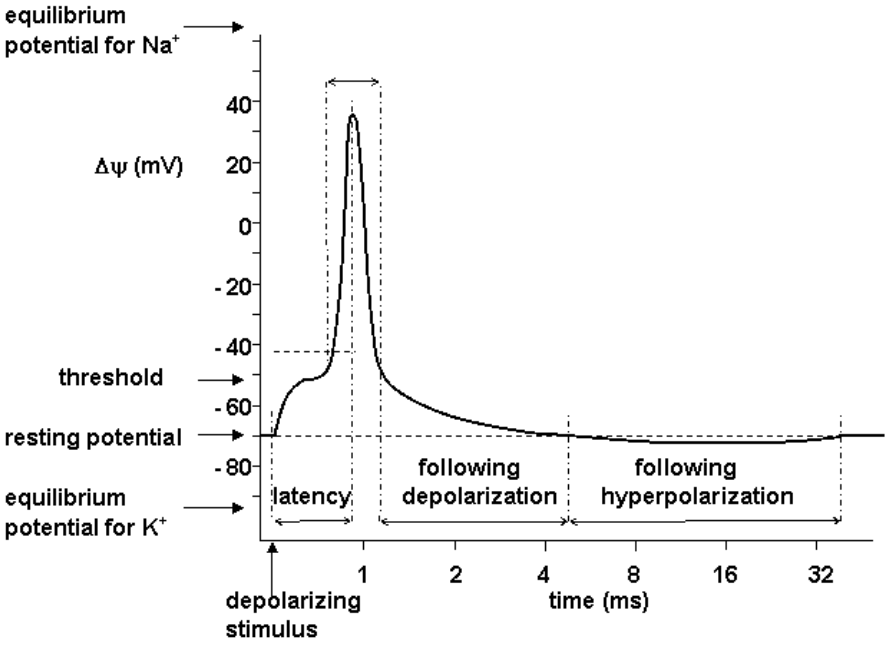


Fig. 2.3: Action potential[15]

The sequence of changes in the transmembrane potential led by changes in ionic concentrations across is referred to as nerve impulse or action potential (shown in Fig. 2.3). This signal propagates along the membrane as an unattenuated signal. The conduction occurs as the potential difference between activated and un-activated regions of the membrane create small local currents that circulate between them. These currents flow in such a direction that would cause stimulation in the un-activated region leading to the same process of the nerve impulse to be triggered again at this region (Fig. 2.4). This

shows that neural signal conduction is the repetitive recreation of the action potential along the membrane.

A generated action potential does not attenuate during propagation and is characterised by a shape and amplitude that is independent of the strength of the stimulus. In fact, in neurophysiology, information about the stimulus strength and latency that triggered the action potentials is coded in the frequency of the action potential firing (please refer to Fig. 2.5 for frequency coding). As can be seen from this figure, a larger and longer stimulus produces a higher frequency of action potentials firing in comparison to a smaller and shorter stimulus.

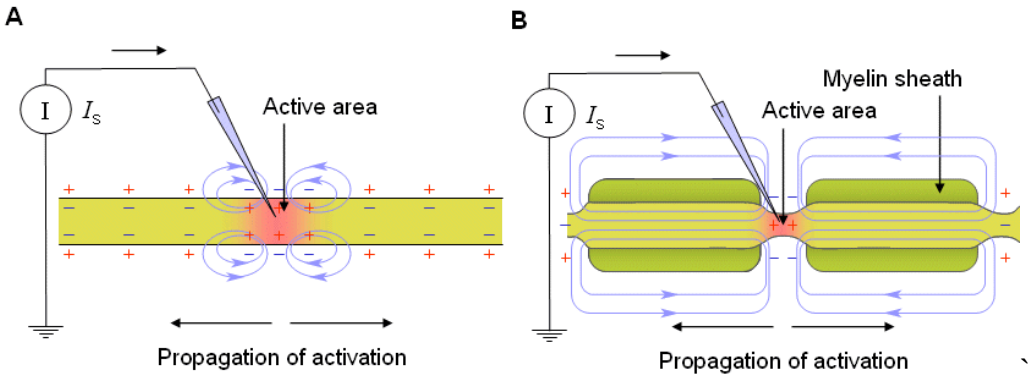


Fig. 2.4: Conduction of an action potential in an axon. (A) continuous propagation in an unmyelinated axon, (B)Saltatory conduction in a myelinated axon[13]

Stimulation can either increase the positivity of the inner surface of the membrane relative to the outer surface which triggers an action potential in the membrane once the threshold has been reached. This type of stimulation is said to be excitatory or depolarizing. Or it can increase the negativity of the inner surface of the membrane relative to the outer surface which decreases the probability of firing. This type of stimulation is said to be inhibitory or hyperpolarising and it can be used to silence a particular nerve cell and prevent it from firing. If the depolarizing stimulus is insufficient for the trans-membrane potential to reach the threshold, the membrane will not fire an action potential and the stimulus pulse will simply decay. If the depolarizing stimulus is strong enough for the trans-membrane potential to reach the threshold, a propagating non-decaying action potential is fired.

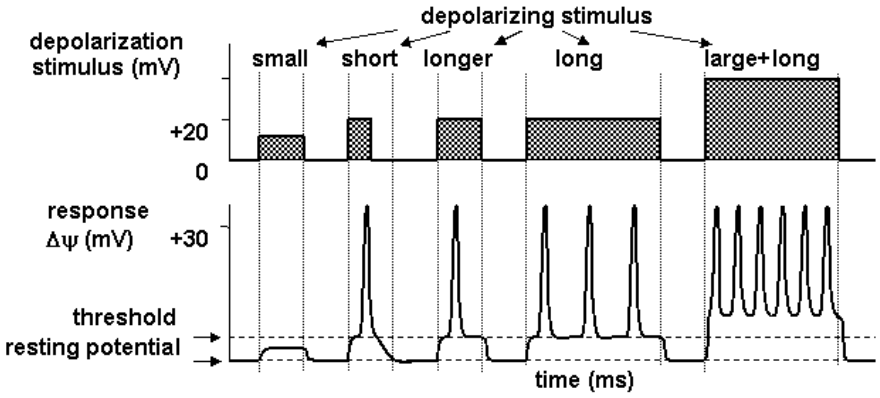


Fig. 2.5: Frequency coding of neural signals[15]

2.2.3. The Hodgkin Huxley membrane model

The mechanisms for the creation and propagation of action potentials can be modelled into an equivalent electrical circuit using an empirical model established by Hodgkin and Huxley. The model is based on their seminal experiments which used voltage clamp on giant axons of the Squid. The motivation behind this model is to derive equations that can be used to calculate action potentials theoretically with reasonable accuracy.

The model developed what is known now as "the parallel conductance model" which defines the current flowing across the cell membrane during excitation. It represents ion conducting channels as four separate current branches as illustrated in Fig. 2.6. These four branches are current due to sodium ions, current due to potassium ions, current due to leakage caused mainly by chloride and capacitive current due to the displacement and separation of ions by the membrane.

The ion permeability of the membrane to each ion type is represented by its conductance per unit area as:

$$G_{\mathrm{Na}} = \frac{I_{\mathrm{Na}}}{V_{\mathrm{m}} - V_{\mathrm{Na}}} \quad \text{(Equ. 2.2)}$$

$$G_{\mathrm{K}} = \frac{I_{\mathrm{K}}}{V_{\mathrm{m}} - V_{\mathrm{K}}} \quad \text{(Equ. 2.3)}$$

$$G_{\mathrm{L}} = \frac{I_{\mathrm{L}}}{V_{\mathrm{m}} - V_{\mathrm{L}}} \quad \text{(Equ. 2.4)}$$

Where G_{Na}, G_k, G_L are the membrane conductances per unit area for sodium, potassium and other ions referred to as leakage conductance [S/cm2], I_{Na}, I_k, I_L are the electric currents due to sodium, potassium and other ions (leakage current) per [mA/cm2], V_{Na}, V_k, V_L are Nearst voltage for sodium, potassium and other ions (leakage voltage) [mV], V_m is the membrane voltage .

The above Nernst voltages are defined by the Nernst equation as:

$$V_{Na} = -\frac{RT}{zF} \ln \frac{C_{i,Na}}{C_{o,Na}} \quad \text{(Equ. 2.5)}$$

$$V_K = -\frac{RT}{zF} \ln \frac{C_{i,K}}{C_{o,K}} \quad \text{(Equ. 2.6)}$$

$$V_{Na} = -\frac{RT}{zF} \ln \frac{C_{i,l}}{C_{o,cl}} \quad \text{(Equ. 2.7)}$$

Where R is the gas constant which is 8.314 J/(mol.K), T is the absolute temperature, for Na and K z= +1, and for CL z=-1, F is the faraday constant [9.649x104C/mol], $c_{i,Na}, c_{i,k}, c_{i,cl}$ are the intracellular concentrations for Na, K and CL respectively, $c_{o,Na}, c_{o,k}, c_{o,cl}$ are the extracellular concentrations for Na, K and CL respectively.

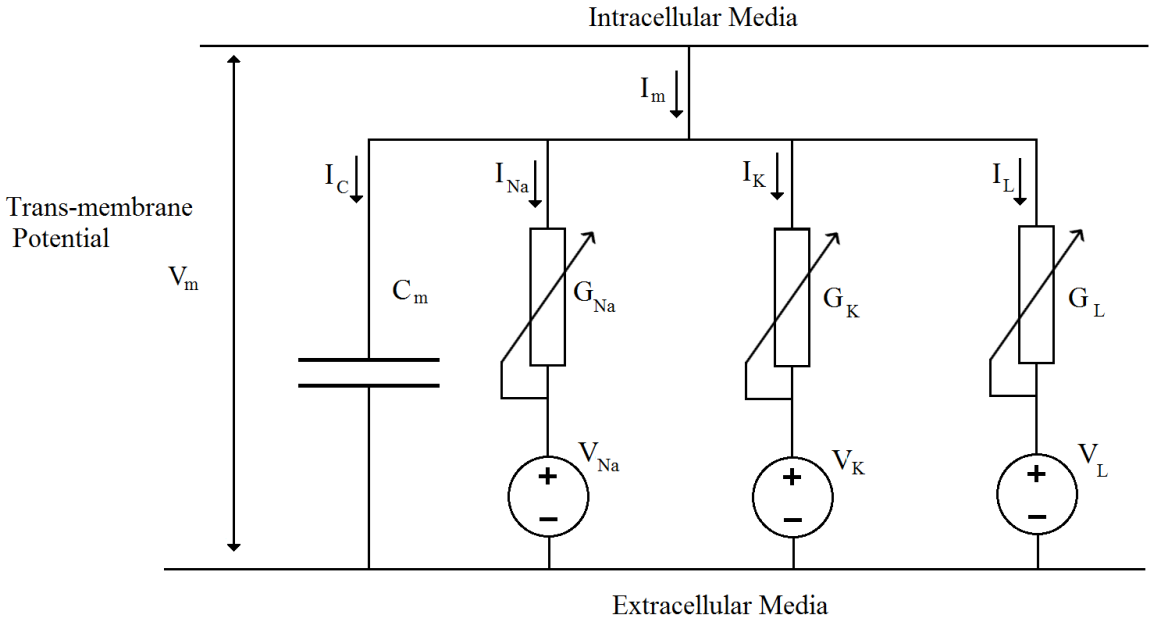


Fig. 2.6: The equivalent circuit for a patch of neural membrane based on the Hodgkin-Huxley model

The overall membrane potential V_m is formed by the sum of all the different ion channels. The driving force for each ion is given by the difference between the membrane potential and the Nernst voltage for that ion type. By assuming a constant field across the membrane and maintaining that at the resting potential, the sum of the ion currents from all ion species must be zero, the equation for the membrane voltage becomes:

$$V_m = \frac{RT}{F} \ln\left(\frac{P_k c_{i,k} + P_{Na} c_{i,Na} + P_{cl} c_{o,Cl}}{P_k c_{o,k} + P_{Na} c_{o,Na} + P_{cl} c_{i,Cl}}\right) \qquad \text{(Equ. 2.8)}$$

Where P_K, P_{Na}, P_{CL} are the permeability for K, Na and Cl respectively

The total membrane current can be obtained by summing the branch currents, hence:

$$I_m = C_m \frac{dV_m}{dt} + (V_m - V_{Na})G_{Na} + (V_m - V_k)G_k + (V_m - V_L)G_L \qquad \text{(Equ. 2.9)}$$

An expression for the different ion conductances is required to solve (Equ. 2.9). To do this, Hodgkin and Huxley suggested a gating system for channels. They assumed the existence of ion specific charged particles inside the membrane that do not directly

transport the ions but allow the ion to pass through the membrane by permitting them to be placed in specific sites in the membrane. The rate at which these ions transport has a direct effect on the conductances as it defines the rate at which the maximum conductances are reached. The model did not investigate the nature of these gating particles but only used them to determine how open the ion channels are for each ion type.

For potassium, the model revealed during experiments that for this ion species, the time variation of the conductance was following a 4^{th} power variable, which follows 1^{st} order kinetics. They then assumed an n-particle which can be electrically charged to control the gating of the potassium channels by allowing them to be either open, closed or somewhere in between these two states (Fig. 2.7). n was defined as the probability of finding the particle in the open state whereas $(1 - n)$ was the probability of finding the particle in the closed state, given $0 \leq n \leq 1$.

With the change in the trans-membrane potential, the distribution of the transport-particle changes resulting in voltage-dependent transfer rates for the ion species (α_n and β_n) that are defined in Table 2.1. Given an initial value for the probability n , subsequent values can be calculated using the following differential equation:

$$\frac{dn}{dt} = \alpha_n(1 - n) - \beta_n n \qquad \text{(Equ. 2.10)}$$

Where α_n is the transfer rate from closed to open, β_n is for the reverse transition, n is the fraction of n-particles in the open state, $(1 - n)$ is the fraction of n-particles in the closed state.

According to (Equ.2.10) the rate of increase in the probability of n-particles being in the open state ($\frac{dn}{dt}$) is dependent on their open state fraction (n) and their closed state fraction ($1 - n$) and on the transfer rate coefficients α_n and β_n. The n-particles are electrically charged and their transfer rates are voltage dependant and not time dependant.

$\alpha_n = \frac{0.1 - 0.01(V_m - V_r)}{e^{1-0.1(V_m - V_r - 1}}$	$\beta_n = \frac{0.125}{e^{0.0125(V_m - V_r)}}$
$\alpha_m = \frac{2.5 - 0.1(V_m - V_r)}{e^{2.5-0.1((V_m - V_r)-1}}$	$\beta_m = \frac{4}{e^{(V_m - V_r)/18}}$
$\alpha_h = \frac{0.07}{e^{0.05(V_m - V_r)}}$	$\beta_n = \frac{1}{e^{3-0.1(V_m - V_r)+1}}$

Table 2.1: Expressions for transfer rate coefficients [13]

The 4th power variable found in the potassium conductance variation means that the potassium gate has four n-particles that need to be in the open state for the potassium channel to be open. Hence the probability of the channel to be open is n^4, given that the probabilities of the particles to be open are independent of one another. Thus, the conductance of potassium per unit area is given by:

$$G_K = G_{K,max}.n^4 \qquad \text{(Equ. 2.11)}$$

Where $G_{k,max}$ is the maximum conductance for the state when all channels where open. Fig. 2.7 summarises the idea of the Hodgkin-Huxley model for potassium conductance. Part A of the figure illustrates the response of the n-particles to a sudden depolarisation. To begin with, the fraction of n-particles in the permissive open position (n) is small since α_n is small and β_n is large. Consequently, the potassium channels are closed. Depolarisation increases α_n and decreases β_n allowing n to increase exponentially and reach a maximum value of n_∞. When four n-particles occupy the site around the channel inside the membrane, the channel opens suggesting that the conductance of potassium (G_K) is proportional to n^4 as expressed in (Equ. 2.11). The thickness of the two opposing arrows shown in Fig. 2.7(A) corresponds to the magnitude of the transfer rate coefficients α_n and β_n which are also represented by the curves in Fig. 2.7(B). The response of n and n^4 to a sudden depolarisation is illustrated in Fig. 2.7(C)[13].

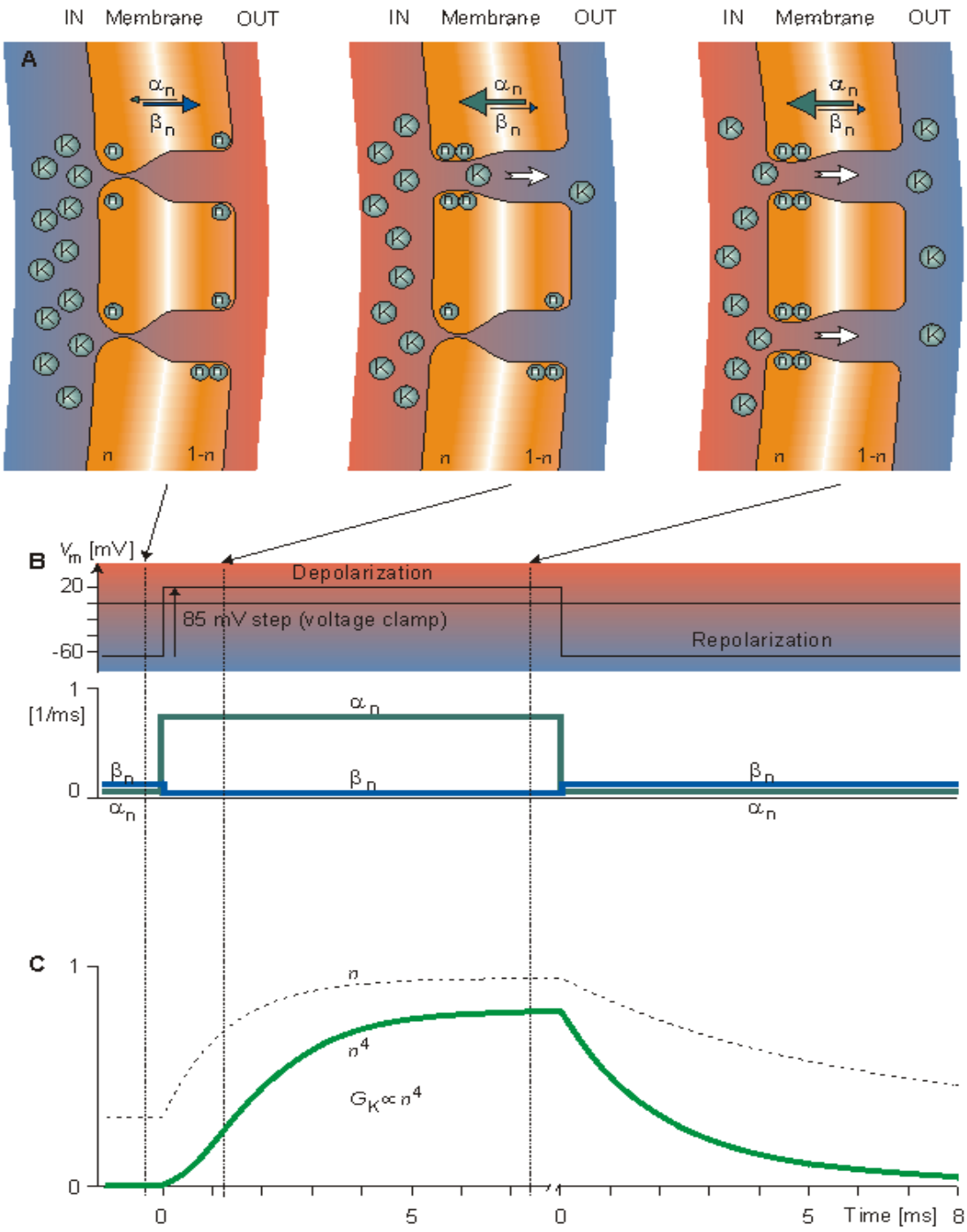


Fig. 2.7: The process for determining the variation of potassium conductance during depolarisation and repolarisation in the voltage clamp mode based on the Hodgkin-Huxley model. (A) The response of n-particles to a sudden depolarisation. (B) The transfer rate coefficients response (α_n and β_n) to sudden depolarisation and repolarisation. (C) n and n^4 response to a sudden depolarisation and repolarisation (potassium conductance G_K is proportional to n^4).

For sodium, the model assumed two types of transport particles; the m-particle as the channel activating particle and the h-particle as the channel inhibiting particle. The electrically charged m-particle has an activating probability 'm' whilst the h-particle has a non-inhibiting probability 'h'. The position of these particles control the opening of the sodium channel indicating that they have two states; an open permissive state and a closed non-permissive state. *m* represents the fraction of these particles in the open state whist *(1-m)* represents the fraction of these particles in the closed state (with $0 \leq m \leq 1$). It was found during the experiments conducted by Hodgkin-Huxley that unlike potassium conductance, the rise in sodium conductance produced by membrane depolarisation is not maintained. The decrease in sodium conductance was attributed to the existence of an inactivation process represented by the introduction of an inhibiting h-particle. The dimensionless parameter *h* represents the fraction of these particles in the permissive non-inhibiting state whist *(1-h)* represents the fractions of these particles in the non-permissive inhibiting state. The expression for the voltage and time dependant transitions of the m-particles and the h-particles between the open and the closed positions is similar to that for potassium. Hence the equations for voltage dependant transfer rate coefficients relating to the m- and h-particles (α_m, β_m and α_h, β_h respectively) are provided in Table 2.1. These follow a 1st order kinetic process. Similar to potassium, the behaviour of sodium activation can be described by the following 1st order differential equations:

$$\frac{dm}{dt} = \alpha_m(1 - m) - \beta_m m \qquad \text{(Equ. 2.12)}$$

$$\frac{dh}{dt} = \alpha_h(1 - h) - \beta_h h \qquad \text{(Equ. 2.13)}$$

Where α and β correspond to the voltage dependant transfer rates coefficients.

The Hodgkin-Huxley model proposed that the channel is transitioned into in the open state by three m-particles occupying the specific sites reserved for open state inside the membrane, (Fig. 2.8A) and the channel is not inactivated by one h-particle in the inhibiting state. As a result, the sodium conductance is proportional to $m^3 h$, and hence:

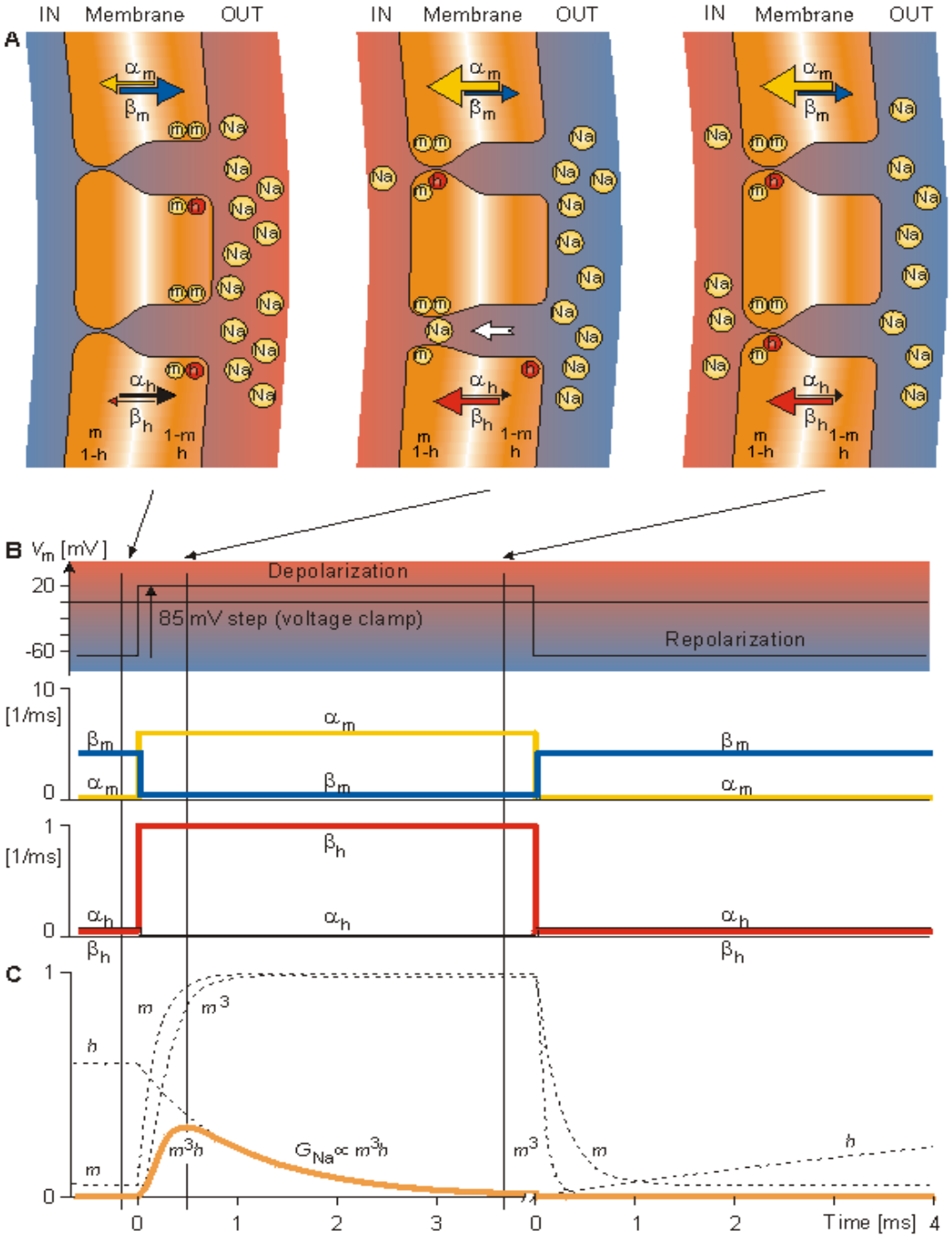


Fig. 2.8: The process for determining the variation of sodium conductance during depolarisation and repolarisation in the voltage clamp mode based on the Hodgkin-Huxley model. (A) The response of m- and h-particles to a sudden depolarisation. (B) The transfer rate coefficients response (α_m , β_m , α_h and β_h) to sudden depolarisation and repolarisation. (C) m , h , m^3 and m^3h response to a sudden depolarisation and repolarisation (sodium conductance G_{Na} is proportional to m^3h)[13].

$$G_{Na} = G_{Na,max} \cdot m^3 h \qquad \text{(Equ. 2.14)}$$

Where $G_{Na,\max}$ is the maximum value of sodium conductance [mS/cm^2]

Fig. 2.8 summarises the idea of the Hodgkin-Huxley model for sodium conductance similar to what was done for potassium (shown in Fig. 2.7). Part A of Fig. 2.8 illustrates the response of the m- and the h-particles to a sudden depolarisation. At first, the fraction of m-particles in the permissive open position (m) is small since α_m is small and β_m is large. Hence the sodium channels are closed. On the other hand, the initial fraction of h-particles in the non-inhibiting open position (i.e. outside the membrane as shown in the figure), *h*, is large as α_h is large and β_h is small. Depolarisation allows α_m and β_h to increase, β_m and α_h to decrease. The magnitude of these coefficients is indicated by the thickness of the opposing arrows in Fig. 2.8(A) and by the curves in Fig. 2.8(B).

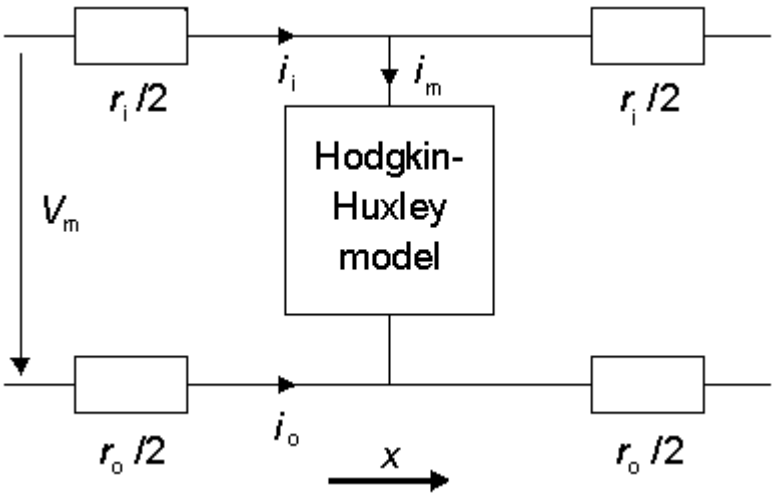


Fig. 2.9: Equivalent circuit to model to incorporate action potential conduction [13]

The parameter *m* has short time constant which allows the channel to open quickly while *h* has longer time constant which delays the closing of the channel. This results in pulse like behaviour (as shown in Fig. 2.8C). The channel transporting sodium opens when three m-particles occupy their sites around the channel on the inside of the membrane and one h-particle occupies a site on the outside of the membrane. Initially, the sodium conductance is proportional to m^3. This is because *h* (representing the fraction of h-

particles in the non-inhibiting state) is initially large and non-inhibiting h-particles occupy the open site of the channel outside the membrane (Fig. 2.8A and C). Soon after, the longer time constant for the parameter *h* allows the inhibiting h-particles to move to the inside of the membrane, blocking the sodium channels. Therefore, as presented in equation [2.13], the behaviour of the sodium conductance G_{Na} is proportional to m^3h.

The Hodgkin-Huxley model developed expressions to describe the voltage dependent transfer rate coefficients based on experimental measurements, in addition to equations for the ionic conductances and the transmembrane current. Values were given to the constant parameters in these expressions, and a model describing the membrane properties that enable the generation of action potentials was realised.

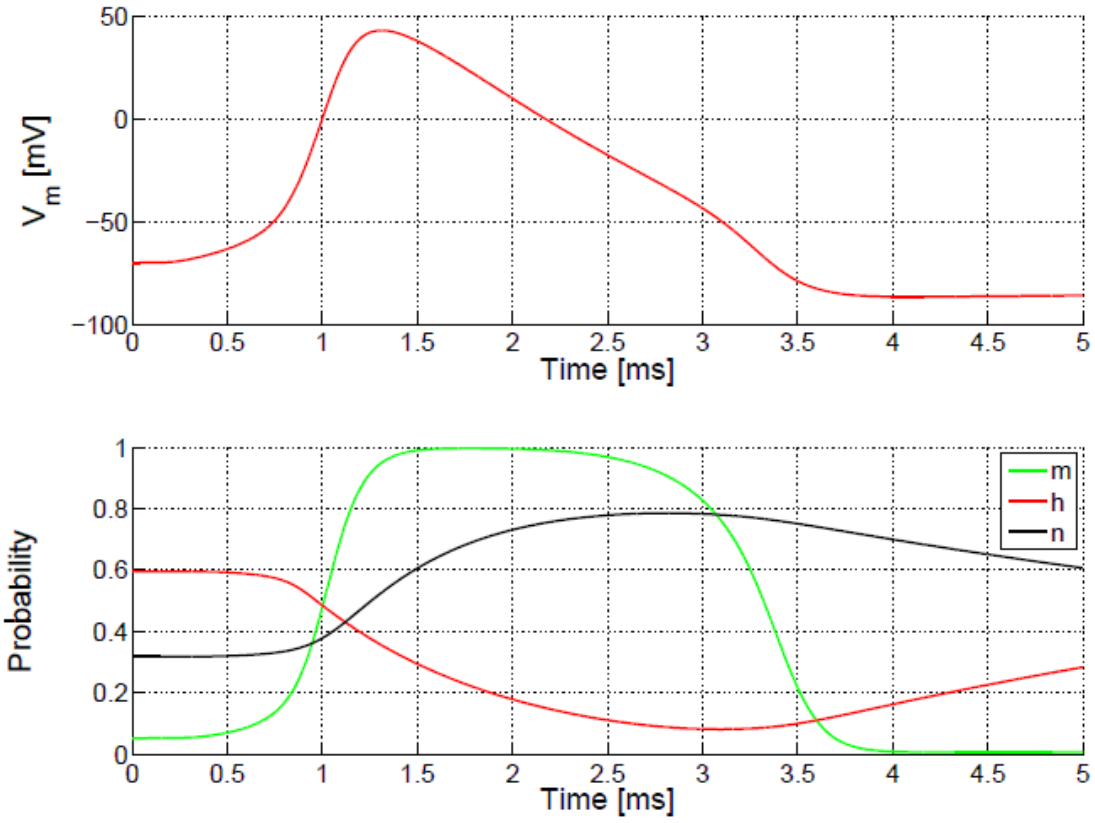


Fig. 2.10:Action potential computations based on the Hodgkin-Huxley model. Top- computed action potential halfway a 50μm long axon based on Hodgkin-Huxley model, Bottom- gating parameters for the ion channels[5]

However, to describe the propagation of the action potential, the model needs to incorporate an axial component in the trans-membrane current. Fig. 2.9 illustrates the

equivalent circuit model for propagating action potential in unit length area of unmyelinated axon. r_i and r_o respectively represent the intracellular and the extracellular resistances of the axon per unit length whilst the Hodgkin-Huxley model connects the inside and the outside. The total membrane current in this model can be written as the following cable equation:

$$i_m = \frac{1}{r_i + r_o} \frac{\delta^2 V_m}{\delta x^2} \qquad \text{(Equ. 2.15)}$$

Substituting for i_m in (Equ. 2.9), produces a partial differential equation that describes action potential propagation as it depends on the x coordinate along the axon besides its time dependency. The equations can be solved for the membrane voltage under activation with the help of mathematical software package such as MATLAB. This allows for action potentials and other variables to be plotted and studies as illustrated in the example shown in Fig. 2.10.

2.3. The brain and the peripheral nervous system

Action potentials generated at the distal axonal part of a sensory neuron travel to the cell body, located in the root ganglion on either side of the spinal cord, and are then relayed to other neurons until they reach a particular location in the brain. Signal processing takes place in the neural cell bodies at each stage.

The brain consists of five main parts shown in Fig. 2.11. They are:

1. The cerebrum
2. the inter brain
3. the midbrain
4. the pons varolli and the cerebellum
5. the medulla oblongata

The cerebrum is the largest part of the brain and is made up of the two cerebral hemispheres separated by a deep fissure. It has strong folds with a surface area of 1600cm^2 and a 3 mm thickness. Particular areas in the cerebral cortex are mapped to

specific functions for certain parts of the body (Fig. 2.12). The left hemisphere is for sensory control whilst the right hemisphere for motor control. The cortex consists of 6 layers each containing different types of neurons. It consists of neurones and unmyelinated axons which together form grey matter, and white matter which is mainly consists of myelinated fibres that link various regions of the CNS.

The brain is enclosed in three meninges (layers) and housed in skull bone for protection. The meninges consist of three layers: the dura mater, the arachnoid mater and the pia mater whose primary function, together with cerebrospinal fluid, is to protect the CNS (the brain and the spinal cord). The dura mater is the outermost layer and it is relatively thick and resilient.

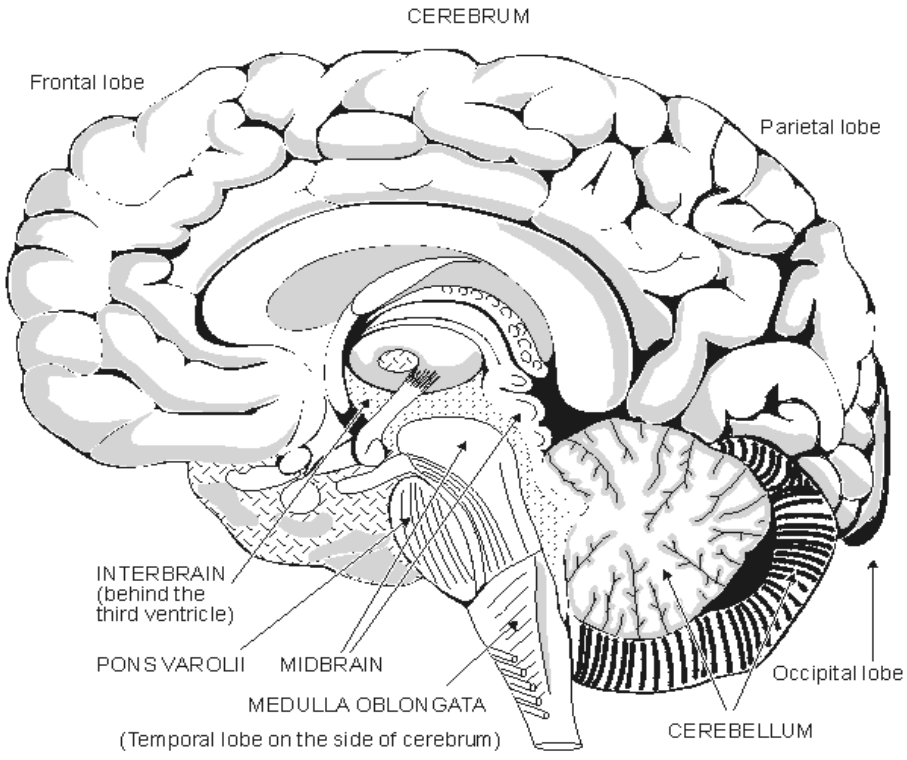


Fig. 2.11: The brain anatomy[13]

The arachnoid is the middle layer. It is thin and transparent with a spider-web like structure. The pia mater is a very delicate membrane which firmly attaches to the brain surface. The subarachnoid space is the space that separates the arachnoid and pia and is

normally filled with cerebrospinal fluid which serves as a buffer for the brain's cortex providing mechanical and immunological protection.

The nervous system has four major pathways to the brain. These are visual path, and the auditory path, the cutaneous path from the skin and the kinaesthetic path from the muscles. Muscles control can be lost through disruption to the kinaesthetic path which connects to the motor cortex. Specific sections of the motor cortex control specific muscles groups as has been shown through various studies. Research has also pointed out that imagined movement can also activate the same regions in the motor cortex. This can have a very useful application in neuro-prosthetics, where the imagined activity can be monitored and used as an input to cognitively control prosthesis or a computerised system.

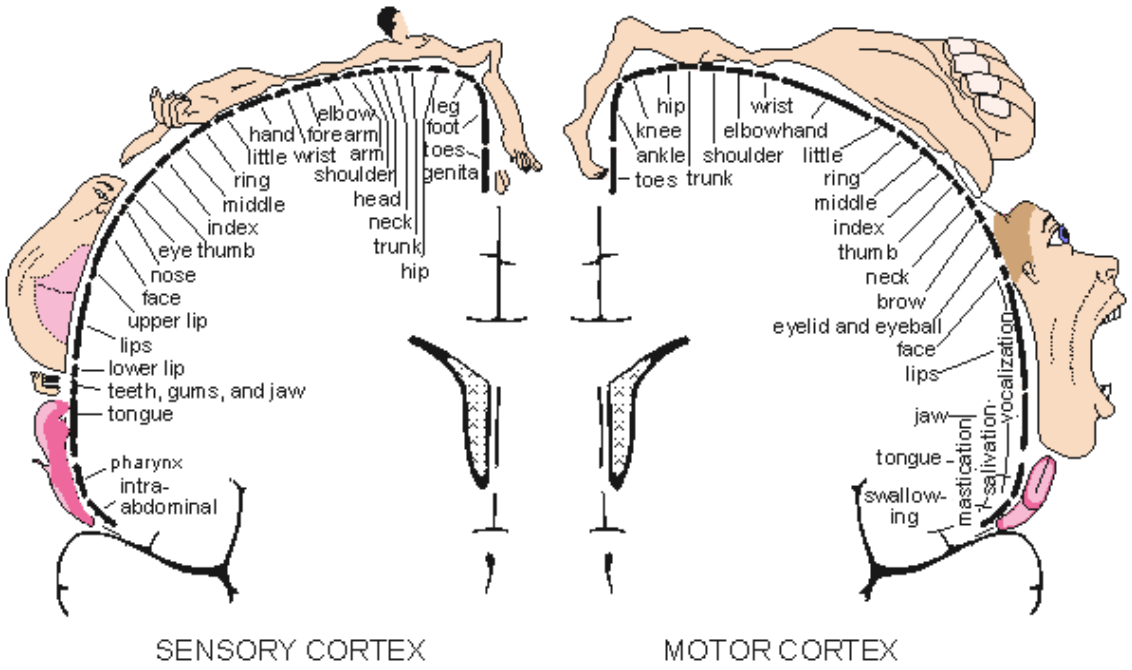


Fig. 2.12: mapping sensory and motor functions in the human cortex[13]

Unlike the brain, the neural structure of the PNS is less complex. As illustrated in Fig. 2.13, a peripheral nerve consists mainly of nerve fibre bundles that connect neurons in the CNS to their sensory and motor receptors in the body. Hence, the PNS communicates all sensory information and motor function between the brain and the body's periphery. In

PNS, the individual axons are surrounded by connective tissue called endoneurium. They are grouped into bundles referred to as fascicles which are enclosed by perineurium; a sheath of connective tissue. The fascicles are organised based on destination rather than function. The individual fascicles clustered and attached together by a collegen matrix called the epineurium which provides mechanical protection and support. Blood vessels also travel along the length of the fascicles providing vital nutrients and oxygen supply[5].

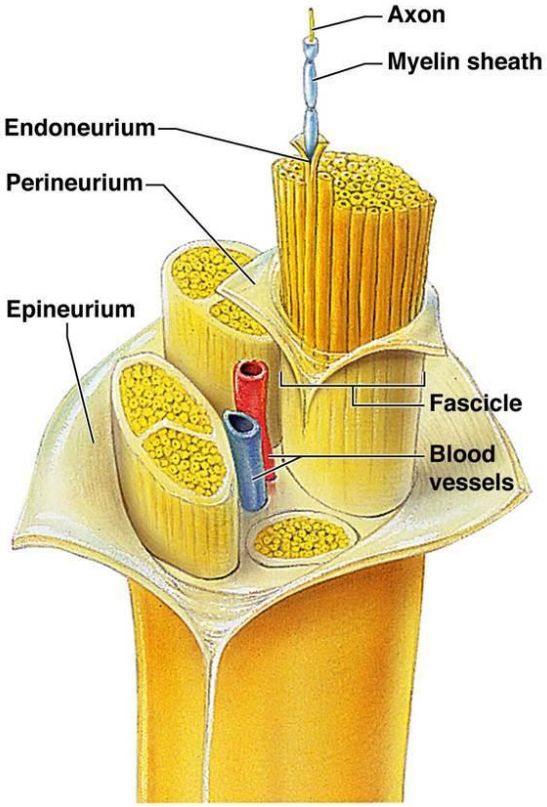


Fig. 2.13: Illustration of the structure of a peripheral nerve[16]

In contrast to the CNS, the PNS is not protected by bone and hence it is more susceptible to trauma. However, nerve fibres in PNS have the ability to regenerate after injury unlike axons in CNS. If a nerve is severed or crushed, the distal part disconnected from the cell body degenerates while the proximal part still connected to the cell body regenerates. This allows a degree of functionality to be restored to the affected body part. This feature has been exploited with the design of regenerative implants to capture useful information from the proximal stump and feed this to drive muscle simulators or artificial limbs.

2.4. Chapter Summary

The SPNI implant, whose design and fabrication is the focus of this thesis, will be used to stimulate and/or record from nerve fibres. Hence gaining an insight into the nervous system and its constituents, in addition to the mechanisms governing the generation of neural action potentials, is of great importance. This chapter has, therefore, introduced the nervous system which consists of the central nervous system (the brain and the spinal cord) and the peripheral nervous system. An insight into the complexity of the central nervous system was also given through a concise explanation of the anatomical composition of the brain. The peripheral nervous system which is anatomically less complex was also discussed and the differences between two systems (i.e. the central and the peripheral nervous systems) were highlighted. A substantial part of this chapter was dedicated to the neuron which is considered the building block of the nervous system. The mechanisms for generating propagating action potentials rely on the properties of the neural cell membrane which were explained and described based on the Hodgkin-Huxley model.

The next chapter presents a review of the various neural implant types that have been designed to stimulate and record from the nervous system. The advantages and the limitations of each implant type were also highlighted.

3. REVIEW OF INTERFACING TECHNOLOGY

3.1. Introduction

This chapter will present the methods that have been developed to examine neural cells and their activity. The advent of microelectronic technology has made it possible to fabricate suitable electrical interfaces that can be used to gather information from and stimulate neural tissue. Various designs have been custom made to match the anatomical requirements of the neural tissue; these can be grouped into interfaces developed for the peripheral nervous system (PNS) and those developed to interface with the central nervous system (CNS). The most common examples for each camp will be discussed in the remainder of this chapter. A brief review on the materials used to fabricate neural interfaces and their biocompatibility is also provided towards the end of the chapter. The information presented here is compiled mainly from the following resources: the review of implants and technology developed to record from the PNS by Navarro et al, the review of interface technology for CNS and PNS taken from Neuroprosthetics: theory and Practice [11], Methods for recording electrical signals from neural tissue chapter in the thesis titled Novel processing routes for neural interfaces by Richard Barrett[17], the review chapter of Brain computer interfacing technology in the thesis titled Mechanical design of an inject-able micro-sensor for neural connection within the motor cortex of the human brain by John P.F. Spratley[18], and finally from review journal article titled: A critical review of interfaces with the peripheral nervous System for the control of neuroprostheses and hybrid bionic systems [19].

3.2. Review of peripheral nerve interfacing technology

The fascination of humans by the possibility of interfacing and controlling artificial prosthesis with biological signals has led to the development Functional Electrical

Stimulation (FES) and neuroprostheses. A substantial research and resources have been dedicated to develop neuroprostheses and bionic systems that connect the human nervous systems with electronics or artificial limbs. This is done with the hope of restoring motor and sensory function in disabled patients. Neural interfaces are used by various neuroprostheses to interface with peripheral nerves or muscles for neuromuscular stimulation or signal recording. The aim of this section is to provide a critical review of the peripheral nerve interfaces available with an insight into their clinical or research based uses. The focus is particularly on the characteristics and suitability of different types of electrodes, and their biomedical applications

Recent advances in technology in conjunction with a more advanced understanding of neural functions have made the construction of bi-directional interfaces, more feasible. These interfaces can allow an exchange of information between the central nervous system and computerized artificial instruments by means of micro-wire or microelectrode arrays implanted in the brain or in the spinal cord.

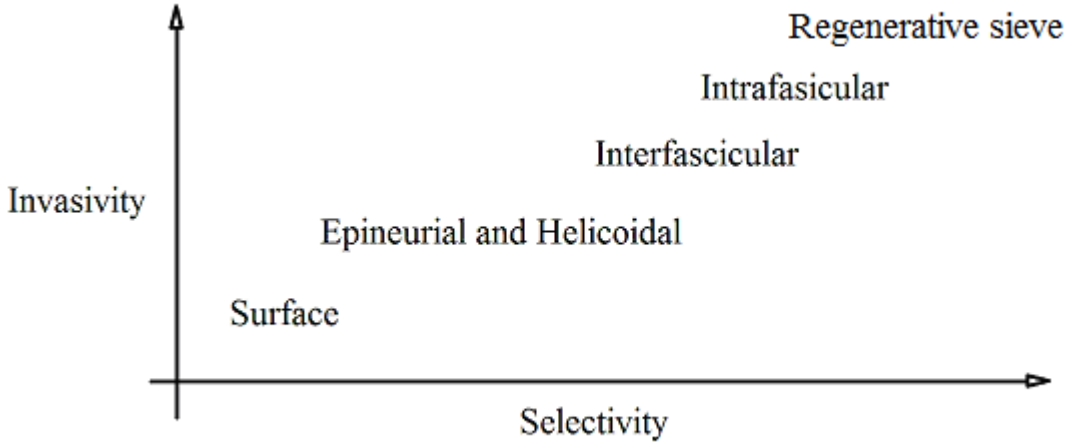


Fig. 3.1: invasiveness Vs selectivity for different types of electrodes interfacing PNS[19]

3.2.1. Interface Electrodes

If the application of the different types of electrodes is considered, the level of selectivity of stimulation or recording from individual nerve fibres or motor units increases in

parallel with the invasiveness of the electrode implantation (see Fig. 3.1). For example, surface and muscular electrodes can only stimulate and record EMG activity from the underlying muscles. Extra-neural electrodes (such as cuff and epineurial electrodes) provide simultaneous interface with a many axons in the nerve, while intra-fascicular and sieve electrodes inserted in the nerve may interface small groups of axons within a nerve fascicle. However, these interfaces are also tailored to a particular state of the nerve; the cuff and intra-fascicular electrodes can be applied to intact nerves whereas regenerative sieve electrodes are implanted in transacted nerves and need time to allow regeneration of the axons through the sieve implant for several months.

3.2.2. Non-invasive Electrodes

Surface electrodes

These are the only non-invasive electrodes available. They usually consist of metal plates with an electrolytic gel applied to the skin of the subject to carry out stimulation or recording in the form of ECG, EMG or an EEG. Materials such as silver, silver chloride, gold or platinum have been used in these electrodes as they give good impedance and durability. Surface electrodes can be used to stimulate or record from nerves located subcutaneously. They are extensively utilized as simple stimulating electrodes in rehabilitation to activate muscles, ease chronic and acute pain by activating large afferent fibres in peripheral nerves supplying the affected skin region. These electrodes have also been employed in sophisticated FES systems such as devices designed to provide walking assistance (WalkAid [20]) and correction of foot drop in hemiplegic patients in the 90s [21] (Fig. 3.2). Although these electrodes are flexible and non-invasive, they have several limitations. Daily placement and frequent calibration is a requirement in addition to the low reproducibility and quality of the recorded signals. This is because the impedance at the electrode-skin interface is largely variable amongst individuals at low frequencies while the decline of impedance with time is dependent on the electrode type at high

frequencies. However, they still can find a suitable application in the easy to use temporary electrotherapy which does not require highly skilled operators.

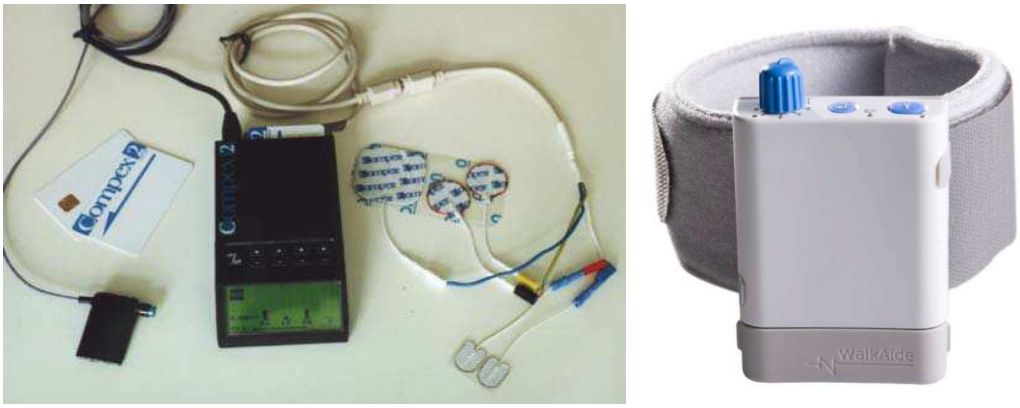


Fig. 3.2: Surfaces electrodes; Left – surface electrode, Right- Walkaid stimulator[17]

3.2.3. Invasive electrodes

Muscle electrodes

To make the interface of the electrode and muscle more effective, the electrodes are brought and placed closer to the targeted nerves. This is done with two muscle type electrodes namely the epimysial and intramuscular electrodes which can be considered to make the first step in increasing invasiveness in favour of a better interface.

Epimysial electrodes are positioned directly on the surface of the muscle through surgery and sutured or anchored into epimysium. They are normally made of conducting platinum-iridium disks backed onto a silastic casing which is flexible biocompatible material that provides mechanical support for attachment and insulation to prevent the stimulus signal from activating un-intended fibres. They are considered to have a good signal to noise ratio in general attributed to their position close to their target muscle and their large electrode surface area which provides precise selectivity to the target muscles.

Epimysial electrodes can be used to record EMG, but they are mainly employed as muscle stimulators (Fig. 3.3). They have also been suitably used to coordinate stimulation of several muscles in complex motor prostheses like grasping systems and walking systems [22-23]. However managing many epimysial electrodes on several muscles becomes a challenging task due to the interconnection between them which poses a possible source of failure. Another drawback is the high energy consumption needed to activate muscles via its deeply embedded efferent nerves. The epimysial interface is affected by the mechanical changes of the muscle during contraction which might limit the interface performance. Hence, an effective interface needs to be maintained by accommodating for changes in muscle shape before and during stimulation.

Intramuscular implanted electrodes are made of single-strand multifilament stainless steel Teflon insulated wire with exposed tips (for active electrode sites) and wound in a helical conformation when used in FES applications. However they can be as simple as an insulated wire with a bare tip. The bare tip of the electrode is placed into the muscle with a guide (to avoid surgery), leaving the wire routed outside of the skin which may cause discomfort and tissue damage. Another drawback is the lack of selectivity of motor unit activation within the muscle. In addition, the electrodes may eventually break or fail with repeated muscle contractions although issues have improved with development in electrodes and lead wires [24]. Similar to epimysial electrodes, these electrodes also have high energy consumption as they have to stimulate the efferent nerves located deep in the concerned muscles.

Muscle electrodes have been applied to deliver stimulation for denervated muscles after plexus or peripheral nerve injuries to avoid or minimize muscular atrophy which means higher voltage doses for longer duration done in cycles to avoid problems related to excess charge. The system is harvested once the regenerating axons reinnervate the muscles.

Another type of muscle electrodes is the Bionic Neuron (BION) stimulator developed by Loeb et al. in 2001. It contains a small cylindrical capsule with an integrated component connected to electrodes which are sealed to the capsule’s ends. BIONs are considered

intramascular electrodes as they are implanted within the muscle with an insertion tool. The main difference between them and conventional intramascular electrodes is that BIONs are operated wirelessly via a radio frequency link to transmit the signals recorded. Experiments have proven the stability and biocompatibility of these electrodes when implanted in animals to access their suitability as long term implants. In humans, they have been used to stimulate denervated muscles to prevent muscular atrophy and are also widely used in FES systems to correct foot drop.

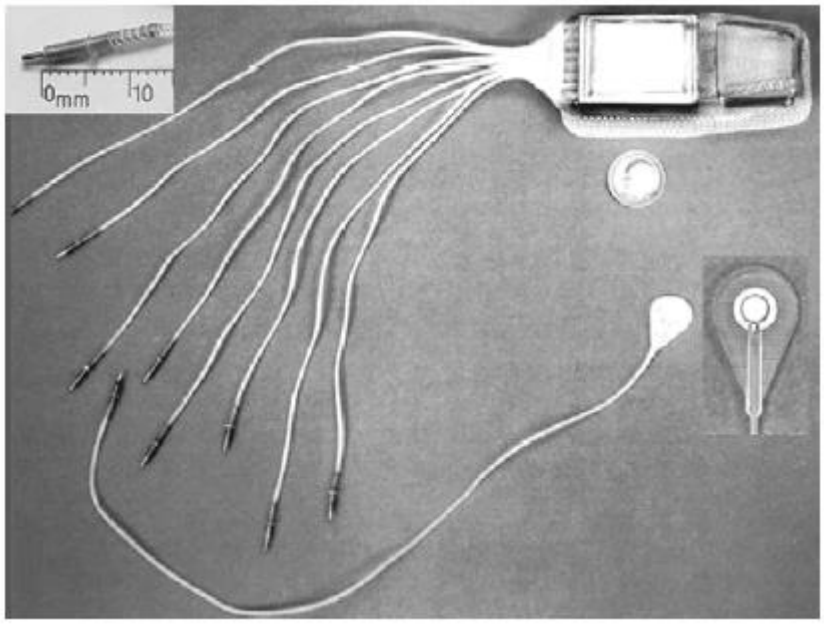


Fig. 3.3: Eight channel stimulator with one Epimysial Electrode (the insert on the right)[19]

Extraneurial Electrodes

These types of electrodes constitute the next degree of invasivity after muscle electrodes, as they are positioned close to or attached directly to the epineurium which is the outer sheath of target nerve. They are made of platinum or platinum-iridium wires with an insulating biocompatible material and two or more exposed surface electrode sites (Fig. 3.4). Epineurial electrodes require delicate surgery to be sutured to the target nerve and hence are susceptible to be torn from the nerve due to excessive motion or presence of tension in the leads. They are though less likely to cause damage to the nerve trunk, and are considered generally to be stable which means better selectivity in activating nerve

fascicles. Epineurial electrodes have been employed in FES systems to alleviate chronic neuropathic pain and improve foot-drop. Bipolar and selective stimulation can be obtained by attaching several electrodes to the nerve each requiring individual surgery. However, this comes at a cost of an increased level of invasiveness to the patient.

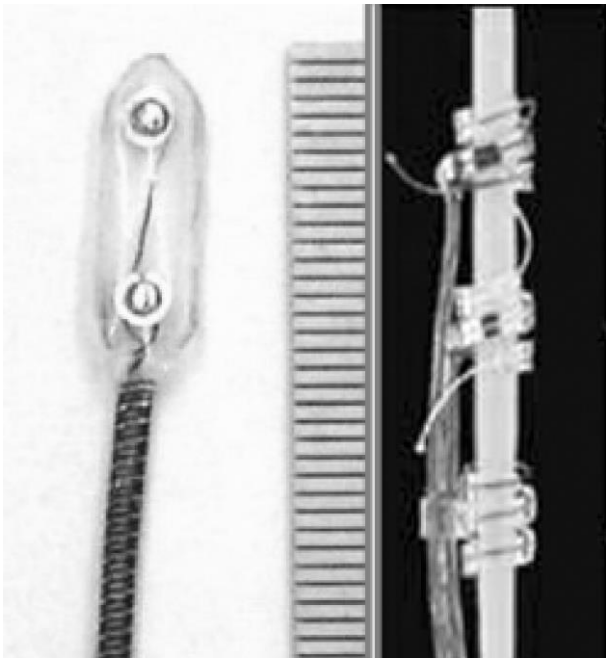


Fig. 3.4: Examples of epineurial electrode, Left- epineurial electrode (From Finetech implantable Drop foot), Right- helicoidal electrode (Cybertronics)[26]

Helicoidal electrodes have an open helical design made of flexible platinum ribbon which conforms to the shape of the targeted nerve when placed around it, and hence they are less invasive and traumatic to the nerve than epineurial electrodes as they do not require attachment to the epineurium (Fig. 3.4 Right)[25]. Despite their ease of implantation and explantation, their open structural design causes a reduction in the selectivity of these devices when compared to the epineurial electrodes. They have been commonly used in FES applications related to the vagus nerve to improve conditions such as epilepsy and sleep apnea.

Book electrodes are another type of extraneurial electrodes which are commonly used to interface to the sacral spinal roots for the treatment of urinary bladder disorders. The implant made of silicone rubber block with embedded deep trenches resembling the pages

of a book (Fig. 3.5). Each trench hosts three platinum electrode sites, two of which act like anodes whilst one act like a cathode. The interface is established by placing the sacral spinal roots surgically in the trenches which are then covered by a silicone flap and secured in place with glue. Helical cables made of insulated cooper wires allow connection of the electrodes into a control unit, in addition to providing high flexibility and mechanical strength. They have reached clinical application after being commercialised as Finetech –Brindley stimulators [27] which are used nowadays by more than 2000 patients worldwide. However, despite the excellent results obtained from years of clinical experience, these devices are still considered very big and would certainly benefit from miniaturization which has become essential to reduce the invasiveness of surgery and minimise the risks of open vertebral column procedures.

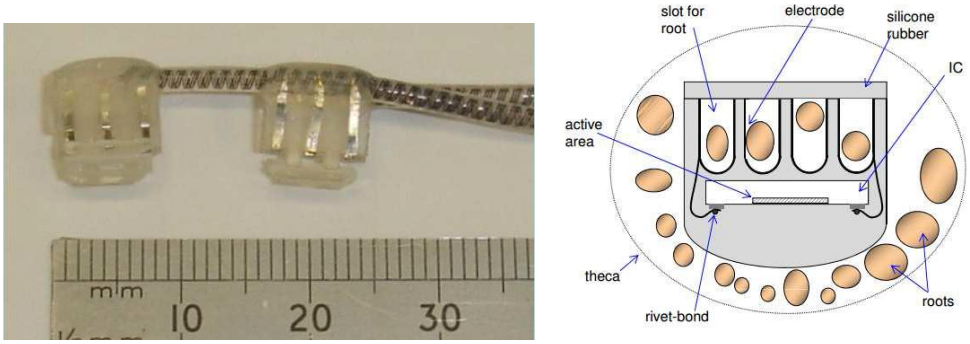


Fig. 3.5: Book electrodes implant, Left- standard three channel book electrode (Finetech brindley), Right- Schematic of book electrode in operation[17]

Cuff electrodes

A nerve cuff, as the name suggests, is a neural interface that can wrap around and completely encircle a nerve like a sleeve. It connects to the nerve without compromising its integrity via two or more electrode sites on its inner surface which are routed with insulated lead wires for accessibility (Fig.3.6). They are commonly fabricated in split-cylinder or spiral cuff configuration which gives them many advantages over other interfaces that have been discussed; when the cuff is completely sealed along its length, cross-talk, which can contaminate the signal recordings with undesirable noise from neighbouring structures, is minimised. The stimulation current in perfectly sealed cuffs is confined to the inner volume of the electrode which prevents signal attenuation or signal

loss caused by current spilling over to the neighbouring structures. This results in the required stimulation current being an order of magnitude less compared to the other discussed interfaces. However correct positioning of the electrode leads to minimise mechanical distortion and increased proximity with snugly fitted cuffs.

As the nerve tissue is very delicate, special precautions have to be taken when designing cuff electrodes so that any damage to the implanted nerve is avoided (especially for nerves subject to excessive motion like in the limbs). Therefore, cuffs have to be very flexible and able to conform easily to nerve shape so that stretching or compressing the nerve is avoided. This is why helical cuffs and spiral cuffs are generally designed to have slightly larger diameter than the target nerve to allow a reliable interface without compromising the nerve integrity. Snugly-fitted nerves allow for better signal amplification through nerve confinement giving better signal to noise ratio for neural recoding, in addition to needing a smaller stimulus current. However, various studies have demonstrated that implanting snugly fitted cuffs chronically, results in loss of large nerve fibres which are extremely sensitive to compression.

The main drawback with cuff electrodes is their low selectivity; initial studies that tested the recording selectivity of multiple small electrodes inside cuffs found only modest differences in their recorded signals. However, this can be improved if the continuity of the space between the nerve and the cuff wall is broken up so that the “tunnel” is compartmentalized into several separate “chambers” around the nerve that are isolated from each other and separate electrodes are placed inside each chamber. The chambers are created by longitudinal insulating ridges that just make contact with the nerve. The parallel ridge geometry is ideally suited for peripheral nerves and greatly enhances the recording selectivity achieved from electrodes in separate regions of the nerve trunk. This compartmentalisation solution works for the superficial nerve axons located at or close to the nerve surface while it would still be difficult for the cuff electrodes to stimulate axons that lie deeper inside the nerve. Recruitment starts first with populations of axons located on the nerve periphery, whereas stimulating deeper nerve fibres require a developed technique known as Flat Interface Nerve Electrodes (FINE). These work by flattening the

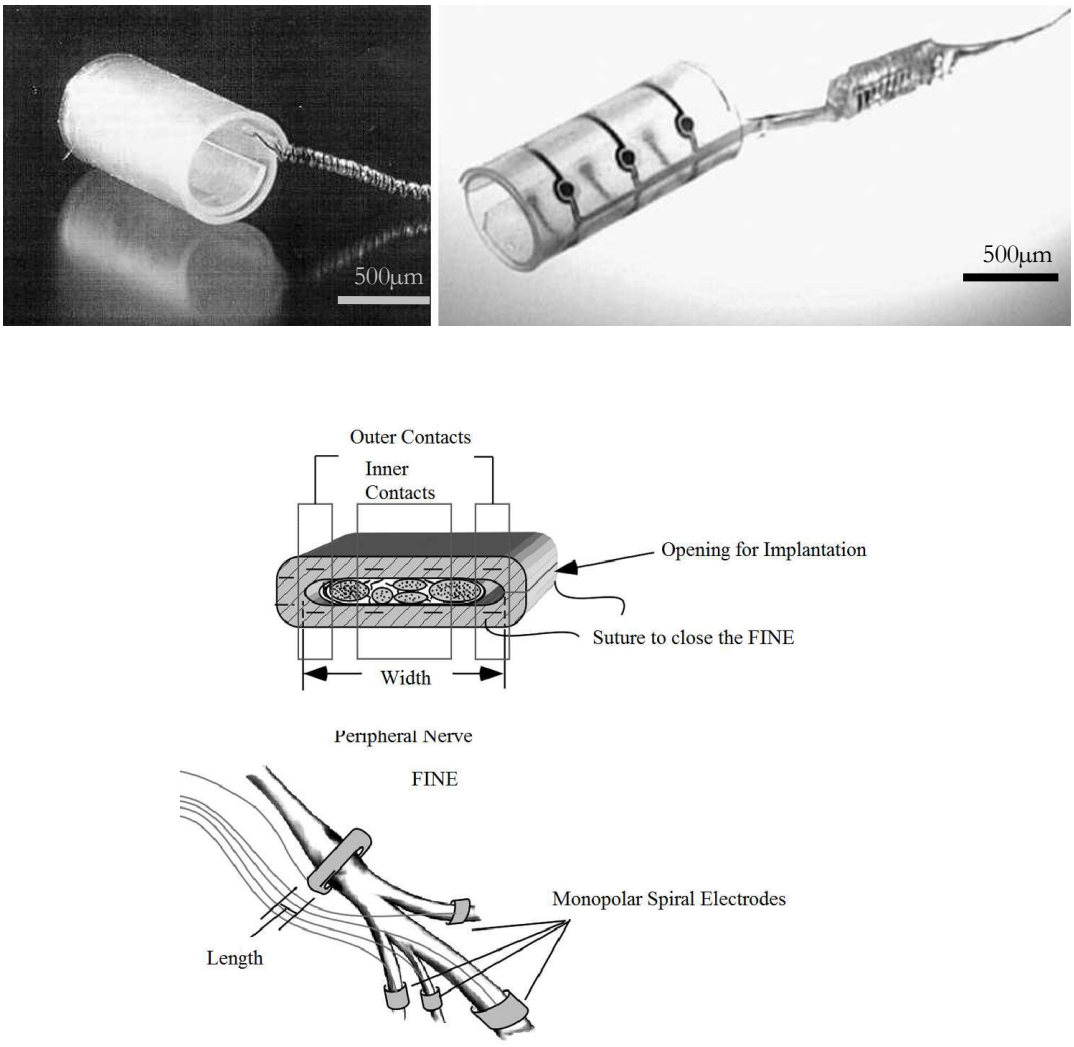


Fig. 3.6:Examples of Epineurial electrodes, Top- cuff electrode, Bottom two: schematic of FINE electrodes implanted on a peripheral nerve[17]

nerve trunk to bring axons that reside deeper inside the nerve closer to the surface which improve selectivity during recording and stimulation. However a major issue with this technique is the significant nerve damage that can be caused when a high reshaping force is applied. This has been shown after 1 to 3 months implantation, where high reshaping force resulted in substantial nerve damage and low reshaping force resulted in less nerve damage. Hence a compromise between selectivity and nerve damage has to be reached if this technique is to be used to improve selectivity to a degree [28].

Intraneural Electrodes

Intrafascicular (intraneural) electrodes are designed to be placed inside the peripheral nerve to improve selectivity and increase signal to noise ratio of the recorded signal. The electrodes are in direct contact with the targeted neural tissue, thus when stimulated, the intended nerve fascicles are triggered with minimised cross-talk to the neighbouring fascicles. Therefore, a relatively smaller stimulus current can be used compared to the stimulation current levels used in extraneural electrodes [29]. These electrodes can be made flexible based on polyimide or silicon implants or inherently conductive fibres.

Longitudinally implanted intrafascicular electrodes (LIFEs) offer a means of interfacing to restricted subsets of axons within fasciculated peripheral nerves. LIFEs are constructed from thin insulated conducting wires (such as Pt-Ir or metalized Kevlar fibres) with bared tip constituting electrode sites which are typically 250-1500 μm (Fig. 3.7). They started off as a single channel and were then developed into multi-channel LIFEs. Using metal wires in LIFEs triggers a foreign body reaction coating the electrodes with fibrous tissue sheath which gradually decreases the signal to noise ratio as the fibrous tissue thickens. This is thought to be caused or worsened by the motion of the stiff metal wires, and so these are normally replaced by flexile polymer filaments.

The intrafascicular electrodes are implanted within the individual nerve fascicles in a longitudinal fashion with the aid of tungsten needle which is pushed few millimetres within the endoneurium parallel to the course target nerve fibres. The electrode is then pulled through the fascicle until the electrode active site is placed in the centre of the fascicle. Implantation of LIFEs for 6 months showed that the implants are biocompatible apart from a slight thickening of the fibrous tissue around the active electrode site that became apparent with long term implants.

LIFEs demonstrated good selectivity in stimulation and multi-unit extracellular recording. They are particularly useful in FES systems applications and are being investigated for safety in long-term implantation in animals in parallel to their effectiveness in humans. LIFEs have also been implanted into the proximal stump of injured nerves in subjects with limb amputation, and the tests showed the ability of these implants to record activity

related to the missing limb movements. However, to selectively stimulate fibre bundles innervating the intended muscle groups, a number of LIFEs need to be implanted in different fascicles, which is a challenging task requiring fairly invasive and delicate surgery.

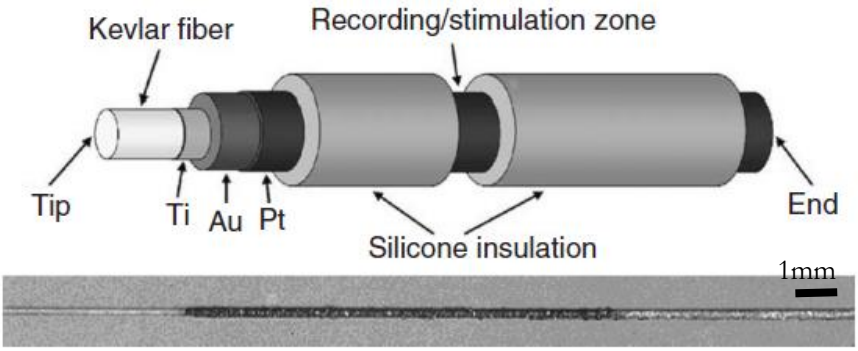


Fig. 3.7: Schematic of LIFE electrode[19]

Regenerative sieve implants

Regenerative implants are developed to interface a potentially high number of nerve fibres using arrays of holes with built in electrodes around them. They are normally placed between the stumps of severed nerve and time is given to allow axons to regenerate through the holes making it possible to record and stimulate individual axons or small fascicles (Fig. 3.8 Top). However, the success of these types of implants is heavily dependent on success of axonal regeneration through the *via*- holes, in addition to degree of nerve damage caused by the mechanical constrictive forces within the holes and the compatibility of the implant components.

Axonal regeneration and the ability to record neural activity through regenerative implants was demonstrated in peripheral nerves of some animals like rat [30]. However axonopathy signs were frequently observed with these silicon based interfaces which limits the growth of the regenerating axons depending on the hole dimensions. Selectivity would be maximised if individual axons grow through one hole that matches an axon's diameter (2 to 10 μm). However this is impossible as nerves do not regenerate through

such small holes and hence a balance has to be struck between the number of holes in the implant and their diameters.

A common example of regenerative implants is the sieve implant which is a flat device made of a substrate perforated by *via* holes through which regenerating nerve fibres grow. Active sieve implants have contact microelectrodes at these holes that can be used to record neural signals or stimulate nerve fibres. Sieve implants have been fabricated based silicon substrate and flexible polyimide with electrodes around selected holes (Fig. 3.8 Bottom). The flexible polyimide implants were found to be biocompatible and stable over month of *in vivo* implantation giving better regeneration compared to the silicon counterparts.

Different implant models differ depending on where they will be implanted. The sieve implants are adapted to fit their target nerve. An example is the sciatic nerve of rats that has a diameter of 1.5 mm. The maximum area available for holes in the sieve substrate is almost the same as the nerve diameter.

Having high transparencies is desirable for nerve regenerations through the sieves. However, the maximum hole area of the device is limited by the mechanical strength of the substrate, meaning that there has to be a compromise between the device transparency and the mechanical strength of the structure and the area for lead-out wiring. The non-hole area of the substrate must be large enough to accommodate electrodes and their tracks. It was found from previous studies that a hole diameter of 40 μm and a pitch of 70 μm (Transparency%=57[1]) was favourable for axonal sprouting and hence resulted in good axonal regeneration through the sieve devices. A hexagonal hole arrangement was selected to achieve the highest possible relative hole area (about 16% higher compared to a square arrangement of holes at a given hole diameter and pitch). The depth of the structures (holes) is generally limited to 0.5 mm. Such devices are based on a 2D designs

[1] Transparency of the device is defined as ratio of the open area occupied by air over the total cross-section (which is air +polymer). Transparency T(%) can be expressed as: $T(\%) = \frac{w}{S+w}$ where w is the channel (air) and S is the spacing between the channels (i.e the width of the channel wall)

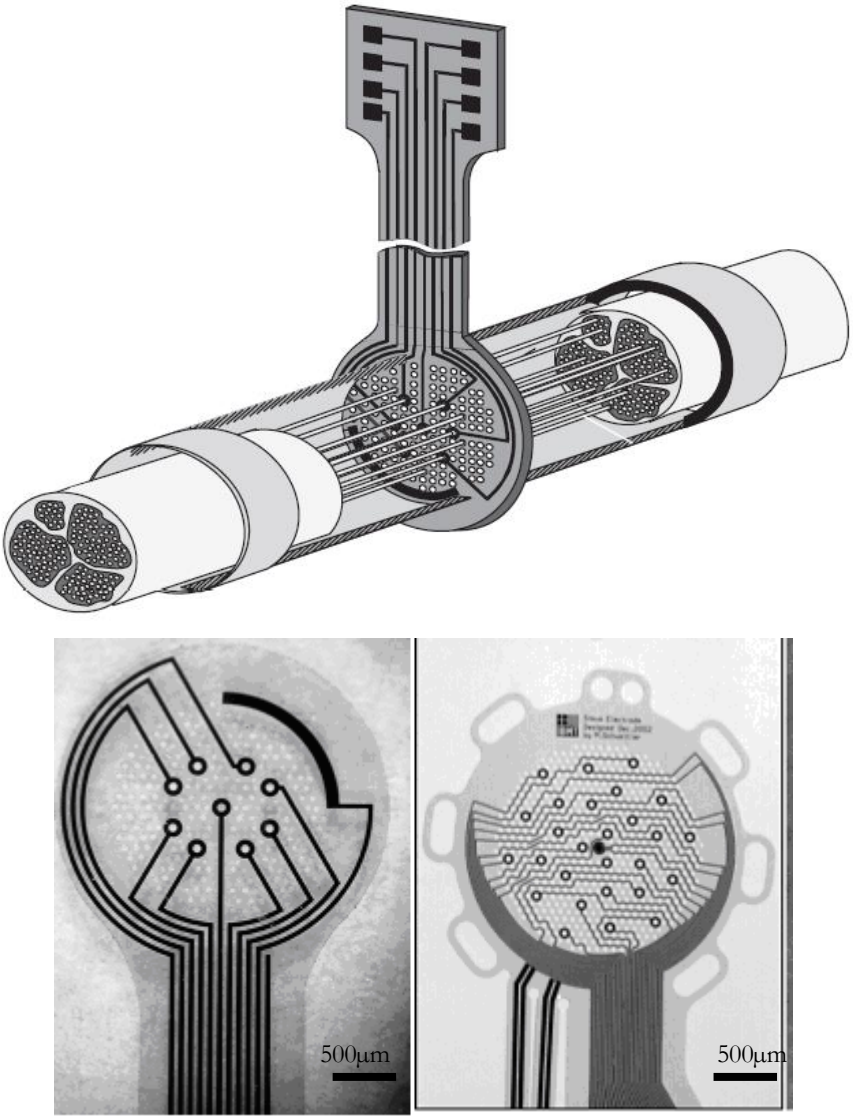


Fig. 3.8: Examples of Sieve regenerative electrodes, Top- sieve electrode in situ, Bottom- two different sieve electrode designs (notice the fringes added on the periphery of the bottom right design; they are normally used for attachment)[19]

rather than a more complex 3D architectures which is beneficial as it means that fabrication process is easier. Recording from such implants is also advantageous because of the stability of the interface between the target nerve fibre and electrodes; the whole interface is fixed in place once neural tissue has regenerated through the *via* holes which means more reliable recordings over extended periods of time. However, the amplitudes of the axonal extracellular signals recorded for the individual axons are extremely small (10 to 500 μV). Consequently, a significant improvement of the signal to noise ratio is required if these devices were to succeed in clinical applications. The work presented in

this thesis suggests an implant design that can reliably improve the signal to noise ratio. The design concept is based on micro-channels acting as signal amplifiers for the nerve fibres enclosed in within them. The chapters to follow will present the design of such implants and their fabrication process in greater details.

3.3. Review of brain nervous system interfacing technology

Similar to the peripheral nerve interfaces, the methods used to interface to the central nervous system (CNS) are also divided into non-invasive interfaces used outside the body, primarily EEG, and invasive interfaces implanted into the body which mainly include electrocorticography (ECoG) or implanted microelectrodes. This difference between the two method camps is illustrated in Fig. 3.9. Non-invasive devices are designed to measure a large number of neural signals while invasive devices are used to record the potential changes in the surrounding cortical region evoked by attempted or imaginary movement or caused by a cognitive task. These kinds of potentials can also be detectable via the non-invasive methods; like visually evoked potentials (VEP), Audio/aural Evoked Potentials (AEP).

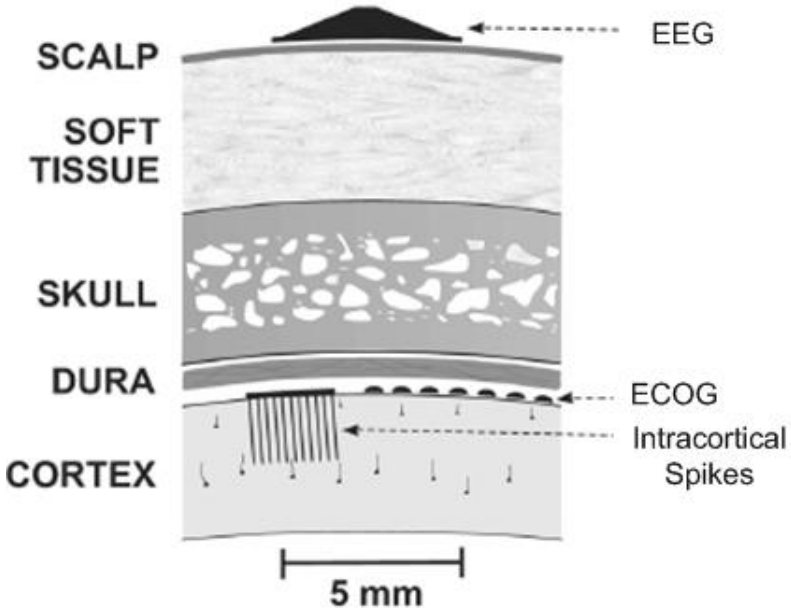


Fig. 3.9: three main variations of Brain Computer Interface (BCI) electrodes; EEG, ECoG and intracortical implanted electrodes [31]

3.3.1. Electro-encephalography (EEG)

EEG activity was discovered by Hans Berger in 1929[32]. It is a non-invasive method used to record brain activity by placing an array of electrodes at regular intervals across the scalp Fig. 3.10. A differential amplifier is used to amplify the recorded signal from each electrode by a factor of 1000 to 100000. A conductive gel is normally used to improve the connectivity between the electrode active site and the scalps. EEG relies on a strict electrode arrangement for repeatable recordings and accuracy in signal detection. The electrodes are precisely positioned relative to one another and fixed to two anatomical points namely the nasion (the point between the forehead and nose) and the inion (the base of the skull at the rear of the head).

EEG is used in a variety of applications to monitor brain activity. Amongst the applications: seizure diagnosis for epilepsy and non-epileptic seizures, investigating sleep patterns and sleep disorders, diagnosing problems related to the central nervous system and mental illnesses. For typical clinical application, the system uses 19 recording electrodes and a ground reference. This number can be increased or decreased as needed. However spatial resolution of the signals limits the number of electrodes that can be used to a maximum of 256 electrodes equally distributed across the scalp. Fig. 3.10 illustrates EEG 256 maximum electrode arrangement in use and schematic for standard placement of electrodes as specified in 1947. The main drawback with EEG is that the skull acts as an electromagnetic shield which blurs the signal resulting in low resolution.

3.3.2. Electro-corticography (ECoG)

ECoG operate on the same principle as EEG, the only difference is that the electrodes in ECoG are positioned on top of the cortex region being examined inside the skull. Because of the invasiveness of ECoG, the portion of the brain that can be covered by the ECoG electrodes is small and is normally limited to a specific region of the cortex. The spatial resolution is much better within the skull which means that the ECoG electrodes are much

smaller and much more compactly spaced compared to EEG electrodes. Fig. 3.11 illustrates an array of ECoG electrodes in operation.

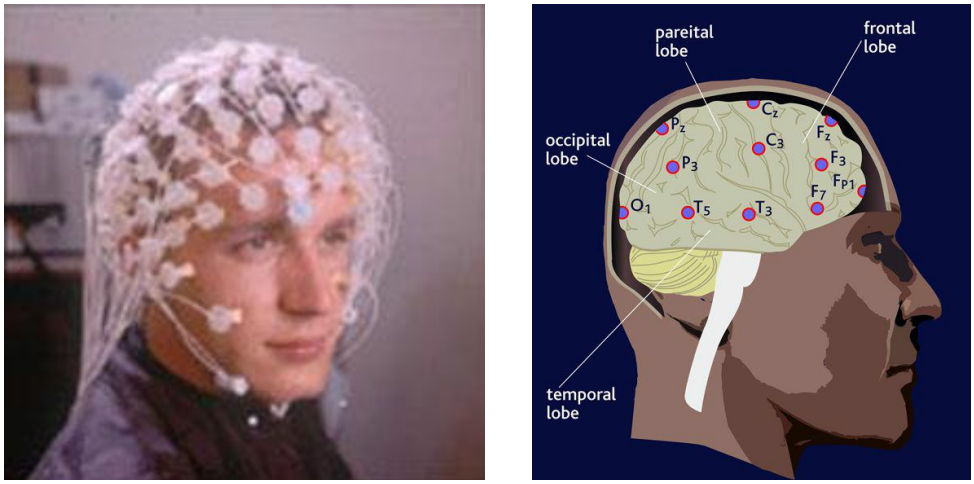


Fig. 3.10:Electroencephalographic (EEG) System, Left- 256 electrode EEG system in operation, Right- Standard EEG electrode placements [33]

3.3.3. Penetrating implanted electrodes

Penetrating electrodes were mainly developed and costumed to interface with the central nervous system albeit some have been investigated as PNS interfaces. They are considered the most invasive of the Brain Controlled Interface methods (BCI). They have broadly been used to measure single unit or multi-unit neural activity (activity of individual or small groups of neurons). Numerous designs for these electrodes have been custom made to serve particular applications. Using advanced micro-fabrication techniques such as precision mechanics, microelectrodes with multiple electrodes sites have been developed in 1D, 2D and 3D arrays based on glass, silicon or polyimide substrates (Fig. 3.12 and Fig. 3.13 [36]). The electrode designs can be categorized into designs that have a proximodistal plane electrode arrangement where the electrodes are placed at and can record different brain depths and those that have a transverse plane electrode arrangement where the electrodes are designed to be placed and record at the same depth.

The Michigan array and Utah array constitute the most commonly used proximodistal and transverse electrode arrays respectively. These will be discussed in further details in addition to the micro-wire electrodes which make up the majority of custom designed group.

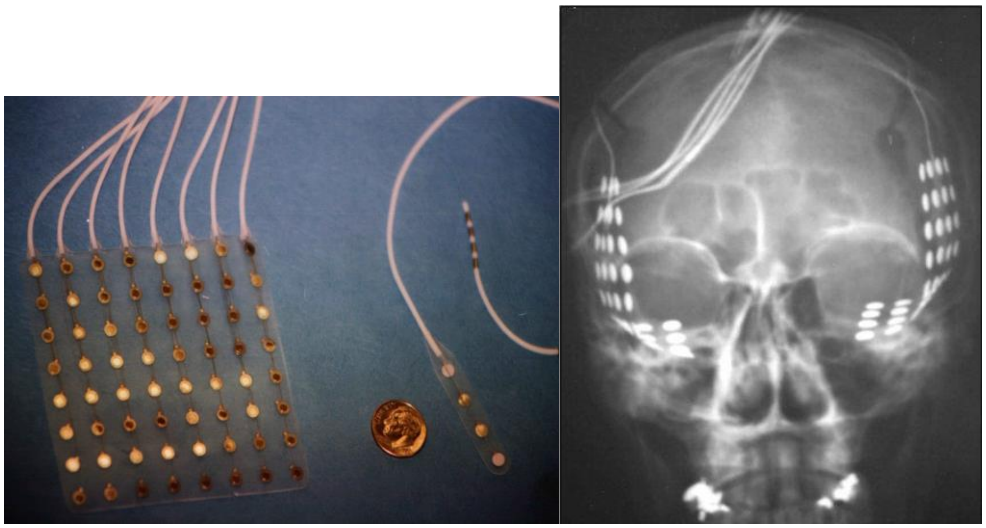


Fig. 3.11: An Eletro-corticogram system, Left- Selection of ECoG electrode arrays compared to a US penny for scaling, Right- x-ray of skull showing ECoG electrode array implanted bilaterally [34-35]

Michigan array

The Michigan array evolved from one of the first silicon-based microelectrode arrays and has been developed by the University of Michigan in 1985. It is produced in large numbers as a single –shaft, multi-shaft or 3D stacked multi-shafts [36-38] (Fig. 3.12). Each shank is either needle shaped or wedge shaped and carries several patterned microelectrode sites giving a higher site density with minimal tissue displacement in comparison to a micro-wire bundle. The high spatial resolution is also reproducible as inter-electrode spatial relations are defined during photolithographic processes and thus remain fixed. This was not previously possible with the wire bundles.

The array is fabricated using photolithographic and other IC techniques from silicon of a thickness between 15 and 100μm thick depending upon application. The metal wiring is sandwiched between silicon dioxide and silicon nitride used an insulation layer with the

wiring exposed at a number of sites down the length of the shaft constituting the active sites. The shafts penetrate into the neural tissue making recording and stimulation possible at depths defined by the active sites of the electrode. Michigan probes have been connected to flexible polyimide interconnect cables for chronic recording using a ball bonding technique which provides a neat interconnection method beneficial for long term recording. Transverse arrays of the proximo-distal probe have been developed from the Michigan probes offering a three-dimensional array of recording sites (Fig. 3.12 bottom left).

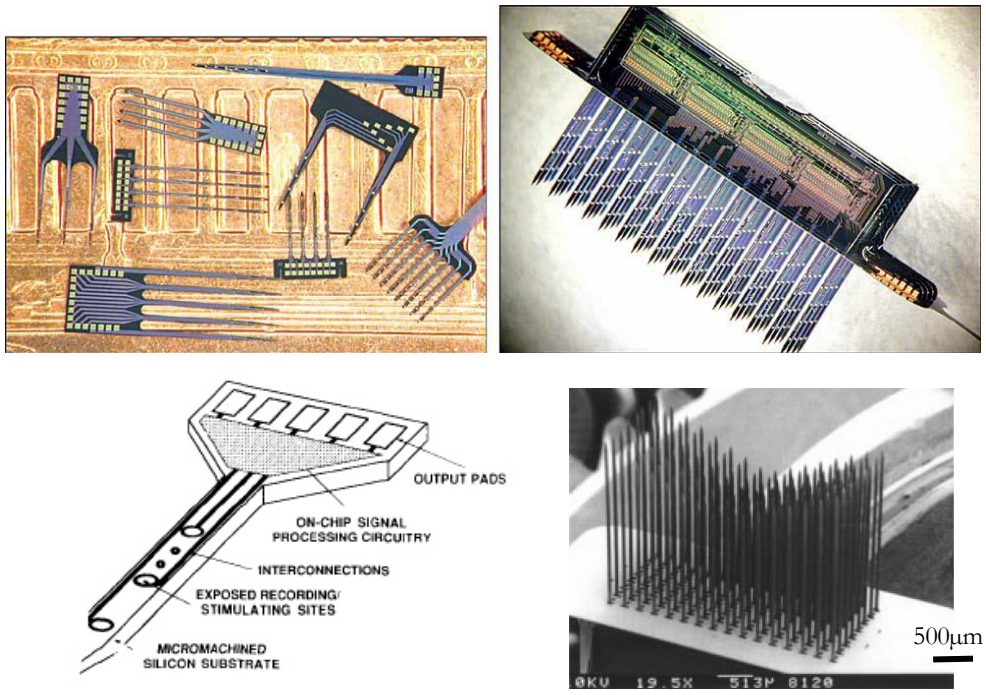


Fig. 3.12: The Michigan Electrodes, Top left- a variety of different silicone probes placed on the back of a U.S. penny, Top right- four 64 site probes assembled into a three dimensional structure, Bottom left: Schematic of single shank Michigan probe, Bottom right- Multi-shank Michigan array [39-40]

Utah array

The Utah Electrode Array is an intracortical three-dimensional electrode array which was developed by the University of Utah in 1991. It consists of 100 conductive electrodes in a 10x10 array (fabricated based on silicon or silicon-glass technology). Each electrode shank is 1.5 mm long and 90µm thick at its base and sharpened to a point at the tip. The shanks are electrically insulated with polyimide and the tips are coated with platinum to

increase the charge transfer from the neural tissue (Fig. 3.13). The spacing between the electrodes is 400μm. To permit precise excitation of fibres at different depths, a graded design of the Utah Array was made. The length of the microelectrodes in this design increases from 0.5 through to 1.5mm which means that nerve fibres can be excited at various depths (Fig. 3.13 Right).

Similar to the Michigan array, the use of Utah arrays has been explored in a variety of applications and has become a de facto standard. They are able to record single unit activity and have precise spatial distributions which are very beneficial though this comes at a compromise on the flexibility to move individual electrodes relative to each other when tracking for a particular neuron. Examples of Utah Array applications include the auditory and visual cortex of a cat, cochlear nerve and the dorsal root ganglion. The graded version was used as implant in the cochlear nerve.

.

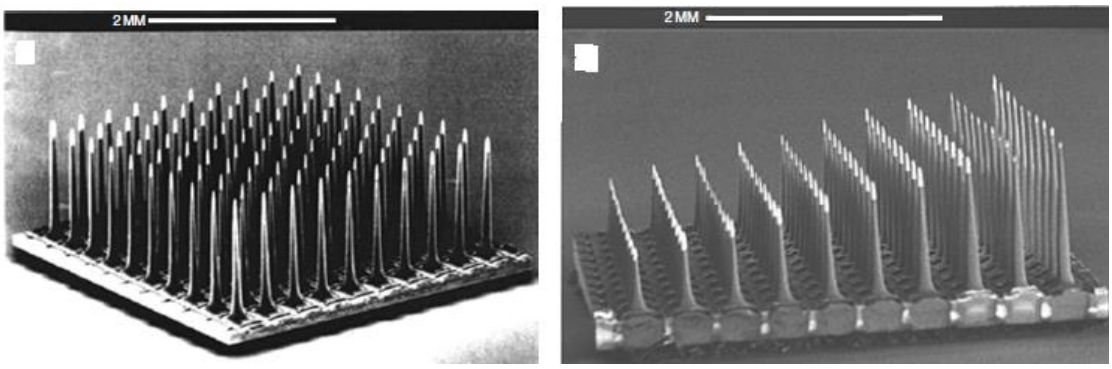


Fig. 3.13: The Utah Array. Left- three-dimensional array features 100 silicon-based microelectrodes, each with a platinum-coated tip, Right- The slanted array has been used to stimulate fibres at different depths in the cochlear nerve [41].

Microwire electrode

Insulated micro-wires were the first implantable electrodes used to record chronically from the brain. These wire electrodes were developed in the 1950s and were made from an insulated tungsten wire with an exposed tip for the electrode site (Fig. 3.14). The data collected by Williams et al. in an experimental study showed that single unit recordings can be maintained for three months. The most popular types of wires used are tungsten

and platinum. The integrity of the wire insulation is paramount because if the insulation is compromised and the wires come into contact with each other or with the surrounding tissue then the recording will be compromised. The two commonly used insulating materials are polyimide and Teflon.

To minimize disturbance to the surrounding tissue, the micro-wire electrode needs to be thin enough while having enough stiffness with the right tip shape to penetrate the dura layer and reach the target intended brain structure without breaking and with minimal bending while traversing the tissue to get to the right position. These electrodes have generally been produced by hand in the lab with a focus on the tips. Micro-wires with 25µm to 50µm diameter offer the best compromise between size and stiffness. They can penetrate the brain dura and have enough rigidity to reach the correct position. Any electrodes smaller than that find it difficult to break through the dura and can easily be diverted from their intended brain structure by fibre bundles; so they normally do not end up where they are supposed to be.

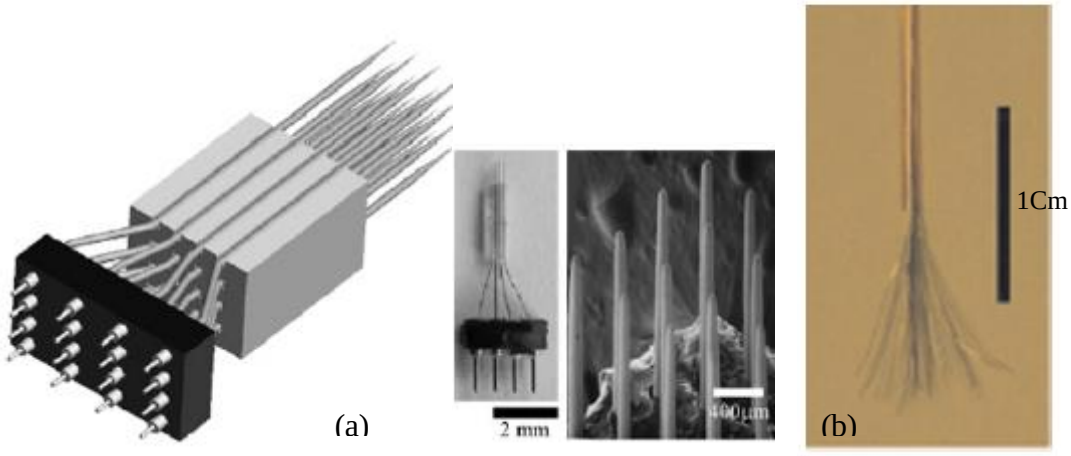


Fig. 3.14: (a) well defined wire electrode array (design concept, Fabricated device and SEM of the spike tips), (b) Microwire bundle (Scale Bar =1cm)[18]

Over time the recordings obtained using micro-wires give better long-lasting recordings with the single unit recording lasting for about a year in some studies. One benefit to using arrays of micro-wires is the ability to shape and position them to record from different positions. At the time of implantation, they can also be manipulated to conform to the brain structures and ensure proper placement in the intended area of interest.

Fabricating these wires in different lengths means that neurosurgeons can use them to access deep brain structures.

There are three main drawbacks to using micro-wires for neural interfaces. Firstly, they have low signal to noise ratio, Secondly, the complexity of integrating on-board electronics to condition the neural signal. Positioning signal conditioning circuit as close to the electrode as possible is crucial for noise reduction and achieving this with micro-wires is quiet difficult. Last but not least, these micro-wire electrodes have variable recording characteristics as they are generally produced by hand and there has been no method to fabricate them using batch processing. This significant variation in the recording characteristics means that impedances are not properly matched between the electrodes and the on-board electronics.

To overcome the above problems, alternative electrodes known as thin film electrodes have been developed using batch processing. These are electrodes that have similar recording characteristics, high signal to noise ratio, and the ability to integrate on board electrodes in a close proximity to the neural interface.

3.4. Materials used in neural interfaces

It is essential for materials used in neural implants to be stable because it is expected to remain in the body of the patient for many years. The materials used have to be inert in the absence or the presence of electrical signals in the physiological environment. This is because any corrosion or degradation of the devices may lead to implant failure and bio-toxicity caused by the toxic substances being released from the implant. Besides being corrosion-resistant, it is also important for the metallization material to have minimal energy requirement during stimulation and stable impedance and frequency response. Silicon and flexible polymer such as polyimide are widely used in the fabrication of CNS and PNS neural interfaces respectively, as they are compatible with advanced micro-fabrication techniques making it possible to fabricate the devices with high precision in addition to fast prototyping and reproducibility.

Techniques such as photolithography and etching are commonly used to define and pattern the required dimensions of the device features with a high degree of accuracy. Silicon is the main material for CNS implants as it has many excellent attributes that justify such application; these include biocompatibility, ability to push miniaturization to the edge in micro-fabrication, ability to fabricate miniaturized devices that are stiff enough to penetrate through the neural tissue to reach their neural target. Any level of flexibility is reached by reducing the device feature dimensions to a degree that can make the interface mechanically fragile. An important advantage of silicon based micro-devices is the ability to fabricate integrated circuits for signal conditioning and processing on the same silicon substrate.

Silicon is considered brittle and is hence less suitable for making PNS implants which require a high degree of flexibility necessitated by the presence of excessive motion. Polyimide, on the other hand, is so far the favourable material for PNS implants because of its high flexibility, biocompatibility in addition to compatibility with micro-fabrication techniques. In microelectronics, polyimide has primarily been used as an insulating material or as a dielectric between two layers for instance in multi-chip modules where layers of polyimide can be easily spin coated successively. Photo-sensitive polyimides have only recently been used in neural implants as they have the advantage of reducing the number of processing steps involved in micro-fabricating the devices. This widens the range of implant designs that can be executed with less challenging processing steps. Polyimides are used as the main material to build the backbone of the neural implants in this thesis. So the material is used as a substrate, an insulation and micro-channel layer (the fabrication steps will be discussed in details in chapter 7 of this thesis).

3.5. Biocompatibility

In the context of material science, the ability of the material to perform specific application in a host environment that responds with suitable reaction to the implanted material is known as biocompatibility. The neural interface is implanted with the intention

to record from or stimulate neural tissue and the body responds to the implanted device with a foreign body reaction as self-defence mechanism to protect itself. Biocompatibility is the important factor that can balance the foreign body reaction to the implant and allow the device function appropriately within the physiological environment. A material is considered biocompatible if it is not toxic, harmful or damaging to the biological tissue.

Using different methods in fabrication can create different physiological responses in the host tissue. This can be attributed to differences in the chemical, mechanical or physical properties of the material or even variation in surface finishes. Hence it is important to bear in mind when designing an implant that the implant material itself cannot be classified biocompatible, as the classification must include the processing steps of the fabrication and its parameters. In recent years, materials have particularly been developed to be biocompatible so that they can be used in the fabrication of neural implants. The ISO standard 10993: *Biological evaluation of medical devices* provides a summary of all the materials developed in this endeavour.

There are two sides into the biocompatibility of a material and these are structural biocompatibility and surface biocompatibility. The former relates to structural properties such as material flexibility and stiffness and its ability to imitate the properties of the target biological tissue. Whereas the latter is concerned with the properties that are in direct contact with the biological environment namely chemical, physical, morphological and biological properties. The material should be stable and durable enough to survive the harsh physiological environment should have the right surface and structural properties and not release any toxic substances so that an adverse foreign body reaction is avoided or minimized. Although, a mild inflammation is to be expected, a strong foreign body reaction should be evaded as this can result in the implant being encapsulated in a sheath of thick fibrous tissue and eventually lead to implant failure. This is normally an issue in devices designed for long term applications where a durable and a stable interface needs to be maintained throughout the length of implantation.

3.6. Chapter summary

This chapter reviews critically the interfacing technology that has been developed so far to explore neural cells and their activity. Various neural interfaces have been custom made to match the anatomical requirements of their intended implantation site; these can generally be grouped into interfaces developed for Peripheral Nervous System (PNS) and those developed for the Central Nervous System CNS. The most common examples of neural interfaces have been discussed and an insight into their clinical or research based applications is given. The review focused particularly on the characteristics and limitations of each interface type.

As discussed at the beginning of this chapter, if the application of the different types of electrodes is considered, the level of selectivity of simulation or recording from individual nerve fibres or motor units increases in parallel with the invasiveness of the electrode implantation. For instance surface and muscular electrodes can only record EMG activity from the underlying muscle whist extra-neural electrodes (such as cuffs) can provide simultaneous interface with many axons on the surface of the target nerve. On the other hand, Intra-fascicular and sieve electrodes inserted in the nerve can interface a small group of axons within a nerve fascicle.

To obtain fine motor control of prosthetic limbs, a high level of selectivity is required and this can only be achieved by using an interface that can selectively record from various groups of nerve fibres within the targeted nerve. Cuff electrodes have relatively low selectivity as they can only record from superficial nerve axons located at or close to the nerve surface while it is still difficult for them to stimulate or record from axons that lie deeper inside the nerve. Using an intra-neural implant type (such as LIFEs) would require the implantation of several to obtain recordings from different nerve fibres which is not practical. Interfacing at the higher end of selectivity requires a sieve type implant. These devices are developed to interface a potentially high number of nerve fibres using arrays of holes with built in electrodes around them. They are normally placed between the stumps of severed nerve and time is given to allow axons to regenerate through the holes making it possible to record and stimulate individual axons or small fascicles. Recording

from such implants is advantageous because of the stability of the interface between the target nerve fibre and electrodes; the whole interface is fixed in place once neural tissue has regenerated through the *via* holes which means more reliable recordings over extended periods of time. However, the amplitudes of the axonal extracellular signals recorded for the individual axons are extremely small (10 to 500 μV). Consequently, a significant improvement of the signal to noise ratio is required if these devices were to succeed in clinical applications.

The work presented in this thesis suggests an alternative implant design that can reliably improve the signal to noise ratio. The design concept is based on micro-channels acting as signal amplifiers for the nerve fibres enclosed in within them. The chapters to follow will present the design of such implants and their fabrication process in greater details.

4. MICRO-CHANNELS ARRAYS AS AXONAL AMPLIFIERS IN REGENERATIVE NEURAL IMPLANTS

4.1. Introduction

While most of the neural interfaces that have reached clinical application are stimulating devices [42], fewer recording devices have reached that stage. Cuff recording electrodes have been well established in animals and in humans. They have been applied to experimentally detect activity in small sensory nerves and provide feedback for Functional Electrical Stimulation systems (FES). Recording nerve activity allows the opportunity to provide control information (feedback) to the nerve stimulators. A more challenging problem is to record information from truncated nerves in the amputation stump and use it for fine motor control of prosthetic limbs. Although Cuff electrodes are used for whole nerve recording and seem like a contender for this application, the cuff microelectrodes can only make contact and record from fibres near nerve periphery whilst it is difficult to record from deeper remote fibres on the inside of the nerve [19]. Needle electrodes/arrays can penetrate the nerve and offer more sensitivity and selectivity by being in closer contact with fibres [43-45]. Utah array is an example of this type of penetrating electrode, and although it has been successfully used to record from the peripheral nerves of cats but less than 50% of the electrodes were able to record action potential [46]. The Utah array has been implanted in the median nerve of a volunteer to control a hand prosthetic [47]. The issue with using penetrating needle type electrodes for long term implantation is the encapsulation of electrode sites with fibrous tissue and the unstable interface between the electrode site and the nerve due to movement [48-50]. This can often lead to changing signal levels or changing the populations of axons that the contact electrodes are recording from.

Recently the interest in regenerative implants has also significantly risen. An example of this type of interface is regenerative sieve electrodes [50] which can offer a constant

fibre/electrode contact once the axons grow through the sieve holes bearing the microelectrodes. Although the number of holes in sieves can be made generous but a trade-off has to be made between the lead-out space and the space left for axon regeneration [51]. This means that the number of microelectrodes is limited in practice in favour of regeneration, and many of the contacts are inactive or silent.

The complexity of the human peripheral nervous system is perplexing. For example, there are over 30 muscles in the human forearm controlling the movement of the wrist and digits. Most movements use a combination of several muscles. Each muscle is supplied by a large number of axons making it capable of a wide range of contractile forces. The flexor digiti minimi responsible for the flexion of the little finger has around 130 axons [52]. Low frequency activity in small set of axons (the rest of the axons remaining inactive) produces contraction. Increasing the frequency of action potentials and the number of axons being activated results in a gradual increase in the force.

When considering high precision control, one can assume that the bare minimum for the number of active contacts to achieve an acceptable function is to record at least from one axon supplying each muscle replaced by the prosthesis. For instance for a forearm-level prosthesis the number of active contacts required would be 30-40, which is far higher than what has been achieved using any peripheral neural interface. The number of functioning and independent electrical connections that the interface makes with the axons in the nerve determines how much information can be extracted from the neural interface. However, the number of active contacts in the current interfaces is generally far less than the number of contacts it possesses as many of these contacts fail to pick up the signal or detect a signal from a neighbouring contact i.e. crosstalk [53] [54].

Neural interfaces work by detecting action potentials (AP) propagating along the nerve fibres. An action potential normally has amplitude in the region of 100mV with the majority of the signal occurring inside the cell. The change in potential on the extracellular side is much less. This is because the extracellular fluid surrounds the axon in large volume and has a low resistivity, combined with small ionic AP. The result are extracellular signals in the order of $\approx 10\mu V$ to $\approx 500\mu V$ [55], making signal detection via

neural interfaces very challenging as long term implants rely merely on extracellular recording. The potential difference between the internal surface and the external surface of the axon membranes is known as the membrane voltage (V_m) and is defined as [10]:

$$V_m = V_{in} - V_{out} \qquad \text{(Equ. 4.1)}$$

Where V_{in} is the potential on the internal surface of the axon membrane and V_{out} is potential on the external surface of the axon membrane.

At equilibrium (no action potential), the membrane voltage is resting at -70 to -80mV. Fig. 4.1 illustrates two adjacent nodes of Ranvier in a myelinated axon and travelling action potential (AP). As the AP propagates along the axon, each node depolarizes the next by local currents flowing in loops. The current flows as the membrane potential V_m of the node on the left is more positive than the membrane potential V_m of the resting node on the right. The internal and the external currents are equal and opposite whilst the difference in V_m drops across the resistances of the extracellular fluid (R_{ecf}) and the axon (R_{axon}) and hence can be expressed as:

$$\delta V_{out} = iR_{ecf} \qquad \text{(Equ. 4.2)}$$

$$\delta V_{in} = -iR_{axon} \qquad \text{(Equ. 4.3)}$$

And hence:

$$\frac{\delta V_{out}}{\delta V_{in}} = -\frac{R_{ecf}}{R_{axon}} \qquad \text{(Equ. 4.4)}$$

A range of values is quoted in literature for the axoplasm resistivity (ρ_{axon}). A value of $1.1\,\Omega.m$ was selected based on calculations reported in McNeal[56]. In a $10\mu m$-diameter

myelinated axon (with an assumed internode length of $300\mu m$[2]), R_{axon} is calculated to be $4.2M\Omega$ per internode, using the following equation:

$$R_{axon} = \frac{\rho_{axon} L}{A} \qquad \text{(Equ. 4.5)}$$

Where ρ_{axon} is the axoplasm resistivity, L is the internode length and A is the cross-sectional area of the myelinated axon

It is however much more challenging to predict R_{ecf} which depends on a set of factors including:

1. the extracellular fluid with other cellular material (other axons), giving inhomogeneous extracellular resistivity
2. Because of the fibre alignment, the extracellular resistivity is anisotropic meaning lower longitudinally than transversely. This anisotropy is reflected in an axial and radial resistivity.
3. Deposited fibrous tissue is common in and around implants, this might increase R_{ecf}. A higher packing density of fibres would limit interstitial fluid resulting in similar effect. On the other hand, reduced amount of cellular material allowing a higher interstitial fluid volume reduces R_{ecf}.

A well-established design measure, for implants relying on extracellular recording is low instrumentation noise (thermal noise) which can be expressed as [17]:

$$V_{rms} = \sqrt{4K_B TR\Delta f} \qquad \text{(Equ. 4.6)}$$

Where T temperature in degrees Kelvin, R the resistance, K_B Boltzmann constant and Δf is the operating bandwidth for the electrodes.

[2] Myelin segment (internode) length in normal (uninjured) nerves varies with fiber diameter but in regenerated nerves it has a relatively constant value of about 300 μ m [58]. Because fibers growing through an interface are of necessity regenerating, we have used this value for all sizes of simulated myelinated fiber.

So for a metal electrode operating within a frequency range of 10KHz, with an impedance of $1M\Omega$, the thermal noise at body temperature (37^0C) is around $13\mu V$ *rms* which is $40\mu V$ peak to peak. This is close to the extracellular Action Potential signal levels. For instance, for a signal less than $20\mu V$, it would be difficult to differentiate between the real signal and the thermal noise signal.

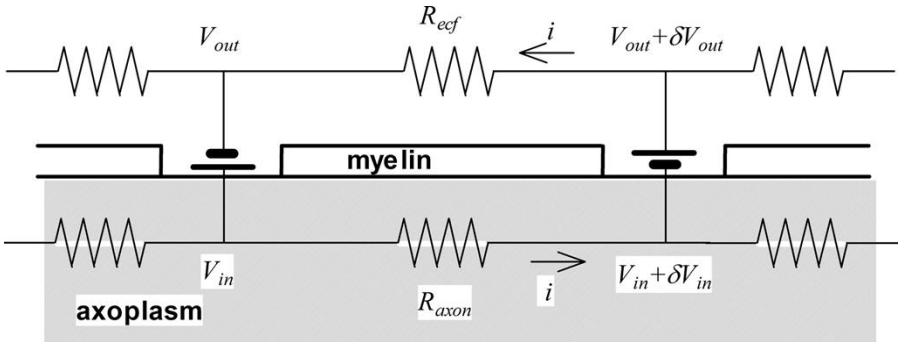


Fig. 4.1: Local currents during depolarization of an axonal membrane[10]

Besides the low levels of the extracellular signals, they also very rapidly decay with respect to distance away from axonal membrane. To effectively record extracellularly, the electrodes must be placed as physically close to the fibre as possible which may be unrealistic with the current technology used *in vivo* applications. The positioning is even more difficult for mylinated axons as the trans-membrane current is concentrated close to the nodes of Ranvier (sketched in Fig. 2.4). If the signal is to be detected, the electrode needs to be placed close to a node of Ranvier. The sieve electrodes and needle electrode tips are thin, having 10 to 20 μm width. This makes these devices unreliable as the chance of a node of Ranvier of a given axon coinciding with the sieve plane or the needle electrode tip is very small hence making many of such electrode sites inactive.

If the extracellular voltage δV_{out} is amplified, the ability of the electrodes to detect the signal will improve. This can be done by making the medium more resistive by increasing the resistance R_{ecf}. One way is to do this is to significantly alter the composition of the ECF so that its resistivity ρ_{ecf} (and hence R_{ecf}) is sufficiently increased to improve signal

recording. However this method will affect nerve physiology and compromise its viability.

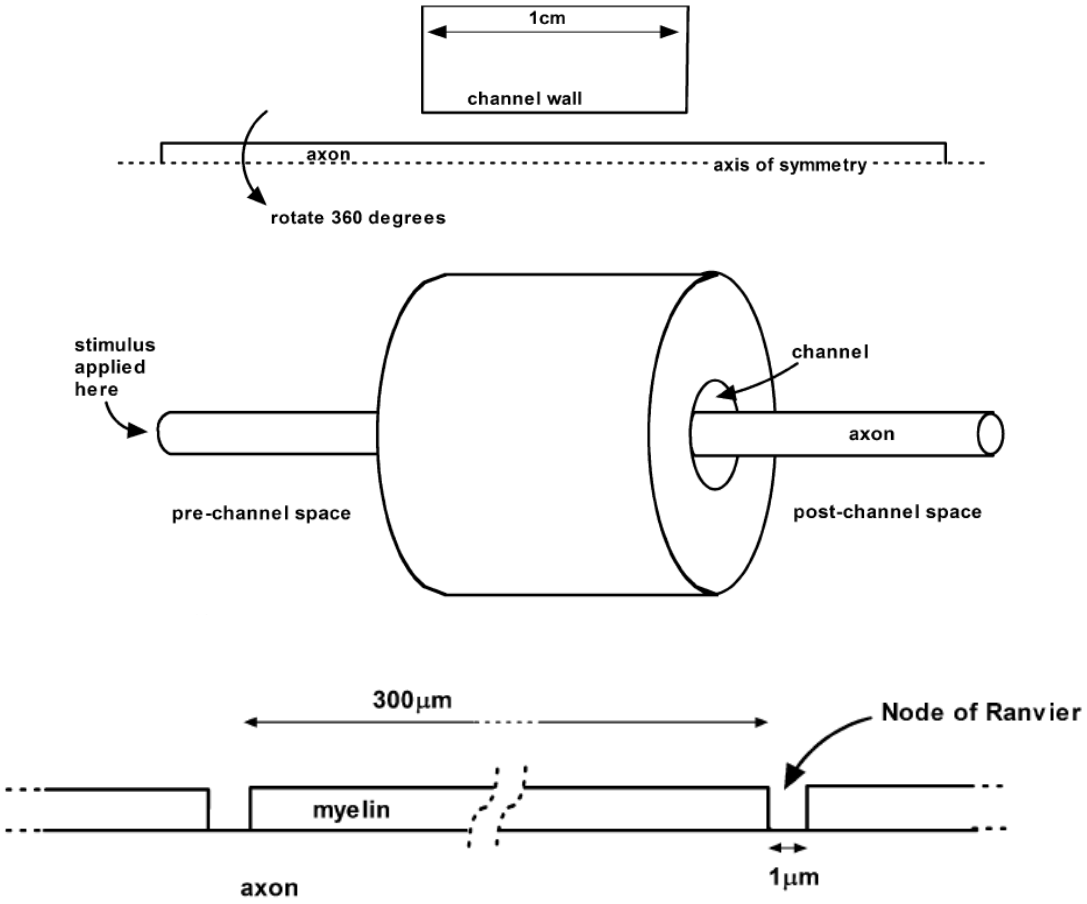


Fig. 4.2: Simulation geometry used in FEM analysis by Fitzgerald et el[10]. Top- 2D axisymmetric unmyelinated axon. Middle- the 2D model is swept over 360^0 to give a 3D structure. Bottom- Myelin segments added for myelinated axons in the model

Alternatively, the extracellular resistivity can be increased in the region of the electrode whilst avoiding any changes to the physiological composition of ECF. This can be achieved by reducing the ECF volume surrounding the electrode. This concept was initially investigated by Huxley and Stampfli [57] who confined a nerve fibre in glass capillary of about $40\mu m$ to illustrate Saltatory conduction in myelinated axons. The extracellular resistance was measured to be $0.5\,M\Omega$. Further investigation by Loeb and Colleagues mathematically showed that signals in the order of 1mV might be recorded from short and very narrow tubes [58].

To fully appreciate the effects of confining axons in micro-channels and evaluate if this design structure can constitute a suitable foundation for the design of peripheral nerve interface, Fitzgerald et al[9] used finite element modelling (COMSOL) to answer a number of related questions which included:

- What are the extracellular signal levels that can be recorded from an axon confined in a micro-channel?
- What are the effects of axon size and micro-channel cross section on the recorded signal?
- Does electrode-axon proximity within the channel have any significance?
- Does electrode positioning with respect to node of Ranvier have any effect?
- Is there a difference in the relative signal size for different types of axons (myelinated vs. unmyelinated)?

By answering these questions, one can calculate the ideal dimensional parameters for the proposed neural implant. This modelling study can be used as preliminary design base for a neural implant that is capable of stimulating and recording from a small number of regenerating axons enclosed in micro-channels (for signal improvement).

An asymmetric geometry was drawn in COMSOL in two dimensions as shown in Fig. 4.2 (Top) and a program was written to sweep the 2D geometry through 360^0 about the axis of symmetry to obtain the 3D structure of the axon running through the micro-channel (Fig. 4.2 Middle). A modelled segment of the axon was left exposed on either side of the channel so that a travelling action potential could be recorded before, during and after it passes the channel.

Two separate models were constructed to account for the differences between unmyelinated and myelinated axons. The former model consisted of the interior of the axon and the exterior space forming the extracellular space. The two spaces were modelled as volume conductors, with a resistivity P_{axon} and p_{ecf} respectively, and separated by a thin film representing the axonal membrane based on Hodgkin Huxley equations [59].

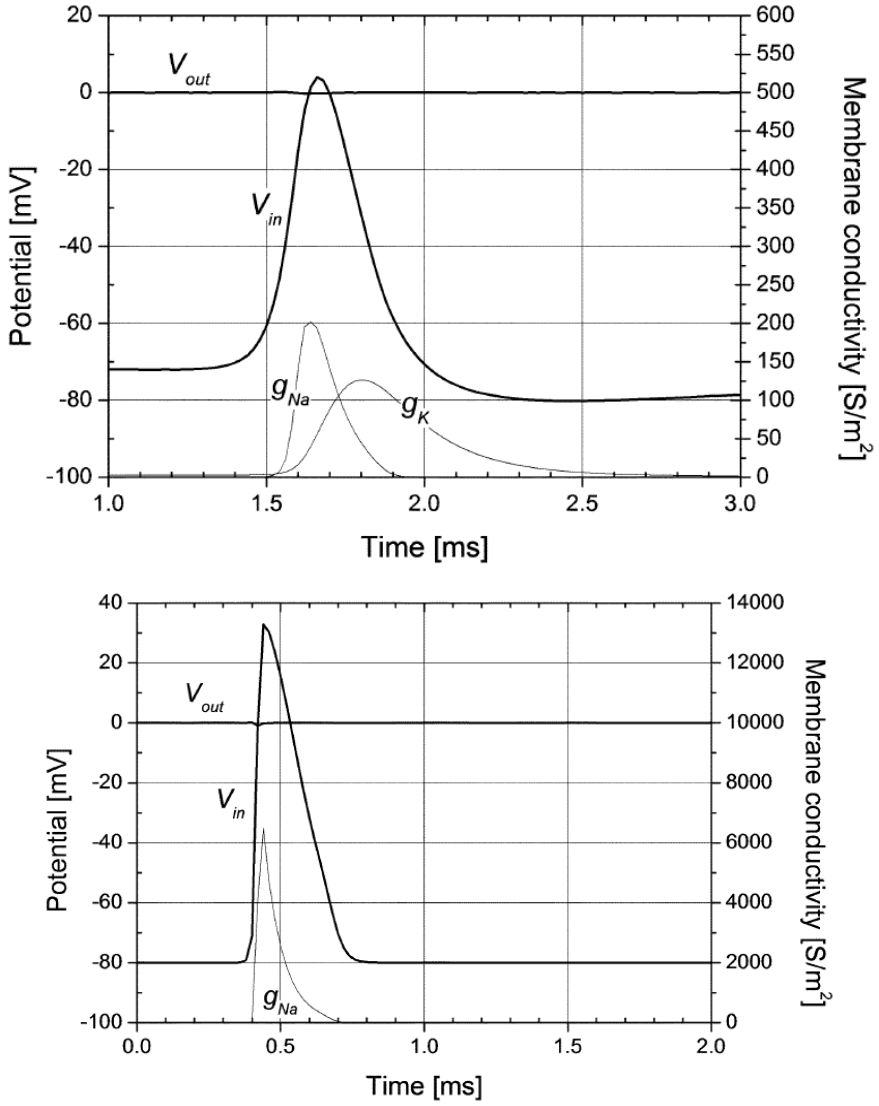


Fig. 4.3: Modelled Action Potential for: Top- a $2\mu m$ diameter unmyelinated axon, and Bottom- $10\mu m$ diameter myelinated axon outside of the channel[10]

The model for the myelinated axon used a different modelling process to account for the myelin segments and the difference in signal propagation compared to the unmyelinated axon (Fig. 4.2 Bottom). The myelin segment in uninjured normal nerves varies with fibre diameter but is constant at about 300 μm in regenerated nerves [60] which are similar to the nerve fibres regenerating through the neural interface presented in this thesis. The variation in axonal diameter and conduction velocities of both myelinated and unmyelinated axons were also accounted for.

The Action potential was modelled for a $2\,\mu m$ diameter unmyelinated axon and is shown in Fig. 4.3(Top). The conductances are also provided. Similarly, the action potential and conductances for a $10\,\mu m$ diameter myelinated axon were also computed and are shown in Fig. 4.3 (Bottom). For both myelinated and unmyelinated modelled axons, extracellular potential V_{out} measured is extremely small compared to the internal potential V_{in} and the change in V_{out} can be barely seen in both figures.

4.2. Extracellular Amplification through confinement

The changes in the Action Potential for a $10\mu m$ diameter myelinated axon pre-channel, mid-channel and post-channels are illustrated in Fig. 4.4. The channels have $1000\mu m^2$ cross-section and 1cm length. 1cm segment of the axon is exposed on either channel side. As can be seen in Fig. 4.4(a) representing the potential in the pre-channel space, again V_{out} is so small compared to V_{in} that it can hardly be seen. The effect of confining the axon in a micro-channel is illustrated in Fig. 4.4(b) where it can be noted that the internal potential V_{in} has dropped from $35mV$ to $20mV$ whilst the extracellular potential V_{out} has considerably been amplified. V_{out} signal appears triphasic with an initial and a final positive phase mediated by a larger negative phase with a maximum of about $10mV$ which is within the recordable range for the peripheral neural interface we would like to develop. The negative phased potential in V_{out} is opposite but coincides with the peak in V_{in}. This explains the drop in the amplitude of V_{in} which accounts for the expected increase in V_{out}. The positive phases, accompanied by similarly sized pulses of the same sign in V_{in}, correspond to the abrupt change in R_{ecf} as the AP enters the channel and then emerges from the channel. This results in a net shift of positive charge into the channel in both cases. Fig. 4.4(C) shows that the waveforms return to their original shape in the post-channel space once the AP has emerged from the micro-channel.

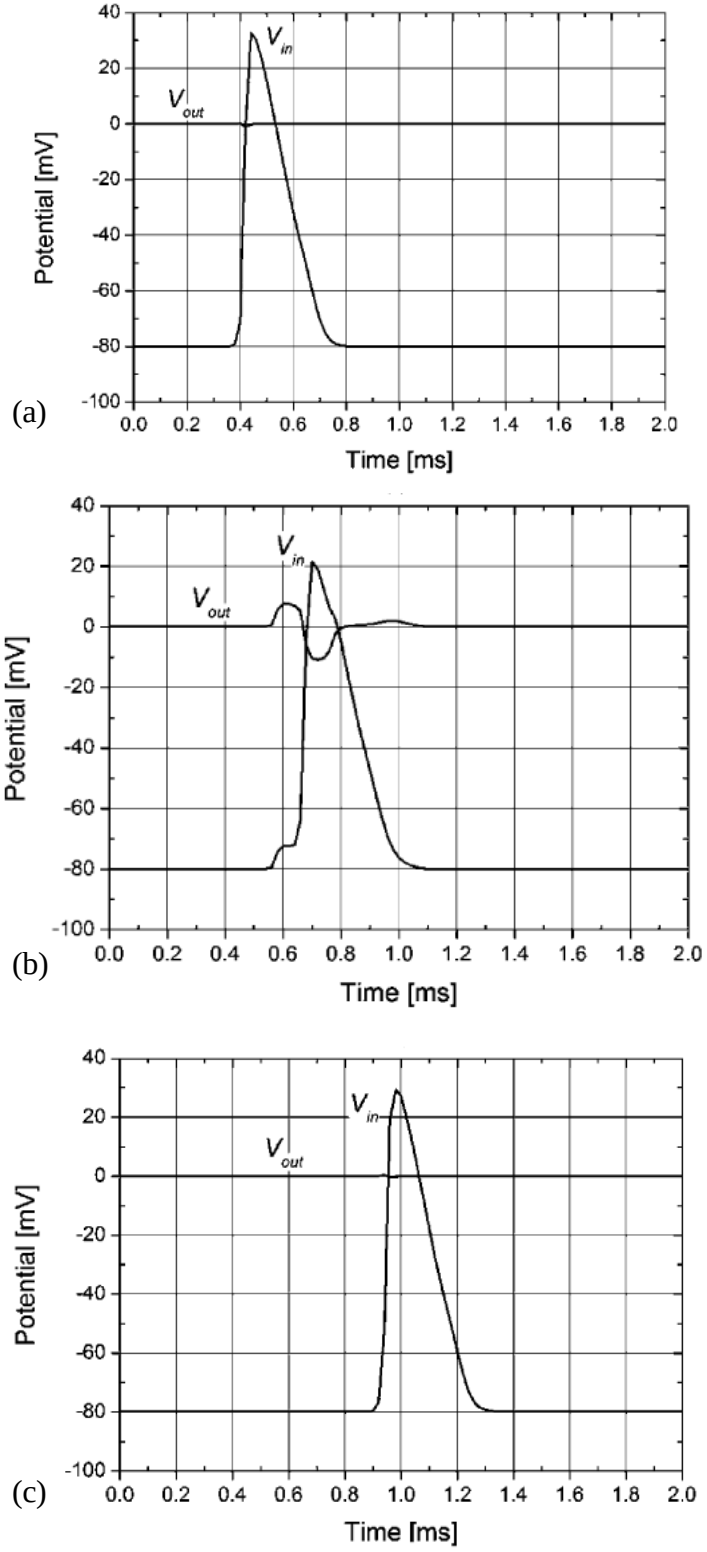


Fig. 4.4: Modelled Intracellular (V_{in}) and extracellular (V_{out}) voltages for a 10 μm myelinated axon (a) before it enters the microchannel, (b) Halfway the channel, and (c) after emerging from the micro-channel[10].

4.2.1. Effect of varying channel cross-sectional area and axon diameter

While keeping a constant axon size, the channel cross-sectional area was varied and the effect this has on the amplitude of the extracellular signal V_{out} for myelinated and unmyelinated axons is shown in Fig. 4.6. Increasing the channel size resulted in a decrease in the amplitude of V_{out}. This is as expected since increasing the size of extracellular volume conductor is accompanied by a reduction in R_{ecf}.

Similarly, the effect of varying the axon diameter while keeping the channel cross-sectional area constant is investigated and the results are plotted in Fig. 4.7 for myelinated and unmyelinated axons. As can be seen, increasing axonal diameter is accompanied by a significant increase in the amplitude of the extracellular signal. This is because at lower axonal diameter, R_{axon} decreases with the raise in the intracellular conducting volume leading to an increase in $\frac{R_{ecf}}{R_{axon}}$ and hence an increase in the extracellular signal amplitude (Equ.4.4). On the other hand, at higher axonal diameters, the axon begins to occupy a considerable amount of the channel space resulting in an increase R_{ecf} which enhances the effect of the decreasing R_{axon}.

4.2.2. Effect of varying channel length

In the previous analysis the channel length was set constant at 1cm. The effect of channel length on signal amplitude was also explored. The result of varying the channel length from 2mm to 1cm in increments of 2mm for $10\,\mu m$ diameter myelinated axon with $1000\mu m^2$ cross-sectional channel area is plotted in Fig. 4.8. The increasing channel length enhances the extracellular signal amplitude and hence the ability to record these signals. The rate, at which the signal increases, decreases at higher channel lengths suggesting a saturation point at which the increase in the signal amplitude is negligible.

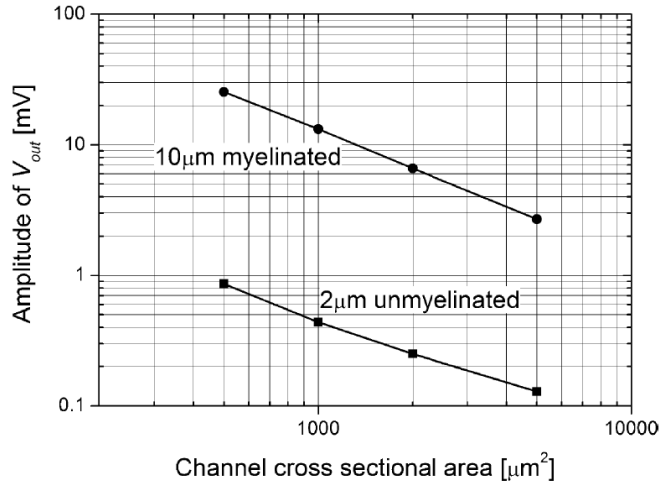


Fig. 4.5: The amplitude of V_{out} versus the channel cross sectional area.

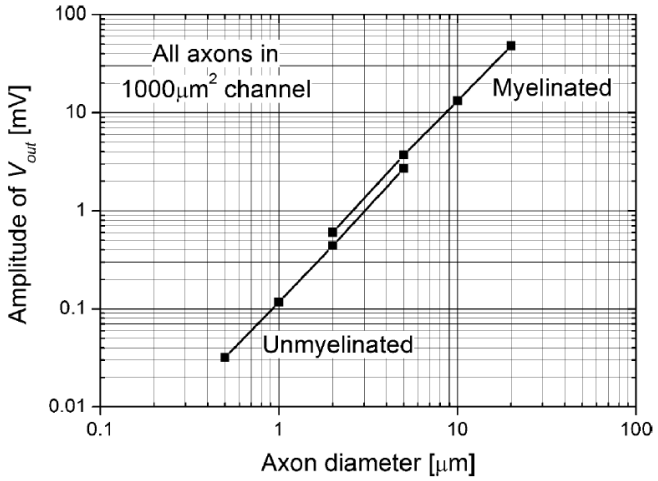


Fig. 4.6: The Amplitude V_{out} versus the axon diameter[10].

4.2.3. Radial potential distribution

The change in V_{out} with respect to the radial distance from the centerline of a $10\,\mu m$ myelinated axon was also examined (see Fig. 4.9). The channel length and the area were set to 1cm and 1000 μm^2 respectively, and the measurements were taken at a node of Ranvier when the signal is at its maximum. Prior to channel entry, the axon has a peak of 0.1mV at its external surface, while at the channel centre, the enclosed axon has an amplified signal amplitude V_{out} of over 10mV. Furthermore, prior to channel entry the

signal V_{out} has declined by 86% at the radial distance corresponding to the channel wall, whilst in the channel there is less than 1% redial reduction of the signal.

The channel confinement makes the extracellular signal almost constant transversely across the channel. This indicates that currents in the micro-channel are nearly completely longitudinal. The longitudinal character of these currents makes recorded extracellular signal independent of the position of the axon with respect to channel centre line. Hence moving the modelled axon off channel centre will not change the magnitude or the direction of the current or extracellular resistance and hence the generated potential gradient along the channel is also unaffected. With the voltage being transversely constant across the channel, it is not required for the microelectrode surface to be close to the axon it is recording from. Therefore, it should make no difference to the recoding whether the axon is in direct contact with the surface of an electrode in the channel wall or is on the opposite side of the channel.

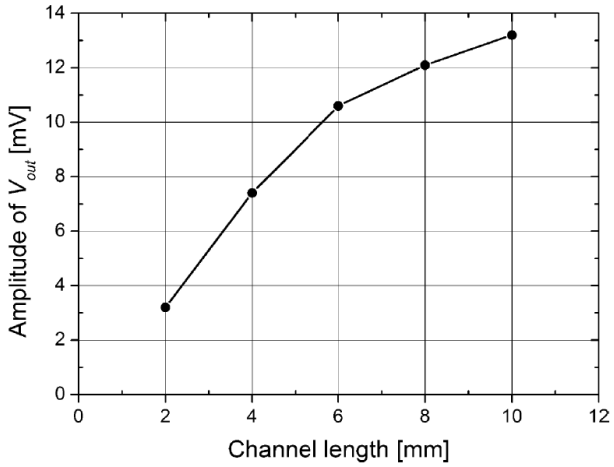


Fig. 4.7: The Amplitude V_{out} versus the length of the channel[10]

4.2.4. Amplitude versus axial position

The amplitude of the extracellular signal was also computed for both the myelinated and the unmyelinated pre-channel entry, as it travels along the channel and as it emerges from the channel. The data is shown in Fig. 4.9 (a). In the case of the unmyelinated axon, the

signal rises for the first 0.5 mm into the channel and then levels off to start decreasing from a similar distance from the channel exit to return to its original level before entering the channel. On the other hand, myelinated axons display a different behaviour. As the AP enters the channel, the extracellular signal amplitude progressively rises to reach a peak and then gradually drops to its pre-channel entry level at the channel exit.

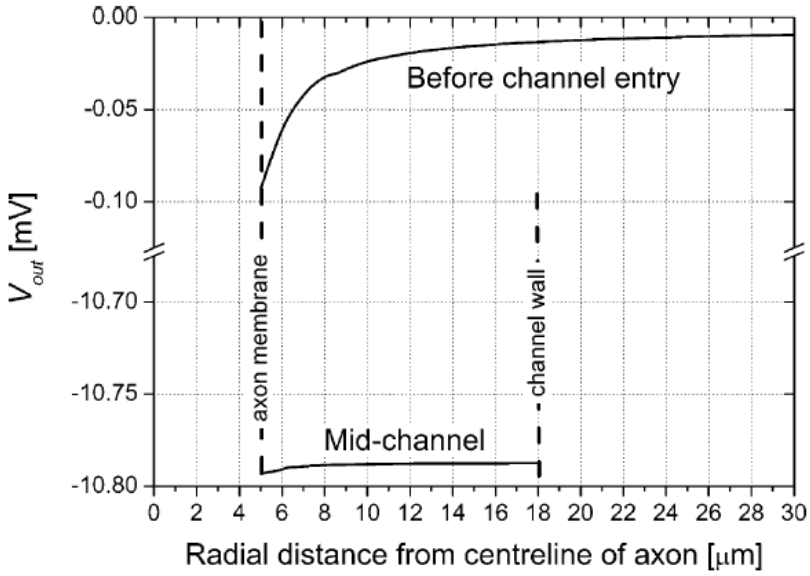
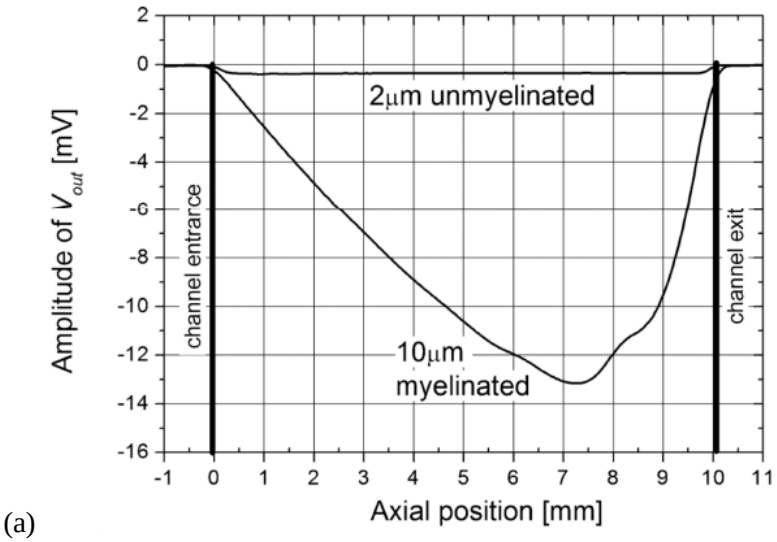


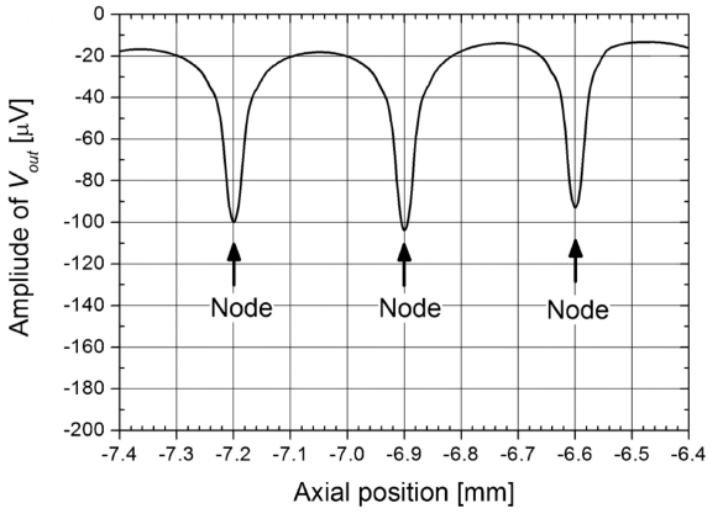
Fig. 4.8: V_{out} amplitude versus radial distance from the centerline of a 10 μm myelinated axon[10]

The difference in the pattern of the extracellular voltage for myelinated and unmyelinated axons can be attributed to propagation velocities. Unmyelinated axons have a slow velocity which implies that the action potential spreads over a short distance into the micro-channel (estimated to be 0.5mm for 1 μm unmyelinated axon in the model) and stays constant until it approaches the exit from a similar distance. Myelinated axons, however, have a much higher propagation velocity resulting in the AP occupying a much longer axon segment. For instance, for a 10 μm myelinated axon, a fibre transmitting a 0.5ms duration action potential at a velocity of 50m/s would spread over a region of 2.5cm. Therefore, the amplitude of the extracellular signal does not level off but gradually rises along the channel until it reaches a maximum where it turns and falls to its pre-channel level at the channel exit. Further signal growth is obtainable with a considerable increase in the channel length. The signal growth saturates when the channel length prior and post the microelectrode site is greater than the spatial distribution of the action

potential[3]. This would require the channel length to be several centimetres which is impractical for the design of most neural interfaces. If the channel is shorter than the spatial distribution of the action potential, the signal will be less than its theoretical maximum. However the longer the channel the more closely it will approach this theoretical value.



(a)



(b)

Fig. 4.9: (a) V_{out} amplitude versus axial position in a 1000 μm^2 channel for a 2 μm diameter unmyelinated axon and 10 μm diameter myelinated axon. (b) a close up into a 1mm section of the same 10 μm diameter myelinated axon approximately 7mm before channel entry[10]

As one might expect, the signal peak is not at the centre of the channel but shifted two thirds from the channel entry and the amplitude is 85% of the peak at mid-channel. This

[3] This ensures that the extracellular impedance is raised over the entire distribution of the action potential.

shift in the maximum can be explained by a progressive cancelation between the extracellular currents responsible for the initial positive phase of V_{out} and the following negative phase. This is because the former is a standing wave existing simultaneously at all points in the channel, as it is caused by a temporary shift of charge into the channel, while the latter is a travelling wave of the AP that passes along the channel. Therefore the two phases gradually cancel each other out and then gradually separate with distance along the channel. By placing the electrodes at the location of the peak, the recorded signal can be maximized.

Relationship to node position

A close up into 1mm segment of the same $10\mu m$ myelinated axon before channel entry reveals a heavy dependence of the extracellular signal V_{out} on the axial position (Fig. 4.9b). When comparing this to the recorded signal inside the channel (Fig. 4.9a), it is found that channel confinement does not only significantly amplify the signal amplitude V_{out}, but it also makes the signal independent of the node position for the duration of the channel length. Thus by enclosing the axons in a micro-channel, the problematic requirement of placing the electrode near a node of Ranvier no longer applies.

The amplification advantage of the micro-channel can be seen by comparing the maximum amplitude of V_{out} which is 13mV with that prior to channel entry (at the nodes of Ranvier) which is $100\mu V$. This yields a gain greater than 100 which makes axonal micro-channel confinement a very attractive solution.

Fibre selectivity

The signal amplification drops to unity at the channel exit. This is beneficial as it suggests that the amplified signal is unlikely to be picked up by an electrode in a neighbouring channel meaning less crosstalk. As mentioned earlier, adequate information to drive prosthesis can be derived by interfacing to a small proportion of axons. These axons are

normally the largest myelinated fibres that control voluntary muscles. It is essential to be able to distinguish signals in these axons from those produced by small unmyelinated fibres occupying the same channel. This fibre selectivity in a single micro-channel could potentially be accomplished by making use of the size differential between myelinated and unmyelinated fibres which has a highly desirable effect on the relative amplitude of V_{out}. For instance, a $10\mu m$ myelinated axon confined in $1000\mu m^2$ channel has 25 times higher extracellular amplitude V_{out} than that for a $2\mu m$ unmyelinated axon confined in the same channel. With a simple thresholding circuit fibre type selectivity could be achieved. However it is crucial to bear in mind that the axons that the neural interface will be recording from are regenerating axons, and hence their diameter is at first significantly smaller than the original distal part, which implies that the recorded signals will initially be small. This means that fibre type selectivity will be very low at the beginning but as the fibres grow over time, both the recorded signal and the fibre type selectivity will improve[10].

To summarize, Fitzgerald et al has illustrated some important benefits of the micro-channel confinement through finite element modelling. These benefits include:

- Considerable amplification of extracellular axonal signals
- The axons are no longer required to be placed near the surface of the electrode and the electrodes no longer need to be positioned close to nodes of Ranvier for recording
- A large number of channels are functionally active
- Minimized cross-talk
- Improved fibre –type selectivity

This study has provided us with a way to estimate the optimal location for any particular geometry for the intended implant and hence can be used as an initial design platform for realising a regenerative implant aimed at recording from a small proportion of regenerating axons confined in a micro-channel for signal enhancement.

4.3. In Vitro study of Axon outgrowth through 2D array of micro-channel[4]

Now that the theoretical platform for design criteria has been established through the finite element modelling, some experimental validation needed to be done to confirm these findings, optimize implant model dimensions address other biological issues such promoting regeneration through growth factors, and ensuring a sufficient supply of oxygen and nutrients within the channel.

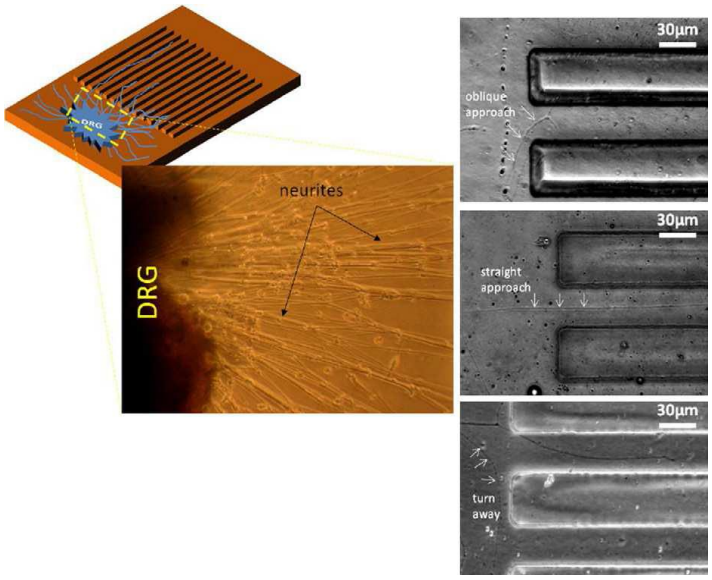


Fig. 4.10: Dorsal Root Ganglions cultured onto polymide arrays have an oblique approach, straight approach or turn away [61]

Using in vitro cultures of dorsal root ganglion, Lacour et al [61], investigated axon outgrowth through arrays of 2D micro-channels as a function of channel size, shape and transparency to optimize the micro-channel parameters (cross-section and density) and examine the effectiveness of artificial mechanical guidance on growth of axons through poylimide micro-channels. The passive 2D channel arrays used in the study were fabricated by casting of polymer based materials using specially prepared silicon moulds. Two materials were used Pyralin2611 and photo-sensitive polyimide (Durimide7020). Each device prototype consisted of an array of parallel micro-channels and a flat plating area at one end of channels to seed dorsal root ganglion (DRG).

[4] This section is based on findings reported by Lacour et al in [61] S. Lacour, *et al.*, "Polyimide micro-channel arrays for peripheral nerve regenerative implants," *Sensors and Actuators: A Physical,* vol. 147, pp. 456–463, 2008.

DRG were placed on the plating area of various polymeric channel arrays with different transparencies [5] (see Fig. 4.10). The Samples were cultured for up to two weeks and neurites from DRG grew towards the channels. The finding suggested that the proportion of the axons entering the channels increases with transparency and therefore the wider the channels and the narrower the channel spacing is the better. To achieve more than the required 80% of regenerating axons entering the channel, a transparency of at least 50% needs to be used (Fig. 4.11).

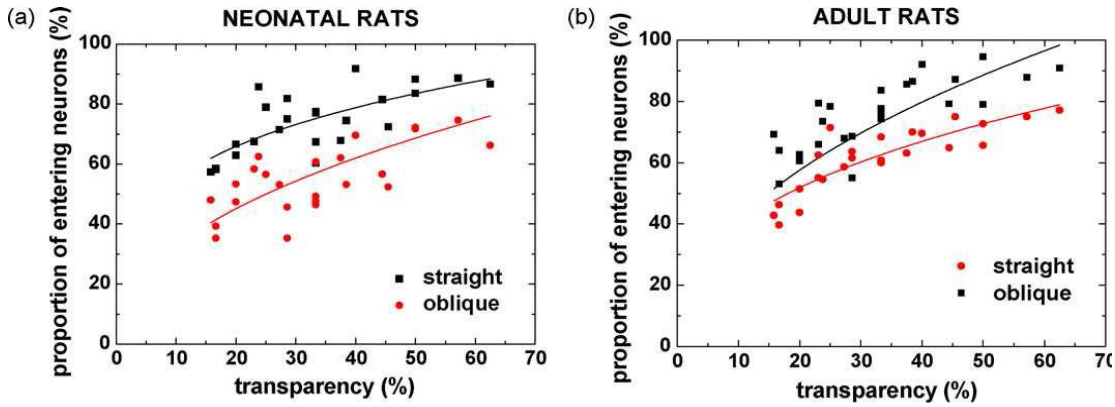


Fig. 4.11: Proportion of neurites entering channels versus channel array transparency for (a) neonatal rats and (b) adult rats. Neurites that entered the channels parallel to the channel axons were recorded as 'straight', while neurites approaching the channels at a 30^0 angle or greater were recorded as 'oblique'[61]

4.4. 3D micro-channel structure investigation *in vivo*[6]

Now that the ability of the micro-channels to support regenerating axons has been confirmed in 2D planner channels, the next important step is to transfer the 2D planner structure into a 3D interface. Five different types of devices were fabricated to optimize

[5] Transparency of the device is defined as ratio of the open area occupied by air over the total cross-section (which is air +polymer). Transparency T(%) can be expressed as: $T(\%) = \frac{w}{S+w}$ where w is the channel (air) and S is the spacing between the channels (i.e the width of the channel wall)

[6] This section is based mainly on work conducted by S. P. Lacour et al and reported in: S Lacour, J Fitzgerald, N Lago, E Tarte, SMcMahon, and J Fawcett. Long micro-channel electrode arrays; a novel type of regenerative peripheral nerve interface. *IEEE Trans on Neur. Sys and Rehab Eng*, 17:454–60, 2009.[61] S. Lacour, *et al.*, "Polyimide micro-channel arrays for peripheral nerve regenerative implants," *Sensors and Actuators: A Physical,* vol. 147, pp. 456–463, 2008.

and validate the design of the implant[6]. Three types were passive devices designed to evaluate the *in vivo* outgrowth and vascularisation through arrays of micro-channels. Each type tests a particular feature of the implant design to assess its effect on regeneration. Type 1 devices (Fig. 4.12a) were Silicon sieve devices fabricated with a range of channel cross-sections and transparencies with a fixed channel length of 0.5mm. Type 2 devices (Fig. 4.12b) fabricated in different lengths of 1mm to 5mm by casting of PDMS on a grid of nylon filaments as it is not possible to achieve such channel length using silicon. These devices had a fixed channel cross-section and transparency. Type 3 devices (Fig. 4.12c) aim to assess the biocompatibility of polyimide *in vivo* and nerve regeneration through rolled 3D polymeric implant. These devices were made of spin-able polyimide and photo-sensitive polyimide with channel width of 70μm, channel height of 20μm-40μm, channel length of 6mm and channel spacing of 30μm. The implants were fabricated by spin coating and curing a Pyralin 2611 layer on carrier wafer and then spin coating, patterning a 20μm-40μm thick layer of photosensitive polyimide (PSPI 7020) on the previous layer. After curing, the samples were peeled off, rolled and inserted into a 1.5mm inner diameter silicone tube.

The last two types of the five (type 4 and 5) were active devices intended to assess ability to record and stimulate nerve fibres enclosed in micro-channels *in vitro*. Type 4 using a similar method to type 2 (casting PDMS) but incorporated embedded electrodes into the channel walls by wrapping the filament with fine gold before casting. Pulling out the filament after curing leaves behind an array of channels with embedded electrodes. The channels were 90-130μm in diameter, 6-10mm long. Type 5 were similar to type 3 devices with addition of embedded electrodes which were incorporated into the devices by thermally evaporating and patterning a gold metallisation layer on the top of the PI2611 layer. An insulation layer made of PSPI7005 was spun and patterned to insulate the electrodes before spinning the PSPI 7020 channel layer. The devices were cured, peeled off the wafer and then inserted into a silicone tube similar to the one used for type 3 devices.

After implantation of the passive devices for 4 to 12 week in the sciatic nerve of an adult rat, the implant and the attached nerve were harvested to evaluate regeneration and

vascularisation through micro-channels as a function of channel cross-section, transparency and length. Fig. 4.13 shows transverse sections of a mini-nerve that had regenerated axons through a 100µm wide micro-channel in type 1 implant (sieve implants). The regenerated fibres had a similar morphology to those regenerating without the presence of an implant or through a plain silicone tube. There was limited axon regeneration around the periphery of the implant; the channels in this region were occupied by unmyelinated fibres and other cells such as Schwann cells and fibroblasts (Fig. 4.13c). The regenerated neural tissue hosted in the micro-channels had the structure of mini-nerve fascicle consisting of clusters of axons and bloods vessels and bounded by a distinctive connective tissue sheath (Fig. 4.13 b,d,e).

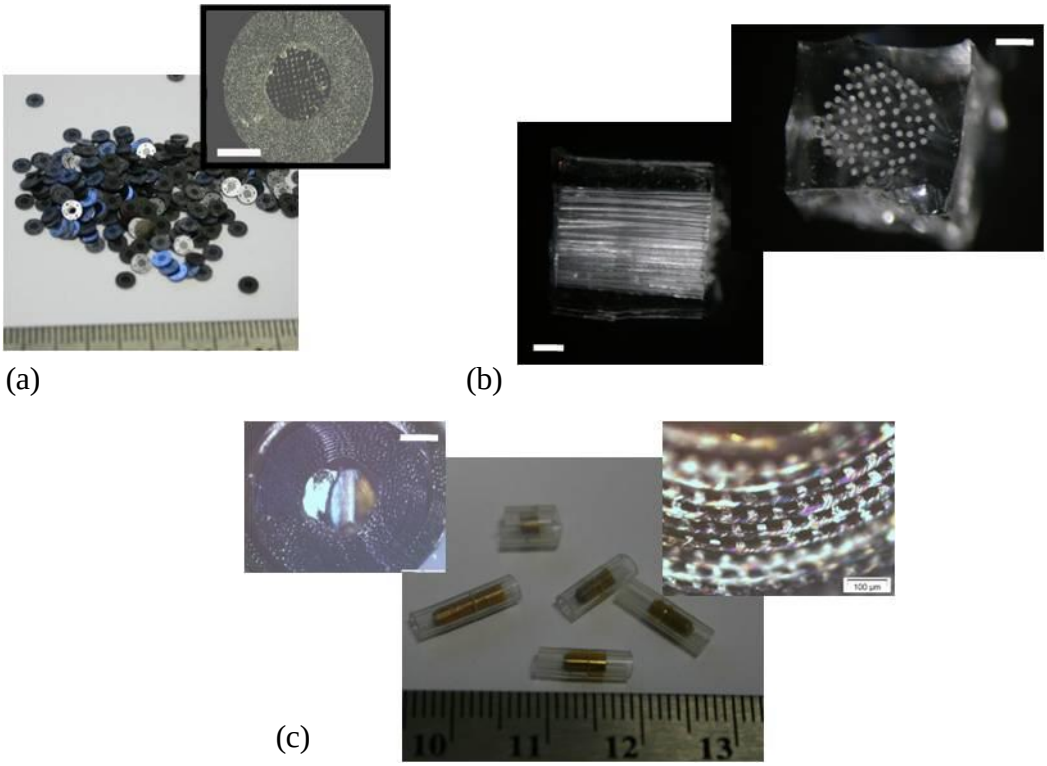


Fig. 4.12: Optical micrographs of micro-channel implants. (a) Type 1- batch processed Short silicon implants, with a length of 0.5mm, a channel diameter range of 55µm - 100µm (scale bar: 1mm). (b) Type 2- Long silicone micro-channel implants, prepared by casting silicone over a grid of 100µm diameter nylon filaments, and pulling out the filaments once silicone had set. The implants host bundles of parallel channels over a 1.5mm diameter cross section, and 1mm to 5mm lengths. Scale bars are 0.5mm. (c) Type 3. Rolled polyimide implants prepared using standard planar micro-fabrication processes. Micro-channels shown on the right have a cross of 70µmx40µm. Rolls were held in a silicone tube of 1.5mm inner diameter matching rat sciatic nerve diameter. Scale bar: 0.5mm[62].

By analysing the results, it was clear that larger channels supported more myelinated axons and the larger the channel cross-section the better myelinated axons regenerate. 100 μm side channels sustained nearly four times more myelinated axons than their 55µm counterparts (Fig. 4.14). Channels with 100 μm x100 μm cross-section, a transparency of 0.49 and 1mm channel length supported the best reinnervation. Transparencies beyond 0.4 did not seem to improve axon outgrowth significantly. There was some regeneration through long micro-channels (4-5mm) but the quality of reinnervation seemed to decline sharply for lengths greater than 2mm (Fig. 4.15). Good vascularisation was observed with blood vessels growing through long channels for up to 5mm which is vital for the provision of oxygen and nutrients to the regenerating tissue.

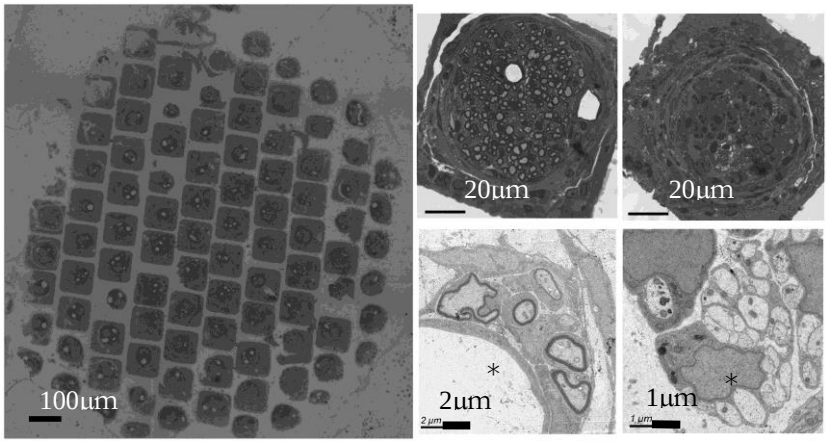


Fig. 4.13: Micrographs of transverse sections of regenerated nerves through type 1 micro-channels (sieve implants). (a) Array of mini-nerves growing through a type 1 implant, at the distal end of the channels. Micro-channels are 100µm side (Scale bar: 100µm). (b-c) Typical regenerated mini-nerves (scale bar: 20µm). Micro-channels may be filled with unmyelinated and myelinated axons and blood vessels (b) or mainly with fibrous tissue (c). (d-e) TEM (Transmission Electron microscopy) images of a mini-nerve showing myelinated fibres that regenerated close to a blood vessel (d – asterisk), and Schwann cells with unmyelinated fibres (e – asterik)[62].

Although no adverse reaction to the PI/PSPI implants was recorded, unfortunately, axon regeneration through these devices was still low after 12 week of implantation. The majority of micro-channels were filled by connective tissue and blood vessels. This was attributed to channel cross-section and transparencies being too small to support good regeneration. A fibrous tissue sheath was enclosing all the regenerated mini-nerves, and

in some cases occupied half of the channel area that was meant to be for regenerating axons. The rectangular cross-section of the PI/PSPI rolls was not ideal for reinnervation as the micro-channels were frequently almost fully occupied by fibrous tissue which limits the area available for growing axons. Ideally, a circular area is favourable since it would optimize the space available for axon regeneration but since this not feasible through planar micro-fabrication, a square channel cross-sectional area would probably minimize the amount of space occupied by fibrous tissue.

Type 4 active devices consisting of 90 to 130μm diameter, 6 mm long channels were used to conduct an *in vitro* study to experimentally investigate the electrical properties of recording and stimulating nerve fibres inserted through micro-channels. It was possible to record extracellular voltages of up to 500μV through an electrode placed halfway the channel. The recorded signal increased with decreasing channel diameter, increasing channel length and increasing axonal diameter which is in agreement with the modelling results discussed in the previous section. The channel confinement seemed to also remove the dependence of the recorded signal on proximity of the recording electrode to a node of Ranvier. This is essential as it is difficult to predict where the nodes on the regenerating nerve will be and hence one has little control in placing the electrode close to a node. In addition, micro-channels seemed to also be efficient in stimulating. Stimulation was accomplished using very small currents and short time pulses of 1μA for 50μs which is 10 times lower than existing intra-neural stimulators.

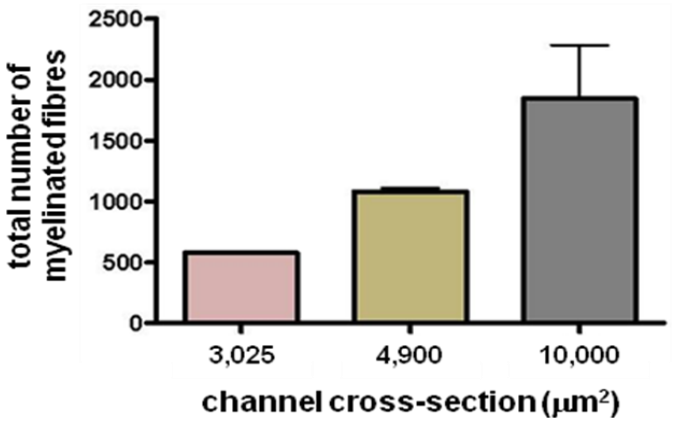


Fig. 4.14: Effect of channel geometry on axon regeneration through type 1 micro-channel arrays. All data were obtained 30 days post-implantation. (b) Number of regenerated myelinated fibres as a function of channel size. Implant transparency was 0.49[62].

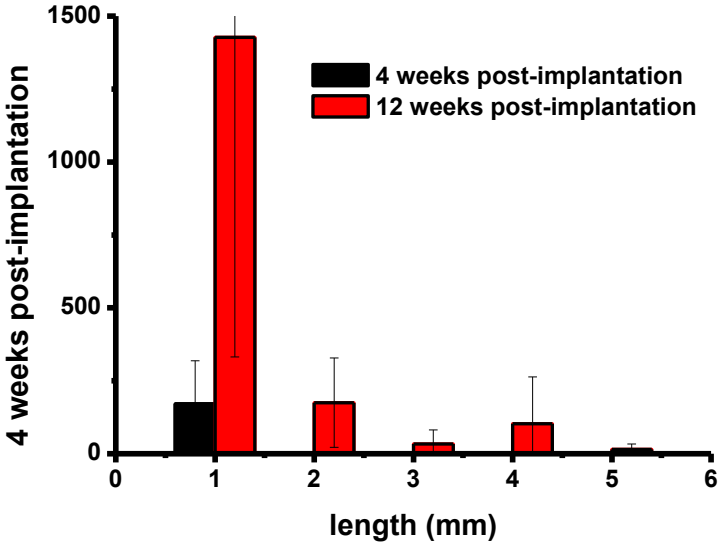


Fig. 4.15: Number of regenerated myelinated axons as a function of micro-channel length at 4 and 12 weeks post-implantation[63]

Finally, type 5 devices (similar to type 3 with embedded electrodes) were fabricated as an initial prototype to test using this approach to design 3D implants. The impedance for an electrodes positioned at the channel midpoint was 1.1 $M\Omega$ at 1kHz compared to an initial unrolled impedance of 1 $M\Omega$ at 1kHz which indicates that rolling has not affected the functionality of the embedded wiring. The impedance of the electrode did not change after 5months of being held in a roll. This suggests this electro-mechanical design of making 3D micro-channel implants with embedded electrodes should be reliable to use for long term regenerative implant.

4.5. Chapter Summary

To summarise, the theoretical modelling conducted by Fitzgerald et al [9] has shown that micro-channels can act as axonal amplifiers where the recorded extracellular signal is considerably amplified through confinement of the axon in a micro-channel. Besides amplification, the modelling has also illustrated the benefits of housing axons in micro-channels. These include:

- Minimized crosstalk and good fibre type selectivity

- Freedom from the need to bind axons to electrodes as the axonal signals recorded inside the micro-channels are radially independent of proximity to the axon surface.
- Freedom from the requirement of positioning the electrodes close to a node of Ranvier as the signals recorded inside the micro-channels are axially independent of proximity to a node of Ranvier, allowing a large number of micro-channels to be functionally active.

This modelling study has also provided us with suggestions to optimise the dimensional parameters of the SPNI implant. The suggestions include:

- Channel lengths of up to 1Cm can be considered
- The optimal position for the implant micro-electrodes are two thirds from the micro-channel entry as the maximal signal amplification is at this point. Placing the microelectrodes at mid-channel would give 85% of the peak
- Signal recorded inside the micro-channels are inversely proportional to the micro-channel diameter or cross-section. Hence smaller micro-channel diameter or cross-section can result in better amplification

The in vitro study conducted on 2D planner channels reported by Lacour et al[59] suggested that the proportion of axons entering channels increases with device transparency where wider channels and narrower spacing supports more regeneration. Axonal regeneration and vascularisation through micro-channels were evaluated *in vivo* [60] as a function of device transparency (micro-channel cross-section and micro-channel spacing) and micro-channel length. Micro-channels with $100\,\mu m$ x$100\,\mu m$ cross-section, a transparency greater than 0.49 and 1mm channel length supported the best reinnervation. Growth of axons through longer channels (up to 5mm long) has been demonstrated, although the quality of reinnervation seemed to decline sharply for lengths greater than 2mm. and requires substantial improvement.

The study also showed that a rectangular micro-channel cross-section is not ideal for regeneration as micro-channels were almost completely filled with fibrous tissue which limits the space available for growing axons. A square channel cross-sectional area

(which is possible through 2D planner micro-fabrication) would probably minimize the amount of space occupied by fibrous tissue. The electrical properties of recording and stimulating nerve fibres inserted through micro-channels were also investigated in this study. It was possible to record extracellular voltages of up to 500μV through an electrode placed halfway the channel. The recorded signal increased with decreasing channel diameter, increasing channel length and increasing axonal diameter which is in agreement with the modelling results discussed in this chapter. The channel confinement seemed to also remove the dependence of the recorded signal on proximity of the recording electrode to a node of Ranvier. This is essential as it is difficult to predict where the nodes on the regenerating nerve will be and hence one has little control in placing the electrode close to a node. In addition, micro-channels seemed to also be efficient in stimulating nerve fibres. Stimulation was accomplished using very small currents and short time pulses of 1μA for 50μs which is 10 times lower than existing intra-neural stimulators.

The research in this thesis uses the design suggestions in this chapter to optimise the design and the fabrication of the SPNI implant that has the ability to efficiently record from and stimulate axons that have grown through its micro-channels. The next chapter introduces and discusses the design of such a neural interface in details.

5. DESIGN CHAPTER

5.1. Spiral Peripheral Neural Interface- The SPNI

When the peripheral nerve is injured, the axons in the distal part of the nerve become disconnected from their corresponding cell bodies and hence degenerate with time. The proximal part, however, is still connected to the cell bodies in the dorsal and ventral ganglion roots. This gives the proximal axons the ability to regenerate. When the gap between the two nerve endings is short, a direct tension free suture constitutes the best chance for good functional recovery. However, when the gap between the nerve endings does not allow for a direct suture, an artificial bridge, in the form of hollow tube whose internal diameter matches nerve's diameter, can be used. Because of the huge number of axons in a single nerve, regenerating fibres are often misrouted to the wrong receptor cells, resulting in poor functional recovery. In cases where the functional recovery post the lesion is not achieved or when there is complete amputation of the limb, finding a method for extracting neural signals and identifying the regenerating fibres would be very useful. The extracted and processed signals could then be used to drive muscle simulators or supply input signals to a prosthetic limb.

It has already been reported in Lacour, S.[61] that two dimensional (2D) arrays of micro-channels, ranging in width from microns to tens of microns and few microns in height, can provide good mechanical guidance for neurites *in vitro*. It has also been shown in an *in vitro* study that action potential entering long channels with a diameter ranging from 90 to 130μm were reliably recorded and the nerve fibres inside these channels can be efficiently stimulated[64]. These findings were integrated into a three dimensional bundle of closed micro-channels hosting micro-electrodes. The design of the individual micro-channels will not simply provide mechanical guidance to regenerating axons but will also enable the reliable recording of signals from myelinated

axons through embedded electrodes. Fig. 5.1 provides an illustration for this three dimensional implant so called the Spiral Peripheral Neural Interface (SPNI).

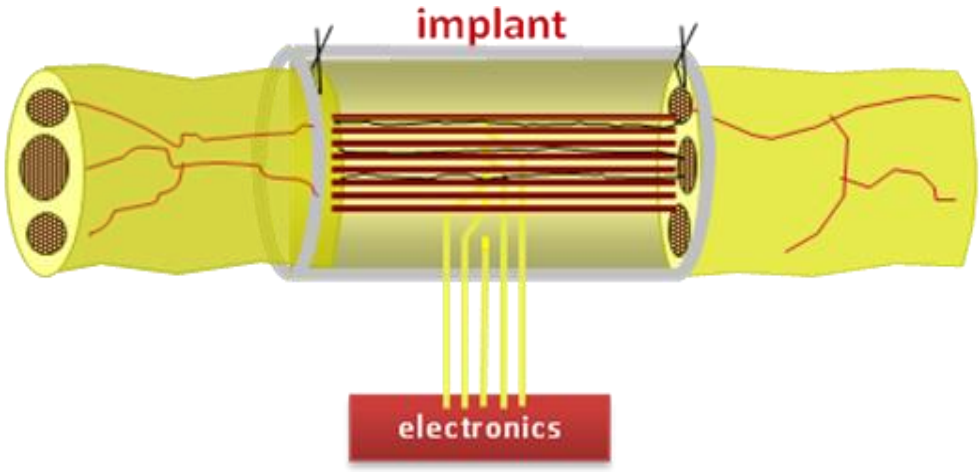


Fig. 5.1: Illustration of the 3D micro-channel implant; the spiral peripheral neural interface (the SPNI)

These implants are produced using polyimide films and planar micro-fabrication technology. The extreme flexibility of the polyimide films, allows the 2D array of micro-channels to be rolled and inserted into a suitable silicone tube whose diameter matches that of the nerve. This produces a 3D bundle of parallel micro-channels with embedded microelectrodes designed to withstand the rolling without any mechanical fracture which is important for implant functionality.

This chapter will first give a design overview of the implant followed by design considerations that guided the selection of the dimensional parameters of the implant such as channels size and length. Furthermore, connection methods used to enable electrical connections to the implant are also discussed. Finally, the neutral plane calculations for the placement of electrodes at the neutral plane are presented in detail.

5.2. Design overview of the SPNI implants

Polyimide was chosen as the base material for the implant because of its biocompatibility, flexibility, and the availability of photo-sensitive polyimides which can be processed by one-step photolithography. The biocompatibility of the polyimides

were evaluated and confirmed through both *in vitro* [61] and *in vivo* [62] studies as mentioned earlier. Two types of the three dimensional implant will be fabricated; passive implants which do not have embedded micro-electrodes and active implant with embedded micro-electrodes. The passive device will be implanted in animals to evaluate axonal regeneration through the micro-channel rolls. Once regeneration has been accessed, active devices will be implanted to stimulate and record from the axons that had regenerated through the micro-channels. Both types of implants consist of concentric rolled layers of micro-channels.

The SPNI active implants are made of four layers as shown in Fig. 5.2 fabricated using planar micro-fabrication technology and these are:

- The first layer is the substrate film which constitutes the structural base for the rest of the implant layers. It is made of Pyralin 2611 which is widely used in neuro-prosthetic implants because of its suitable properties in biomedical applications. These properties include biocompatibility, low water uptake, good thermal stability and electrical insulation properties. The thickness of the substrate layer is important as this will determine the strains that the metal layer will be subject to post rolling. The stress model calculations (detailed in section 5.4.5) showed that the neutral plane will always be halfway the substrate thickness. The thickness of the substrate was chosen to be in the range of 12 μm to 20 μm as this range would provide a durable device substrate and allow the rolling of the implant structure and its safe insertion into the silicone tube (please refer to chapter 7, section 7.9)
- The second layer is the micro-electrode metal layer which will be made of gold and chromium acting as an adhesion layer for gold. The chromium layer will be 50nm thick and the gold layer will have a thickness of 250nm. As chromium is not biocompatible, it will be substituted by Titanium in long term implants. Details related to the dimensions of the gold wiring, the electrode sites and the contact pads are provided in section 5.4 of this chapter.
- The third layer is the encapsulation or the passivation layer which electrically insulates the electrode wiring whilst exposing the recording sites at their corresponding channel, besides the contact pads. The insulation layer is chosen

to have a thickness of 3 μm to 5 μm which is enough to secure good passivation of the gold wiring. Details related to the dimensions of the electrodes, the contact pads and the gold wiring are given in section 5.4. The thicknesses of the substrate and the insulation layers were decided based on the neutral plane calculations[7] for the rolled structure and on what was practically possible. Placing the metal layer at or as close to the neutral plane as possible ensures that the strains on the metal layer in the rolled structure remain low and do not lead to mechanical fracture of the metal wiring. The initial stress model presented in section [5.4.3] suggested that the substrate needs to be 35 μm for the metal layer to be placed at the neutral plane. However fabricating the implants with this substrate thickness was not practically possible as it becomes difficult to roll and insert the structure into the silicone tube[8]. The substrate thickness was then changed to 20 μm as this was the maximum substrate thickness that can still allow the rolled structure to be inserted into the silicone tube reliably. However further investigation into the initial stress model revealed that this model does not accurately calculate the position of the neutral plane. The stress model presented in section 5.4.5 provides a more accurate calculation of the neutral plane for the rolled 3D structure of the SPNI implant. The model concluded that neutral plane of the 3D rolled structure is always located halfway the substrate thickness which means that the metal layer will always experience some compressive strain. Hence substrate thicknesses in the range of 12 μm to 20 μm are a good choice as they would provide a durable substrate that can still allow the rolled structure to be safely inserted into the silicone tube. The strains experienced by the metal layer increase as we move from the outer rolls of the structure towards the inner rolls as the radius of curvature decreases. So based on this and on regeneration results, the electrodes of the implant are distributed across the middle of the 3D structure.

[7] Please refer to section 5.4 for details on neutral plane calculations

[8] The silicone tube is used to prevent the rolled 3D structure from unravelling. It also provides a neat way to handle the implant and provide attachments for the severed nerve stamp as these are sutured to the silicone tube on either side. Please refer to chapter 7, section 7.9 for more details.

- The fourth layer is the micro-channel layer which is patterned so that the electrodes are exposed in the middle of their allocated channel i.e. halfway the channel length (refer to Fig. 5.2).

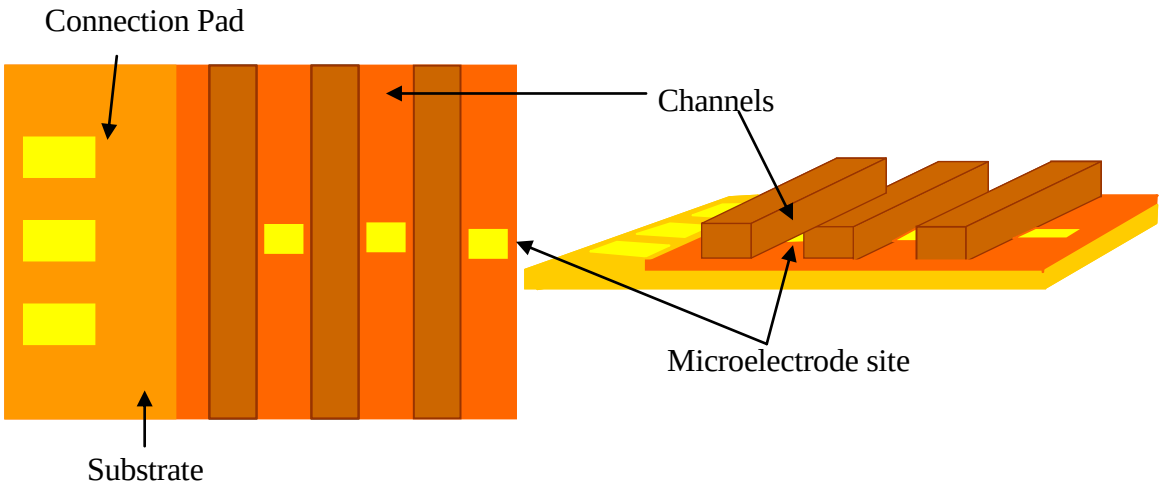


Fig. 5.2: layer layout for the SPNI active devices . Substrate layer thickness (12 to 20 μm), Metal layer thickness (gold is 250nm thick, Chromium layer is 50nm as an adhesive layer), the insulation layer is 3to 5 μm thick with micro-electrode sites (30 μm x100 μm) and track (50 μm) and contact pads (300 μm x2000 μm), the channel layer is 100 μm x100 μm thick.

The dimensions of the micro-channels required for maximum regeneration were decided based on the results of investigating axonal regeneration *in vivo* as a function of micro-channel dimensions namely channel cross-sectional area and channel length. Details of this investigation are presented in sections [4.4] and [5.3]. This study has made a number of suggestions relating to micro-channel dimensions. It has proposed a channel cross-sectional area of 100µmx100µm, a channel spacing of 50µm, and given an indication of the channel length range. The channel length was subsequently chosen to be 4mm as this presents a good compromise to obtain significant signal amplification besides re-innervation and good vascularisation through the micro-channels. Each implant has 180 micro-channels and 20 micro-electrodes in total (please refer to Fig.5.5). The embedded micro-electrodes are distributed evenly across the inner rolls. The total number of channels in the central rolls (layer number 3 and 4 in the rolled structure containing 6 rolls in total) is 60. 20 out of the total 60 channels in the central rolls are supplied with electrodes positioned in the centre of their corresponding

channel. This means that one out of three channels is supplied with electrodes (in the central rolls of the structure) as shown in Fig. 5.5 (b and c).

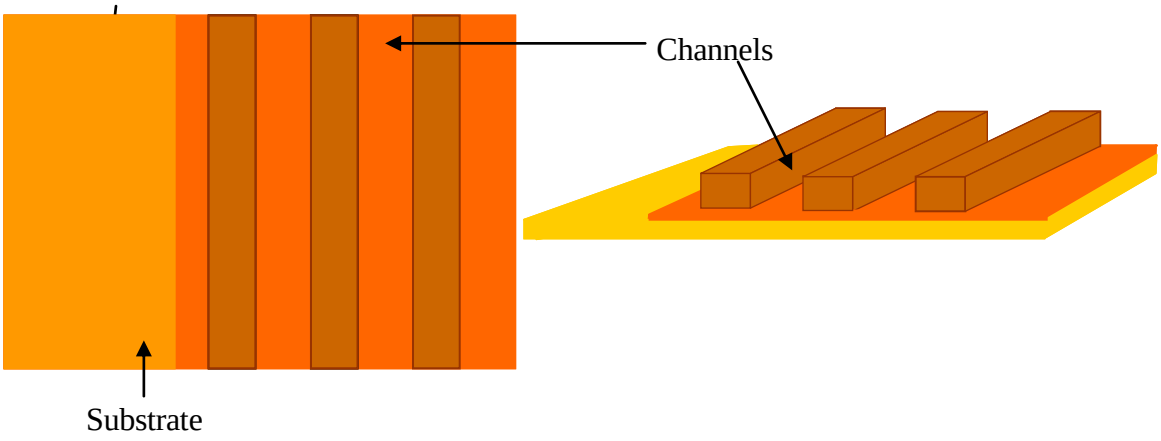


Fig. 5.3: Layer layout for passive devices (passive SPNI implants)

The passive implants, on the other hand, have the same layers as the active implants except for the metallisation layer (as shown in Fig. 5.3) which is not required in the passive implants as these devices are mainly used to evaluate axonal regeneration and optimise channel parameters. To evaluate regeneration through the micro-channel arrays, two sets of 12 passive implants are to be fabricated with channel lengths of 2.5mm and 4mm. These lengths were selected based on the modelling data reported in [9] and the experimental data reported in [60]. The modelling demonstrated that for lengths in the range of 2mm to 10mm, longer channels produce higher recordable signals. This is expected because of the spatial distribution of action potentials (AP) in myelinated axons[9]. The extracellular signals can only reach it maximal theoretical amplification, if the whole action potential is accommodated into the channel so that the extracellular impedance is raised over its entire length. The signal is attenuated where the channel length is smaller than the spatial distribution of the action potential. Nevertheless, the longer the channel the closer it is to its optimal value. *In vivo* data reported in [60] showed that although the quality of re-innervation seemed to sharply decline for lengths greater than 2mm (refer to Fig.4.13), some regeneration was evident through micro-channel lengths of 4 to 5mm. Good vascularisation was also observed with blood vessels growing through the micro-channels with lengths of up to 5mm which is vital for the provision of oxygen and nutrients to the regenerating tissue.

[9] Please refer to chapter [4], section [4.2.4]

Consequently, based on the modelling data and *in vivo* data just explained (which is reported in details in [9] and [60]), lengths of 2.5mm and 4mm were selected for the passive implants to evaluate regeneration through the micro-channels. Implants with 2.5mm long micro-channels are used as a backup in case regeneration through the 4mm long micro-channels was unsuccessful. If regeneration is found to be good through the 4mm long passive implants, 4mm long active implants will be fabricated as this implant length is theoretically expected to offer better signal amplification compared to the 2.5mm long implants. In addition, this length will allow more electrodes per implant (compared to the 2.5mm length) as the extra channel length will allow more space for lead-out electrode wiring. Regeneration through the passive implants will be presented and discussed in chapter [10], section [10.1].

The 2D sheet carrying the device layers is released from the wafer by peeling it off manually. As the substrate layer is made of Pyralin 2611, the individual devices fabricated on the same wafer share the same un-patterned substrate layer. A scalpel blade is used to cut around the footprint of the individual device shown in Fig. 5.4 (top). The two-dimensional implant structure is then rolled to form a three dimensional structure with closed micro-channel arrays and is prevented from unravelling by applying a silicone tube to either end of the roll as illustrated in Fig. 5.4 (bottom). The extension illustrated in this figure carries passivated gold wiring and is designed to have enough length to allow the silicone tubes to be securely fitted to the roll, while permitting access to the contact pads.

The active devices need to be electrically connected to a custom made PCB board to allow access to the electrode channels so that device testing such as impedance microscopy can be carried out, in addition to stimulation and recording *in vivo* post implantation. Ball bonding (MFI technique) will be used as the ultimate interconnection method to connect the electrode channels into IC circuitry. Work[10] has been carried out to optimize design parameters so that the MFI technique can be integrated into the SPNI devices. While this is in progress, an alternative method needs to be used to connect to the

[10] Please refer to chapter 8

SPNI devices, and hence a Zero Insertion Force (ZIF) connector was selected for this purpose. These connectors are normally used for flexible circuits and cables where the contact pads of the cables are inserted into the ZIF connector aligning over the flat gold pins inside. The connector clamp is then pressed down to make and to secure the connections. Hence, the dimensions of the contact pad region need to be designed to match the ZIF connector specifications.

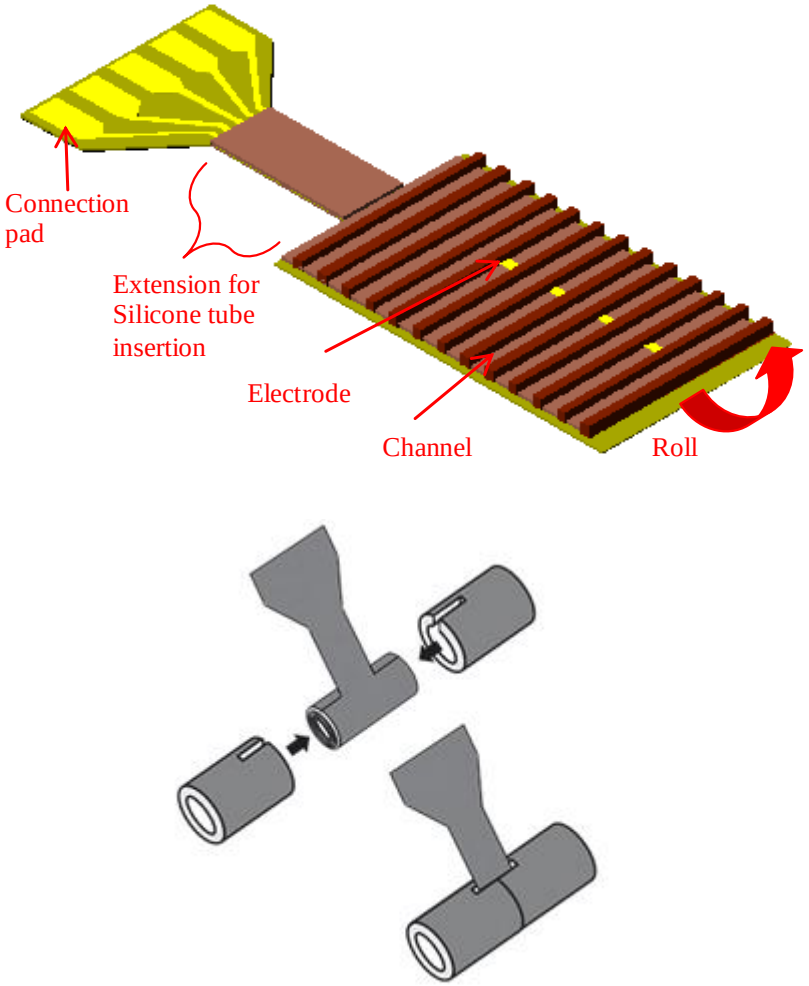


Fig. 5.4: Top- Schematic of SPNI design, Bottom- application of silicone tube to either end of the SPNI roll [65]

5.3. Experimental consideration- the dimensional parameters of the implant

The channel dimensions were selected based on the regeneration results through a set of prototype implants investigated in a series of studies detailed in [62]. Axon outgrowth

through two dimensional arrays of polyimide micro-channels has previously been evaluated as a function of channel width, spacing, and pitch *in vitro*[59]. The channels were prepared by casting polyimide on a silicon mould to form the arrays[11]. It was found that the efficiency with which axons enter the channels is maximal when micro-channels are wide (>30 μm), and when the array transparency (the channel width to pitch ratio) is at least 50% [59].

The series of studies reported by Lacour et al in [60] evaluated the *in vivo* axon outgrowth and vascularisation. It used different implant prototypes[12] to determine the implant dimensional parameters that would optimise axonal regeneration through micro-channels. The variables included micro-channel transparency, micro-channel cross-sectional area, and micro-channel length. This study concluded that axonal regeneration and blood vessel outgrowth can be supported through long micro-channel arrays. It found that micro-channels with large cross-sectional area (100μmx100μm cross-sectional area)[13] supported the biggest number of myelinated axons. It also found that regeneration through long micro-channels (with length greater than 2mm) can be supported because blood vessels, that provide oxygen and the necessary nutrients, also grow with the regenerating tissue into and through the micro-channels. Channel transparency of 0.4 seemed to make the best compromise in improving axonal growth. The quality of regeneration was best for channel lengths of less than 2mm whilst it sharply decreased for channel lengths greater than 2mm[14].

In the same study, the biocompatibility of polyimide implants and nerve regeneration through these implants was evaluated. The implants had a rectangular cross-section of 70μmx20μm (T = 0.32) and 70μmx40μm (T = 0.42), and 4.5 mm length. These implants were implanted for 4 to 12 weeks. Formal toxicity tests reported in [62] showed no adverse reaction to the implanted polyimide and photosensitive polyimide devices. Regeneration through the implants after 4 weeks of implantation was low. At the 12 week post-implantation point, some channels contained regenerated axons; however the

[11] Please refer to chapter [4] section [4.3] for more details regarding this study
[12] Please refer to chapter [4] section [4.4] for more details.
[13] Please refer to figure [4.14] in chapter [4] which graphically presents regeneration results versus micro-channel cross-sectional area.
[14] Please refer to figure [4.15] in chapter 4.

majority of channels only contained connective tissue and blood vessels. The suggested explanation behind this is that the channel cross-sections and transparencies were too small to support efficient axonal regeneration.

A fibrous tissue sheath surrounding all the regenerated mini nerves filled up to half of the available channel area in some cases. This fibrous tissue extending from the channels' rim restricts the channel area available for axonal regeneration. Polyimide implants with rectangular channel cross-sectional area were nearly completely filled with fibrous tissue. To optimise the space available for axons; the implants have to be designed with a circular channel cross-sectional area. However, since this is not feasible for array production using 2D planar micro-fabrication methods, the compromise is to minimise the fibrous tissue by making the channel cross-sectional area as close to a square as possible[62].

Based on the findings in these studies, passive devices (without embedded microelectrodes) with the advised dimensions will be fabricated to re-evaluate axonal regeneration through them. Active devices are then fabricated and implanted for 12 weeks, after which stimulation and recording from the regenerating axons are conducted. The next two sections will explain the design and the fabrication process of the passive and active polyimide devices.

In summary, to optimise the implant design, the series of studies reported in [60] suggest:

- Symmetrical micro-channel cross-sectional area (most probably a square cross-sectional area as it can be easily fabricated using planner micro-fabrication.
- 100 μm x100 μm micro-channel cross-sectional area can be used as it seemed to offer the best regeneration results.
- Transparencies of about 0.4 seemed to offer the best compromise between the space available for regeneration and the durability of the implant structure.
- Micro-channel lengths up to 2mm were found to offer the best regeneration
- Although regeneration decreased sharply for micro-channel lengths greater than 2mm, these lengths still supported some axonal regeneration.

- 12 weeks post implantation seems to be the earliest check point for evaluating axonal regeneration and for performing stimulation and recording experiments, as this will guarantee that sufficient time is given for regeneration through the microchannels.

5.4. Design of electrodes and their placement

Encasing axons in a micro-channel provides signal enhancement and the extracellular signal reaches its maximum amplification at the centre of the channel and decays at the channel ends. For this reason the recording microelectrodes were placed halfway through the channels' length. Each rolled implant is designed to have 20 microelectrodes evenly distributed across the central rolls of the 3D rolled structure where regeneration is expected to be optimal. This was done because experimental regeneration results showed that albeit there was regeneration on the periphery of the rolled device, more regeneration was observed through the inner rolls of the implant. Each electrode site is designed to be $30\,\mu m$ x$100\,\mu m$ with a track width of $50\,\mu m$ as shown in Fig. 5.5[15]. The electrodes and tracks connecting them to the contact pads need to be placed at or as close as possible to the neutral plane of the rolled 3D structure. This is to protect the metal wiring from being overstrained in the rolled 3D structure which may lead to mechanical/electrical failure and hence inability to record or simulate. This is discussed in greater details in the remainder of this chapter in the sections to follow.

5.4.1. The importance of placing the wiring on the neutral plane

The rolling of the SPNI devices into a 3D structure results in compressive strain in the inner rolls which may reach few percent. Whilst the flexibility of the polyimide layers allows them to withstand high strain, careful design needs to be implemented to protect the thin metal wiring constituting the electrodes and their tracks. If this layer is

[15] Please refer to section 5.2 for details regarding the thicknesses of the other layers in the implant

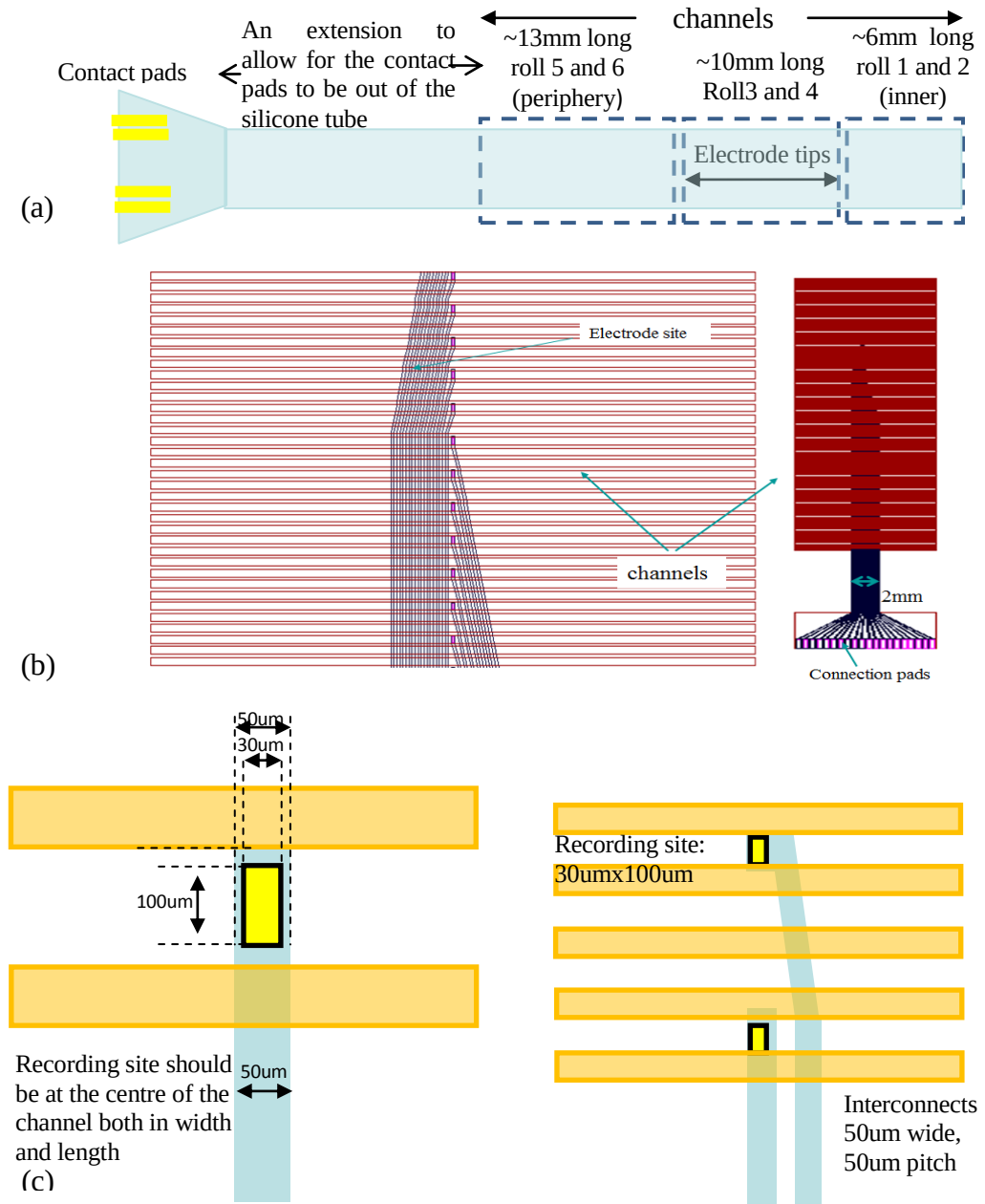


Fig. 5.5: Microelectrode dimension and placement for the SPNI implants; (a) a schematic for location of the micro-electrodes in the 2D structure of the implant. This illustrates the location of the active micro-channels supplied by electrodes and passive micro-channels that contain no micro-electrodes, (b) Mask layout showing the overall device footprint and the microelectrode distribution in the area corresponding to the two central rolls of the structure. 20 channels out of 60 channels in the central rolls (layer number 3 and 4 in the rolled structure containing 6 rolls in total) are supplied with electrodes positioned in the centre of their corresponding channel. (c) The dimensions of the microelectrodes and their location inside their corresponding micro-channel.

overstrained, a mechanical fracture may result leading to an electrical failure, hence loss of ability to record or stimulate through the microelectrodes. One way around this problem is to position the electrode layer at or as close as possible to the neutral plane of the rolled structure where the bending strain is close to 0%. This will protect the embedded electrodes from fracture that might be caused by tight rolling of the structure.

To place the metal film at or as close as possible to the neutral plane, the implant's dimensional parameters need to be optimised. These include the thickness of the substrate, the thickness of the insulation layer, and the thickness of the channel layer. The following section will derive and analyse a stress model for the SPNI and will discuss the requirements for implant optimisation.

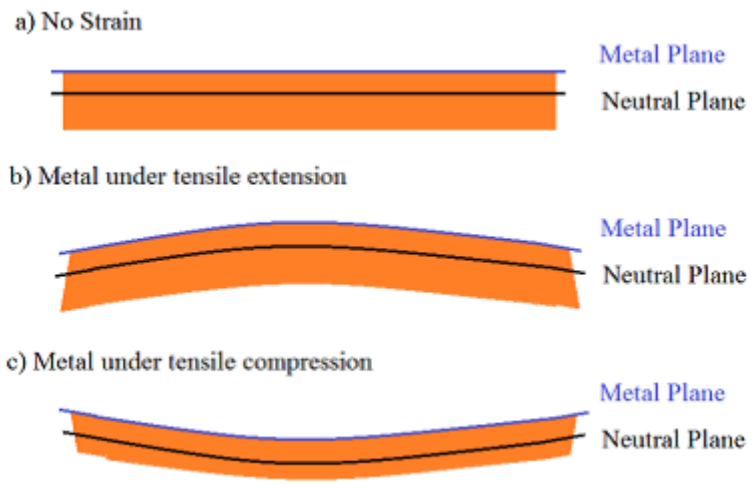


Fig. 5.6: the effect of bending a metal layer sandwiched between two polyimide layers; a- No strain experienced by the layers, b) Tensile Extension of the wiring plane, c) Tensile compression of the wiring plane [17]

5.4.2. Derivation of the stress model[16]

The metal wiring[17] experiences either tensile extension or tensile compression relative the implant's neutral plane during rolling (Fig. 5.6). If this tensile or compressive strain

[16] The style of the work carried out for the stress model is borrowed from [17] R. Barrett, "Novel Processing Routes for Neural Interfaces," Ph.D., The University of Birmingham, 2013.

exceeds the maximum threshold that the metal wiring can withstand, mechanical integrity might be lost resulting in a fracture and hence device failure as mentioned earlier. It is therefore of utter importance to keep the wiring intact by placing the layer at or as close as possible to the structures neutral plane.

Stress in metal layer due to bending

To locate the neutral plane of the implant structure where the strain is zero, the amount of stain is first found using the elastic bending theory. To simplify the derivation, a number of assumptions concerning polyamide implants are made. These include:

- The devices cross-section is prismatic and constant and homogenously flexible in the direction of bending.
- The modulus of elasticity for compression and tension is constant.
- The devices have a linear elasticity within the range of the stresses being exerted

These assumptions serve as a good starting point for the initial theoretical derivations of the neutral plane, although they may not accurately represent the true behaviour of the polyimide devices.

When considering a beam, the neutral plane is the plane whose dimensions are unaffected by the deformation of the beam. This means, it is the plane that experiences no strain during the bending of the structure (so strain is zero at the neutral plane). A transverse load on a rectangular section (see Fig. 5.7) will cause a curved bending which evenly distributes the load through the structure. During bending, the neutral plane (AB) passes through the centroid where both the top and bottom surfaces of the section are equidistant. The bending results in the compression of the line (C'D') by a distance (CD- C'D') whilst the neutral plane remains unchanged which means: (A'B'-AB=0).

[17] Metal wiring consists of the microelectrodes and the tracks

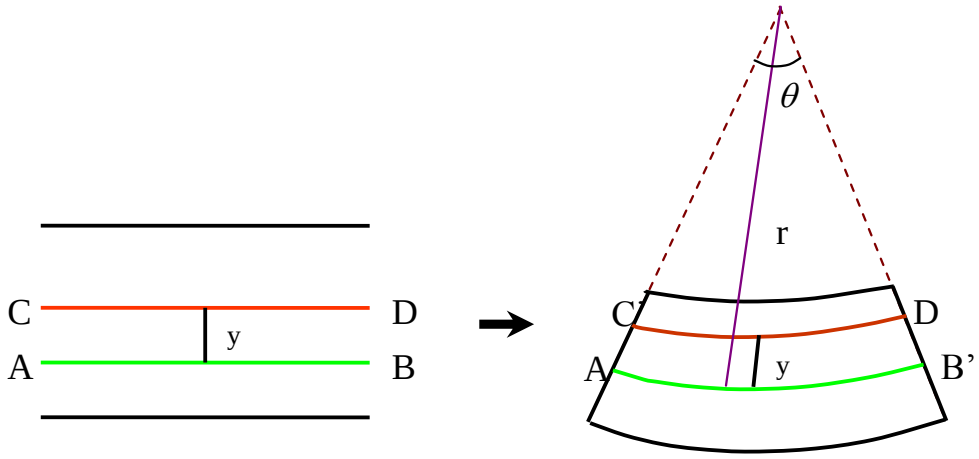


Fig. 5.7: rectangular cross-section prior and post bending; AB is the neutral plane of the structure, CD is a plane that extends the cross –section a distance y from the neutral plane. A'B' and C'D' are the planes through the rectangle post bending. θ is the angle characterising the length of the arcs

The length of the neutral axis is related to its radius of curvature by

$$AB = A'B' = r\theta \qquad \text{(Equ. 5.1)}$$

Where r is the radius of the circle containing the arc A'B', and θ is the angle characterising the length of the arc (A'B'), see Fig. 5.7. Given that the distance between layer CD and the neutral plane AB is y, the radius of curvature for the arc C'D' is r-y. Hence the length of the arc C'D' can be written as:

$$C'D' = (r - y)\theta \qquad \text{(Equ. 5.2)}$$

This means that the arc C'D' is shorter than the neutral axis by $y\theta$. This compression in length is the result of forces due to bending, and the strain $\in$ related to this compression is the ratio of the deformation in length (the difference in length after bending) to the initial length of the structure in which the forces are being applied. This can be expressed as:

$$\in = \frac{C'D' - CD}{CD} = \frac{C'D' - AB}{AB} = \frac{(r - y)\theta - r\theta}{r\theta} = -\frac{y}{r}$$

$$\in = -\frac{y}{r} \qquad \text{(Equ. 5.3)}$$

The equation above shows that the strain magnitude experienced by the metal wiring is dependent on how far it is from the neutral plane. The further away the metal layer is from the neutral plane, the larger the deformation in its length will be and the larger the strain it experienced. The modulus of the material E can be expressed in terms of stress σ and strain ϵ as:

$$E = \frac{stress}{strain} = \frac{\sigma}{\in} \qquad \text{(Equ. 5.4)}$$

And by substituting for $\in = -\frac{y}{r}$ relating the strain to the curvature,

$$\mathrm{E} = -\frac{\sigma r}{y} \qquad \text{(Equ. 5.5)}$$

and hence,

$$\sigma = -\frac{Ey}{r} \qquad \text{(Equ. 5.6)}$$

The bending moment and its relationship with the stress

To derive an expression for the bending moment, we will regard the SPNI devices to consist of isotropic layer extending longitudinally. δy is an elementary strip of thickness which is a distance y away from the neutral axis (see Fig. 5.8), and δA is the elementary longitudinal strip forming a small part of the total area A.

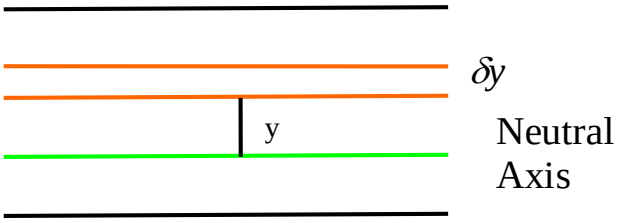


Fig. 5.8: Illustration of the incremental element

During bending the forces exerted by the load will deform the structure. An elementary force δF is the force acting on the elementary area δA, and given that the force is the product of the stress acting on the structure and the area, δF can then be written as:

$$\delta F = \sigma.\delta A = -\frac{Ey}{r}\delta A \qquad \text{(Equ. 5.7)}$$

The force acting on the entire structure an be found by considering the structure to consist of many elemental areas with corresponding elemental forces which are then summed to give the total force,

$$F = \sum \delta F = \sum -\frac{Ey}{r}\delta A \qquad \text{(Equ. 5.8)}$$

If we consider δA to be infinitely small ($\delta A \to 0$), the number of elemental areas to be summed tends to infinity and therefore:

$$F = \int_{Total_area} -\frac{Ey}{r}dA = -\frac{E}{r}\int_{Total_Area} ydA \qquad \text{(Equ. 5.9)}$$

With $\int_{Total_Area} ydA$ being the first moment of area for the section around the centroid.

At equilibrium there is no resultant force acting on the cross section. The position of the neutral axis can be located on the cross-section by equating the resultant force produced by the stress distribution over the cross-sectional area to zero, hence:

$$F = -\frac{E}{r}\int_{Total_Area} ydA = 0 \qquad \text{(Equ. 5.10)}$$

As the radius of curvature r and the modulus of elasticity E are non-zero constants at any given cross section of bent beam, then:

$$\int_{Total_Area} ydA = 0 \qquad \text{(Equ. 5.11)}$$

This states that the first moment of the area of the cross section about the neutral axis must be zero. This condition can only be satisfied if the neutral axis passes through the centroidal axis of the cross section. Consequently, we can determine the neutral axis by finding the centroid of the cross section.

When considering that the internal forces consist of the compressive forces F_C and the tensile forces F_T, the resultant force can then be written as:

$$F = F_C + F_T \rightarrow F = -\frac{E}{r}\int_{A_C} ydA - \frac{E}{r}\int_{A_T} ydA \qquad \text{(Equ. 5.12)}$$

$$\text{F=0} \rightarrow \frac{E}{r}\int_{A_C} ydA + \frac{E}{r}\int_{A_T} ydA = 0 \qquad \text{(Equ. 5.13)}$$

$$\text{Thus } \int_{A_C} ydA = -\int_{A_T} ydA \qquad \text{(Equ. 5.14)}$$

Where A_C and A_T represent the areas under compression and tension respectively. The minus sign indicates that the two areas are on opposite sides of the centroid. To find the centroid, hence the neutral plane, and minimize the strain on the metal layer during the rolling, the area of polyimide on each side of the metal layer needs to be equal.

The composite structure

The equations above assume that the structure is made up of a single homogenous material, and hence cannot be applied directly to determine the neutral plane for composite structures which are made of more than one material. However, we can work around this by transforming the composite structure's cross-section into one made of homogenous single material *(the transformed-section method).* Once this has been done, the neutral plane can be then be found.

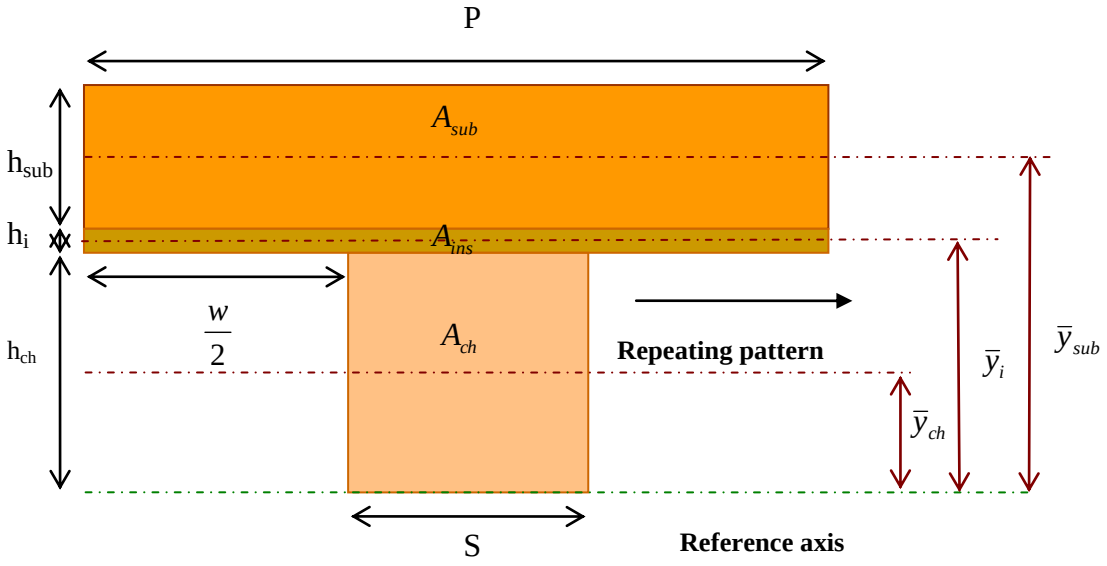


Fig. 5.9: SPNI composite structure

To apply the transformed-section method, let us consider a composite structure made of two materials material 1 with an elasticity modulus E_1, and material 2 with an elasticity modulus E_2. During bending, and provided that the material has linear-elastic behavior, the stress in material 1 and 2 is respectively determined by:

$$\sigma_1 = E_1 \in \quad \text{(Equ. 5.15)}$$

and

$$\sigma_2 = E_2 \in \quad \text{(Equ. 5.16)}$$

Hence by substituting for $\in = -\frac{y}{r}$

The strain in material 1 is $\sigma_1 = -\frac{E_1 y}{r}$ (Equ. 5.17)

The strain in material 2 is $\sigma_2 = -\frac{E_2 y}{r}$ (Equ. 5.18)

As mentioned earlier, the position of the neutral axis is found from the condition that resultant axial force acting on the cross section is zero, therefore:

$$F = \int_1 \sigma_1 dA + \int_2 \sigma_2 dA = 0 \quad \text{(Equ. 5.19)}$$

The first integral is evaluated over the cross-sectional area of material 1 whilst the second integral is evaluated over the cross-sectional area of material2. By substituting for σ_1 and σ_2, we obtain:

$$-\int_1 \frac{E_1 y}{r} dA - \int_2 \frac{E_2 y}{r} dA = 0 \qquad \text{(Equ. 5.20)}$$

Since the curvature is a constant at any given cross section, the above expression can be simplified to:

$$E_1 \int_1 y dA + E_2 \int_2 y dA = 0 \qquad \text{(Equ. 5.21)}$$

The two integrals in this equation represents the first moments of the two parts of the cross-sectional area with respect to the neutral axis. If the structure is made of more than two materials, then additional terms will be added to the equation accordingly. The derivation above leans to the assumption that the two sections of the structure made up of different materials were sufficiently bonded to act as a single unit. Although this assumption is not very practical, it provides a starting point to understand the behaviour of composite structures.

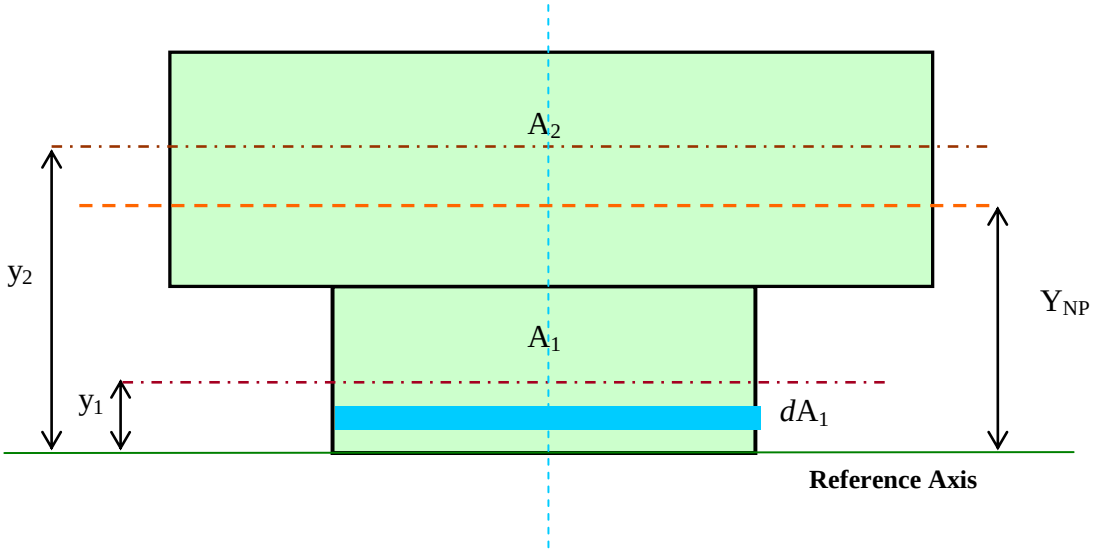


Fig. 5.10: illustration of Parallel axis theorem on a composite structure

The transformed-section method[18]

This method is based on converting the cross section of the composite structure into an equivalent imaginary cross section made only of single material. The new cross section is referred to as *the transformed section.* This imaginary section is then analyzed by applying the method for analysing sections made of a single material.

If we consider a composite structure made of two materials 1 and 2, the neutral plane can be found by satisfying the following equation:

$$E_1 \int_1 y dA + E_2 \int_2 y dA = 0 \qquad \text{(Equ. 5.22)}$$

Where the first integral is evaluated over the cross sectional area of material1 and the second integral is evaluated over the cross-sectional area of material 2. If we divide the equation above by E_1 we obtain:

$$\int_1 y dA + \frac{E_2}{E_1} \int_2 y dA = 0 \qquad \text{(Equ. 5.23)}$$

This indicates that the original structure and its transformed equivalent have the same neutral axis (the neutral axis located in the same place).

Let $n = \frac{E_2}{E_1}$ (Equ. 5.24)

n is a dimensionless factor called the transformation factor. $E_1 > E_2$ means that material 1 is stiffer than material 2 and $n < 1$. Although it is arbitrary, we can chose to transform the less stiff material into the stiffer material which means that the cross-section for material2 is transformed into an imaginary cross-section made of material 1. So if material 2 cross-section had an original width b_2, this width will be transformed into $b_1 = nb_2$. $n<1$ ➔ $b_1 < b_2$

[18] Based on [66] G. James and S. P. Timoshenko, *Mechanics of Materials*, 4th ed. Boston: PWS publishing company a devision of international Thomson publishing, 1997.

which means less of the stiffer material is needed to support a given moment. Once the beam has been transformed into an equivalent structure, the neutral plane can then be found using the parallel axis theorem that will be explained in the section to follow.

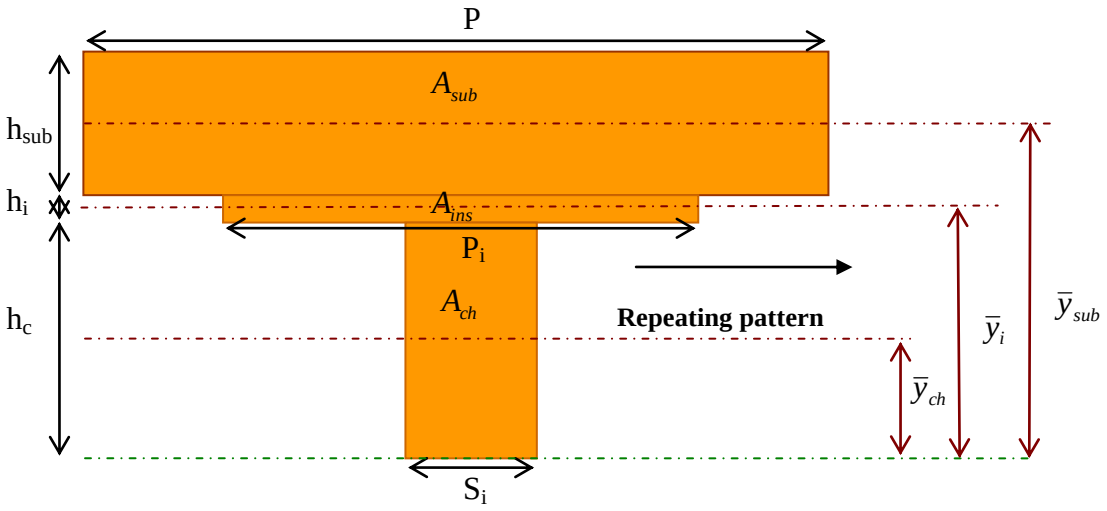


Fig. 5.11: The transformed section for the SPNI composite structure

5.4.3. The SPNI neutral plane – The initial stress model

The location of the neutral plane is dependent on the structure's geometry. The SPNI is a composite structure whose cross sectional area can be divided into simple rectangles with a known area and relative position to the reference axis chosen to be at the top of the channel wall (with the pattern upside down, see Fig. 5.9).

By calculating the effect of each individual rectangle and summing the results, the neutral plane for the entire structure is found. This method is based on the parallel axis theorem which is illustrated in Fig. 5.10 (for a structure composed of two rectangles). The relative position of each individual area is represented by the position of its centroid relative to the reference axis. To compute the neutral axis for the entire structure, the centroid of each area y_i relative to the reference axis needs to be found and multiplied by its area A_i . By summing these areas and dividing by the area of the entire structure, the position of the neutral plane relative to the reference axis is found. This can be expressed as:

$$Y_{NP} = \frac{\sum y_i A_i}{\sum A_i} \qquad \text{(Equ. 5.25)}$$

The area of each rectangle is obtained by multiplying its length by its height whilst its centroid falls at its centre, the mid-point that bisects each area (Fig. 5.9 and Fig. 5.10. The reference axis is chosen to be at the bottom of the upside structure (the top of channel wall). The neutral plane can then be determined by translating the expression above as:

$$Y_{NP} = \frac{(\frac{h_{ch}}{2})(h_{ch}S) + (h_{ch} + \frac{h_i}{2})(h_i P) + (h_{ch} + h_i + \frac{h_{sub}}{2})(h_{sub}P)}{h_{ch}S + h_i P + h_{sub}P} \qquad \text{(Equ. 5.26)}$$

Where Y_{NP} stands for the position of the neutral plane relative the reference axis. For the wiring to be placed at the neutral plane:

$$Y_{NP} = h_{ch} + h_i \qquad \text{(Equ. 5.27)}$$

By substituting for this in (Equ.5.26), the required substrate thickness to place the wiring at the neutral place can be expressed as:

$$h_{sub} = \sqrt{\frac{{h_{ch}}^2 S + h_i^2 P + 2h_{ch}h_i S}{P}} \qquad \text{(Equ. 5.28)}$$

So for $P = 150\mu m$, $h_i = 5\mu m$, $S = 50\mu m$, $h_{ch} = 100\mu m$ ➔ $h_{sub} = 60\mu m$

However, the formula above assumes that the structure is made up of homogenous material and does not take into account that the composite structure is made up of different materials which are Pyralin 2611 for the substrate, the Durimide 7505 and the Durimide 7020 for the insulation and the channels respectively. The three materials have the following respective elastic modulii E_1, E_2 and E_3. Using *the transformed-section*

method we can transform the structure into an equivalent structure made of a single material (PI2611). This is shown in Fig. 5.11.

The expression above for the neutral plane can then be written, based on the SPNI equivalent structure, as:

$$Y_{NP} = \frac{(\frac{h_{ch}}{2})(h_{ch}S_i) + (h_{ch} + \frac{h_i}{2})(h_i P_i) + (h_{ch} + h_i + \frac{h_{sub}}{2})(h_{sub}P)}{h_{ch}S_i + h_i P_i + h_{sub}P} \quad \text{(Equ. 5.29)}$$

$$h_{sub} = \sqrt{\frac{h_{ch}{}^2 S_i + h_i^2 P_i + 2h_{ch}h_i S_i}{P}} \quad \text{(Equ. 5.30)}$$

$$P_i = \frac{E_2}{E_1} P \quad \text{(Equ. 5.31)}$$

$$S_i = \frac{E_3}{E_1} S \quad \text{(Equ. 5.32)}$$

E_1, E_2 and E_3 are the elastic modulus for Pyralin2611, Durimide7505 and Durimide7020 respectively. Hence by substituting for these in Equ.5.29 , we can obtain:

$$Y_{NP} = \frac{(\frac{h_{ch}}{2})(h_{ch}\frac{E_3}{E_1}S) + (h_{ch} + \frac{h_i}{2})(h_i \frac{E_2}{E_1}P) + (h_{ch} + h_i + \frac{h_{sub}}{2})(h_{sub}P)}{h_{ch}\frac{E_3}{E_1}S + h_i \frac{E_2}{E_1}P + h_{sub}P} \quad \text{(Equ. 5.33)}$$

$$h_{sub} = \sqrt{\frac{h_{ch}{}^2 \frac{E_3}{E_1}S + h_i^2 \frac{E_2}{E_1}P + 2h_{ch}h_i \frac{E_3}{E_1}S}{P}} \quad \text{(Equ. 5.34)}$$

Where Y_{NP} stands for the position of the neutral plane relative to the reference axis. So for $P = 150\mu m$, $h_i = 5\mu m$, $S = 50\mu m$, $h_{ch} = 100\mu m$, $E_1 = 8.2GPa$, $E_2 = 2.5GPa$ and $E_3 = 2.9GPa$ ➔ $h_{sub} = 35\mu m$.

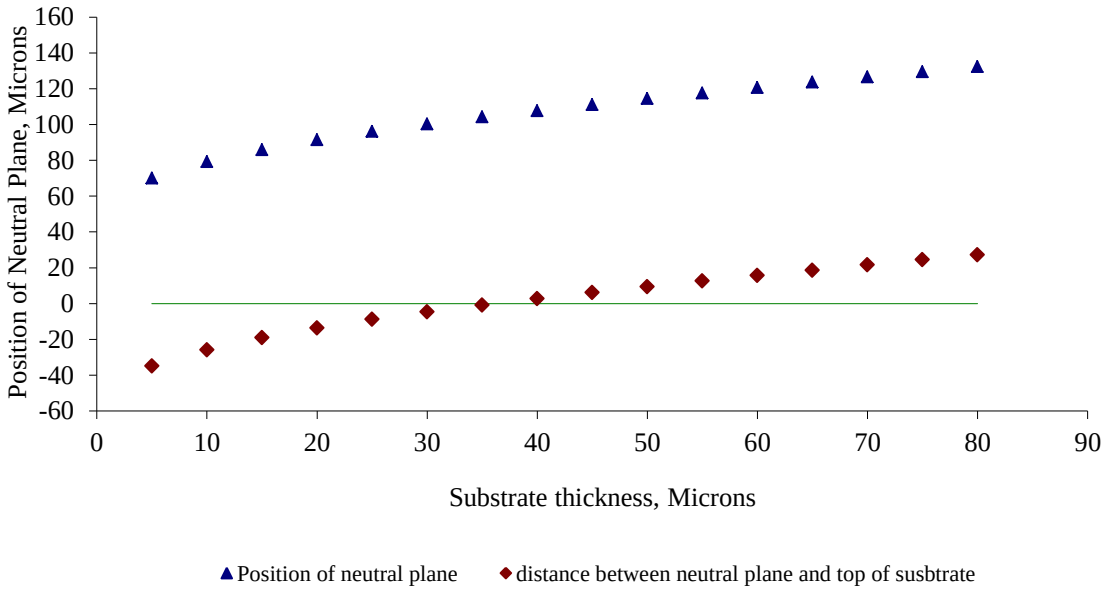


Fig. 5.12: the variation of the neutral plane position with different substrate thicknesses - and the variation of the distance, between the top of the substrate layer and the neutral plane (y, used in strain calculations), with the substrate thickness. The calculations are for an implant with 100 μm x100 μm micro-channel cross-sectional area, 50 μm wall thickness and 5 μm insulation layer. These calculations were based on the initial stress model presented in section [5.4.3]

The height and width of the channels which is found to support good regeneration is 100x100 μm x μm with a channel spacing S of $50\mu m$, this gives a pitch P =150 μm. The insulation height $h_i = 5\mu m$. The substrate height or thickness h_{sub} can be varied to see the effect it has on the neutral plane position. This is presented graphically in Fig. 5.12. In addition, the distance between the neutral plane and the top of the substrate $Y_{NP} - (h_{ch} + h_i)$ is also plotted on the same graph. As the metal wiring will reside on top of the substrate layer, the negative section of $Y_{NP} - (h_{ch} + h_i)$ plot represents the substrate thicknesses for which the metal wiring is under tensile extension whilst the positive

section of the plot represents the substrate thicknesses for which the metal wiring is under tensile compression. The substrate thickness of $35\,\mu m$ corresponding to $Y_{NP} - (h_{ch} + h_i) = 0$ on the plot is the substrate thickness that places the wiring at the neutral plane. This is almost half the required substrate thickness value found when neglecting the differences in the elastic modulus of the substrate, the insulation and the channel layers. This shows that the elastic modulus of the different materials used to fabricated the implant have a significant effect on the position of the neutral plane within the rolled structure, and hence taking this into consideration can yield more accurate results for the neutral plane position and hence the placement of the metallisation layer.

For further clarification, by varying the substrate thickness, the equivalent strain distributed across the different rolls within the 3D structure can also be calculated using the equation $\in = -\frac{y}{r}$ which defines the strain in any plane as the distance to the neutral plane (y) divided by the radius of deformation curvature (r). In the case of the rolled structure, we are interested in calculating the strain for the rolls carrying the metal wiring and these have a radius of curvature of $750\,\mu m$ for the outer roll, $600\,\mu m$, $450\,\mu m$ and $300\,\mu m$ for the inner rolls as illustrated in Fig. 5.13. The central rolls do not contain any wiring and hence were not included in the strain calculations.

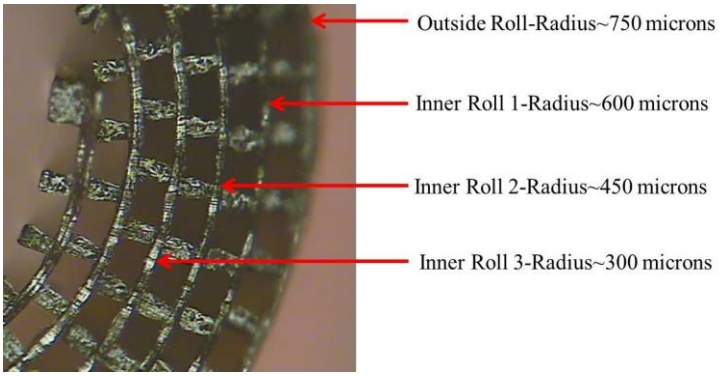


Fig. 5.13: SPNI cross-section, showing concentric rolls and their radii of curvature

The strain across each roll was calculated for various substrate thicknesses and is illustrated graphically in Fig. 5.14. As can be seen, the substrate thickness which places the wiring in all the rolls at the neutral plane is $35\,\mu m$ for which the strain across all rolls

within the structure is zero. Any substrate thickness below 35 μm places the wiring under tensile extension (represented by the positive section of the plots in Fig. 5.14) whilst substrates thicker than this value will place the wiring under tensile compression (represented by the negative section of the plots in Fig. 5.14).

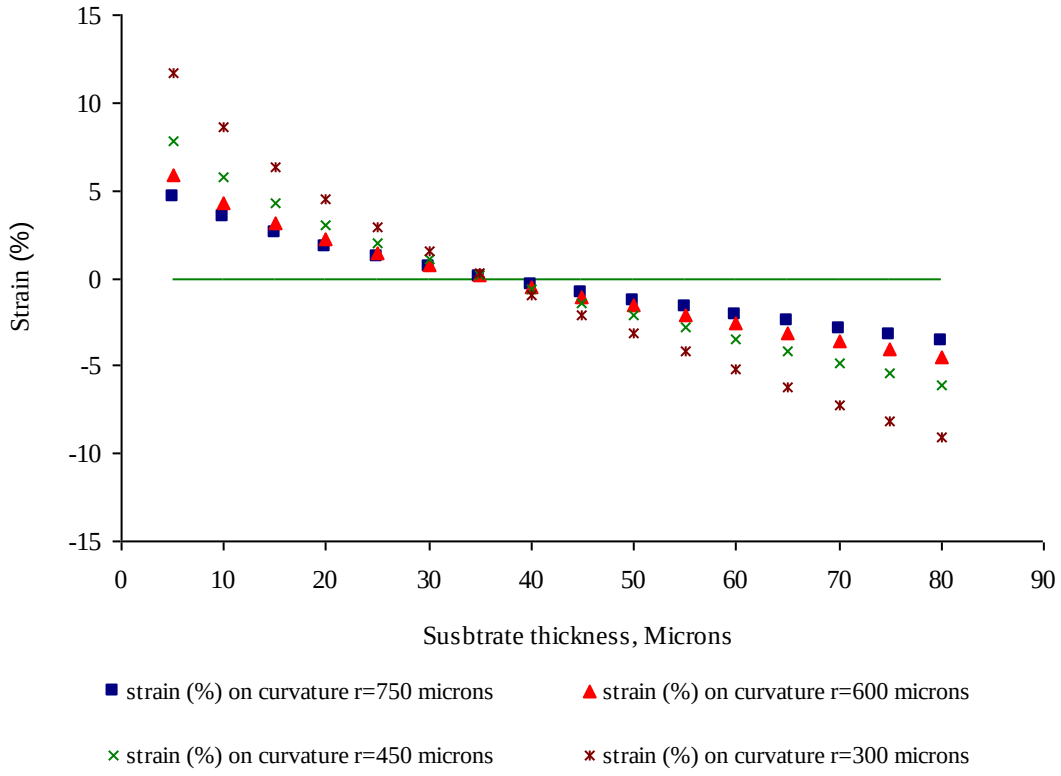


Fig. 5.14: Strain experienced by the wiring at different rolls for different substrate thicknesses. These calculations were based on the initial stress model presented in section [5.4.3]. The other implant parameters included 100 μm x100 μm micro-channel cross-sectional area, 50 μm wall thickness and 5 μm insulation layer.

As confirmed by the graphs below, strains are relatively higher in rolls with smaller radius of deformation curvature. So when the metal wiring is not positioned at, or at a very close proximity to the neutral plane, the strain experienced by the metal layer will increase as we move from the outer rolls towards the inner rolls and hence the strain will be highest in the most inner roll. For instance, for a substrate of 10 μm thick, the strain experienced in the outer roll with a curvature radius of 750 μm is about 3.5% whilst the inner roll in the same structure with a curvature of 300 μm experiences around 8.5% which is more

than double the strain experienced in the outer roll. Although this calculation is elementary and does not necessarily represent a definitive value for the strain experienced by the metal wiring, this amount of strain is considered high and would cause mechanical failure as reported in reference [67-68] .Whereas placing metal wiring at the neutral plane will protect it from experiencing any strain across the entire structure.

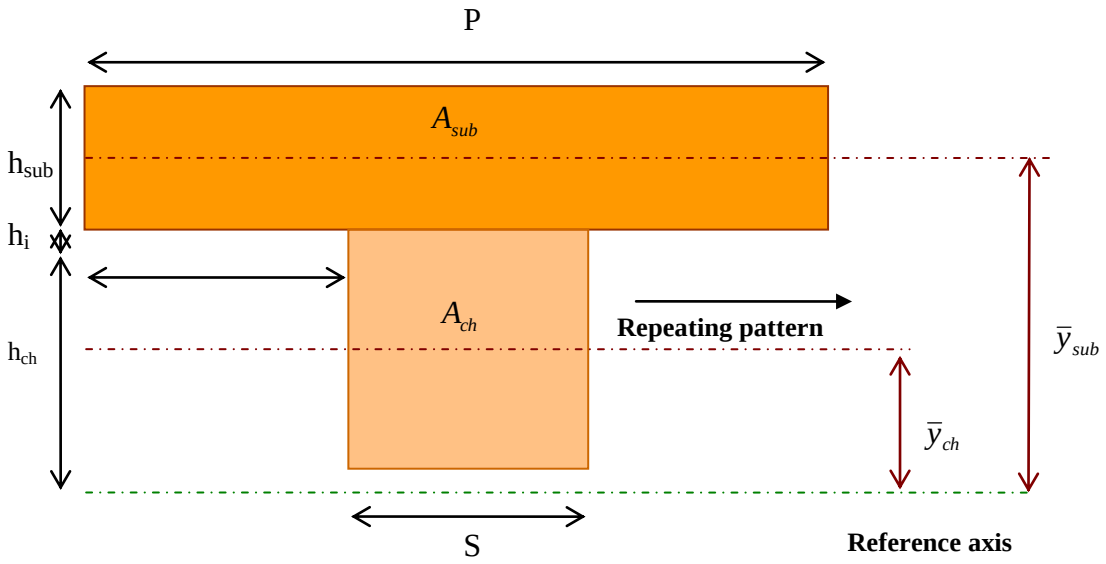


Fig. 5.15: Neglecting the insulation layer of SPNI in neutral plane and strain calculations

5.4.4. The effect of neglecting the insulation layer

The stress model used to initially calculate the position of the neutral plane in the SPNI devices was reported by Lacour et al [61, 69]. This model was initially adopted to drive the fabrication of SPNI devices given the tight time scales to get the implants ready for implantation. However further investigation into the model derivation revealed a misreport of the model's equation and the substrate thickness required to place the wiring at the neutral plane. This subsection aims to clarify the root of the model and correct the miscalculated substrate thickness.

The model reported by Lacour et al follows the same derivation root and calculations as the model reported in section [5.4.3] which uses parallel axis theorem for strain

derivations. The only difference between the two models is neglecting the insulation layer in the neutral plane calculations for the model presented by Lacour et al.

The Lacour model used the parallel axis theorem to express the neutral plane as:

$$Y_{NP} = \frac{A_{sub}.\bar{y}_{sub} + A_{ch}.\bar{y}_{ch}}{A_{sub} + A_{ch}} \qquad \text{(Equ. 5.45)}$$

Where Y_{NP}, A_{sub}, A_{ch}, $\bar{y}_{sub}$ and $\bar{y}_{ch}$ are, respectively, the distance from the neutral plane to the reference plane, the area of the substrate cross section , the area of the channel cross section, the distance from the centroind of the channel rectangle to the reference plane and distance from the centroid of the substrate to the reference plane (in the repeating structure, see Fig. 5.15). By further parameter substitution Equ.5.35 can be written as:

$$Y_{NP} = \frac{(\frac{h_{ch}}{2})(h_{ch}S) + (h_{ch} + \frac{h_{sub}}{2})(h_{sub}P)}{h_{ch}S + h_{sub}P} \qquad \text{(Equ. 5.36)}$$

Further simplification gives:

$$Y_{NP} = \frac{0.5h^{2}{}_{sub}P + h_{ch}h_{sub}P + 0.5h_{ch}{}^{2}S}{h_{sub}P + h_{ch}S} \qquad \text{(Equ. 5.37)}$$

For the wiring to be placed at the neutral plane: $Y_{NP} = h_{ch}$. By substituting this into Equ.5.37, the substrate thickness h_{sub} required to place the wiring at the neutral plane can be expressed as:

$$h_{sub} = \sqrt{\frac{S}{P}}h_{ch} \qquad \text{(Equ. 5.38)}$$

So for $p = 150\mu m$, $S = 50\mu m$, $h_{ch} = 100\mu m$ ➔ $h_{sub} = 58\mu m$

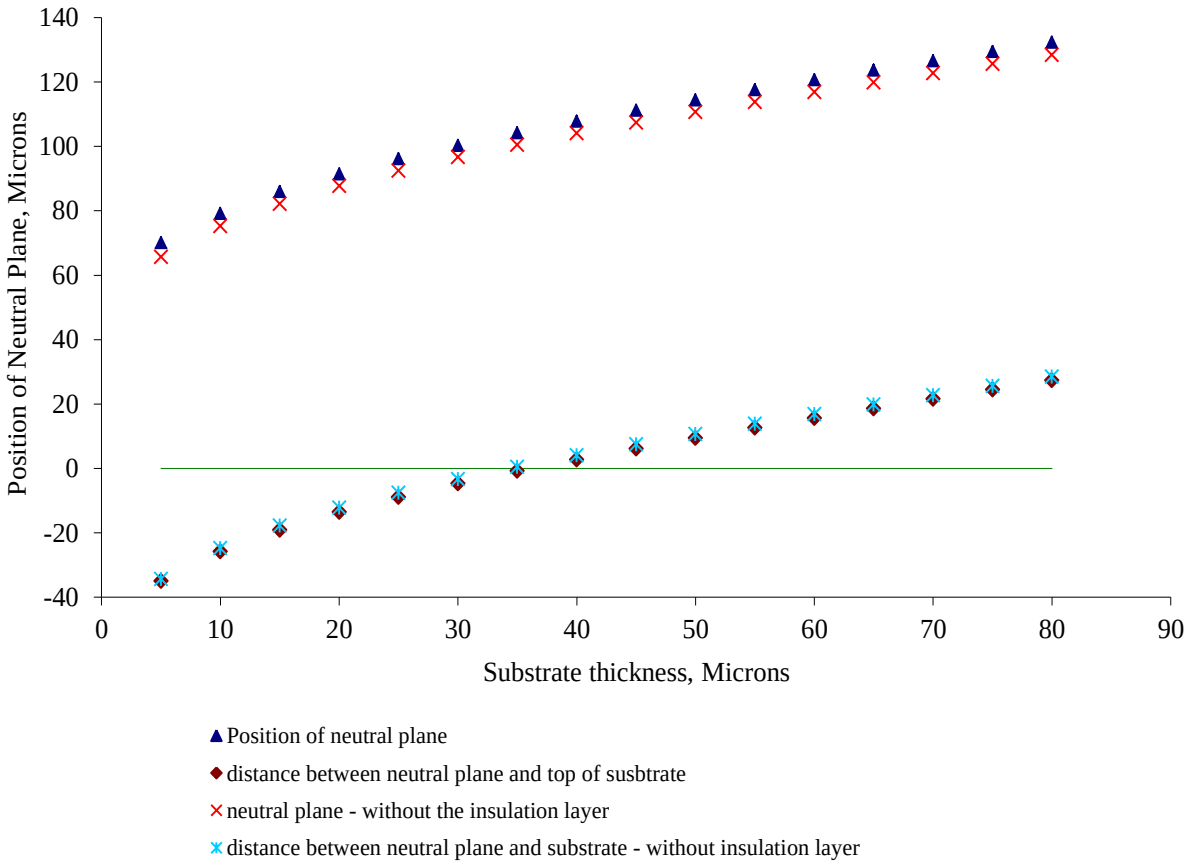


Fig. 5.16: The effect of neglecting the insulation layer in the calculations of the neutral plane position for different substrate thicknesses- and the variation of the value of y with the substrate thickness (y is the distance between the top of the substrate layer and the neutral plane; it is used in strain calculations). The plots are calculated using the initial stress model presented in section [5.4.3] and the model presented in section [5.4.4] which is similar but neglects the insulation layer thickness. The other dimensional parameters of the implant were 100 μm x100 μm micro-channel cross-sectional area, 50 μm wall thickness and 5 μm insulation layer.

This however does not take into account that the composite structure shown in Fig. 5.15 is made up of two materials (Pyralin 2611 and Durimide 7020). This can be rectified to account for the two materials by using *the transformed section method* again to obtain an equivalent structure for the one shown in Fig. 5.15. The parallel axis theorem can then be used to express the neutral plane of the equivalent structure as:

$$Y_{NP} = \frac{(\frac{h_{ch}}{2})(h_{ch} S_i) + (h_{ch} + \frac{h_{sub}}{2})(h_{sub} P)}{h_{ch} S_i + h_{sub} P} \qquad \text{(Equ. 5.39)}$$

This can be simplified further to:

$$Y_{NP} = \frac{0.5 h^2{}_{sub} P + h_{ch} h_{sub} P + 0.5 h_{ch}{}^2 S_i}{h_{sub} P + h_{ch} S_i} \qquad \text{(Equ. 5.40)}$$

By substituting for $S_i = \frac{E3}{E1} S$ (Equ. 5.41)

The above two expressions can be re-written as:

$$Y_{NP} = \frac{(\frac{h_{ch}}{2})(h_{ch} \frac{E_3}{E_1} S) + (h_{ch} + \frac{h_{sub}}{2})(h_{sub} P)}{h_{ch} \frac{E_3}{E_1} S + h_{sub} P} \qquad \text{(Equ. 5.42)}$$

$$Y_{NP} = \frac{0.5 h^2{}_{sub} P + h_{ch} h_{sub} P + 0.5 h_{ch}{}^2 \frac{E_3}{E_1} S}{h_{sub} P + h_{ch} \frac{E_3}{E_1} S} \qquad \text{(Equ. 5.43)}$$

So for $P = 150\mu m$, $S = 50\mu m$, $h_{ch} = 100\mu m$, $E_1 = 8.2GPa$ and $E_3 = 2.9GPa$ ➔ $h_{sub} = 35\mu m$.

This is almost half the value found for the required substrate thickness ($h_{sub} = 58\mu m$) when the difference in the elastic modulus of Pyralin 2611 and Durimide 7020 materials is neglected. This shows that the difference in the elasticity properties between the Pyralin and Durimide materials has to be accounted for if we are to find a more realistic value for the required substrate thickness and place the wiring at or as close as possible to the neutral plane. The calculated value of $35\mu m$ for the substrate thickness matches up with the value found earlier for when the insulation thickness was considered in the calculation. This indicates that the insulation layer thickness (of $5\ \mu m$) has very negligible

effect on the position of the neutral plane. To further show this, the variation of the neutral plane position

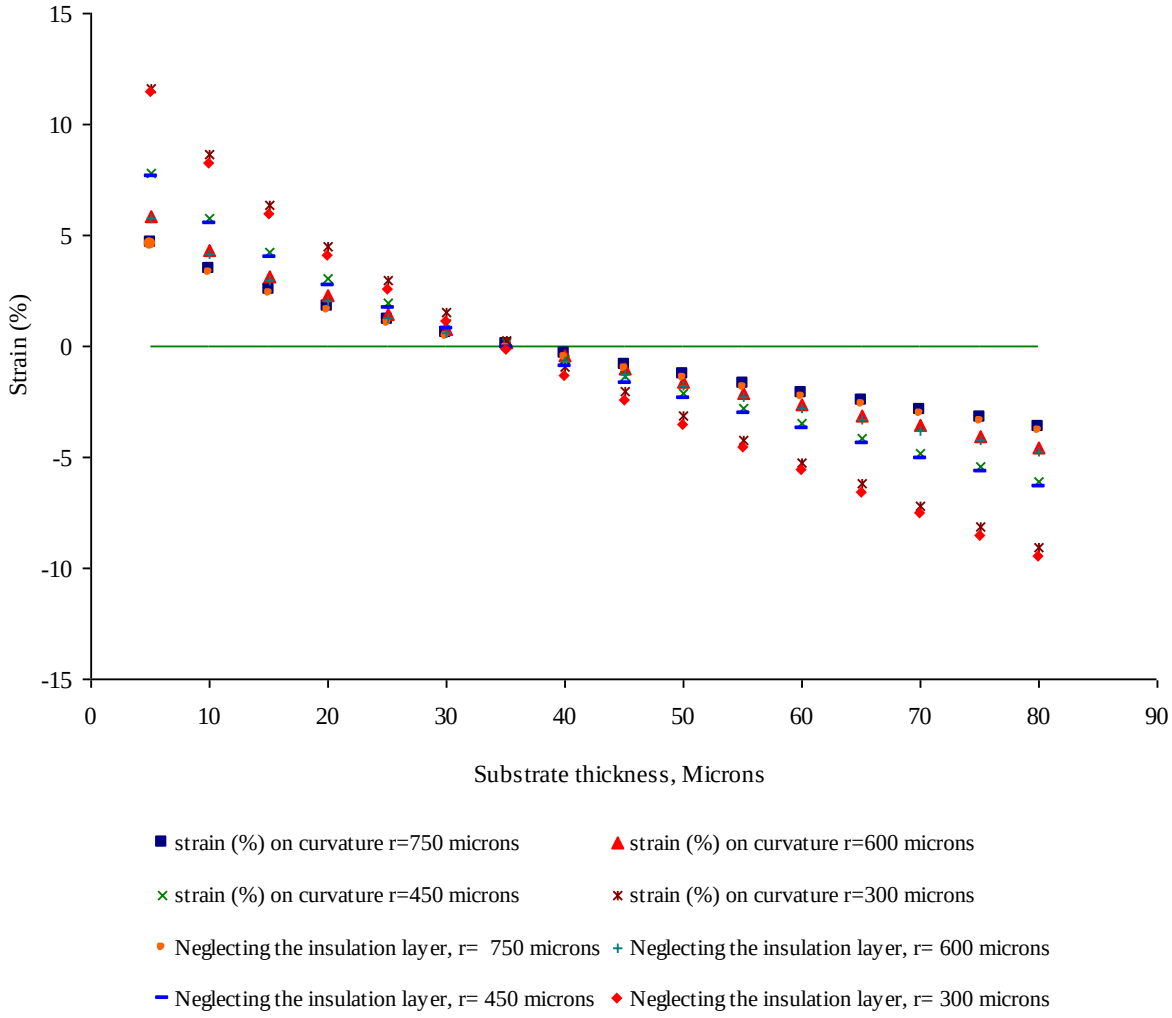


Fig. 5.17: the effect of neglecting the insulation layer on the calculations of the Strain experienced by the wiring at different rolls for different substrate thicknesses. The calculations are for an implant with 100 μm x100 μm micro-channel cross-sectional area, 50 μm wall thickness and 5 μm insulation layer. The plots are calculated using the initial stress model presented in section [5.4.3] and the model presented in section [5.4.4] which is similar but neglects the insulation layer thickness.

versus substrate thickness was plotted to show the effect the insulation layer thickness (of 5 μm) has on the neutral plane position (the case for neglecting the insulation thickness accounts for the model reported by Lacour, S.). This is illustrated in Fig.5.16 which clearly shows that neglecting the insulation layer thickness has a very negligible effect on

the calculations for the neutral plane position and the distance between the neutral plane and the substrate layer (y).

The effect of the insulation layer on the strain calculations is also illustrated in Fig. 5.17. The case for neglecting the insulation layer represents the model reported by Lacour, S. As can be seen, the plots for the strain calculated with and without the insulation layer thickness is almost identical and the insulation layer can be said to have very negligible effect on the strain experienced by the metal wiring in the rolls of the implants.

5.4.5. The Corrected stress model

Fabricating a rolled SPNI device with a substrate thicker than $25\,\mu m$ was not practical as with a thicker substrate the 2D structure becomes stiffer to roll and more difficult to hold the 3D rolled structure in place with the silicone tube. Despite this it was still possible to make few devices with a substrate thickness of $35\,\mu m$. Devices with substrate thickness of around $20\ \mu m$ were also made as compromise to make the substrate layer as close to $35\ \mu m$ as possible but still maintain enough flexibility in the substrate layer, so that the devices are rolled safely without the risk of the structure springing back to the 2D structure. Upon measuring the impedance of these two devices, the measured impedances indicated that the wiring stayed intact in both upon rolling. This is expected for the devices with the $35\,\mu m$ substrate, but not for the devices with the $20\ \mu m$ substrate as the metal wiring in these devices would have been experiencing strains of about 2 to 2.5% on the outer roll and 4.2 to 6.3% on the most inner roll according to the stress model discussed earlier. Any strains higher than 1% are considered high for the metal wiring to cope with and hence the strain values reported for the $20\ \mu m$ substrate would be expected to cause damage to the metal wiring of these devices.

By revisiting and analysing the initial stress model discussed above, it became evident that that the model does not correctly represent rolling process of the devices. To understand this, Fig. 5.18 illustrates a 3D schematic of the structure before rolling with x,y,z axes. Bending the structure about the x axis (in the direction M_x illustrated in the

figure) leads to a positive bending moment M_x acting about the x axis. The cross-sectional area of the structure that the moment is acting on is the same as the cross-sectional area

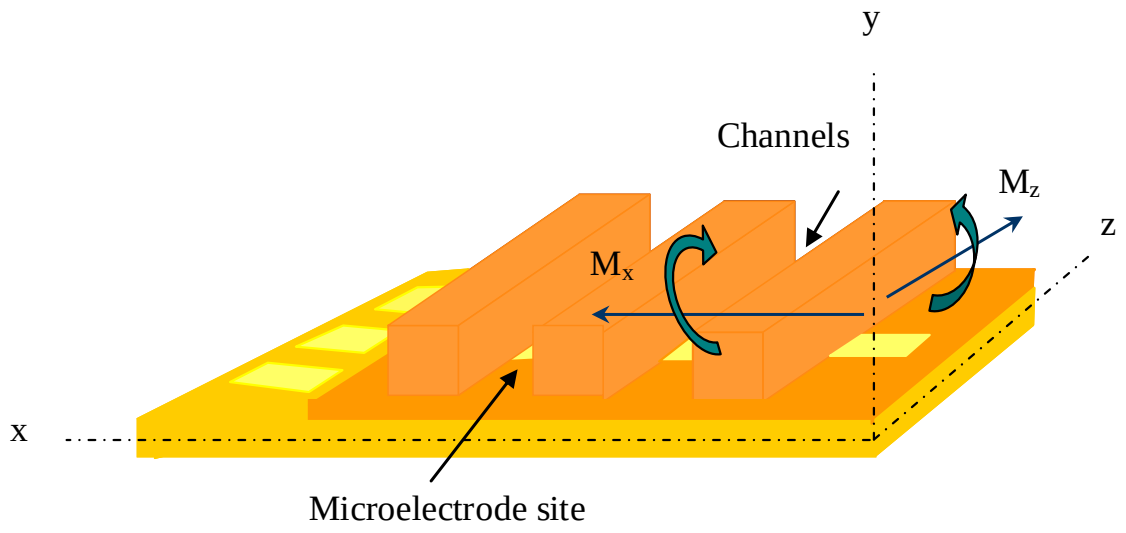


Fig. 5.18: the SPNI 3D structure with x,y,z axes and the bending moments for the initial stress model (Mx) and the corrected stress model (Mz)

used in the previous stress model which is illustrated in Fig. 5.9. The bending moment acting on this structure produces compression on the upper part of the structure and tension on the lower part while the neutral plane of the structure calculated in the previous stress model experiences no strain.

However, the SPNI structure is not rolled or bent about the x axis, but rather about the z axis as shown by the bending moment M_z acting about the z axis as illustrated in Fig. 5.18. This is a very important observation, as it means that neutral place calculation for SPNI composite structure discussed earlier can no longer hold true. The M_z moment will be acting on a cross sectional area composed mainly of the substrate and the insulation layer. During the rolling of the SPNI structures, stresses are mainly induced in the base and the insulation layer of the rolled structure with high stress concentrations around the corners and the regions of where the insulation layer connects to the channel walls. There will be hardly any stresses transferred into the channel walls, and if any that will most likely be very low compressive stresses.

Fig. 5.19 illustrates the updated structure that will be used for the calculations of the neutral plane. The reference axis is still chosen to be at the top of the channel wall. Hence, by applying the parallel axis theorem, the neutral plane can be expressed as:

$$Y_{NP} = \frac{(h_{ch} + \frac{h_i}{2})(h_i P_i) + (h_{ch} + h_i + \frac{h_{sub}}{2})(h_{sub} P)}{h_i P_i + h_{sub} P} \qquad \text{(Equ. 5.44)}$$

With $P_i = \frac{E_2}{E_1} P$ (Equ. 5.45)

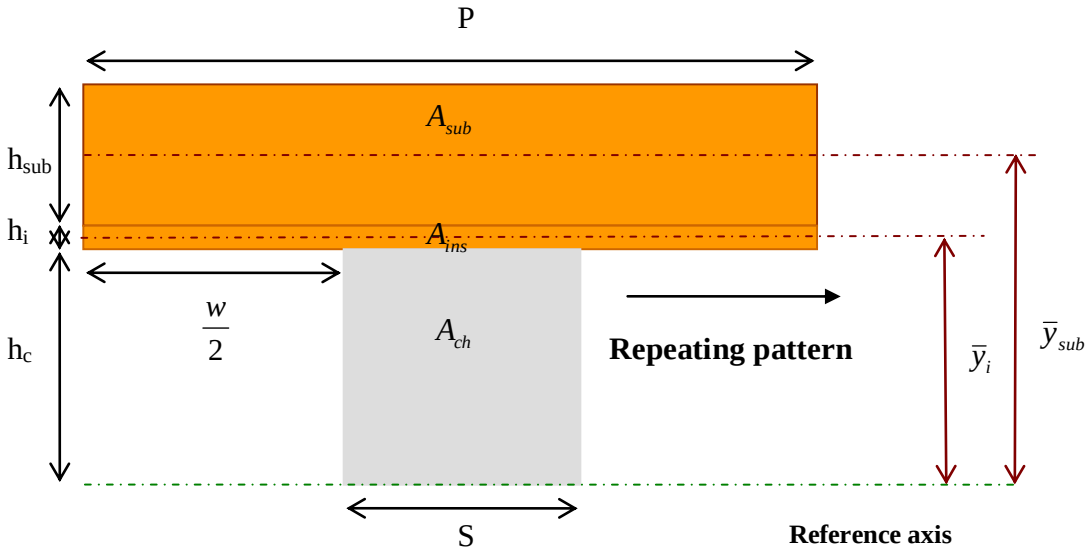


Fig. 5.19: The structure used to calculated the neutral plane in the corrected model

The variables in Equ.5.44 are the neutral plane Y_{NP} the substrate thickness. Hence, the position of the neutral plane can be found by giving values for the substrate thickness. This is illustrated graphically in Fig. 5.20. The neutral plane position changes linearly with the substrate thickness. It can also be noted that the distance between the neutral plane and top of the substrate is always positive. This means that neutral plane position is located within the substrate. The substrate thickness will normally be taken to be more than 5µm to provide enough support for the SPNI structure, whereas the insulation layer will be no more than 5µm. By neglecting the effect of the insulation layer on the position of the neutral plane, Equ.44 can be simplified to:

$$Y_{NP} = \frac{(h_{ch} + h_i + \frac{h_{sub}}{2})(h_{sub}P)}{h_{sub}P} \qquad \text{(Equ.5.46)}$$

Hence:

$$Y_{NP} = h_{ch} + h_i + \frac{h_{sub}}{2} \qquad \text{(Equ.5.47)}$$

$(h_{ch} + h_i)$ is constant and appear in the equation simply because of the reference axis taken to be at the top of the channel (see Fig. 5.19). Equ.5.47 indicates that the neutral plane will always be located halfway the substrate thickness.

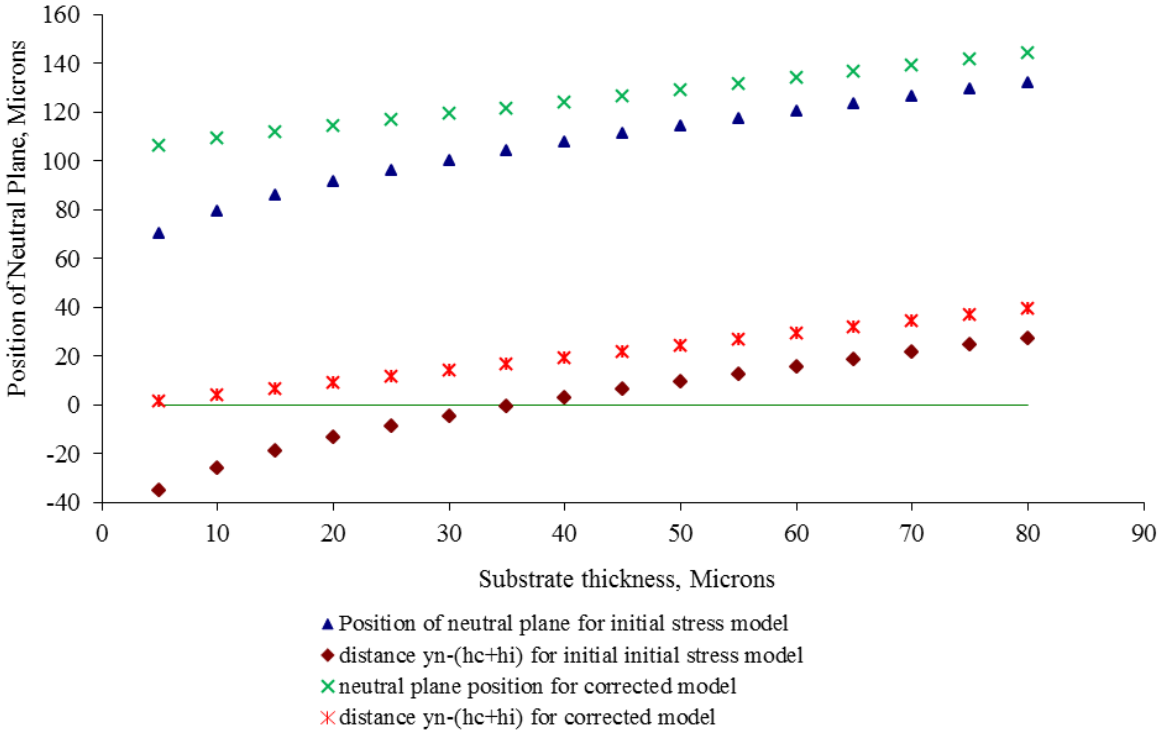


Fig. 5.20: The position of the neutral plane for different substrate thicknesses, and the distance between the neutral plane and the top of the substrate. These were calculated using the corrected stress model presented in section [5.4.5]. The corresponding plots calculated using the initial stress model presented in section [5.4.4] were also included for comparison purposes,

The strain experienced by the metal wiring across the concentric rolls of the SPNI structure can be calculated for different substrate thicknesses using the corrected stress model just discussed. The results are plotted in Fig. 5.21. The strains calculated based on the initial stress model, which no longer applies, is also included for comparison. As can be seen from the corrected stress model plots in contrast to the initial stress model plots,

the strain experienced by the wiring across the rolls for all different substrate thicknesses is always negative indicating that the metal wiring is always under compressive strain.

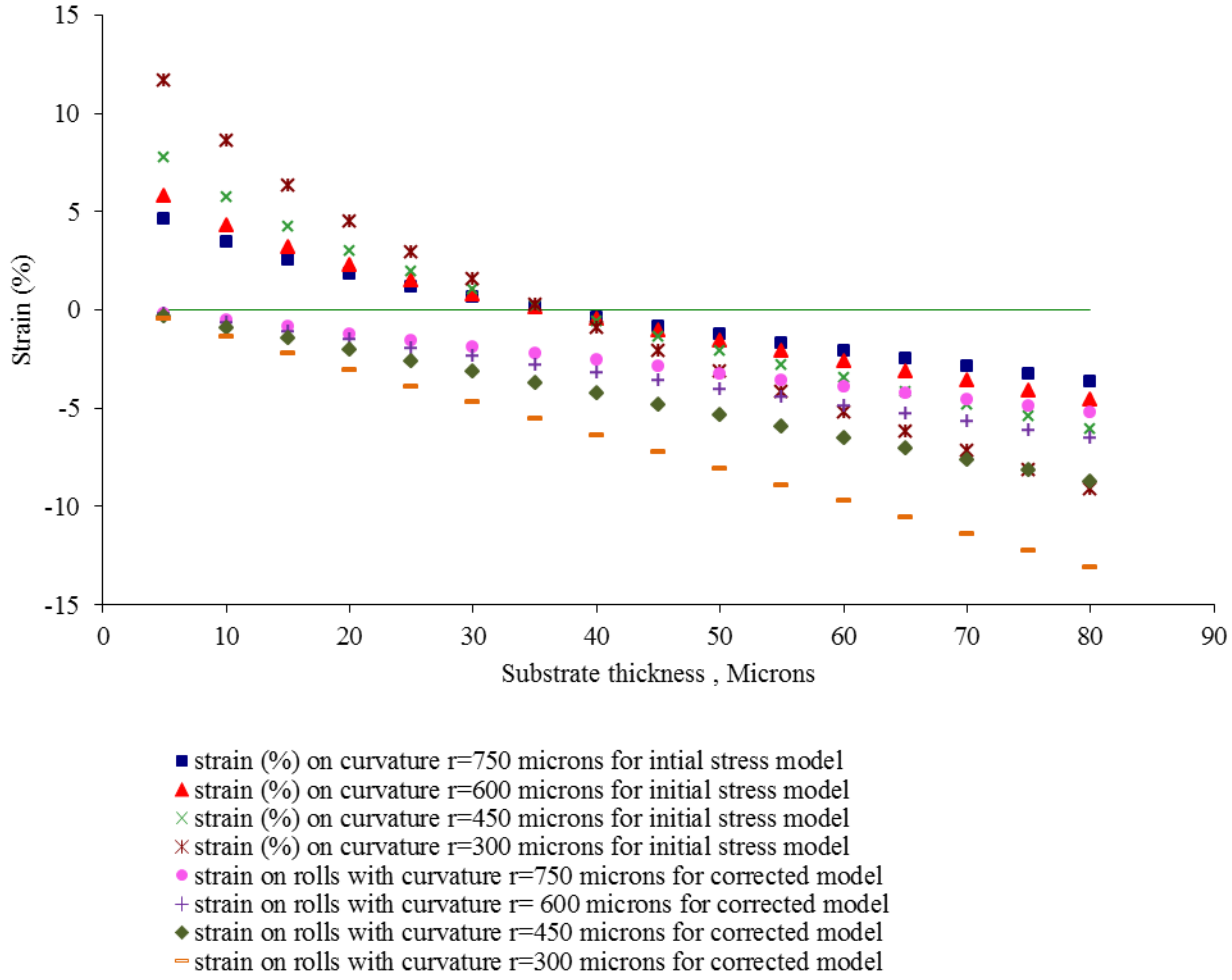


Fig. 5.21: variation of the strain with the substrate thickness across the concentric rolls of the implant based on the corrected stress model presented in section [5.4.5]. Strain plots based on the initial stress model presented in section [5.4.3] are also included for comparison purposes.

For a given substrate thickness, the compressive strain experienced by the wiring seems to increase as we move radially from the outer rolls into the inner rolls. For instance, for a substrate thickness of $10\,\mu m$, the strain experienced by the wiring at the outer roll is -0.5% while it is -1.4% for the most inner roll. As the substrate thickness increases, the compressive strain experienced at each roll also increases. This model clearly explains why the metal wiring of the rolled SPNI structure would not fail at substrate thicknesses lower than 35µm. The wiring is always under tensile compression (rather than tensile

extension) which decreases with the substrate thickness. For devices made with a substrate thickness of 20µm, the compressive strains experienced in the rolls will be in the region of -3% to -1.2% (where -3% is for the most inner roll which does not have any wiring). The compressive strains are lower for thinner substrates. In contrast to the suggestions based on the initial stress model, using thinner substrates is preferable as this will reduces the compressive strain across the rolls.

5.5. Chapter Summary

This chapter focused on the design of the SPNI implant. The implants are designed to have four layers; the first layer is the substrate layer which is will be made of Pyralin 2611 with thicknesses in the range of 12 to 20 μm. The second layer is the metallisation layer which will be made of a 250mn thick gold layer and a 50nm thick chromium layer (used as an adhesion layer). The metal layer will be patterned to produce the micro-electrodes, their wiring and the contact pads. The third layer is a 3 to 5 μm thick insulation layer which will be fabricated using a photo-sensitive polyimide (namely Durimide7505). The insulation layer will be photolithoraphically patterned to insulate the implant wiring and expose the micro-electrodes sites and the contact pads. The fourth layer is the $100\,\mu m$ x$100\,\mu m$ cross-section channel layer which will be made using another type of photo-sensitive polyimide (Durimide 7020). The active implants will have a channel length of 4mm, while the passive implants will be fabricated with 2.5mm and 4mm channel length to evaluate regeneration. The dimensional parameters of the SPNI implant, including those for the individual constituent layers have been detailed in this chapter. The parameters were selected based on the modelling results and the experimental data presented in chapter [4] and reported in [9] and [60].

The design chapter also discussed the need to place the metal layer at the neutral plane of the 3D structure and presented stress models for the calculating the position of the neutral plane in the 3D structure. The initial stress model suggested a substrate layer thickness of $35\,\mu m$ to place the metal layer at the rolled structure neutral plane. However, besides the impracticality of this substrate thickness (difficulty with rolling the devices with such

substrate thickness), it was discovered that this model does not accurately represent the strains experienced by the metal layer in the 3D structure and was, therefore, replaced by another stress model explained in section [5.4.5]. This model suggests that the neutral plane will always be located halfway the substrate thickness and demonstrated that the metal layer will always experience some compressive strain. The strain calculations showed that the strain experienced by the metal layer increases with the substrate thickness and as we move towards the central rolls of the structure. Hence it is preferable to avoid placing the micro-electrodes in the channels of the central rolls of the implant as the metal layer will experience the most compressive strain in these rolled layers. The next chapter presents the micro-fabrication methods that have been used to fabricate and test the durability and functionality of the SPNI implant.

6. FABRICATION AND TESTING METHODS FOR THE SPNI IMPLANTS

6.1. Introduction

There is a wide range of processing technologies available to fabricate neural implants. The quality and the cost incurred by the fabrication depend on the techniques used. The main part of this chapter will describe the techniques used to fabricate the SPNI devices. These include the methods used to clean and prepare the carrier wafer for the fabrication process, the methods used to fabricate and process the polymeric layers of the device, the techniques used to deposit and pattern the metal films for the metallisation layer of the SPNI devices, in addition to the use of plasma etching techniques to clean or define very small feature sizes in the device. The last section of the chapter introduces the methods that have been used to test the SPNI devices. These mainly include the use of Electrochemical Impedance Spectroscopy (EIS) to characterise the impedance/electrolyte interface of the implants.

6.2. Techniques used to fabricate the SPNI devices

6.2.1. Wafer preparation[19]

In case the wafer to be used as a carrier is contaminated, a cleaning step has to be performed. There are different types of contaminants ranging from solvent stains (like Acetone and IPA), dust from the operators or equipment, smoke particles and so on. With the decrease in the miniature feature size that can be fabricated, the permitted contamination particles have also been decreasing in conjunction.

[19] Based on the handbook of microfabrication [70] M. Madou, *The handbook of micro-fabrication: Fundamentals of microfabrication* New York: CRC Press LLC, 1997.

There are different methods for wafer cleaning which include wet treatment and dry cleaning techniques. Except for environmental concerns wet etching still outranks other cleaning techniques. An example of commonly used wet cleaning process is the Piranha clean which uses a mixture of sulphuric acid (H_2SO_4) and hydrogen peroxide (H_2O_2) followed by a deionized water rinse. Various mixture ratios are commonly used; a ratio of 3:1 sulphuric acid/ hydrogen peroxide is normally used. This cleaning technique was used in conjunction with oxygen plasma etch to ensure that the carrier wafers are contaminant-free. A less vigorous and easy cleaning procedure is to use acetone and IPA. This is done by spraying acetone on the wafer while it is spinning to remove organic impurities. Isopropyl alcohol (IPA) is then sprayed to remove the contaminated acetone off.

As part of the carrier wafer preparation, the cleaned wafer is baked at 120^0-150^0C for several minutes to dry off any water molecules. By baking at these elevated temperatures the OH-bonds on oxidized surfaces decompose which improves the resist adhesion. To avoid water re-absorption the resist coating is applied straight after the substrate cools. Adhesion promoters can used to improve the adhesion of Pyralin and Polyimide coating if required. These include the no-diluted VM651 and the diluted ready to use VM652 adhesion promoters. They work by modifying the surface of the carrier wafer and allow chemical bonds to be formed between the wafer surface and the polyimide molecules[71].

6.2.2. Spin Coating Polyimide Resins and photo-resist

After cleaning and priming the wafer with an adhesion promoter, the substrate is then coated with a resin to form a thin uniform polyimide layer. Spin coating is done in three steps: the resist is dispensed into the centre of the wafer; the wafer is accelerated into the final rotational speed to spread the resist and is then spun at a constant speed for a specific time to obtain the desired thickness and a relatively uniform symmetrical flow profile.

The film thickness is inversely proportional to the square root of the spin speed which can be varied to obtain different thicknesses within a certain range. Using highly viscous

resists and spinning at low speeds to obtain thicker layers, requires more time to achieve a final constant film thickness. The final film thickness does not only depend on the resist viscosity and the spin speed, but also on the amount of resist dispensed onto the substrate. The resin contains a solvent in which the polyimide was dissolved in. The solvent evaporates quickly during the first few seconds of spin coating and then a saturated solvent concentration (approximately 15-20% and is higher for thicker films) is reached based on the resist layer thickness. At raised temperatures during softbake, the remaining solvent in the film is evaporated further and the solvent concentration is reduced to a value typically around 5%. The spin profile represents the relationships between the resulting film thickness and the spin speed used and is generally available from the material suppliers.

The same spin coating process is used for both polyimide resins and photo-resists. Normally the polyimide layers become an integral part of the device as is the case with polyimide in the SPNI devices, while photoresit layers are used as a means to pattern another surface (such as a deposited thin metal film) or perform lift-off. Two photoresists used in this thesis are: S1813 (Microposit, shiply) and SPR-220-7 (Megaposit, Shipley).

Edge- Beads[20]

Spin coating does not always produce flat and uniform coatings especially in the case of coating thick resist films. Slightly thicker contour forms on the periphery of the wafer producing an 'edge bead'. This can have undesirable effects like reducing the resolution of the photolithographic process by introducing an undesired proximity gap between the layer and the mask during exposure, and may also cause the mask to stick to the layer. Methods to remove the edge bead have been investigated and these include:

- A 'spin off' of the edge bead by suddenly raising the spin speed at a certain point in the coating. But this can only be effectively used with resists that have a low enough solvent concentration to avoid further thinning, with a low enough viscosity at the edge bead to allow "spin-off".

[20] Based on reference [72] (2013, *Theory And Application of Photoresists, Developers, Solvents and Etchants revised 2013, Website: http://www.microchemicals.com/downloads/application_notes.html.*

- For thick films or resist with high solvent concentration, a thermal increase in viscosity during soft-bake can lead to a growth in the edge bead. This can be prevented by introducing a delay between the coating and the soft-bake. The delay time depends on the resist film thickness but can be shortened by applying moderate step temperatures. i.e. a stepwise temperature increase.
- Multiple coating with an elevated spin speed for each coating cycle can minimize the formation of an edge bead.
- If possible, the outer pieces of the substrate carrying the edge bead can be removed using lithography whereby a specific mask is used to allow the edge bead to be washed off post-exposure. A different mask can then be used to pattern the wafer. If this was not possible, a manual removal of the edge bead from wafer the periphery can be attempted but caution must be taken as this may cause 'T-topping'.

Thick Resist Films: optimised Spin Profiles and Multiple Coatings

Thick resist films normally end up with higher solvent concentration at the end of spin coating compared to thinner layers [72]. This can cause softening during softbake leading to the formation of an edge bead or reduced edge coverage. A double or multiple coating can be used to homogeneously dry off the resist during coating without significantly losing thickness homogeneity (please refer toFig.6.1). If a single spin method is used to obtain the required film thickness, the softbake process has to be carefully designed and planned to take into consideration the thickness of the resist film and the high solvent concentration. Otherwise problems will rise during sofbake such as bubble formation from the evaporating solvent in addition to the edge bead growth. As mentioned earlier, a delay between spin coating and softbake can also be introduced to improve the situation.

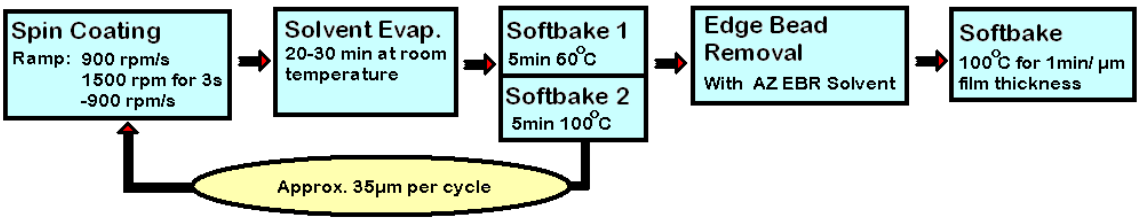


Fig. 6.1: An example of multiple coating chart[72]

6.2.3. Softbaking of Polyimide resins and photoresist

After spin coating wafer, the remaining solvent concentration is approximately between 15 to 40 % depending on the layer thickness. The softbake steps that follow reduce the remaining solvent concentration in the resist to about 4 to 7%. By removing enough solvent from the resist layer, the liquid photoresist or polyimide are turned into a dry, semi-cured layer that is suitable for photolithographic processes.

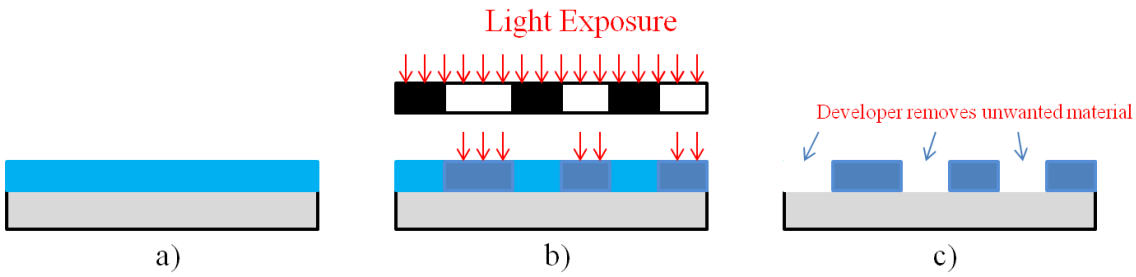


Fig. 6.2: The photolithographic process for negative photoresist- a) film is spin coated onto the wafer, b) only selected regions of the layer are exposed to UV light using a mask, c) development removes resist in unwanted regions[17].

The softbake parameters such as starting temperatures, ramping steps and holding times are important for the success of subsequent processing steps. Softbake temperatures need to be high enough to reach the boiling point of the solvent and the glass transition temperature of the binder but low enough to avoid destruction of the photo-active compound. Insufficiently softbaked films show high dark erosion during development leaving a too small resist structure that is less sharp then desired. Performing a sufficient softbake reduces this effect. On the other hand, long/hot softbake thermally and partially decomposes the active compound resulting in a reduced development rate. This means that development will take longer which may result in increased total dark erosion. A trade off compromise between the sufficient solvent evaporation and minimized photo active compound loss is a softbake at 100^0C for 1 minute per 1µm resist film thickness on a hotplate. In addition to solvent removal resist adhesion is increased during softbake and resist/substrate stresses are reduced [72].

Solvent evaporation is highest at the beginning of the softbake and then drops quickly to reach an almost constant value. The solvent evaporation rate drops during softbake for the following reasons:

- The evaporation rate is proportional to the surface solvent concentration, and
- The solvent diffusion towards the resist surface strongly drops in solvent-poor resist.

For thick resist films, the thicker the layer the smaller the softbake parameter window formed by baking temperature and time becomes for a proper process result. If the softbake parameters are not carefully calculated to suit the film thickness, we may end up with the following problems:

- A too short softbake can result in increased in high dark erosion during development.
- Trapped solvent in the form of bubbles and deformations, caused by high temperature ramping rates and non-heating uniformity through the thickness of the resist layer. If the evaporating solvent (gases) cannot dissipate from the resist film fast enough due to high resist thickness bubbles are formed and strong mechanical stresses develop causing cracks in the film.
- An overly long softbake can decompose part of the photoactive compound leading to a reduced development rate. Furthermore, the very low solvent concentration makes the resist film very brittle and susceptible to the formation of cracks. These can sometimes be seen as bubbles in the resist film.

For softbaking thin photoresist layer (such as the S1813 used in this thesis), the sample was placed on a hotplate which has been preheated to 120^0C and held at this temperature for 6 minutes. Whereas for the thicker photoresist SPR-220-7, the sample was placed on hotplate preheated to 90^0C where it was held for 2 minutes, then transferred onto a second hotplate that has been preheated to 120^0C and was held there for another 6 minutes. After completing the softbake, samples were left on the bench to cool down for at least 20 minutes before any further processing. This is to allow rehydration of the layer before exposure for a reasonable high development rate and contrast. By leaving the sample to

sufficiently cool down, diffusion of water molecules takes place from air into the resist film allowing the layer to re-hydrate after the soft-bake.



Fig. 6.3: Polaron Thermal Evaporator

6.2.4. Photolithography

Photolithography is the process of transferring a pattern from a master mask to a slave material (photosensitive material). The mask design and production is relatively a costly process and usually one mask is repeatedly used to generate a large number of slave components. The photoresist is exposed to UV light through a master mask of clear and opaque areas. This is done to transfer the mask image onto the slave photosensitive material by selectively exposing areas of the material while blacking out others so that the material can be patterned upon development.

The types of radiation, materials, and tools are important characteristics of the photolithography process, but the basic steps are generally the same as those of conventional optical lithography. After spin coating and softbaking the photoresist for a uniform solidified layer, exposure to UV light is performed through a mask to transfer a desired pattern to the resist layer.

Exposure and development

The photoresist layer is light sensitive polymers. Patterns can be created in the resist by exposure through a mask containing the pattern. Exposure will either increase or decrease the solubility of the exposed area in a suitable solvent (developer) depending on the resist type. There two types of resist, a positive and a negative. Positive resist will become more soluble in exposed regions while negative resist will become less soluble in the exposed regions. When a positive photoresist is exposed, the energy from the UV light photons breaks the chemical polymer chains making the resist material more vulnerable to a particular solvent (developer). Hence during development, the exposed regions are removed at a much higher rate then the unexposed regions. The result is an exact image of the mask pattern. The negative resist on the other hand, works in the exact opposite way. Upon exposure, the UV light photons react with the exposed area making the polymer chains more cross-linked and hence making these regions less vulnerable to the solvent during development. The result is an inverse image or copy of the mask pattern. The difference in solubility between exposed and unexposed area results in the reproduction of the mask image into the photoresist. During development, the developable regions defined by exposure are removed leaving behind resist structures.

Photolithography can only produce two-dimensional devices or 2.5 Dimensional devices by stacking more multiple 2D layers. There is also a limitation to the resolution of photolithography. Correct feature size must be maintained as the performance of the device depends on the size of the patterned structures. In the shadow printing mode (contact and proximity), the theoretical resolution R, i.e., the minimum resolved feature size R_p is calculated by Equ.6.1 [18]:

$$R_p = \frac{2}{3}\sqrt{\lambda(s+\frac{z}{2})} \qquad \text{(Equ. 6.1)}$$

Where s is the distance between the mask and the photoresist surface, λ is the wavelength of light used, and z is the photoresist thickness. This means that if contact printing (s=0) was used with a UV light wave of 248nm and a photo-sensitive polyimide layer thickness

of 100μm, then the theoretical maximum resolution of photolithography is a feature size of about 3 μm. The resolution can be increased to allow for smaller feature sizes by using shorter radiation wavelengths, and a thinner photoresist layer which is possible with high quality photoresist. Another determinant factor for the feature size especially for the metallization process is the shape and the integrity of the side walls. Factors affecting the shape of side walls include photoresist thickness used, the radiation wavelength and the process steps that define the angle of the side walls. A negative resist is usually used to ensure better definition of the pattern as the development differential between exposed and unexposed resist is much higher than with positive resist [28].

The result after development is the removal of resist from locations that the mask defined for the application of metal. The wafer is then is hard-baked on a hot plate at around 150^0C to evaporate the remaining solvent and ensure good adhesion between the remaining resist and the wafer. In addition, the photo-active compounds are destroyed during hard-bake making the processed layer photo insensitive and thus unaffected by any further processing. After development, regions of the substrate are no longer covered by the photoresist film. Further subtractive or additive processing can now be performed, either by etching unprotected areas or by depositing layers over exposed layers of the substrate (lift-off). The photoresist, therefore, must be capable of reproducing desired pattern images and providing protection, or resistance, for the substrate in subsequent processes. Schematic of negative photolithographic processes is shown in Fig. 6.2. The photolithography steps are detailed in the next section.

6.2.5. Evaporation and Fabrication of Thin Metal Features

Thermal Evaporation

Thermal evaporation is used to deposit thin metal films such as gold and platinum. These layers are patterned to define the electrode sites, the tracks and connection pads of the neural interfaces. Thermal evaporation is based on the melting and boiling off of a heated material onto a substrate in a vacuum. A good vacuum is needed to avoid contamination

and oxidation reactions at the source which may lead to impurities being formed. The samples to be coated are placed upside down in a vacuum chamber. This chamber is then pumped down to a pressure of at least $1x10^{-5}$mbar before any metal evaporation can be started. The metal is evaporated by passing a high current through metal containment structure (a tungsten boat or filament). This so-called method of resistive heating heats up the metal and sublimes it. Because of the vacuum, the sublimed metal particles have high mean free path allowing them to travel as far as the surface of the sample. Upon arrival to the sample surface, they cool down depositing a pure metal film on the substrate sample surface.

The thickness of the deposited film is proportionally dependant on the amount of source current used to boil-off (sublime) the heated metal and on the amount of time for which the metal is allowed to sublime. The higher the current and longer the evaporation time, the thicker the deposited film is.

For devices fabricated in this thesis, a polaron thermal evaporator (Quorum Technologies, Discontinued) shown in Fig. 6.3 was used to evaporate the metal layers. Metals such as titanium and chromium generally reveal very good adhesion to resist or polymeric layers. On the other hand, noble metals such as gold or platinum have poor adhesion to resist or polymeric layers. Due to the lack of bonding sites on the metal surface, adhesion promoters are unable to significantly improve metal adhesion. The best solution for this problem is to first apply a thin layer of few nm of Titanium or Chromium as an adhesion layer between the resist and the noble metal layer. The metal layers for neural interfaces fabricated in this thesis are fabricated by thermally evaporating a thin chrome layer followed by a gold layer.

6.2.6. Etching and other surface treatments

The metallization layers can be patterned using either wet etching or dry etching. In either case the wafer is exposed to an etching process which will remove material from both the exposed metal layer and the photoresist. However the choice of the photoresist

needs to such that the metal is removed at a much higher rate and thus photoresist protects the metal it is covering for the duration of the etching process [18].



Fig. 6.4: Etching profiles- a) Amorphous isotropic etching, b) Perfectly anisotropic etching

Wet etching

Wet etching is the process of removing material by immersion in a chemical liquid etchant. The chemical reaction taking place at the liquid-material interface creates an etch attaching the metal layer at the exposed regions. The metallised pattern is created by the photoresist protecting the regions where the metal structures are to be defined. After this, the resist layer is washed off from the surface using acetone and IPA. The result is a metal pattern that has been transferred from photo-lithographically patterned resist into the metal layer via a wet etching.

For the SPNIs developed in this thesis, S1813 or SPR-220-7 are used to define regions for the electrode sites, tracks and the connection pads on the metallisation layer. The gold layer is etched by immersing the sample in a potassium iodide solution for about 40 seconds and then rinse off the remaining etchant with deionised water. The exposed chrome regions are then etched away by immersing the sample in a chrome etchant for about 15 seconds and rinsing the sample straight after with deionised water to stop the process.

Although wet etching is a simple and effective to use for the etching of large and shallow substrates, undercutting of the resist layer can be an issue. In the amorphous Gold and chrome materials the etchant etches in all directions from the contact point resulting in an isotropic profile, as shown in Fig. 6.4 (a). Wet etching is very cheap compared to dry etching as it requires no costly machinery or equipments other than the essential precautions for chemical handling and storage. However, as it is a process involving liquid, there is no precise control over the etch rates (as they depend on the concentration,

the amount of agitation used and the etchant temperature), in addition to undercutting and the impossibility of achieving perfectly vertical sidewall profile as shown in Fig. 6.4.(b).

6.2.7. Dry Etching

Dry etching is the alternative method to wet etching. It can solve the problems encountered with wet etching such as undercutting and hence allows a much smaller feature size to be fabricated. Dry etching methods include Reactive Ion Etching (RIE), Deep Reactive Ion Etching (DRIE), Ion Beam Milling (IBM) and Oxygen Plasma etch.

Ion Beam Milling

Ion beam milling (IBM) is a dry etching technique used to realise small feature sizes that cannot be successfully patterned with wet etching. In the scope of this thesis, it will be used to pattern the metallisation layer of the devices and define the electrode sites, tracks and the connection pads of the SPNI implants. Besides having excellent feature repeatability, IBM is capable of defining smaller electrode foot prints, hence allowing the possibility of increasing the number of electrodes per device. Before starting the IBM process, the sample pattern to be etched needs to be prepared first. This is done by spin coating and patterning a photoresist layer on the sample layer to be etched which creates a mask that protects the desired regions in the metal layer.

The wafer sample is then placed in the Ion beam miller for dry etching of the metal layer. The chamber housing the sample is then pumped down to a pressure below 10^{-6} mbar resulting in a large mean free path. Argon gas is pumped into the chamber and a plasma is formed through an RF source. The plasma ions are extracted, formed into a beam, accelerated and fired towards the surface of the sample where bombardment of the exposed metal atoms takes place resulting in a patterned metal layer. The ion beam etching features are highly directional and controllable. This allows the anisotropic sidewall profile to be realized and minimizes the problem of feature undercutting which allows for much smaller feature sizes to be fabricated.

The IBM system used (Oxford Applied Research IM150) contained a turbo-pump to pump down the sample chamber to the required pressure, an ion beam gun to make and direct the argon plasma. An RF source kept at 150W was used to form the argon ions whist the screen and the accelerator voltages were set to 500V and 200V respectively. 20 minutes was sufficient to mill the metal layers for the neural interface device[21]. The Ion Beam Miller was connected to a computer that shows live the current etch rate at the layer currently being etched, and as materials such as gold and resist have very different etch rates one can use this to determine if metal layers have fully been etched by watching for a dramatic change in etch rate. Visual inspection under a microscope can be used to confirm the outcome.

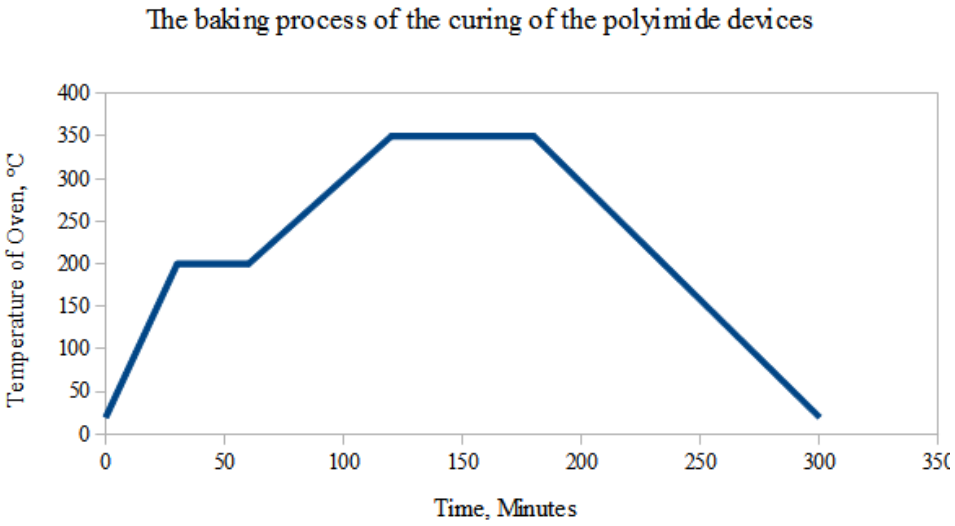


Fig. 6.5: Full curing temperature profile for polyimide

Oxygen Plasma Etching

Oxygen plasma clean is another dry etching method used to etch away undesired materials. It is similar to Ion Beam milling in that it uses a plasma of ions to knock out

[21] This could be determined via a computer that shows live the rate at which the atoms are etched at the current layer. As material such as gold and resist have very different eth rates one can use this to determine if metal layers have fully been etched through by watching the change in etch rate

atoms from the sample substrate upon collision. However, unlike IBM, Oxygen plasma etching is isotropic and the plasma particles bombard the sample surface in all directions.

The Oxygen Plasma Etch is performed by placing the sample in a chamber which is then pumped down to reach an appropriate pressure. Only several minutes are needed to pump down the chamber as the pressure required for OPE is considerably higher than that required for IBM. A flow of Oxygen is then allowed into the chamber and ionized by applying a large potential difference between the anode and cathode. This potential creates an electric field which causes free electrons in the oxygen gas to accelerate towards the anode leading to collision between fast moving, hot electrons and slow moving cold oxygen molecules. This results in ionized oxygen molecules which have lost an electron from their outer shell. These free electrons lead to further reactions causing a cascade effect which forms a plasma.

The oxygen plasma etching is used as a surface treatment to free the sample from any organic contaminants or organic materials. It can also be used to roughen the sample surface and improve adhesion to subsequent layers. In this thesis, Oxygen plasma etching was used as a de-scum method to clean the microelectrode site and connection pads from any polymeric residues. It was also used to etch Pyralin sample made to test the MFI technique discussed in chapter 8. A barrel etcher (Femto model from Diener Electronics) is used to perform the Oxygen plasma etch/clean. The samples were first transferred into the etcher and chamber was then pumped down to a pressure of about 1mbar (The manufacturer manual). The oxygen plasma was then formed and the samples were etched for 10 minutes to de-scum or roughen the sample's surface. However to etch through thicker layers of polymeric materials longer etching times are required. Once the etching of the desired region has been achieved, the etcher was vented to release the sample.

6.2.8. Curing of the polyimide structures

One specific characteristic of polyimide is its requirement for extensive curing after the device fabrication is completed. This is done to imidize the polyimide layer and drive off

any remaining solvent. Without being fully cured, the polyimide structures would not have the same properties; they would not be as durable and they would have an increased water up-take and an increased potential absorption of contaminants. This would have a detrimental effect in long term performance of the implanted devices.

The full cure has to be carried out in a nitrogen free environment to avoid burning the material. The temperature profile illustrated in Fig. 6.5 is programmed into a conventional oven to perform the full cure of polyimide. After loading the sample, a constant flow of nitrogen is allowed into the chamber and will be maintained throughout the cure process to provide an oxygen free atmosphere in the oven. A pump can be used to pump the oven chamber to certain pressure before the nitrogen flow is started. The oven is heated up from room temperature to 200^0C at a rate of 2.5^0C/minute. The temperature is then held at this value for 30 minutes before it is allowed to increase further. This is to allow enough time for the oven chamber housing the sample to achieve the required oxygen free environment before temperature rose above 200^0C. Presence of oxygen above 200^0C would cause burning of the polymeric layers which have a serious impact on the properties of the materials leading to device damage and failure. The temperatures, then, raise to 350 ^{0}C at a 4 ^{0}C/ min rate and the sample is baked at 350 ^{0}C for 60 minutes before it is allowed to cool down to room temperature.

6.2.9. Methods to determine the film thickness

One way to measure film thicknesses is to use a surface profiler (DEKTAK Bruker Corp.). The DEKTAK works by dragging a low force stylus across the sample surface and recording any variation in the step height. The system can measure step variations in the range of 200 to 655000 Å according the DAKTAK supplier. However, when measuring the thicknesses of very thin films, the effect of factors such as fabrication defects, contaminants and the shape of the stylus can easily dominate the step reading. Hence, thicknesses below 0.5μm are always approximate. Thicknesses of very thick layers (such as the channel layers for SPNI) that are out of the DEKTAK measuring range are measured using micrometer or an optical microscope. SEM was also used to measure

thicknesses of device structures and layers fabricated in this thesis, however, because of the need to coat the samples with a thin gold layer before they could be viewed under SEM meant that these devices can no longer be used for any further testing or implantation.

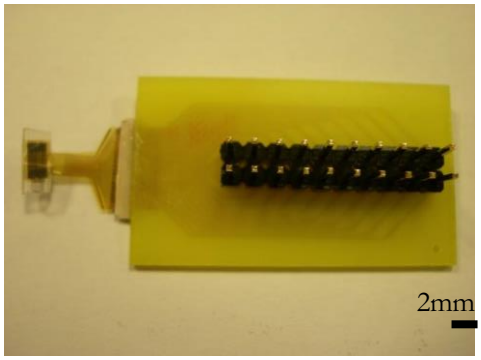


Fig. 6.6: Using a ZIF and a convention PCB to access the SPNI microelectrodes

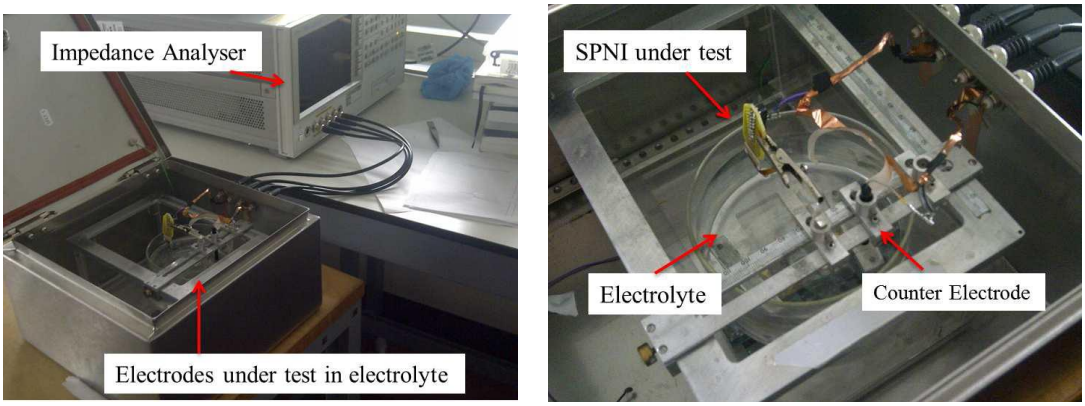


Fig. 6.7: The experimental set-up to perform Electrochemical Impedance Spectroscopy (EIS)- Left; Positioning of SPNI and counter electrode in the electrolyte, Right; Electrodes under test connected to Network Analyser[17].

6.3. Techniques used to test the SPNI polyimide devices

6.3.1. Electrochemical Impedance spectroscopy

Electrochemical Impedance Spectroscopy (EIS) is used to assess the ability of these implants to record from and stimulate neural tissue. This is mainly done by characterizing

the electrode/electrolyte interface of the implants' micro-fabricated electrodes. This section describes the experimental set-up to conduct EIS on the SPNI microelectrodes and the operational principle behind this technique.

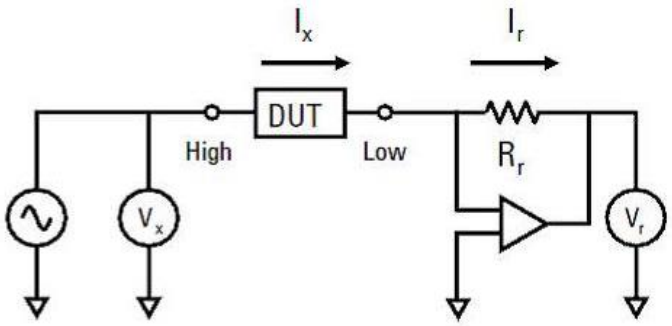
During EIS, the electrical impedance and phase are measured at various frequencies by exciting the electrode with sinusoidal voltage or current. The data is presented in an impedance and phase spectra. The frequency range used is normally between 10Hz to 100KHz as it is the range which contains the frequency range for physiological signals and the separation which can notably be made with solution resistance. In normal EIS practice the applied source signal is (1 to 10 mV) AC signal as this will make the system pseudo linear.

EIS measurements were carried out using a network analyzer (HP 9424, Hewlitt Packard) connected to an electrochemical cell made up of two electrodes and an electrolyte solution. The first electrode was the micro-fabricated electrode to be characterized and the second is a counter platinum electrode with a 0.4 cm diameter. The counter electrode is designed to have a very large surface area compared to the micro-fabricated electrode so that the impedance of the former is negligible compared to the latter. The electrolyte is a physiological saline designed to mimic the environment that the neural interfaces will be exposed to. It consists of 8.6g of sodium chloride, 0.3g of potassium chloride and 0.33g of calcium chloride dissolved in one litre of deionised water. A 5mV sinusoidal source signal and frequency ranges of 10Hz to 100KHz were used for impedance measurements of the devices fabricated in this thesis.

To enable access to the 20 channels of the neural device, the implants were inserted into a matching 20 pin ZIF connector which was in turn mounted on and glued onto a conventional PCB allowing access to the different channels of the device (see Fig. 6.6) . In the case of ball bonded samples to an alumina substrate; the substrate was glued onto the PCB and then bonded using the ball/wire bonder[22]. To carry out EIS, the sample was lowered just enough to immerse the part containing the microelectrodes in the saline while keeping the rest of the device , especially the connection pads, above the saline to

[22] Please refer to chapter 8 for more details on (The Kulicke and Soffa gold ball bonder)

avoid short circuiting the device. The device was fixed in place using a crocodile clip as illustrated in Fig. 6.7. Each channel representing a device microelectrode was accessible by connecting to the corresponding DIL socket.



(b) Impedance measurement using an operational amplifier

Fig. 6.8: the principle of the auto-balancing bridge method [17]

The operational principle of the Network Analyser[23]

To carry out the impedance measurements of the electrode under investigation, an electrochemical cell and a network analyser are used. The electrochemical cell consists of the chamber containing the electrolyte and the electrodes necessary for the measurement; the counter electrode and the working electrode (which is the electrode to be characterized). The principle of impedance measurement is illustrated in Fig. 6.8. To measure the impedance of the device under test, the potential (voltage) at the low terminal of the device under test has to be kept constant at zero. This is done through an auto-balancing bridge consisting of IV converter amplifier whose non-inverting input is connected to the low terminal of the device under test while the inverting input and the output are connected to the signal source and the resistor R_r respectively. This set up provides a feedback loop which constantly monitors the potential at the low terminal and

[23] The style of this section is based on [17] R. Barrett, "Novel Processing Routes for Neural Interfaces, " Ph.D., The University of Birmingham, 2013.

adjusts it accordingly. The current Ix flowing through the test device is the same as I_r the current flowing through the resistor R_r to maintain a zero potential at the low terminal. The voltages V_x and V_r can be measured using a voltmeter, and hence by applying Ohms law the impedance Z_x can be calculated using the equation:

$$Z_x = \frac{V_x}{I_x} = R_r \frac{V_x}{V_r} \qquad \text{(Equ. 6.2)}$$

Measurements through this method have high accuracy and very low error in the range of 0.008% with a small source signal in the range of 1 to 10 mV. The analyzer can measure impedances as small as $3\text{m}\Omega$ and as big as $500\text{M}\Omega$ and a phase between 0 and 90 ^{0}C. To efficiently extract the measured data, the impedance analyser was controllable via a Lab View program written by Andreas Frommhold.

6.4. Chapter summary

This chapter presented the methods used to fabricate and test the SPNI implants. 2D planner photolithography was the main technique used to pattern the various layers of the device. The process steps for the techniques used were explained in details. Thermal evaporation was the method of choice to evaporate the implant's metal layer. Dry and wet etching techniques were also explained as these were used to pattern the device metal layer. Electro-chemical Impedance Spectroscopy was used to test the functionality of implant micro-electrodes and hence assess their ability to record from and stimulate neural tissue. The next chapter will introduce and explain the fabrication process of the SPNI implants in details.

7. FABRICATION OF SPNI DEVICES

7.1. Introduction

This chapter presents a detailed discussion of the fabrication process of the SPNI implants[24]. The aim is to develop an optimised process for fabricating SPNI devices which have been redesigned based on input from previous electrical and biological testing (such as regeneration results). As mentioned in the design chapter, passive devices will first be fabricated to evaluate regeneration through them and access the suitability of their dimensional parameters for optimal regeneration. Active SPNI devices with embedded electrodes are then fabricated to access their ability to stimulate from and record neural activity from regenerated axons. The recording sites of the microelectrodes are incorporated into the micro-channels and exposed in the target channel through windows in the insulation layer. The electrodes are accessible through contact pads which can be used to connect the devices to IC circuitry. The active and passive devices are fabricated using the same fabrication process, except for the metal layer where it is left out in the passive the devices as these do not require any wiring. The process steps for fabricating the devices are shown in Fig. 7.1[25].

7.2. Materials

The SPNI implants were fabricated using non photo-definable and photo-sensitive polyimide (PSPI) materials. Pyralin2611, is supplied by HD Microsystems, and the Photo-definable Durimides(7505 & 7020) are supplied by Fujifilm Electronic Materials.

[24] Please refer to chapter 5 for details regarding the implant design, its dimensions and the thicknesses of its constituent layers.

[25] The process flow is for active implants; the fabrication steps for the passive devices are the same except for the steps related to fabricating the metal wiring where this can be skipped for the passive devices as it is not required.

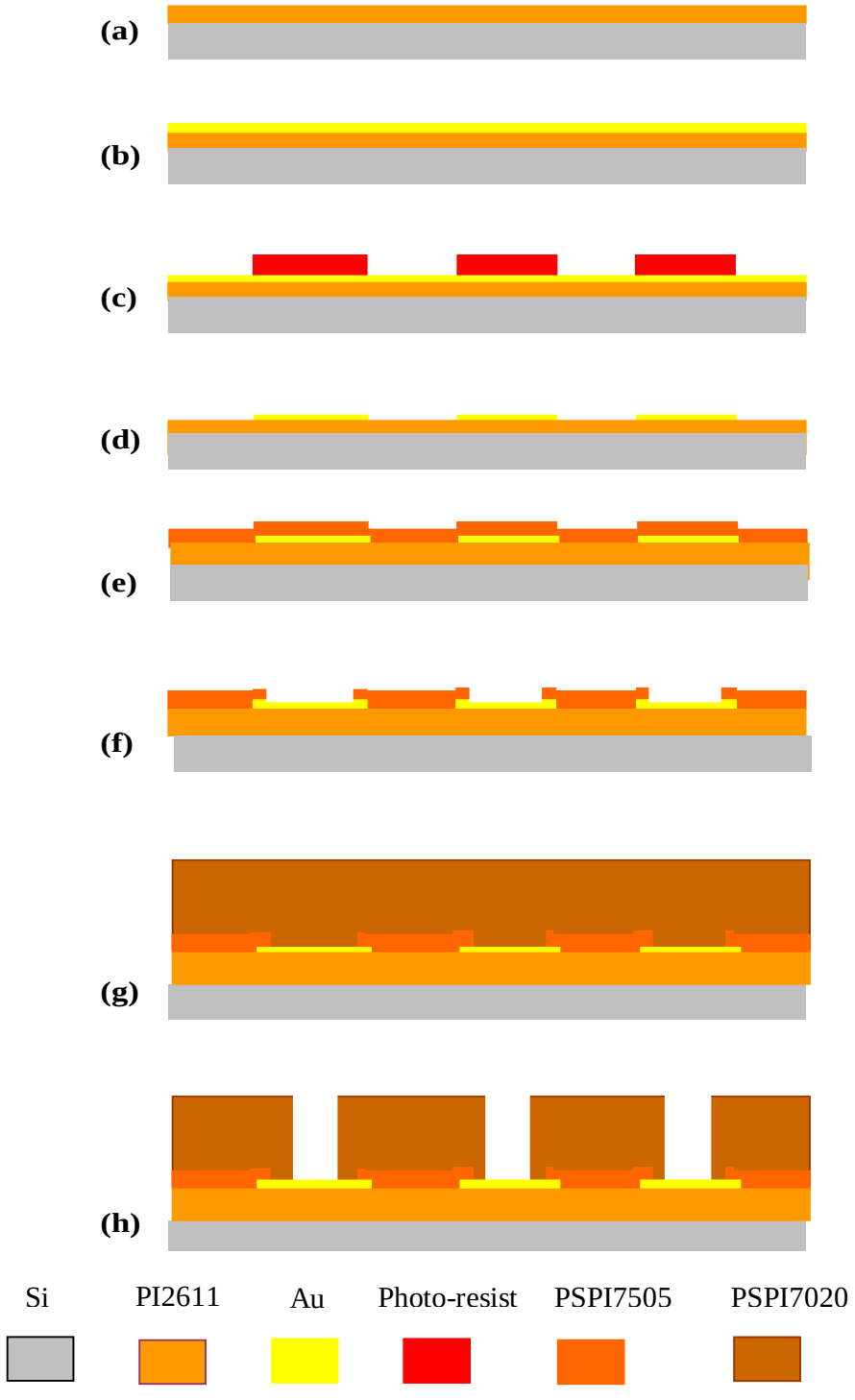


Fig. 7.1: Process steps for fabricating the SPNA devices

Pyralin2611 is widely used in neuro-prosthetic implants because of its suitable properties in biomedical applications. These properties include biocompatibility, low water uptake, good thermal stability and electrical insulation properties. Durimides, on the other hand, arephoto-definable polyimides and, hence, can be patterned photo-lithographically. They contain an internal adhesion promoter, eliminating the need for an additional priming step. The biocompatibility of Durimides has been proven *in vitro* [63] and is being evaluated in *vivo* [62]. The micro-electrodes are made of patterned gold films which are thermally evaporated on the substrate. Chromium is an adhesion layer for gold but because of its bio-toxicity it will be substituted by titanium in future fabrications of SPNI devices[26].

7.3. Wafer preparation and substrate adhesion

The fabrication processes discussed in this thesis starts by cleaning a (100) silicon wafer that has been pre-treated with a 250nm oxidised surface layer (supplied by Compart technology Ltd). These wafers, also known as carrier wafers, have been used in micro-fabrication processes for years because of their good resistance to chemical processes and thermal stability during curing at raised temperatures. The SPNI devices are fabricated on a 4'' diameter carrier wafer to increase the device yield per wafer. However, these wafers can be cut into smaller carrier wafers of various sizes using diamond edge cutting blade or programmable dicing saw. The surface of the carrier wafer can be cleaned using acetone and isopropanol (IPA). The wafer is cleaned by first rinsing the wafer surface with acetone to remove organic contaminants and then rinsing the surface with IPA to remove the contaminated acetone. Following the acetone/IPA clean, the wafer surface is dehydrated through baking on a programmable hotplate at a 150 ◦C for 5 minutes. This allows any water molecules that have condensed onto the wafer surface from the surrounding environment to evaporate leaving behind a dry and a clean wafer surface.

De-lamination related to poor adhesion was a common problem during the fabrication of the SPNI substrate layers. To minimize this problem and improve adhesion to the carrier

[26] Please refer to chapter 5 for details regarding the implant design, its dimensions and the thicknesses of its constituent layers.

wafer more elaborate wafer cleaning techniques were used. These included the use of piranha solution made of H2O2+H2SO4 and O2 plasma etch. The two techniques were either used separately or in conjunction with each other.

7.3.1. Pyralin substrate adhesion

The first problem encountered at the beginning of the fabrication process was the adhesion between the Pyralin substrate and the 4'' carrier wafer; de-lamination and large air bubbles were observed between the wafer surface and Pyralin substrates after the samples had been cured (hard baked). At first, we suspected that this may be due to contamination of the wafer surface. Hence, a stronger cleaning procedure was used to decontaminate the wafers. This included the use of a Piranha solution (also known as the piranha etch) which is a mixture of 50% sulphuric acid (H_2SO_4) and 50% Hydrogen Peroxide (H_2O_2). The mixture is a strong oxidising agent and hence will remove most organic contaminants in addition to making the surface more hydrophilic. Oxygen plasma etch was also performed to remove any remaining contamination. It also roughens the wafer surface which can improve wafer adhesion to subsequent layers. Details on how the oxygen plasma clean is performed can be found in chapter 6 section [6.1.7]. A barrel etcher[27] was used to clean the 4'' carrier wafers. This was done by first placing the samples in the etcher, closing the chamber and pumping the chamber pressure down to about 1mbar (manufacturer recommendation). The formed oxygen plasma etches the samples for 10 minutes which is sufficient for the purpose of cleaning the carrier wafers. The chamber is then vented at the end of the process to release the samples.

However, the de-lamination and large air bubbles persisted even after the carrier wafer has undergone de-contamination through the methods just explained. This has led us to think that the large bubbles and de-lamination could be caused by another factor other than contamination. Large bubbles of trapped air were frequently seen between wafer and the de-laminated substrate layer which might be caused by the way the solvent in Pyralin resin evaporates through the thickness of the layer during the hard bake. To investigate

[27] Femto Model from Diener Electronics

this, Pyralin substrates with various thicknesses were prepared by varying the time and the speed of the spin coating then fully curing these samples in the furnace in an oxygen free environment. The adhesion between the Pyralin layer and the wafer is then compared against the thickness of the Pyralin layer to see whether the thickness of the Pyralin layer has any effect on its adhesion to the career wafer.

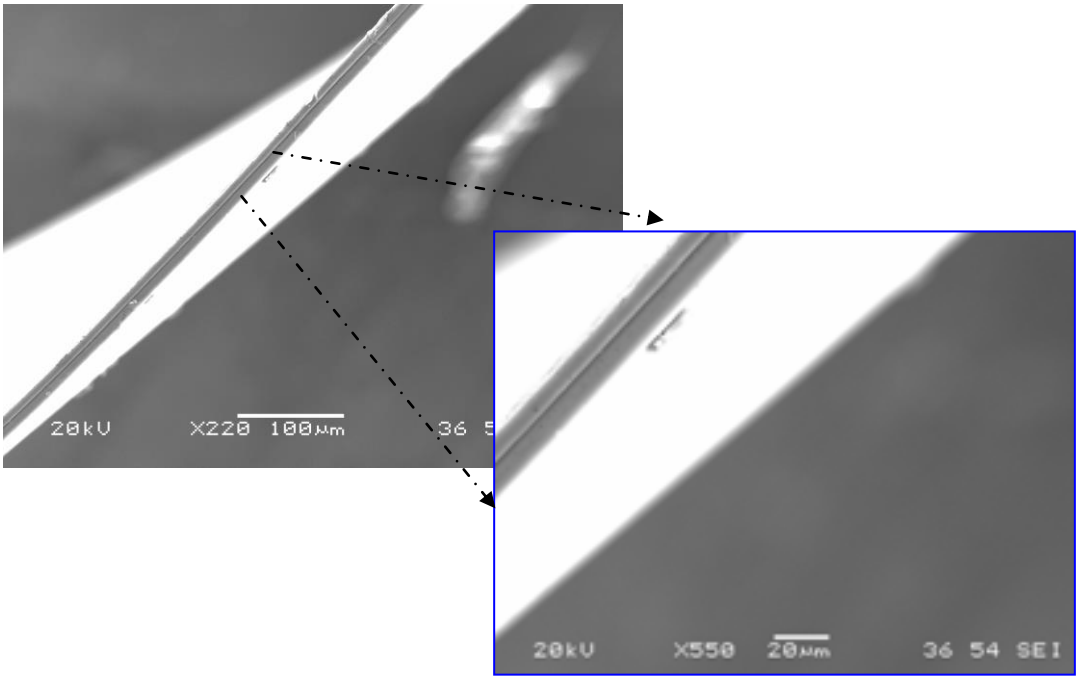


Fig. 7.2: SEM image of 20µm thick substrate layer cross-section , fabricated using multiple spin coating with full cures in between. First a layer of PI2611 is spin coated on a 4'' wafer and then fully cured. A second layer of PI2611 is spin coated on the top of the first layer and then the whole wafer is fully cured to give a to total thickness of 20 µm. Specific spin speeds are used to obtain this thickness. The inset is a zoom into the substrate cross-section.

Results from this experiment showed that de-lamination between the Pyralin layer and the wafer was strongly associated with the thickness of the Pyralin layer; Thinner Pyralin layers seemed to have better adhesion to the wafer surface. This can be explained by the amount of solvent evaporating of the Pyralin resin during the hard bake and the variation in the heating uniformity across the layer thickness. Thicker layers of Pyralin tend to trap evaporating solvents during curing (mainly at the bottom of the layer) which can then collect to form a large bubbles of trapped air. As the bubbles increase in size with more trapped gases, de-lamination of the Pyralin layer occurs at these regions. Therefore, in

order to achieve a good adhesion between the Pyralin layer and the surface of carrier wafer, the spin coated Pyralin layer thickness needs to be kept thin enough to allow the solvents to evaporate evenly through it and avoid bubble formation (and hence de-lamination during full cure). Consequently, fully cured substrate layer thicknesses of 12µm or less are recommended and these are obtainable with spin speeds of 1500 RPM or over (60 seconds spin time).

However, fabricating thicker layer substrates may be necessary to place the metal wiring in the neutral plane as explained in the design chapter. In an attempt to fabricate thicker layers of Pyralin that do not de-laminate from the wafer surface, a diluted[28] solution of polyimide adhesion promoter (VM651) was used to modify the wafer surface and enhance its adhesion to the Pyralin layer. However the adhesion between the Pyralin layer and wafer was too strong for the layer to be mechanically peeled off even with an over-diluted[29] solution of the adhesion promoter, which is problematic as it is the method that will be used to release the polyimide device for rolling at a later stage in the fabrication process. It is therefore necessary to maintain the ability of peeling off the Pyralin layer from the carrier wafer manually after full cure.

7.4. Increasing the thickness of the substrate layer

The substrates that were fabricated initially were to be used for the fabrication of passive devices, and so having a particular substrate thickness at this stage was not necessary. However, for active devices having a precise substrate thickness is of paramount importance in placing the metal layer of the microelectrode on the neutral plane of the rolled structure according to the preliminary stress model (used in calculating the neutral plane position). So, for the passive devices, the substrates were prepared by spin coating a layer of PI2611 on a 4''silicon wafer using a programmable spin coater. The wafer was first spun at 200 rpm spin speed for 10 seconds to spread the dispensed PI2611 material

[28] 0.1% VM 651 to deionized water concentration was prepared according the VM651 datasheet (In 1000 ml deionized water add 1 ml VM 651)
[29] 0.05% VM651 over-diluted solution was prepared

and then at 1500RPM for 60 seconds to give the required layer thickness of 12 μm [30] (after full cure). The wafer is cured in a programmable oven in a nitrogen environment at 350 ◦C according to the curing curve provided in Fig.6.5.

The neutral plane calculations based on the initial stress model suggested a substrate layer thickness of 35 μm for the microelectrodes and their wiring to be placed at the neutral plane of the rolled structure. However, the thickest cured Pyralin layer that can be fabricated with a single spin coating and without compromising adhesion to the carrier wafer is only 12 μm. Spin coating Pyralin at a lower speed will result in poor adhesion between the layer and the silicon wafer as explained earlier. This means that substrates thicker than 12μm cannot be achieved via single coating but rather through multiple coating of Pyralin. The idea is to spin coat the first Pyralin layer for a thickness of no more than 12 μm. This layer will provide good adhesion to the carrier wafer but can still be easily peeled off to release the device at a later stage. Two subsequent Pyralin spin coatings can bring the substrate to the required thickness of 35 μm. However, it is important to fully cure the Pyralin layer/s after every coating. This is because Pyralin layers that are partially cured can still evaporate solvent during subsequent cures which can cause trapped gases and hence delamination between the layers constituting the Pyralin substrate. This was recognized by the initial attempts at making thick Pyralin substrates through two Pyralin coatings without a full cure in between. This was processed as follow:

1. Spin coat Pyralin 2611 at 1500 rpm for 60 seconds
2. Using a programmable hotplate, bake the wafer consecutively at 70^0C for 5minutes, 95^0C for another 5minutes, 100^0C for 3min then at 150^0C for 30 minutes.
3. Repeat steps from 1 to 2 for the second Pyralin layer
4. Fully cure the wafer at 350^0C in N2 environment

This method did not succeed as outgasing from the first layer during full cure lead to trapped gas bubbles and delamination between the first and the second layer Pyralin layer.

[30] Spin speed curve in the Pyralin2611 datasheet was used as a rough guide to determine spin speeds that could give certain thicknesses

Therefore, thicker substrate layers were successfully fabricated using multiple spins of Pyralin 2611 with full cures in between coatings. So after spin coating the first Pyralin layer, a full cure is performed at 350^0C in N2 environment to avoid any outgasing from this layer during any subsequent full cures and the same steps are followed with the succeeding Pyralin layers. Fig. 7.2 below shows an SEM image of a Pyralin substrate cross-section with a 20µm thickness obtained using the process steps just explained (multiple spin coating with full cures between the layers). The boundary between the two layers can be easily seen in the SEM image.

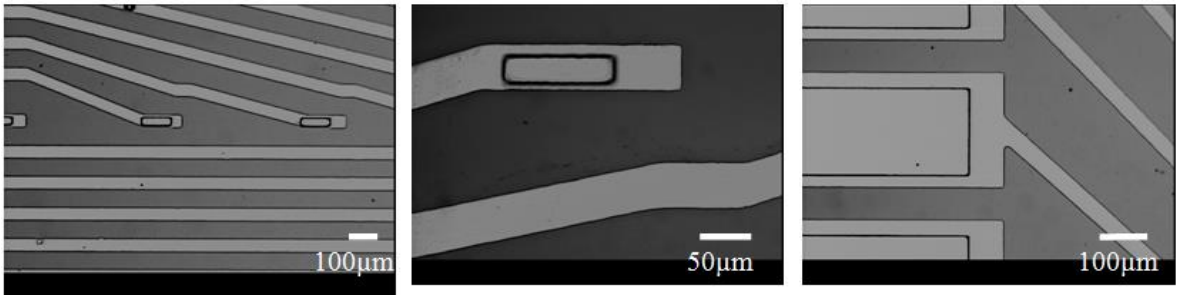


Fig. 7.3: Patterned metal layer showing Micro-electrode sites (top), tracks (top) and insulated connection pads (Bottom)

7.5. Metallisation layer

While this layer is not required for passive devices, it is necessary for active devices as it constitutes the micro-electrode sites, the tracks and the contact pads in these devices. It is composed of 50nm chromium adhesion[31] layer and 250nm pure gold layer. The chrome adhesion layer is evaporated by passing a 50A current through a chrome coated tungsten rod for 30 seconds. The gold layer is then evaporated by passing a 22A current through an alumina crucible containing pure gold pallets for 1 minute. The resultant metal layer is made up of approximately 50 nm chrome adhesion layer and a 250nm pure gold layer.

The metal layer is then patterned with a S1813 photoresist (Microposit, Shipley). This is done by spin coating a 2µm thick layer of photoresist at a 2000 RPM spin speed for 30

[31] The chromium layer is used as an adhesion layer as gold has poor adhesion to polyimide.

seconds. The sample is then placed on a programmable hotplate which has been preheated to 120^{o}C and is baked at this temperature for 6 minutes. The samples are then left on the bench to cool down for at least 20 minutes. Using a Canon mask aligner, a foot print for the SPNI metal layer is obtained by exposing the photoresist layer through a chrome-on-glass mask designed specifically for this layer[32]. The sample is then developed in MF-319 developer. Following this, the wafer is rinsed with de-ionised water and dried with a nitrogen gun. The result is an S1813 mask which protects the SPNI metal layer footprint.

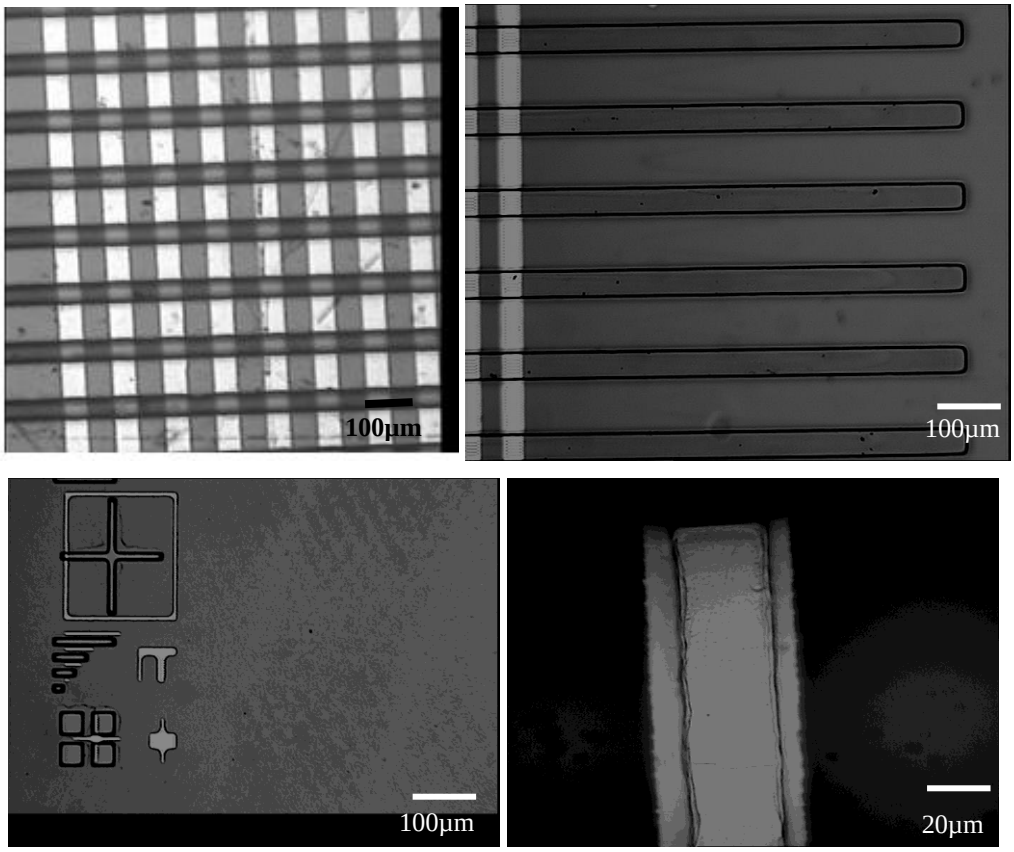


Fig. 7.4: Top: Channel layer aligned over electrode layer. Bottom left: alignment marks, Bottom right: a zoom into the micro-electrode sites

The unwanted metal regions are etched away by placing the wafer in a gold etchant for 50 seconds, and then in a chrome etchant for few seconds. The wafer is then rinsed with de-ionized water to stop the process and dried with a nitrogen gun to reveal a clean pattern.

[32] All the masks used for the fabrication of the various layers of the SNPI implant are designed in house using AutoCAD (Automated Computer Aided Design) and are then fabricated externally as chrome on glass masks by JD Photo-tools. Please refer to appendix A.1 for more details on the mask design.

After this, the photoresist layer is removed by immersing the wafer in acetone and then isopropanol. Fig. 7.3 shows optical images of the patterned and insulated metal layer which is evident with the windows exposing the electrode sites and the contact pads.

7.6. Insulation layer

This layer is used as a passivation layer to expose electrode sites and connection pads while insulating the tracks. It is not required for passive devices as these do not have a metallisation layer. However, it is important to ensure that the chemical and mechanical properties of the passive devices are as close to the active devices as possible. This is because the passive devices are used as an initial stage for evaluating the SPNI implants in terms of regeneration and biocompatibility. Thus, it is important to follow the same processing steps for both the passive and active devices except for the metallisation layer which is absent in the passive devices.

A $3\mu m$ thick insulation layer was fabricated using Durimide 7505 (PSPI7505). The process steps for this layer are as follows:

1. Spin coat PSPI7505 at 3500 RPM spin speed for 45 seconds.
2. Softbake the layer on hotplate at 70 ^{0}C for 5 minutes then increase the temperature to 95 ^{0}C and bake the sample at this temperature for another 5 minutes.
3. Leave the wafer to cool down for at least 20 minutes before exposure.
4. Expose the layer using the mask designed specifically for the insulation layer taking care to align the insulation layer to the underlying metal layer[33] (for active devices).
5. Using a programmable hotplate, post bake the wafer at 95 ^{0}C for 2-3 minutes, and then leave to cool down for few minutes.
6. Develop the layer using combination of developer/rinsing solvent (HTR D-2 and RER600). This is done by placing the wafer in the developer for 1 minute and

[33] All masks used for the fabrication of the various layers of the SNPI implant are designed in house using AutoCAD (Automated Computer Aided Design) and are then fabricated externally as chrome on glass masks by JD Photo-tools. Please refer to appendix A.1 for more details.

then in a mixture of developer/solvent (with a 50/50 ratio) for 10 seconds. The wafer is then placed in the RER 600 solvent for about 1minutes.

7. Repeated step 6 until a clear pattern is seen
8. The sample wafer is then rinsed with D-ionised water and dried with a nitrogen gun
9. To de-sensitize the insulation layer, bake the sample wafer on a programmable hotplate at 150^0C for 30minutes.

The window openings for the microelectrode recording sites in this encapsulation layer were 30µm×100µm. The contact pads had a window opening of 0.3mmx0.5mm in an earlier design which was then changed to 0.3mm x1mm in an updated design to match and allow connection to electronic circuitry through a ZIF connector which will be explained at a later stage (refer to Fig. 7.14 and Fig. 7.16).

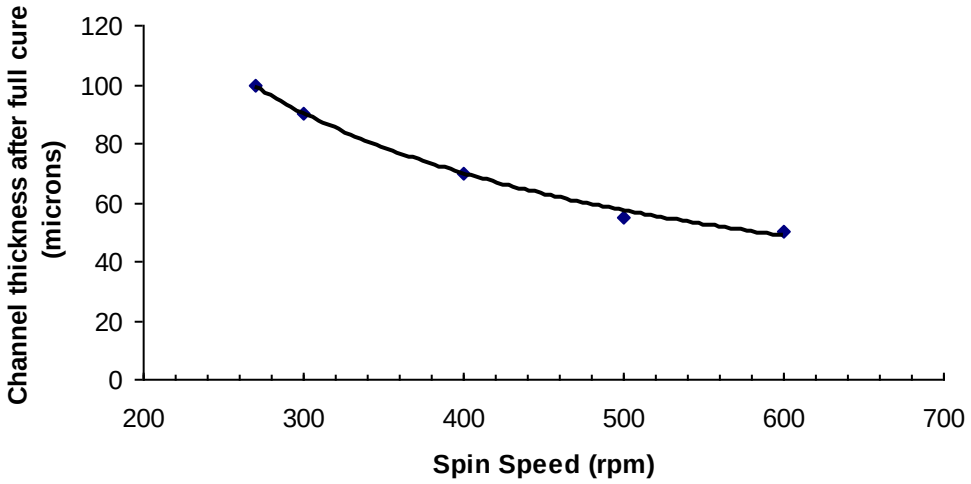


Fig. 7.5: Spin profile: PSPI7020 thickness after full cure vs. spin speed

7.7. Channel layer

The 100 μm polyimide channel layer was fabricated by spin coating Durimide7020 (PSPI 7020) at a suitable spin speed which was experimentally determined as will be explained in section [7.6.1] and [7.6.2]. After pre-baking the layer at slow and smooth temperature

ramp, which was also experimentally selected, the layer is exposed and developed to define the micro-channel arrays. An increase in the layer thickness would require a relative increase in the exposure time, which was also experimentally adjusted. The process steps for fabricating the micro-channels are the same for both active and passive devices. However, alignment of the channel layer to the metal layer is required for active devices and this was achieved via the alignment marks that have been designed into the SPNI masks. A print of the alignment marks used to align the different layers of the SNPI devices during photolithography is shown in Fig. 7.4. The figure also shows micro-channels crossing the passivated metal tracks which are only exposed at the microelectrode sites and at the contact pads. The processed wafer is cured at 350◦C in a N_2 environment and then peeled off the carrier wafer ready to be cut into 2D sheets and rolled to form 3D devices with micro-channel arrays.

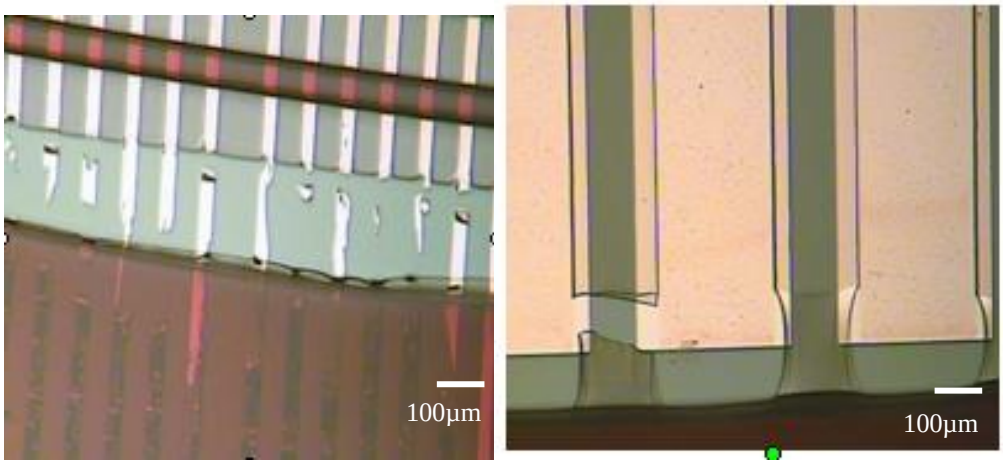


Fig. 7.6: effects of baking regime on the SPNI layers

7.7.1. Spin coating parameters for 100 μm channel height

The datasheet for Durimide7020 reports a maximum cured thickness of about 45 μm as attempting thicker layers need careful consideration of the processing steps of the layer which include a suitable baking regime. As discussed in section [5.3] of chapter 5, a 100 μm micro-channel thickness is required for the SPNI devices, and the process steps for this layer thickness ought to be investigated experimentally. Therefore, the spin speed and the spin time were experimentally varied to determine the values that can give

100 μm micro-channel height after full cure. Fig. 7.5 presents the findings in a spin speed curve, and as can be seen a 100µm thick layer can be obtained by spin coating Durimide7020 at a spin speed of 270 RPM[34] for 60 seconds. A spread spin speed of 200 RPM for 50 seconds was first used to allow the dispensed polyimide to spread and cover the wafer surface before the spinner increases its speed to the specified value to obtain the required thickness.

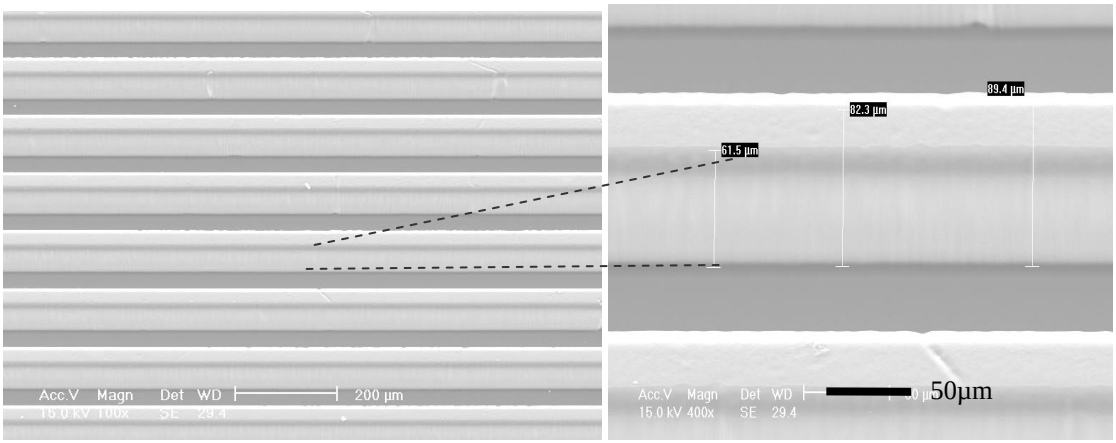


Fig. 7.7: SEM of photosensitive polyimide (PSPI) micro-channels tilted at 30^0

7.7.2. Pre-baking regime for 100µm channel height

During the pre-baking step, the solvent is partially evaporated from the polyimide to allow the photosensitive cross-linker to cross-link successfully during the exposure step. Making PSPI layers with cured thicknesses greater than 50µm requires a slow and smooth temperature ramp during the pre-baking step. If the temperature ramp is not slow enough, there will be non-heating uniformity with a fast solvent evaporation rate. This results in the evaporated gases being trapped at the base of the polyimide thick layer leading to the formation of micro-bubbles and shrinkage in the layer. In addition, the prebaking regime is also important because it affects the properties of the film being developed. If the film is not prebaked carefully, it can lead to high stresses within the layer which may result in film cracks during full cure. Not following a correct pre-baking regime can also have an effect on the interfacial stresses developing between the device layers during full cure

[34] Revolutions per minute

which can potentially lead to device failure. Fig. 7.6 shows a clear example of this where the baking steps of the PSPI channel layer resulted in undesirable internal and interfacial stresses building up during full cure which damaged the metal wiring and the insulation layer making the device un-functional. Hence, it is of paramount importance that a slow and smooth pre-baking step is followed to reduce internal and interfacial stresses and avoid their damaging effect during full cure.

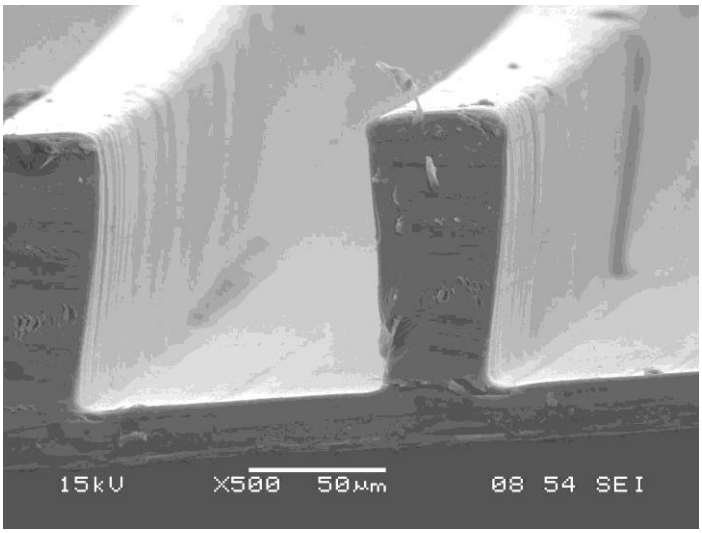


Fig. 7.8: 100µm channel walls. The undercut observed in the channel walls can be attributed to the layer thickness and the exposure time. The photo-sensitive polyimide used to make the channels is a negative material, consequently under-exposing a thick channel layer (thickness>50 μm) through the mask can lead to an undercut feature in the channel walls during development. This can be improved by adjusting the exposure time further.

Therefore, to fabricate micro-channels with a height of 100µm after full cure, a very slow and smooth prebake needs to be used so that bubble formation, layer shrinkage and high internal stresses in the layer are avoided. The ramping rate and temperature were determined experimentally by spin coating several layer of Durimide7020 at 270RPM spin speed for 60 seconds. The layers were then pre-baked starting at different temperatures. Starting the pre-bake at any temperature higher than 35^0C has led to the formation of bubbles in the layer. Hence, it was decided to start the bake at a temperature of 30^0C or lower. The spin coated samples in the next set were baked successively on the same hot plate and at the same starting temperature (30^0C). However, the temperature was set to ramp up at a different rate for each individual sample. It was observed that the

samples with ramp up rates of more than 0.5^{0}C/minute developed bubbles and shrinkage. Therefore a temperature ramp up rate of 0.3-0.4 ^{0}C/min was selected which has been confirmed to be a suitable ramp up rate after re-testing. The temperature for the pre-bake would be set to ramp up at this rate from the starting temperature of 30^{0}C until 95^{0}C. It is then left to bake at this temperature for a further 10 minutes after which it is taken off the Hot Plate to cool down for at least 20 min before exposure.

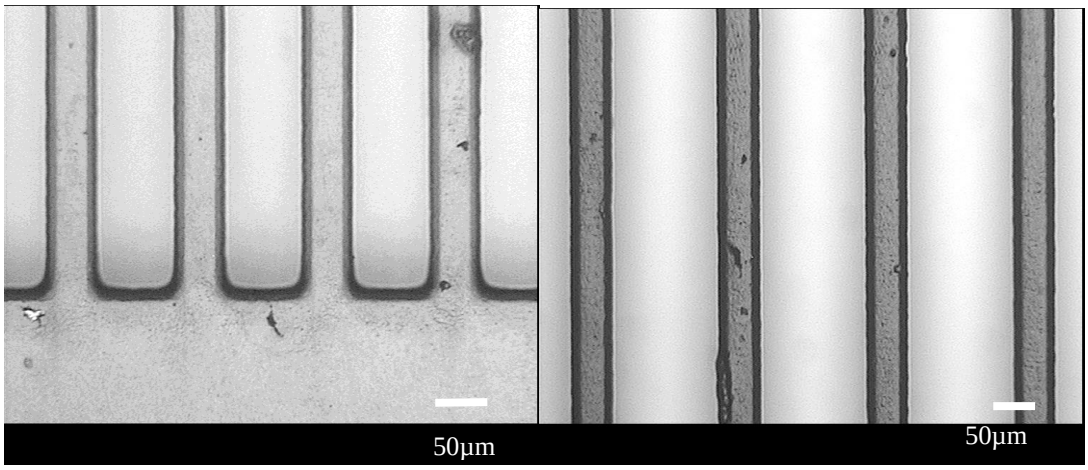


Fig. 7.9: Channel walls- left channel walls before cure. Right: Channel walls after full cure

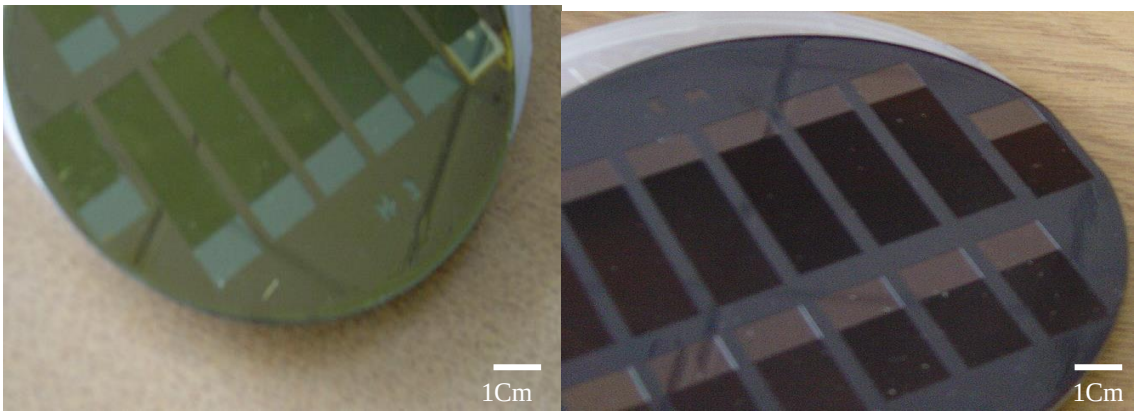


Fig. 7.10: partially and fully cured PSPI (Before and after cure)

To summarize, the processing steps for the micro-channel layer are as follow:

- Spin coat PSPI7020 at 270 RPM spin speed for 60 seconds
- Soft-bake the layer on hotplate at temperature ramp up rate of 0.3^{0}C/minute starting from 30 ^{0}C until 95 ^{0}C. Leave the sample to bake at 95 ^{0}C for another 10 minutes

- Leave the wafer to cool down for an hour or more before exposure
- Expose the layer with UV light in the wavelength range of 380 to 400nm using a Canon mask aligner. The UV light is shined through a chrome glass mask (designed specifically for the micro-channel layer[35]) after aligning the channel layer to the underlying insulation layer (for active devices).
- Post bake the wafer at 95 ^{0}C for 2-3 minutes, and then leave to cool down for few minutes
- Develop the layer using a combination of developer/rinsing solvent (HTR D-2 and RER600). This is done by placing the wafer in the developer for 1 minute and then in a mixture of developer/solvent (with a 50/50 ratio) for 20 seconds. The wafer is then placed in the RER 600 solvent for about 2minutes. These 3 steps need to be repeated until a clear pattern is seen, and for the 100µm thick channel layer this can take more than 20 repetitions. The beaker containing the wafer needs to be constantly shacked to aid pattern development. An ultrasonic bath may be used at a suitable setting to speed up the process. The wafer is rinsed with DI water and dried with a nitrogen gun once a clear pattern has developed.

The processed device layers are ready to be fully cured in a programmable oven according to the curing curve presented in chapter 6 section [6.1.8]. Following the full cure, the samples will be cut and rolled. Further details regarding the curing, the cutting and the rolling of the devices are provided in section [7.7] and [7.9] of this chapter.

To get a clear 3D view of the channel walls and height, SEM (Scanning Electron Microscopy) was used as an alternative imaging technique. The samples had to be coated with a thin layer of gold to be able to visualise them under SEM. This means that any PSPI devices imaged with SEM cannot be reused for implantation. The image illustrated in Fig. 7.7 is for thick channel device viewed at a 30^0 tilt angle. The micro-channel wall height is worked out by using the following equation:

$$Channel_height = \frac{measured_value}{\sin(tilt_angle)}$$

So by substituting to the equation above: *Channels height = = 61.5/0.5= 123 µm*

[35] All masks used for the fabrication of the various layers of the SNPI implant are designed in house using AutoCAD (Automated Computer Aided Design) and are then fabricated externally as chrome on glass masks by JD Photo-tools. Please refer to appendix A.1 for more details on the mask design.

In an attempt to get a vertical/top view of the channel cross sections, the polyimide sheet were cut off across the channels and have been placed vertically on the SEM holder. The cross section of the channel walls is shown in Fig. 7.8. As it can be deduced from the image the channel walls are about $100\mu m$. The undercut observed in the channel wall can be attributed to the layer thickness and the exposure time. Because the photo-sensitive polyimide used to make the channels is a negative material, under-exposing a thick channel layer (thickness>$50\ \mu m$) through the mask (designed for the channel layer) can lead to an undercut feature in the channel walls during development. This can be improved by adjusting the exposure time. However care needs to be taken to avoid over-exposing the channel layer as this might result in an inability to wash away the material through the full depth of the channels, and consequently the microelectrode sites may not be fully exposed.

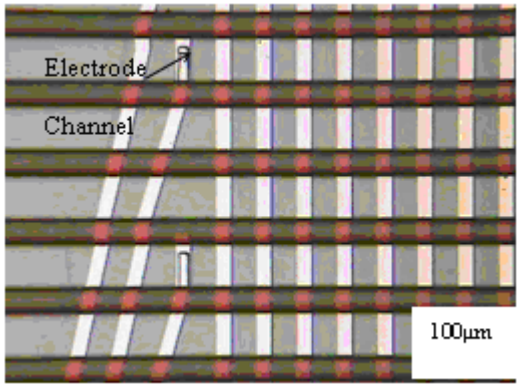


Fig. 7.11:Optical image of the SPNI device at the micro-electrode sites

7.8. Curing

As discussed in chapter 6, curing is a hard-bake through which any remaining solvent in the polyimide layers is driven off and the layers are imidized into the final structures[36]. Fig. 7.9 shows a sample of passive channel devices before and after cure. The loss of solvent during full cure made the channel walls darker and narrower causing a widening

[36] The full curing regime for the polyimide devices is explained in Chapter 6 (the methods chapter)

of the channel width. The samples of PSPI cured up to 200^0C (partially cured) seemed to have a golden yellow colour as shown in Fig. 7.10 whilst samples cured up to 350^0C (fully cured) appeared to have a darker colour which ranged from dark golden brown to dark brown. It was expected for thick samples of PSPI to have a darker colour after full cure as more solvent is driven off and the increase in layer thickness would make the sample look darker. However, there was a colour variation between fully cured PSPI samples with the same layer thickness which was linked to variations in the properties of the different PSPI batches used. To ensure that the change in colour was not due to contamination or oxidation during full cure,

- The furnace chamber used for curing the PSPI samples was de-contaminated by a wash in the PSPI solvent RER600 and then by acetone and isopropanol.
- The oxygen content of the furnace chamber was then pumped down and kept as low as 0.02mbar prior to starting the nitrogen flow. This was done to prevent the oxidation of PSPI samples for temperatures higher than 200^0C

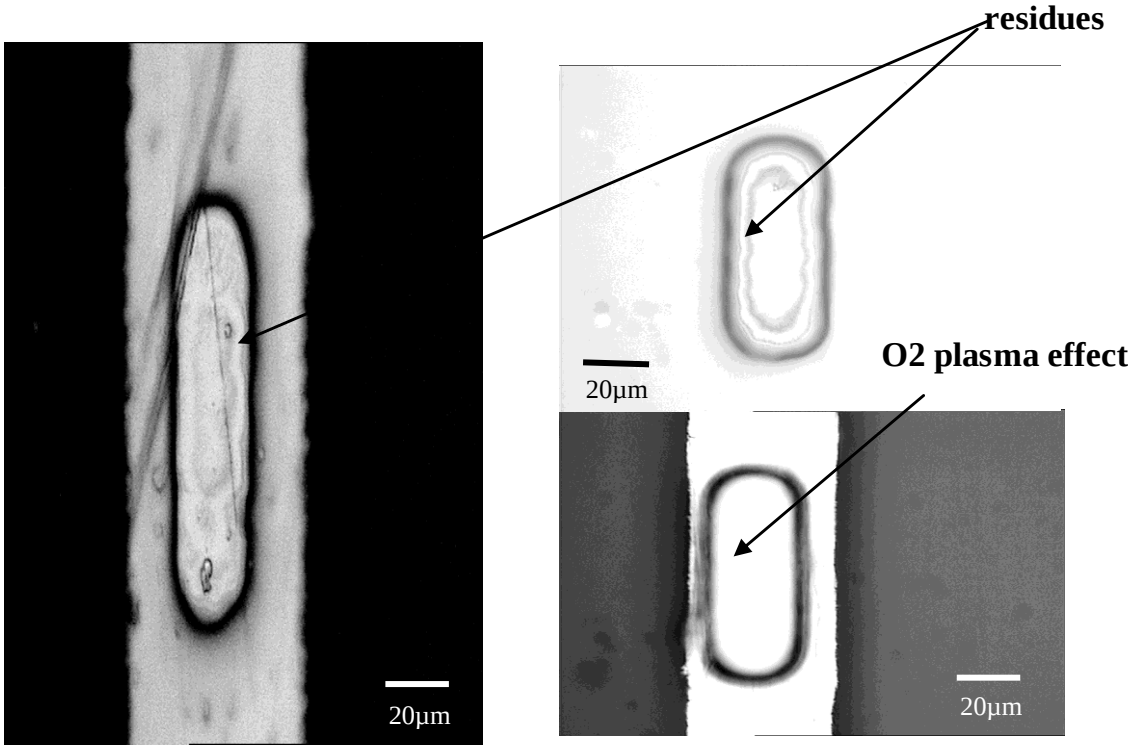


Fig. 7.12: the de-scum process: left- Micro-electrode site requiring de-scum, Top right: Microelectrode with PSPI residues before de-scum, Bottom right: the microelectrode after de-scum

However, the colour variation seen between the cured PSPI samples persisted whilst this was not happening with the Pyralin 2611samples. To confirm that the colour variation

was due to variations between different batches used, we communicated with the PSPI manufacturing company and they kindly prepared a PSPI 7020 sample and fully cured it using the process steps provided by us. Their cured sample was of a similar colour to the samples cured in our furnace (dark brown) which confirms that the dark colour seen was not caused by cross contamination or oxidation during full cure. The active devices are cured in exactly the same way as the passive devices at 350^0C in an oxygen free environment with a continuous flow of Nitrogen. Fig. 7.11shows the channels and the electrode sites of an SPNI device after full cure.

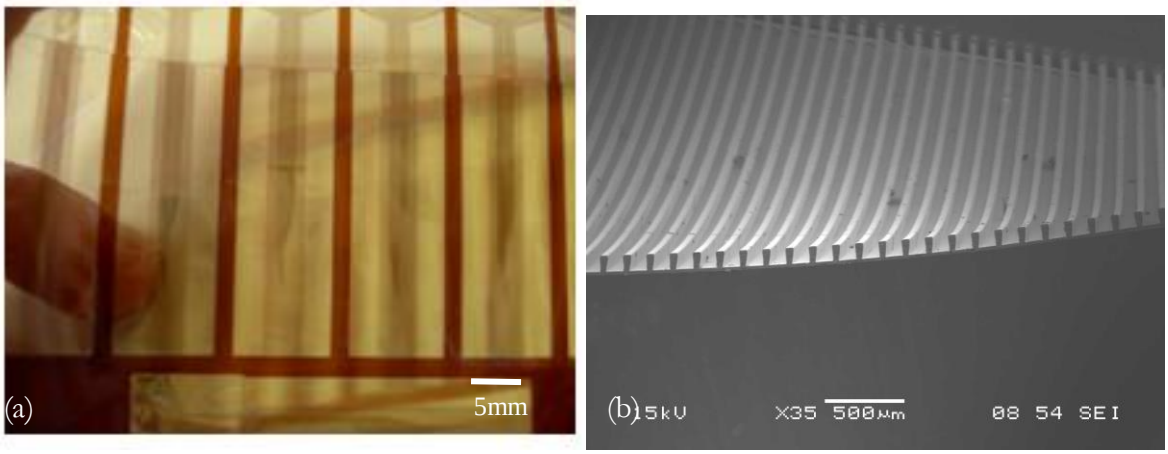


Fig. 7.13(a) sheet of the polyimide layers peeled off and ready to be cut, (b) SEM image for a sheet of polyimide layer that has been cut and which is ready to be rolled

7.9. De-scum of microelectrodes

This step is performed to clean the electrode sites from any remaining polyimide residues. This is done by etching away the residues using oxygen plasma etch for 10 minutes. Fig. 7.12 shows the electrode site before and after the de-scum process. As it can be seen, the polyimide residues at the gold electrode site were removed by the oxygen plasma etch making the site cleaner and fully exposed.

7.10. Cutting and rolling the devices

After peeling off the processed fully cured layers, the individual devices were separated by cutting through the Pyralin substrate with a scalp blade and following around the device foot print. For passive devices, dicing saw was also used to cut out the devices. Fig. 7.13 (a) shows a sheet of Polyimide that was peeled off the carrier wafer, ready to be cut into separate the individual devices. The figure also shows an SEM picture for the PSPI device before rolling.

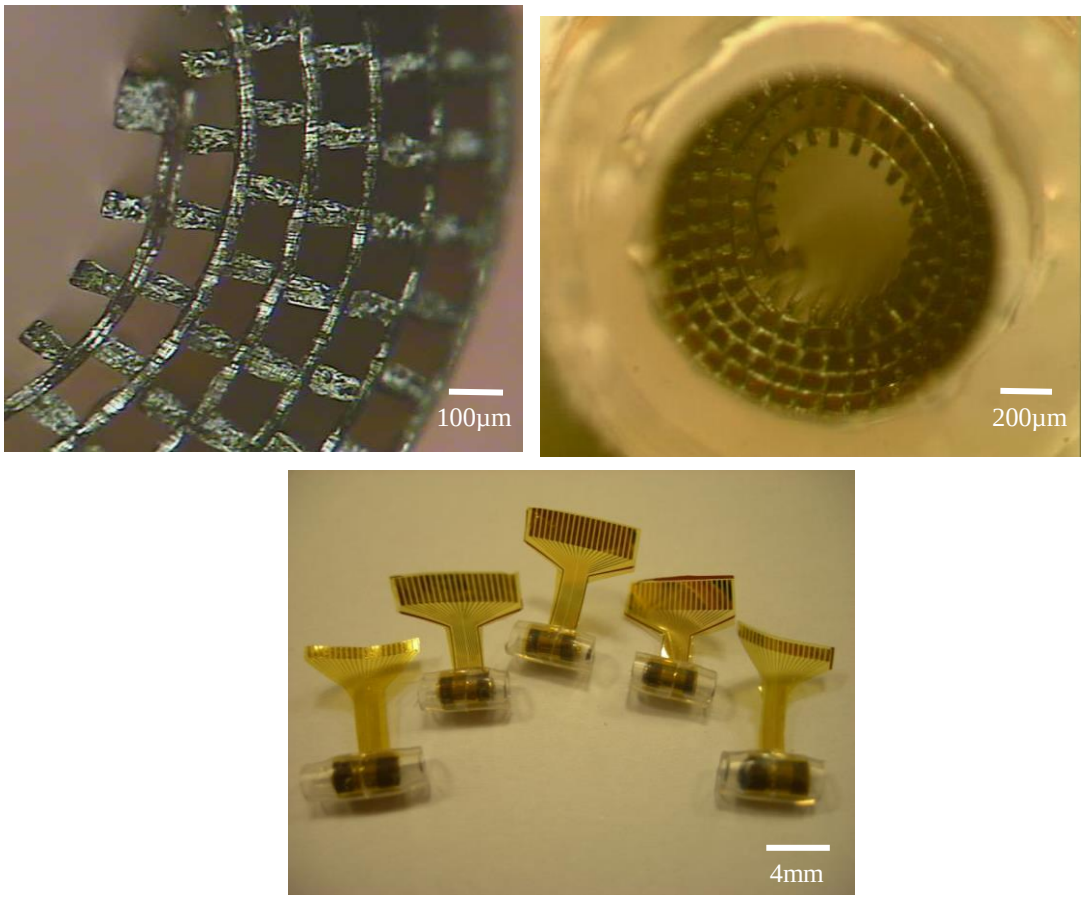


Fig. 7.14: Left rolled a PSPI device, Right: A PSPI roll inserted into a silicone tube, Bottom-SPNI devices rolled and held in 3D structure with a silicone tube whist allowing access to the connection pads.

To form 3D polyimide implants, the 2D sheets of PSPI devices were rolled[37] using a manual device roller. The end of PSPI sheet was clamped into a pair of tweezers that were connected to a manually operated rotating mechanism. The tweezers were then gently turned to form a tight spiral in the direction perpendicular to the channels. The rolled up sample is then inserted into a silicone tube with a diameter of 1.5mm. An excess of 1mm on either side of the silicone tube is deliberately left so that the injured/cut peripheral nerve can be stitched on either side of the tube. The silicone tube is used to prevent the rolled structured of the device from unravelling. Fig. 7.14 shows an optical picture of rolled up device with 4 and 1/2 rolls placed in a silicone tube with an internal diameter of 1.5mm to match the diameter of the sciatic nerve of rat where this device is to be implanted.

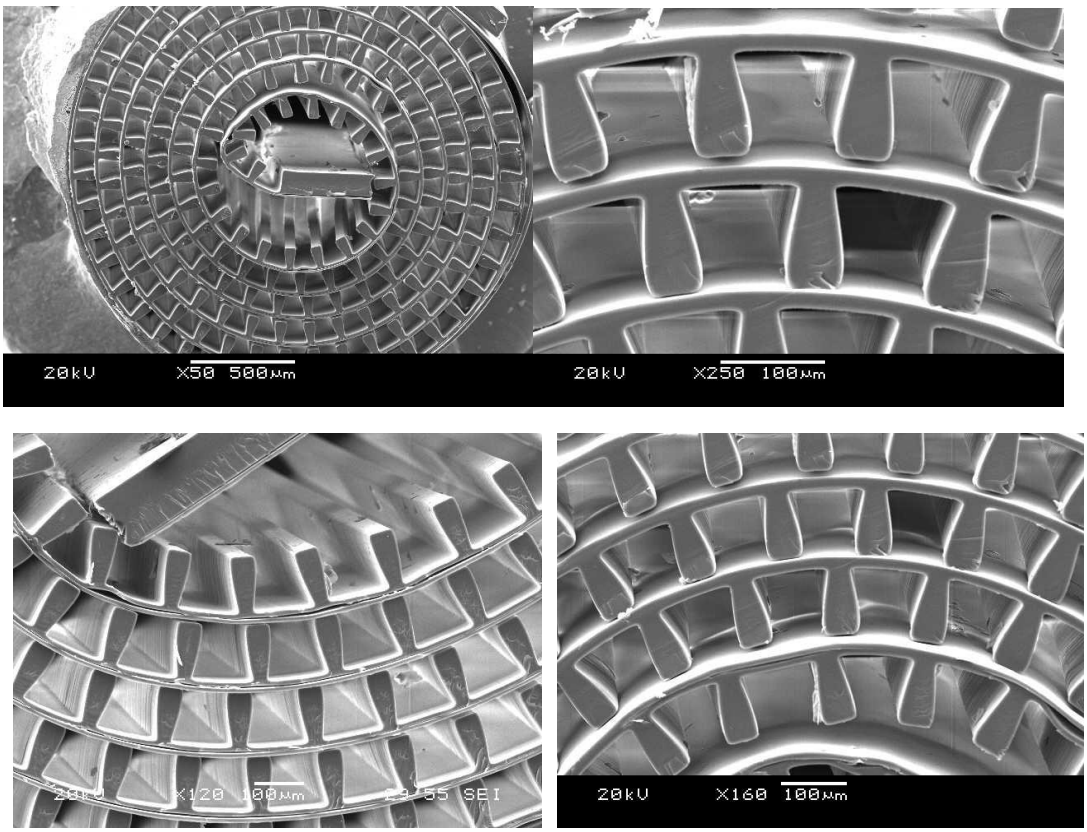


Fig. 7.15: SEM of cross sections of rolled PI devices with 100 μm high channel walls

[37] The effect of rolling on the metal layer of the SPNI devices is investigated by measuring the impedances of the micro-electrodes (using an impedance analyzer) which are presented and analyzed in chapter [9].

Rolled samples of SPNI devices have also been inspected under SEM. Fig. 7.15 shows a sample of the SEM images that have been taken for some of the rolled devices. The micro-channel walls and the formed micro- channels can be clearly seen in these pictures and the SPNI sheets have adequately been rolled into 3D SPNI devices. However getting a perfect seal for each micro-channel might require some further work. The central part of the roll caused by the current rolling method will be blocked by a thin dental thread before implantation to deter axons from growing into this part.

7.11. Connecting to the SPNI devices

The active devices are electrically connected to a custom made PCB board via a mounted ZIF connector. Besides enlarging the connection pads of the SPNI device to match the geometry of the ZIF connector, the overall thickness of the device had to also be enhanced with a support. This was achieved by gluing a custom made silicon support to the back of the connection area of the SPNI device. This is done to allow for a secure fitting of the contact pads into the ZIF connecter. The electrical contact between the ZIF pins and the contact pads of the SPNI device is established by closing the ZIF clamp. Fig. 7.16 shows an SPNI device inserted into a ZIF connector which has been mounted on a custom made PCB board.



Fig. 7.16: the SPNI device inserted into a ZIF connector to access its 20 electrode channels via dill sockets mounted on the PCB.

7.12. Chapter summary

This chapter presented in great detail the fabrication process of the SPNI implants and the issues faced during this process. The SPNI implants were successfully fabricated using photolithographic techniques mainly to pattern the various layers of the device. Thermal evaporation was used to evaporate the device metal layer while dry etching techniques such oxygen plasma etch were used to clean surfaces and de-scum the microelectrode sites and contact pads from contaminants or any polymeric residues. Besides optical microscopy, Scanning Electron Microscopy (SEM) was utilised to visualise the implants prior and post rolling. A Zero Insertion Force (ZIF) connector was incorporated into the implant to gain simultaneous access to the 20 embedded micro-electrodes. However, this is a temporary solution and a more suitable interconnection method is being developed to enable a practical and a durable interconnection of the SPNI implants to electronic circuits which is necessary if the implants are to be used for long term implantation. The suggested connection method is the Microflex Interconnection technique (MFI). The next chapter presents this technology in details and the work done to incorporate it into the SPNI devices.

8. OPTMISATION OF THE MFI TECHNIQUE FOR INTERCONNECTION WITH POLYMERIC DEVICES

8.1. Introduction

There are important and mandatory requirements that have to be met when considering interconnection to the SPNI devices. These include biocompatibility of all the materials used to avoid bio-toxicity, lightweight for minimal mechanical traumatization, and flexibility to follow movements inside the body, and small dimensions to minimize traumatisation during implantation[73]. Conventional interconnection techniques like solder, silver epoxy or ultrasonic bonding cannot be used because of biocompatibility or due to degradation of the coupling as a result of biological fluids in the PNS[73].

In this section we investigate the suitability of the ball bonding as a means to connect the SPNI devices to external circuitry. This involves designing test structures to optimise the technique for SPNI devices and updating the fabrication process. The ball bonding technique is called Microflex interconnection technique (MFI). It works like a kind of micro riveting between two components (the IC/Alumina substrate and a flexible micro cable with pads that have a hole to push the rivet through)[74]. The gold ball from the bonding process serves as micro-rivet. The MFI creates a durable stable electrical connection by thermosonic bonding of gold bump/ball through the substrate of the implant to a gold surface aligned underneath. All the materials used to make the interconnects are biocompatible (gold to gold bond). The technique has already been integrated into different nerve interfaces [73, 75-76].

Developing a durable and reliable connection between the SPNI and the external electronics is of great importance. These peripheral implants are designed to have rolls of

micro-channels[38] through which regenerating axons grow. 20 micro-electrodes are distributed evenly across the central/middle rolls[39] of each implant. To be able to use the implants for any long term application and record from the 20 available microelectrodes simultaneously, practical and durable connections between these implants and the external electrodes needs to be developed. This section will investigate the use of Microflex technology to create a reliable connection between the implant devices and the external circuitry. This includes modifying the fabrication process to incorporate the connection technique.

The active implants require the metal wiring to be placed in the neutral plane. To incorporate this requirement into the implant design a stress model [69] was developed in an earlier related study and was used to calculate the device parameters so that the wiring layer is at or as close as possible to the neutral plane. The study by Lacour et al. reporting the stress model in [61] claims the need for a $25\,\mu m$ substrate to place the wiring at the neutral place, however there is a conflict between the number mentioned in the study and the figure calculated using the stress model which was about $35\,\mu m$ (please refer to section [5.4.3] of chapter 5).

While it is possible to use Pyralin as a substrate, it is easier to fabricate the substrate using PSPI as photolithography is sufficient to pattern the layer without the need to use dry etching. However, as PSPI contains an adhesion promoter it sticks very well to the carrier wafer and hence cannot be manually peeled off to release the devices. A suitable sacrificial layer needs to be used to be able to release the PSPI substrate from the wafer and PMMA was found to be such a substrate. The fabrication process to change SPNI substrate from Pyralin to PSPI was carried out by Richard Barrett. His work showed how PMMA can be used as a sacrificial layer with considerations so that the SPNIs can be released safely from the carrier wafer.

[38]Each SPNI implant has 180 micro-channels in total. Details regarding the dimensions of the SPNI implant and its constituent layers are given in chapter 5 section [5.2]

[39] The number of electrodes was limited to 20 micro-electrodes per implant as the space available for lead out wiring is limited. Please refer to chapter 5 section [5.4] for more details

8.2. Current connection technique for SPNI implants

The in-vivo experiments aim to stimulate and record neural signals from the regenerated axons after three months of implantation. To do this, connection to the contact pads of the devices is required. The initial interconnection plan was to use the ZIF connector designed particularly to interface with the SPNI contact pads. However, the current method for connecting the ZIF into the SPNI contact pads was found to be tricky. This is because the ZIF connector is mounted on a relatively bulky PCB board which, in turn, has to be plugged into a 20 pin female connector. The current contact pad extension[40] on the SPNI devices was too short to allow insertion of the mounted ZIF without the bulk of the PCB and its connector getting in the way. Hence, before the ZIF can be used to connect to the SPNI, some modifications need to be made to the PCB board design to avoid the issues just raised. A simple solution is to extend the distance between the ZIF connector and the PCB SIL header to allow enough distance between the contact pads protruding from the animal thigh and the PCB 20 pin connector.

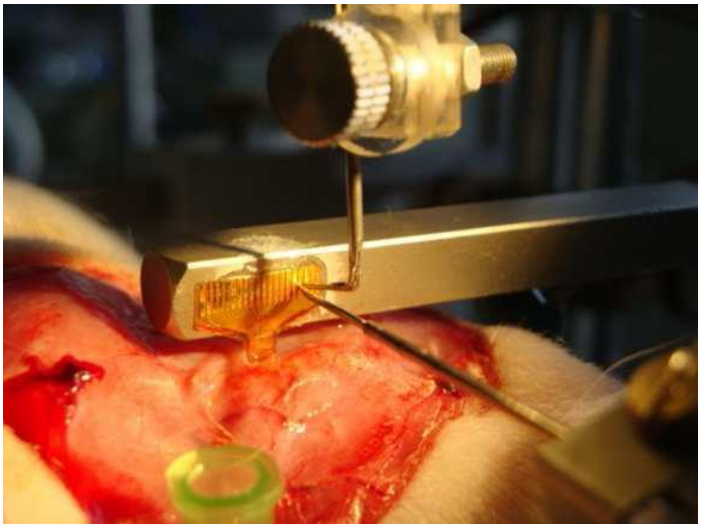


Fig. 8.1: Overview of the experimental setup to connect to the individual microelectrode channels[41]. This the primitive setup used to gain access to the microelectrode channels individually.

An alternative more primitive method was used instead to connect to contact pads individually. This involved sticking the pack of the connection pads area on a metal bar as

[40] Please refer to fig. [5.4] chapter 5 section [5.2] and Fig. [7.14] to view the contact pad extension of the device
[41] Taken during the in vivo recording experiments conducted at kings college

shown in Fig. 8.1 and then connecting to the 20 available electrode channels individually using needle tips. One electrode channel is used as reference whilst recording from another channel. Using this method of connecting to the electrodes means that we cannot stimulate and record from the individual channels simultaneously. This method of connection is far from satisfactory if the implant is to achieve the potential it has been designed for. This applies also to the use of the ZIF connector which can only provide a temporary solution to connect to the 20 channels of the SPNI device simultaneously. However, it is not a suitable solution for long term applications intended for the SPNI implants. The device extension with the contact pad region will be implanted subcutaneously. The wound will be closed and will be left to heal for the implantation period. To record from the implant micro-channels, the wound will be re-opened, and the contact pads will be exposed and freed from the surrounding tissue. The contact pad region is inserted into the ZIF connector to gain access to the implant embedded micro-electrodes. This solution is impractical for the long term implantation as the ZIF connector and its PCB board are un-implantable. Ultimately, for long term applications, the SPNI device and its conditioning circuitry (connected through a suitable interconnection technique) will be chronically implanted and a wireless link will be used for data transmission. However, if this is to be realized, a more practical interconnection technique (allowing a neat simultaneous access to the 20 implant micro-electrodes) becomes necessary.

Device miniaturization has drawn the attention to developing interconnection techniques and materials that are compatible with device requirements. For biomedical implants, there are strong requirements for the devices to be lightweight to minimize mechanical trauma caused to the delicate tissues, flexible to conform to body movements so that the implant can survive long term implantation, biocompatible to avoid bio-toxicity, small in size to minimize trauma during implantation and avoid a severe foreign body reaction in the case of long term implants

Because of device miniaturization and size constraints imposed when aiming for integration to chip sized packages or bare die, it is essential to resort to interconnection techniques like ultrasonic wedge/wire bonding, flip chip technology or similar methods.

Such methods are important if repeatable and consistent bonds are to be realised at this size scale. Ultrasonic wire bonding can be used to bond to polymeric materials, however this method is undesirable due the possibility of short circuits caused by the wires touching each other, in addition to the lack of durable and reliable bonding technique to polymer materials that could withstand the harsh physiological environment of the implant. Encapsulating the implant package in silicone may solve these issues as it acts as a barrier to protect the implant from its physiological environment. Nonetheless, small defects in the silicone can lead to mechanical stresses on the wire-bonds during curing and possibly leading to device failure[68, 77].

An alternative technique to the wedge/wire bonding was developed for the hybrid integration of flexible cables to rigid microelectronic chips. This method was named Microflex Interconnection Technique (MFI) and it has already been effectively incorporated into neural interfaces. Only biocompatible materials are used for devices with biomedical applications. Furthermore, smaller pitches with pads less than 100 µm x100µm can be easily achieved with MFI and standard CMOS chips can be used without the need to resort to expensive processes. The next section describes this technique in more details.

8.3. Microflex Interconnection Technology (MFI)

To stimulate and record from nerve fibres, the neural implant has to be suitably connected to the external electronic circuitry and as mentioned in the previous section Microflex interconnection (MFI) technique was developed for this purpose[78]. For custom small volume production with an integration density similar to flip chip technology producing pitches below 100µm, MFI allows the use of standard integrated circuits.

The Microflex (MFI) technology is adapted from the traditional ball bonding technology where force, temperature and ultrasound are used to bond a gold ball through a hole in the middle of a flexible pad onto a metal layer made out of a suitable material (like gold, aluminium or copper). Combination of different pad and bond metals can be chosen like

gold wire bonding on Aluminum pads or Aluminum wire bonding on gold pad. Metals are selected based on their ability to bond and form electrically reliable interconnects[79].

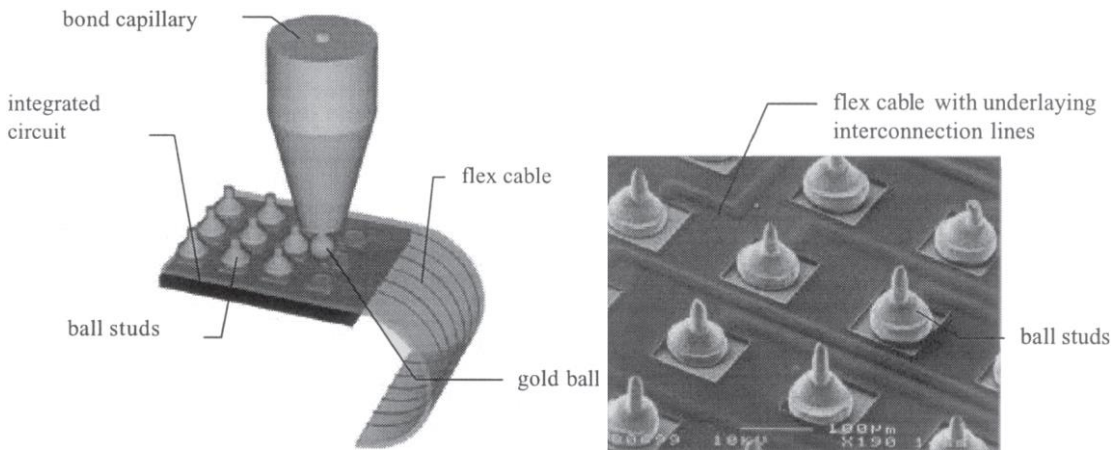


Fig. 8.2: Overview of the Microflex ball bonding technique. Right: SEM micrograph of the contact array, all bonds aligned on the contact pad[73]

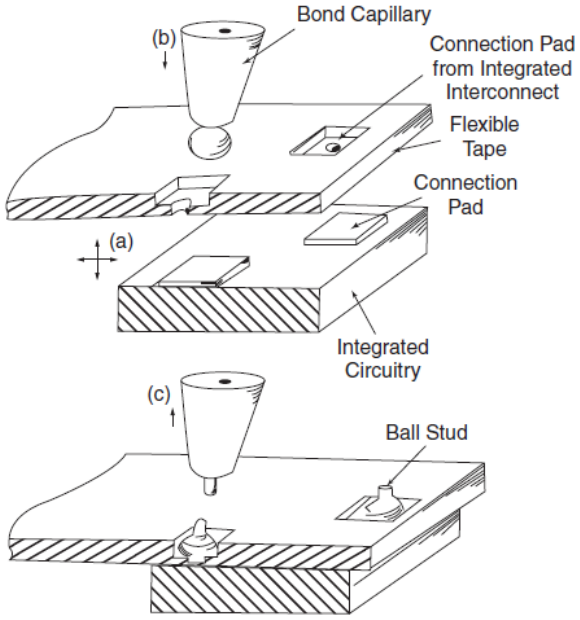


Fig. 8.3: Microflex process steps for a bond[74]

The two pads are coupled with the ball stud that works as a micro-rivet resulting in a mechanically and electrically stable interconnects. A wire bonder with an electronic flame off controller and a gold wire are used for the bonding process. The smallest pitches can be achieved using a bond capillary with a narrow neck.

The Ball-Wedge bonding technique that the MFI was adapted from consists generally of three steps which are:

1. The gold bond is formed by the flame-off electrode on the end of the gold wire.
2. The first ball bond is made on the target connection pad on the chip.
3. The wedge bond is made on the target destination pad. The capillary is then lifted and the wire separates from the wedge bond.

This process has been modified into the MFI technique shown in Fig. 8.2. In principal, MFI works like micro riveting between two components; an IC and a flexible cable with push through holes in the centre of its pads with the gold bond serving as the micro-rivet. With MFI, The traditional bonding process is reduced to the step1 and step2 where the gold ball is formed and bonded to the target pad through a *via* hole in the flexible cable pad. The ball bump remains after the capillary is lifted and the wire is cut.

8.3.1. MFI in greater details

Flexible cable with connection pads that have a *via* hole in their centre has been designed to match the locations and the pitches of the target substrate (e.g., IC) connection pads[74]. In the first MFI step, the optically transparent polyimide cable and the substrate (e.g., IC) are aligned under visual inspection (Fig. 8.3a). The hole in the centre of the flexible cable is placed over the target connection pad on the substrate. The holes are designed to be slightly smaller than the gold stud but large enough to get good contact and realize a bond between the pad on the flexible cable and the pad on the substrate through the gold pump. The alignment is aided with use of micromanipulator. The flame-off electrode forms a gold ball by melting the tip of the gold wire. The bond is made between pads on the flexible cable and the substrate by the ball bond (micro-rivet) which has been set through the hole. The capillary is then lifted off and gold wire is cut making the equipment ready for the next bond. The substrate and the flexible cable are now welded by a bond created by pushing and deforming ball to produce an electrical connection

between the two components by a form of ‘fit and closed linkage’. The interconnects can be encapsulated in silicone rubber to improve their stability and prevent short circuits.

The flexible substrate (cable) used in Steglitz el al studies [70-71] were made out of Pyralin, had a total thickness of 13µm, a via hole of 50µm diameter to get good contact and used 35 µm gold wire[70-71]. Flexible substrates with various thicknesses were fabricated and it was found that flexible substrate thicknesses of 10-15µm are compatible with MFI technique. Bonding through holes over 50µm is possible but this requires a thicker bonding wire and an increase in the pad pitch resulting in a lower integration density.

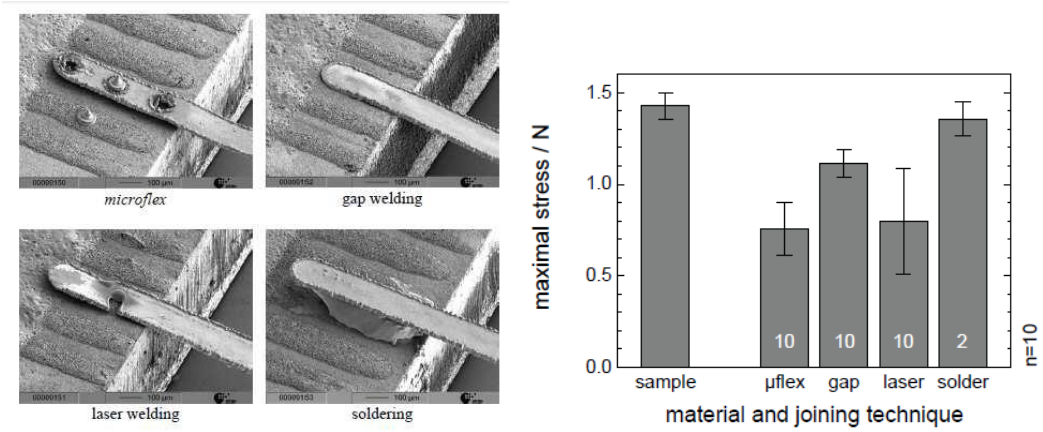


Fig. 8.4: Comparison of the relative strengths of interconnection technologies for neural implants[76]. Left; Examples of bending techniques used to conduct the tensile experiments, Right; Results of the tensile experiment[76].

The MFI technique was applied to bond PI 2611 with thicknesses of 10-15µm and pad hole size of 30µm to IC pads with 30µm width and 70µm pitch. A 25µm thick wire with a 35µm ball was used to obtain sufficient coverage of flexible pad metallization and a sufficient large area to successfully bond to the substrate underneath [70-71]. Studies have proved MFI to have very reliable and robust electro-mechanical Contacts under different test conditions. The resistances prior thermal/mechanical tests were around 100-200mΩ for a single bond. The resistances were measured again post thermal/mechanical tests and confirmed no bond failures[78].

The MFI has been implemented in different designs such as cuffs, sieves fabricated using PI as a substrate material. MFI was found to be the most suitable technique to bond to these devices after investigating their various characteristics such as impedance and flexibility. Ceramic substrates have been previously investigated as a potential carrier for electronics and wireless data transfer systems. They are also a suitable choice for biomedical implants as they are biocompatible[80]. It has been reported that MFI bonds withstand less maximum stress when compared to gap welding and soldering. However, MFI was not the main cause of failure. Stress graphs showed that stress concentration on the *via* hole in the flexible substrate material lead to mechanical fatigue resulting in bond failure. To solve this, the ratio of substrate material area to *via* hole area needs to be increased in addition to increasing the number of bonds to spread the stress over larger number of points which reduces the amount of stress each individual hole is subject too. These suggestions have led to serial connection scheme as shown in Fig. 8.4.

A long term study on microelectrodes connected to ceramic substrates using MFI, proved the ability of this technique to sustain long term implantation[75]. The MFI bonded region of the device was encapsulated in an epoxy (silicone) to guard the interconnects in the harsh physiological environment and act as a shock absorber against external forces. The impedance of the electrodes was measure pre-, during and post-implantation to investigate if the interconnects were still intact. The electrode impedance remained relatively constant over a course of 18 weeks suggesting no systematic degradation to the device and its interconnects caused by long term implantation[75]. This study illustrates the suitability of MFI for long term implantation in physiological media which means that it constitutes a perfect solution for the interconnection problems that we are facing with the SPNIs.

8.4. Integration of MFI into SPNI fabrication process

The SPNI design and fabrication process need to be optimized to incorporate the Microflex technique. The updated SPNI design that allows for MFI integration is illustrated in Fig. 8.5; the layers of the device need to be modified so that the connection

pads have via holes with the right dimensions that enable the use of MFI to ball bond through them. The device substrates were initially made using Pyralin 2611 which requires a dry etching process to etch the *via* holes for the MFI bonding. However, this was abandoned as Richard Barrett was able to develop a fabrication process for a sacrificial layer that is compatible with photo-sensitive polyimides [14], hence allowing us to use PSPI 7020 as a substrate for SPNI devices instead. PSPI 7020 has already been utilized for the fabrication of SPNI channels and can be simply patterned using photo-lithographic techniques negating the need to use a dry etch process to pattern the substrate. The subsections to follow will discuss in greater details modifications to the SPNI design and fabrication to incorporate MFI.

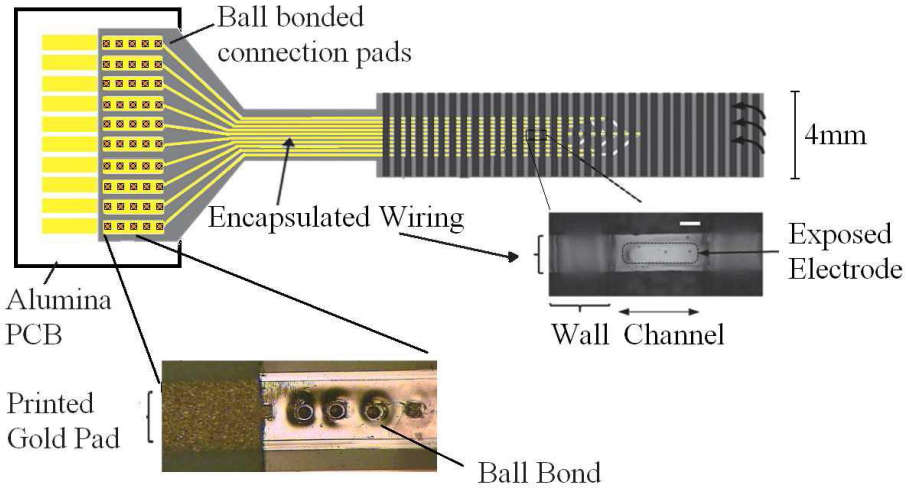


Fig. 8.5: Updated design of SPNI devices to incorporate Microflex Technique [17]

8.4.1. Fabrication of Pyralin test structures

To be able to establish a reliable durable Microflex connection we need to determine the substrate thickness that we can bond to without difficulty and the holes size that can make this possible. To do this, we have designed various test samples. The first set of test samples is where we vary the *via* holes size (bonding holes) from 20µmx20µm to 60µmx60µm in steps of 5µm. Ball bonding through samples with holes sizes less than

35µmx35µm was difficult, whilst this was easily achievable with samples that had via hole sizes between 45µmx45µm to 60µmx60µm.

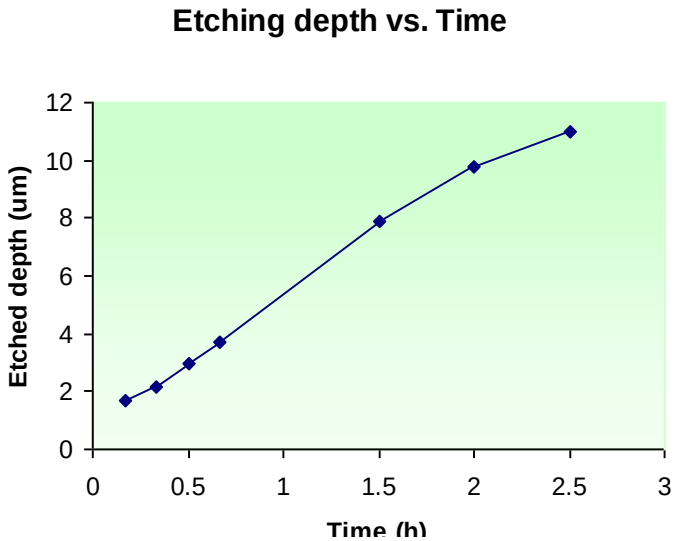


Fig. 8.6: Etch profile for Pyralin 2611 in oxygen plasma

Initially, we started fabricating the test samples using Pyralin 2611 as it was the material used to fabricate the SPNI substrate so far. The test samples for Pyralin were prepared by spin coating PI2611and fully curing the sample at 350^0C in a nitrogen free environment. An aluminium mask was used to prepare the PI samples for dry etching (using oxygen plasma). To prepare the aluminium mask a negative resist was patterned before thermally evaporating the aluminium layer. Lift off is then used to obtain the aluminium mask. The sample is transferred into an oxygen plasma etcher (barrel etcher) to etch the Pyralin holes. To establish the etch rate of Pyralin, the etched depth of the sample was checked after every 10 minutes in the initial first hour and every half an hour thereafter. The etched depth was recorded every time to the produce the graph in Fig.8.6. As it can be seen from the graph, the etching rate of Pyralin starts up slow at the initial 40 minutes and then speeds up after that. For example, it took half an hour to etch 3 microns of Pyralin at the beginning and two hours to etch through 10 µm of the layer at a later stage. After via holes have been etched in the PI, chrome and a gold layer have been thermally evaporated for the metal tracks and patterned to define the tracks. The samples were then aligned and bonded to bonding test target underneath (few bonds are shown in Fig. 8.7).

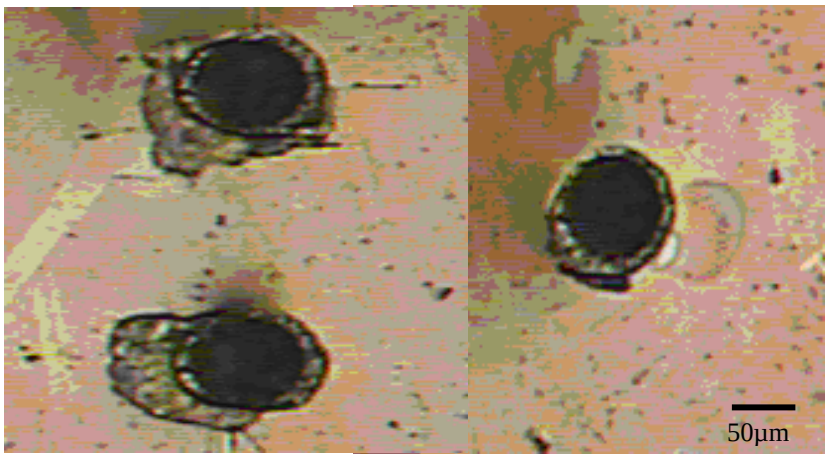


Fig. 8.7: Ball bonds on through a Pi2611 substrate

To check if the bonds have made electrical connections between the pads on the Pyralin (PI2611) and the test target we used a probe station to measure the resistance of these interconnects. The results are summarized in the table below. The first probe of the probe station was placed on the test target (as reference), whilst the second probe was placed at three different positions consecutively and this is to measure the resistance of the path between the first and the second probe. For the first position, the second probe was placed on a ball bond sitting directly on the gold test target. While the second position for the second probe was on ball bond riveting the pyralin(PI) through the via hole into the test target. The resistances for the paths of the first and the second position were found to be the same. Hence, the resistance for a gold ball bond riveting a Pyralin sheet through a via hole onto a gold test target underneath is the same as the resistance of a ball bond sitting directly on the same gold test target. Nevertheless, by placing the second probe on the gold pad on the pyralin sheet (the third position for the second probe), the measured resistance between the first and the second probe was 100mΩ to 125 mΩ. The resistance for this third path is expected to be higher than the resistances of the first two paths as the resistive path is longer for the third position of the probe. However the measured resistances (of 100mΩ to 125 mΩ) are still considered reasonable suggesting that the gold bond has succeeded (mechanically as well as electrically) in connecting the PI gold pad to the gold test target underneath.

Position of second probe	Resistance (mΩ)
Bond on Target	34-40
Bond on PI	33-45
Connection Pad	100-125

Table 8.1: Path resistances at various probe positions. The first probe is placed on the gold test target as a reference, whilst the second probe was placed at three different positions consecutively; the second probe is first placed on the bond sitting directly on the gold test target (bond on target), then it is placed on the bond riveting the pyralin through a via hole onto the gold test target underneath, and finally it is placed on the connection pad on the Pyralin substrate. The resistance of the path at each position is measured and the results are presented in this table

However, investigations into ball bonding through Pyralin2611 have not been taken further as work was being carried out by my colleague Richard Barratt to substitute the Pyralin2611 substrate with a photosensitive polyimide (Durimide7020)[42] equivalent. This is advantageous, as the PSPI substrate can be simply patterned using photolithography and does not require the use of a dry etching method unlike Pyralin2611. This makes the processing of the substrate much easier negating the need to cut around the SPNI device foot print, in addition to being able to neatly define the via holes for the MFI technique. However, as the photosensitive polyimide (Durimide7020) contains an internal adhesion promoter, the SPNI devices can no longer be released by manual peel off, and thus the use of a suitable sacrificial layer is required for the safe release of the devices. The investigation carried out by Richard Barrett, to choose a suitable sacrificial layer that is compatible with the fabrication process of the SPNI devices, is presented in the next section. The remainder of this chapter discusses the fabrication of the test samples based on the photo-sensitive polyimide (Durimide7020, Fujifilm Electronic Materials Electronic Materials), and the optimization of the MFI technique to ball bond to this material.

[42] Durimide 7020 (Fujifilm Electronic Materials) was selected as an alternative substrate material to Pyralin2611, because it has a suitable thickness range which allows various substrate thicknesses to be made. In addition the biocompatibility of this material has already been investigated as it is used to fabricate the implant micro-channel layer.

8.4.2. Investigation of sacrificial layer[43]

Silicon wafers are used as a carrier substrate to fabricate SPNI devices and they have extensively been used for over 3 decades in the fabrication of MEMs. Pyralin has frequently been used as a substrate in flexible polyimeric devices because of its desirable material properties and the ability to peel it off the carrier wafer in the case of SPNIs. However it is not photosensitive and hence cannot be photolithgraphically patterned. PSPI, on the other hand can be patterned using photolithography but cannot be used as a substrate without a suitable sacrificial layer. The PSPI contains an internal adhesion promoter which makes it adhere very well to the carrier wafer, and therefore can no longer be peeled off manually. Thus a suitable sacrificial layer is required to be able to release the devices at the end of the fabrication process.

Releasing micro-machined devices has been a common issue in many micro-machining applications and hence has widely been investigated in the recent year. A large number of sacrificial layers are available ranging from metal to semiconductor insulators. The most common method of removing a sacrificial layer is wet etching and dissolution in an appropriate solvent. This method will take a long time to release devices/structures with large surface area as it is heavily diffusion dependant and the solvent will take time to etch away the sacrificial layer starting from the edge as is the case with the SPNIs.

Investigation into a suitable sacrificial layer compatible with PSPI fabrication processes was conducted by my colleague Richard Barrett. Aluminium was first investigated as it has previously been used as a sacrificial layer for Pyralin and hence was supposed to be compatible with other SPNI processing steps. 300nm Aluminium layer was thermally evaporated onto a silicon wafer. A thin adhesion chrome layer was evaporated first before the Al. After fabricating the PSPI layer, the wafer was placed in MF319 to remove the sacrificial layer. After 72 hours in the MF319, the devices were still not released and the PSPI was severely damaged by the solution as shown in Fig. 8.8. Hence, using Al as a sacrificial layer for SPNI devices was abandoned and other options were explored.

[43] This section is based on [17] R. Barrett, "Novel Processing Routes for Neural Interfaces, " Ph.D., The University of Birmingham, 2013.

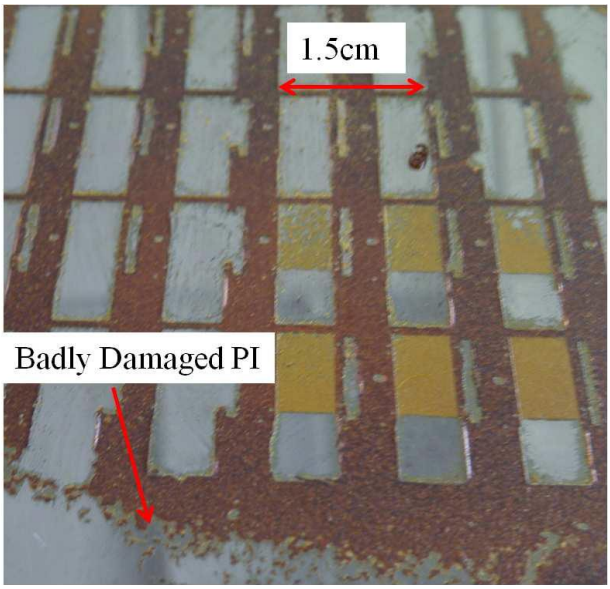


Fig. 8.8: Failed release of the PSPI structures on Aluminium[17]

Poly-methyl-methacrylate (PMMA) is an organic resist that is commonly used as a sacrificial layer in many micro-machining applications such as the fabrication of flexible bio-sensors. Studies suggest that PMMA is compatible with polyimide but do not make a reference to photo-sensitive polyimide. Special considerations need to be taken into account when integrating the PMMA into the SPNI fabrication process. These considerations include:

1. PMMA becomes porous once exposed to UV light. This increases the etch rate during development but can potentially cause problems during the full curing step. The Exposed PMMA shrinks at room temperature over time and the shrinking rate increases with temperature leading to cracks in the PMMA layer which can potentially affect any further fabrication. So PMMA should not be based at temperatures higher than 150^0C during the SPNI device fabrication.
2. The volatile gases produced by PMMA during UV exposure can be trapped between the PMMA and the PSPI substrate layer causing delamination and bubble defects. This effect can be reduced by baking PMMA in an incremental fashion, i.e. increasing any subsequent baking steps relative to the previous step which agrees very well with the slow ramp baking regime of the SPNI devices.
3. PMMA has tendency to absorb water and IPA which causes swelling and hence tension between the layer interfaces leading to adhesion failure. This problem can

be minimized by reducing the amount of water and IPA used during the development of SPNI.

4. Cleaning the wafer with Acetone and IPA before spin coating the 1st layer is avoided as acetone can attack the PMMA layer. The dehydration bake at 150^0C is also skipped as it is not compatible with PMMA. The substrate is cleaned using combination of oxygen plasma and UVO surface treatment.
5. Normally a less than 1µm thickness is chosen for the PMMA layer, however in the case of SPNI process, the PMMA sacrificial layer needs to be thicker to survive the prolonged exposure polyimide solvents and oxygen plasma etching. Hence a 3 µm thickness is chosen.

To prepare the PMMA sacrificial layer for the SPNIs[44], the material was spin coated and baked at 180^0C for 10 minutes. PSPI samples with various thicknesses were prepared by spin coating at different speeds and patterned using photolithography after which they were fully cured. Apart from a slight curl of the PSPI layer around the wafer periphery, the samples cured fine. The samples were then released by soaking the wafer for 24 hours in a mixture solution of MIBK and IPA at a ratio 3:1. The samples were peeled off from the wafer using a razor blade and tweezers while wetting the samples with IPA [17]. The result is well defined structures; hence a 3 µm PMMA layer was adopted for further application. Fabricating SPNIs with PSPI substrate are possible since PMMA sacrificial layer can be used to release the devices. Being able to do this means that making test samples to explore incorporating MFI as a connection technology for SPNI, is easier.

8.4.3. Fabrication of test structures based on PSPI

The PSPI samples are fabricated by spin coating the PSPI and photo-lithographically patterning the layer to etch away the holes[45]. The layer is then fully cured at 350^0C in a nitrogen environment. The test samples were designed to have hole sizes ranging from 30 to 60µm in increment steps of 5µm. This is to define which bonding hole sizes are most

[44] The process was developed by Richard Barrett

[45] Fabrication process followed to fabricate the PSPI test samples is similar to the process used to fabricate the SPNI channels

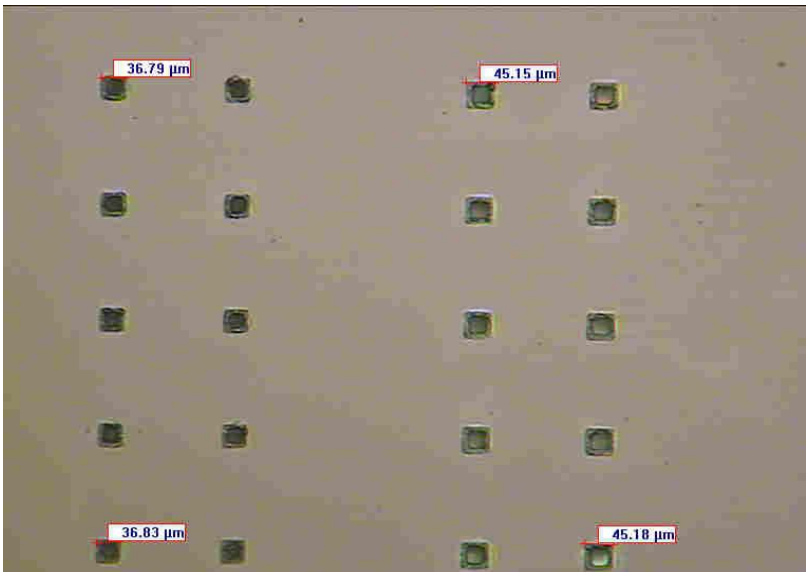


Fig. 8.9: a test sample base layer fabricated using PSPI7020

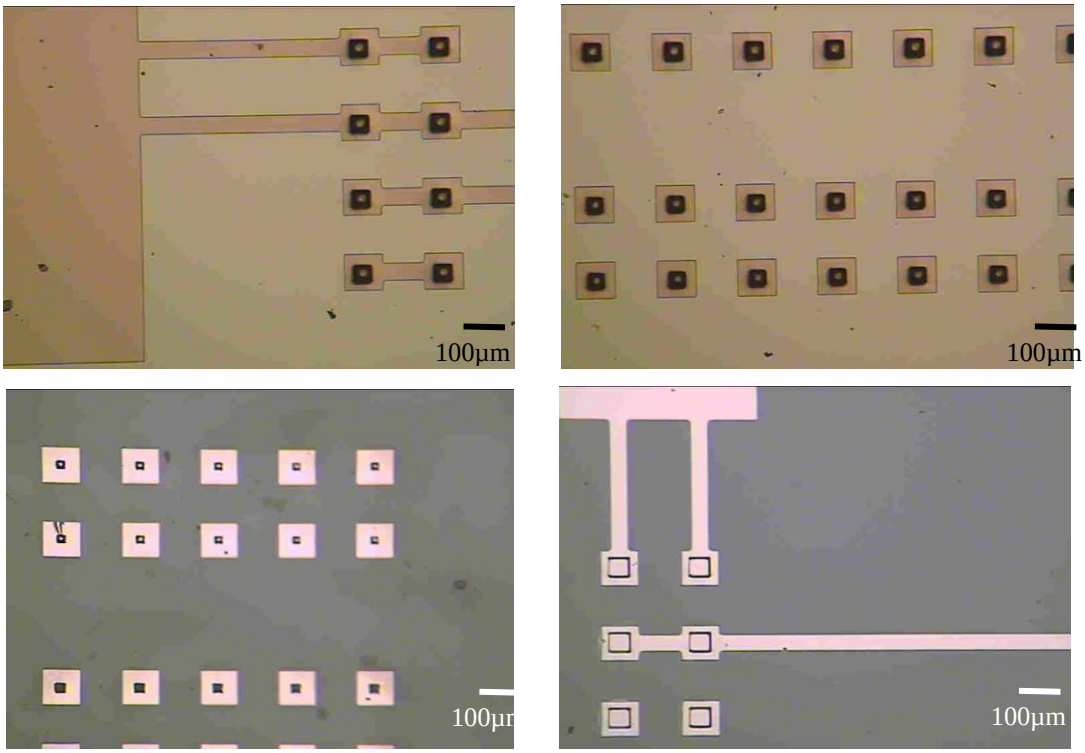


Fig. 8.10: - Top Patterned S1813 layer on a gold layer for two different samples, Bottom- patterned gold/chrome layer on two different samples, S1813 layer is washed off.

suitable and easy to bond to. To determine the hole sizes suitable for bonding, the thicknesses of the PSPI samples were initially limited to 12 µm. A 4'' silicon wafer was cleaned using Acetone and IPA and baked at 150^{o}C for 5 minutes for dehydration. A

3 μm-thick layer of PMMA was spin coated and baked at 180^{o}C for 10 minutes. This was followed by spin coating a layer of Durimide7020 (a photosensitive polyimide, PSPI) at 4000RPM for 60 seconds (for 12 μm thick layer after full cure). For substrate layer thicknesses in the range of 10 μm to 40 μm, spin speeds in the range of 1200 to 5000RPM need to be used. The spin coated PSPI layer is then softbaked at 70^{o}C at 5 minutes on a programmable hot plate, and then at 95^{o}C for another 5 minutes. After the wafer had cooled for at least 20 minutes, it was exposed using a Canon mask aligner for 12 seconds. The sample was then developed using combination of developer/rinsing solvent (HTR D-2 and RER600). To prevent premature release, the amount of developer/solvent used was minimised by using a spray technique through a thin nozzle. The wafer was sprayed with the HTR D-2 developer for 1 minute followed by a developer/solvent (50/50 ratio) mixture spray for 10 seconds. The sample was then sprayed by the RER 600 solvent for about 1minute. These developing steps are repeated until a clear pattern is formed (Fig. 8.9).

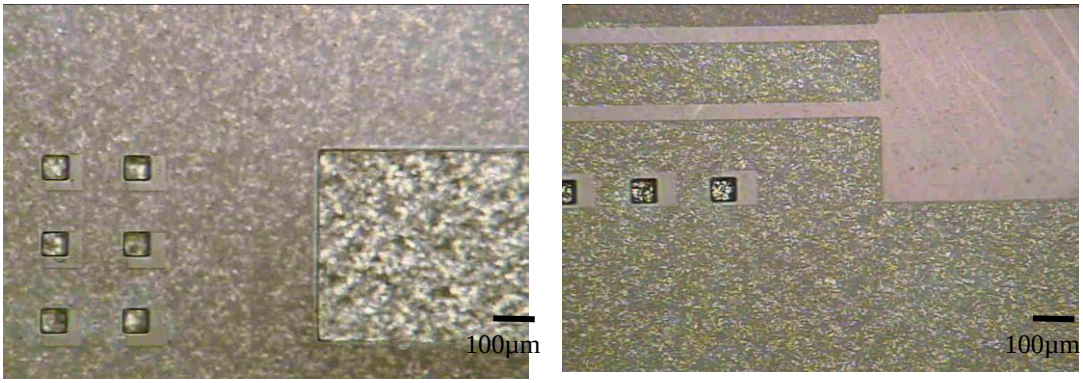


Fig. 8.11: 1 released samples placed on a gold printed substrate (underneath) ready to be ball bonded

The metallisation layer for the contact pads was prepared by thermally evaporating Chrome/Gold layer on the PSPI substrate (with the chrome layer acting as an adhesion layer for the gold). A photoresist S1318 mask was prepared and used to pattern the metal layers. The sample wafer was placed in a gold and then a chrome etchant to etch away the metal layers in unwanted regions and form a clear pattern (see Fig. 8.10). Both partially cured and fully cured samples were prepared according to the polyimide curing curve presented in section [6.1.8] of chapter [6] to see what effect curing has on ball bonding

through PSPI. A 10 minute oxygen plasma clean was performed using an oxygen plasma barrel etcher to de-scum the sample and remove any polymeric residues.

The PSPI test structures were released from the PMMA sacrificial layer by placing the samples in MIBK:IPA (Methyl-iso-butyl Ketone) at a ratio of 3:1 for at least 24 hours. The samples are then peeled from the wafer using a razor blade and IPA. After rinsing and drying the samples, bonding based on the MFI technique can be carried out. Fig. 8.11 shows an example of two different samples ready for ball bonding.

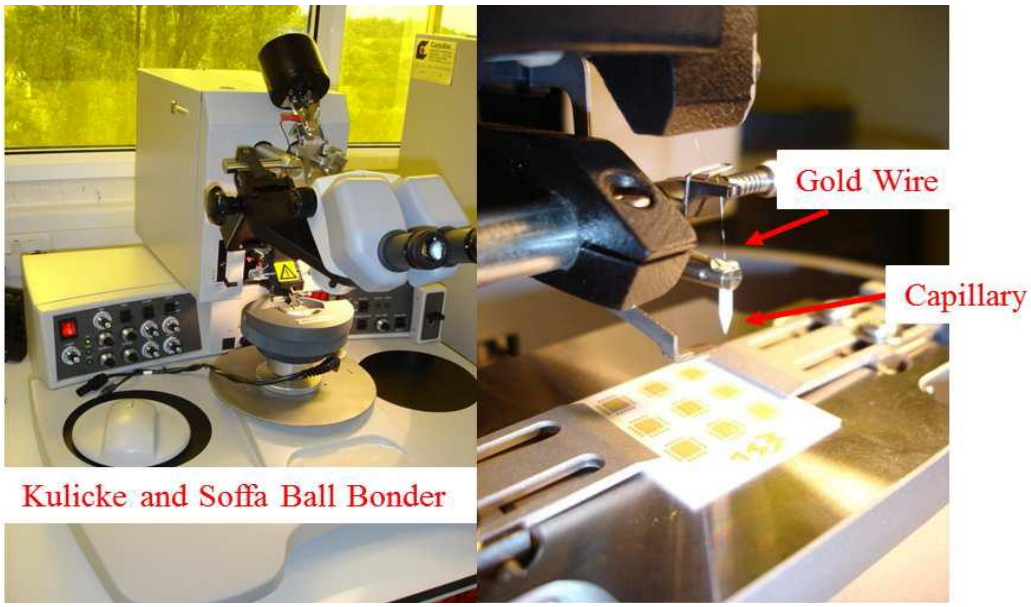


Fig. 8.12:The Kulicke and Soffa gold ball bonder

8.4.4. MFI ball bonding of the test structures

The test samples are then bonded to gold printed alumina substrates through a via hole using a manual wire bonder (Kulicke and Soffa, Model 4522 whose photo is provided in Fig. 8.12) and a 25 micron gold wire. The gold printed alumina substrates were designed in house and fabricated externally by ESL Europe. The MFI bonding was successfully performed on different PSPI test samples. Fig. 8.14 shows SEM pictures of bonds riveting a PSPI onto a gold printed substrate through a *via* hole. The indentation of the PSPI substrate surface around the contour of the bond confirms that the micro-rivet bond presses down on the flexible substrate to make a physical and electrical connection

through the hole with the underlying bonding target. The gold metal tracks for test samples can also be clearly seen. Fig. 8.14 (bottom right SEM image) shows how the gold ball is conformed through the hole thermosonically to make an electro-mechanical connection between the connection pad on the PSPI 7020 substrate and the gold printed test target.

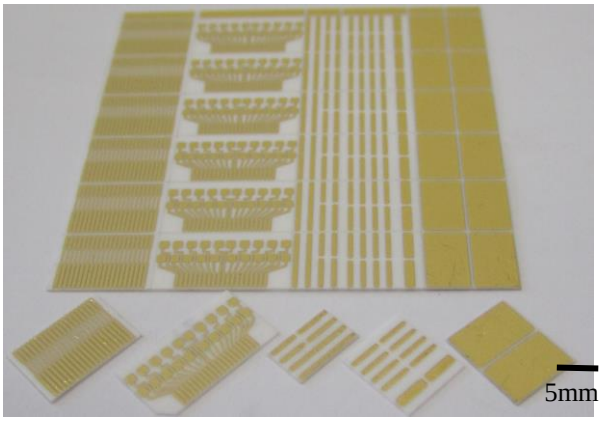


Fig. 8.13: Alumina gold printed bonding targets (substrates)

8.4.5. Varying the thickness of the SPNI

MFI studies reported reliable bonding to polyimide thicknesses between 10 -15µm and these were mostly with Pyralin [73]. However, polyimide thicknesses to be used in this thesis may not necessarily be the same and the PSPI material may have different properties that can influence the maximum bonding thickness. Hence investigating the PSPI thicknesses that can be reliably bonded was important.

To find out the photo-sensitive (PSPI) maximum bonding thickness, different PSPI thicknesses ranging from 10 to 40µm were prepared. These thicknesses were selected to accommodate for the substrate thicknesses recommended by the neutral plane calculations presented in the stress models in chapter 5 sections[46] [5.4.3] and [5.4.5]. The PSPI test

[46] The neutral plane calculations in the initial stress model presented in chapter 5 section [5.4.3] recommended a 35 μm to place the metal layer in the neutral plane of the rolled SPNI structure. The corrected stress model presented in section [5.4.5] corrects the initial model and hence gives more accurate representation of the strains in the rolled structure. This model recommends that the neutral plane position is halfway the substrate layer and hence metal layer will always be under some compressive strain. Hence the substrate layer that is thick enough to provide a durable implant substrate is what is required, and so thicknesses in the region of 12 μm to 20 μm were suggested

samples were prepared by first spin coating the material onto PMMA coated wafers. The samples were patterned using photolithography and then released without cure. The samples were then manually aligned and bonded to gold printed alumina substrate (shown in Fig. 8.13). The ball bonds were performed using ball bonder model shown in Fig. 8.12 (Kulicke and Soffa, Model 4522) and a 25µm gold wire. The size of the ball bonds could be varied using the setting on the ball bonder but for consistency ball bond size was kept between 65-68 µm diameters as recommended by supplier of the wire bonder.

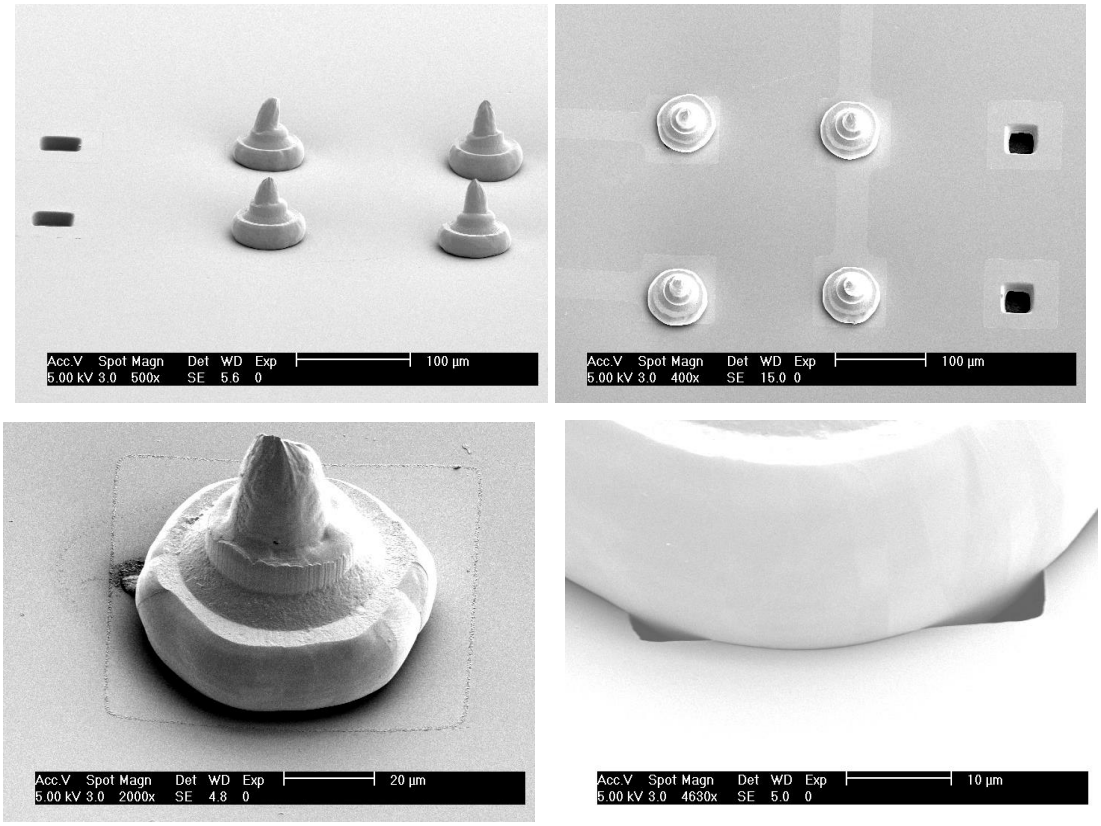


Fig. 8.14: SEM micrograph of ball bonds through PSPSI samples, Top- ball bonds on different test sample designs, Bottom- a zoom into two ball bonds

It was difficult to bond to the uncured PSPI samples because of the elasticity of the material. The bonding force is able to deform the PSPI sample and the ultrasonic energy is then transferred back into the ball bond resulting in an inability to bond to the sample. This is why polymeric material is considered incompatible with the ultrasonic bonding techniques. To reduce the elasticity of the PSPI and hence improve the ability to bond to it the samples need to be fully cured first before attempting to ball bond to them.

So the next set of samples was prepared to have different thicknesses after full cure (thicknesses ranging from 10 to 40µm). Given a suitable hole size it was easy to ball bond samples with substrate thicknesses of less than 20µm, but as the thickness approaches 20µm, ball bonding was becoming very challenging. Substrate thicknesses above this value make it difficult for the ball to reach the bonding target (alumina) through the connection. This agrees with studies of MFI technology conducted earlier. Therefore, thicknesses of no more than 20 μm need to be used to be able to bond to the samples with the MFI technique.

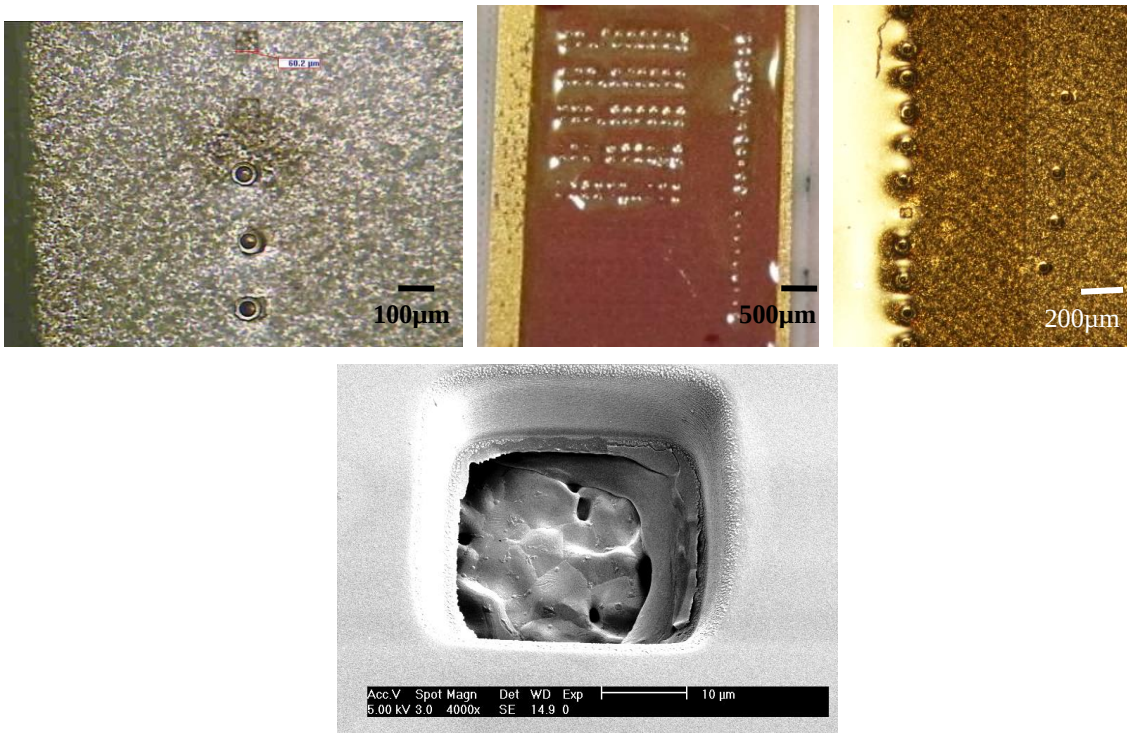


Fig. 8.15: Bonding through different hole sizes, Top right – bonding through different holes sizes on PSPI samples, Bottom- SEM micrograph of a via hole in the PSPI samples (PSPI residues can be seen at the base of the hole)

8.4.6. Varying *Via* hole sizes

The effect of varying the *via*-hole size on ball bonding was investigated after the substrate thickness suitable for bonding has been established. Hole sizes from 30 to 60µm were photo- lithographically defined into the PSPI layer (Fig. 8.9). The same bonding

parameters (which included the bonding force, bonding time and size of ball) were kept the same for consistency. Fig. 8.16 shows an example of ball bonding through different hole sizes. It was not possible to bond through holes smaller than 35µm square. For the PSPI samples a closer look at the holes under a microscope revealed that holes smaller than 35µm square are under-developed as the solvent cannot effectively wash out the PSPI material.

This is illustrated in Fig. 8.9 in which the under-developed PSPI areas are darker. Fig. 8.15 (Bottom right) gives a clear view of some lining residues left in a 35µm square hole due to ineffective development of the hole. This makes ball bonding through these holes difficult. The problem can be solved by performing a de-scum on the samples before release. Ball bonding is more difficult with holes less than 30µm as the *via* hole area is too small to successfully make an electro-mechanical connection. It was easy, however, to bond to hole sizes greater than 45µm square. Hence, substrates were fabricated to have thickness of less than 20µm with hole sizes of 45, 50 and 60µm square. The PSPI samples are fully cured before ball bonding is attempted.

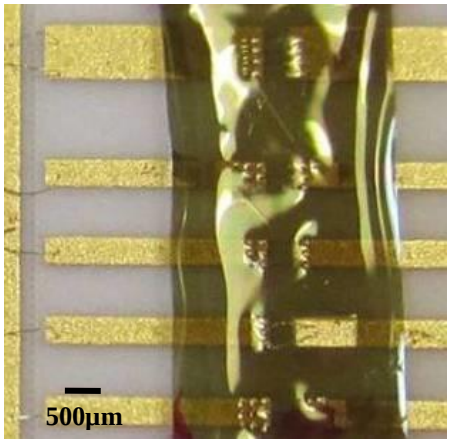


Fig. 8.16: A PSPI sample example to test and measure the resistance of the ball bonds.

8.4.7. Testing of the electrical conductivity of the interconnects

To test that Microflex connections are electrically conductive, samples were designed and fabricated from both PSPI. After aligning the samples to gold printed alumina (shown

earlier in Fig. 8.13), the samples were ball bonded as illustrated in Fig. 8.16. The resistance of the bonds was measured and they were all found to be conductive. The resistance of single bond was around 100 to 200 mΩ which agrees very well with figures reported from earlier studies [70-71].

8.5. Chapter Summary

This chapter has investigated the possibility of using the Microflex interconnection technique (MFI) to establish a durable and reliable method of connecting to the SPNI devices. The first part of the chapter discussed the requirements and the importance of finding a suitable interconnection method to the SPNI devices that would allow electrical connection to be established between the implants and the external circuitry. To be able to use the implant for any long term application and record from the 20 available micro-channels (microelectrodes) simultaneously, practical and durable connections between these implants and the external electrodes needs to be developed.

The current connection method used to connect the devices was also explained alongside its limitations. An overview of why MFI was chosen and the operational principle behind this technique was also described. The remainder of the chapter then discussed the integration of MFI into the SPNI devices. This was achieved by fabricating test structures to investigate the thicknesses and the sizes of the *via* holes that the MFI technique could bond through. In summary, it was found that:

- The PSPI substrate samples needed to be fully cured before ball bonding is attempted. Otherwise ball bonding (using MFI) will fail
- For a suitable substrate thickness (selected to be $12\,\mu m$), ball bonding through hole sizes in the range of 45 µm to 60 µm was straightforward. Whilst it was very challenging to ball bond through hole sizes smaller than 45 µm square. Increasing the *via* hole size beyond 60 µm is of no use, as the hole size will become too large for the ball bond to act as a micro-rivet between the gold printed alumina substrate (or the integrated Circuitry IC) underneath and the flexible polymeric cable with connection pads (that have a push through via hole in their centre).

- Given a suitable hole size it was straightforward to ball bond samples with substrate thicknesses of less than 20µm, but as the substrate thicknesses approach 20µm, ball bonding became very challenging. Substrate thicknesses above this value make it difficult for the MFI gold ball to reach the bonding target (alumina) through the *via* hole of the connection pad. Therefore, the substrate thickness needs to be limited to 20 μm for the ball bonding to succeed with MFI.

Now that the interconnection method has been established, the next chapter will present and analyse the Electrochemical Impedance Microscopy (EIS) data obtained for different SPNI devices. This is mainly done to access the success of the fabrication process (and the interconnection method) in addition to the intactness of the metal layer of the SPNI devices post rolling.

9. CHARACTERISING THE SPNI DEVICES VIA IMPEDANCE SPECTROSCOPY

9.1. Introduction

As mentioned in the methods chapter Electrochemical Impedance Spectroscopy is performed on the fabricated implants to access the success of the fabrication process and the intactness of the implant wiring post rolling. EIS was also used to test and validate the incorporation of the Microflex interconnection (MFI) technique into the fabricated devices, in addition to characterising the electrode/electrolyte interface of the implants' micro-electrodes. The method's chapter has already discussed how EIS is carried out to characterise the SPNI implants. This chapter will aim to analyse the data obtained from EIS for the various SPNI devices. This is done by organising the chapter into two main parts; the first part of the chapter will seek to derive an equivalent circuit model for the electrode/electrolyte interface, whilst the second part will seek to analyse and compare the impedance data obtained experimentally (for various SPNI devices) against the derived equivalent circuit model.

Normally, once the EIS is performed, the data is fitted against an equivalent circuit model for analysis. Mostly, common electrical components such as resistors, capacitors, and inductors are used to create the equivalent model. The selected elements normally represent a physical element in the electrochemistry of the system. For example resistor is normally included in the model to represent the solution resistance. Thus, it is useful to have knowledge of the impedance of the commonly used elements how they translate in the impedance and phase spectra. This will be discussed in the following section in greater detail.

9.2. Modelling Overview-Extracting Model parameters from Data[47]

When it comes to analysing EIS data, it is generally done by a form of data fitting. The analyst attempts to match the measured data to a model with a similar looking impedance spectrum. The degree to which the model's impedance spectrum agrees with the measured EIS data depends on the type of the electrical components constituting the equivalent circuit model and their values. The shape of the model's impedance spectrum is determined by the type of electrical components used and their connection arrangements in the equivalent circuit. So, the sizes of the spectrum features are dependent on the values of the model parameters such as the resistance value of a resistor.

Models used in EIS can be physical, partially or completely empirical (experimental). In physical model, the components used in the equivalent circuit are assumed to represent a physical process in the electro-chemical cell. Often, there is more than one possible equivalent circuit that can be used to describe a given spectrum and hence one cannot assume that an equivalent circuit that fits well into the data spectrum is an accurate representation of the physical model of the cell. Normally, the selection of which equivalent circuit gives the most truthful representation of the actual cell processes is based on knowledge of the physical characteristics of the electro-chemical cell. Even when physical models represent a good fit to the measured data, they should be verified, whenever possible. One way to do this is by altering a single cell component such as increasing surface area or thickness and observing whether the effect this has on the impedance spectrum matches expectations.

On the other hand, in the partially or completely empirical models, the circuit components do not necessarily represent a physical process in the electro-chemical cell. The model is chosen so that its impedance gives the best possible match to the measured impedance. These models can be constructed by subtracting components from a spectrum in a successive manner. If the spectrum is simplified by the subtraction, then the component is added and the same is done with next component impedance until the spectrum is

[47] This section is based on application notes titled: Basics of Electrochemical Impedance Spectroscopy

completely gone. Empirical models can give a good fit of data to a model but their elements may not relate to the cell processes being investigated. Hence, whenever possible, physical models are generally preferable to empirical models. The equivalent models that will be discussed in the following section, do not necessarily represent physical behaviour, as is the case for the Constant Phase Element (CPE), but offer a practical method for interpreting the behaviour of an electrode interface.

9.3. Modelling of Impedance spectra[48]

Once the EIS has been carried out, the measured data has to be fitted to a suitable equivalent circuit model to determine the values of the components constituting the model. As the complexity of the fitting increases with the number of the model components, one should analyze the data before fitting to suggest possible interface components and speculate their potential values. This subsection will discuss the influence of equivalent circuit components on the impedance plots. The modelling of the spectra shown here is based on the work of Andreas Frommhold[5].

When modelling an electrode/electrolyte interface, one has to consider the solution resistance for the current path, and the double layer interfacial capacitance forming between the electrode and its surrounding electrolyte. Hence the simplest model for an electrode/electrolyte interface is a series combination of the solution resistance and the double layer capacitance. This assumes that very high charge transfer resistance prevents a direct current path.

In EIS experiments, double layer capacitors never behave ideally. They rather act like a constant phase element (CPE)[49] defined by the following equation:

$$Z_{CPE} = \frac{1}{Q_0 (j\omega)^n} = \frac{1}{Q_0 \omega^n} \exp(-j\frac{\pi}{2}n) \qquad \text{(Equ. 9.1)}$$

[48] This section is based on the modelling conducted by Andreas Frommhold in [5] AFrommhold, "Nanotexturisation of Gold Surfaces and its Application to Neural Implants," Ph.D., The University of Birmingham, 2010.

[49] It is called constant phase element as the phase element of the impedance Z_{CPE} does not vary with frequency but only depends on the value of n as can be seen from Equ.9.1.

Where n is an empirical constant having values between 0 and 1. Surface roughness is assumed to be the reason behind the non-ideal capacitive behaviour of the interface. The value of n provides a measure for this surface in-homogeneity where only for $n=1$ an ideal capacitance is present and ($Q_0 = C$). The deviation of Q_0 from the ideal capacitor C is presented in the values of n. The effect of n on the impedance and phase plots is illustrated in Fig. 9.1.

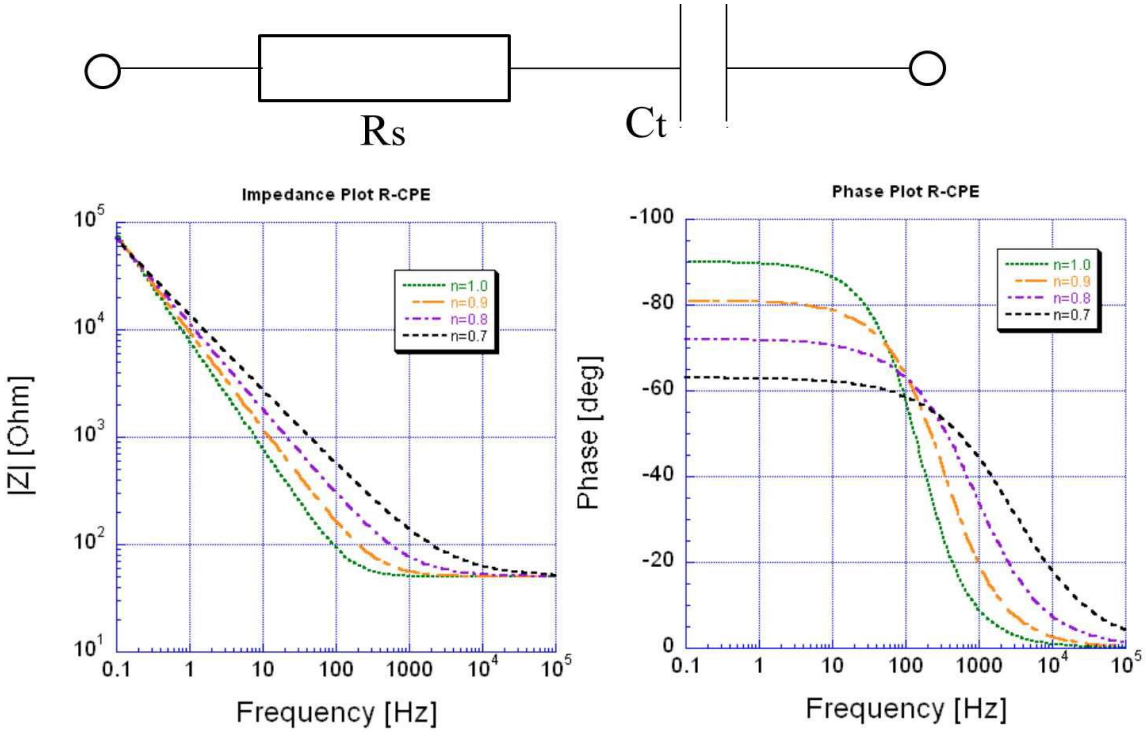


Fig. 9.1: Modelled impedance and spectra for a constant phase element (CPE) in series with a solution resistance. The plots show the effect of varying the surface properties of the electrode by assigning different values to the imperical constant n which is a measure for the surface roughness of the electrode [5]. The plot for the value of n=1 represents the behaviour of an ideal capacitor. As n value decreases, the slope of the frequency dependant part of the impedance plot changes and the cuff off frequency shifts to higher frequencies, whereas the phase drops from -90^0C for ideal capacitance (n=1) to lower values for decreasing values of n.

There are many factors influencing the value of the double layer capacitance such as electrode potential, temperature, ionic concentrations, types of ions etc. Normally an estimate of 20 to 60 μF of capacitance for every $1cm^2$ of the electrode area is assumed [81]. For the modelling, Frommhold in [3] assumed an interfacial capacitance $C = 20\,\mu F$

and a solution resistance $R_s = 50\,\Omega$. Although these parameters might be different in the neural interfaces presented in this thesis, the model can be used qualitatively to draw conclusions on the behaviour of the interface. The micro-electrodes of the SPNI devices have a surface area that is 1000 smaller than surface area of the electrodes being simulated in the model. Therefore, it is expected that the impedance of the SPNI electrodes will be at least 1000 times bigger than the impedance of the modelled electrodes.

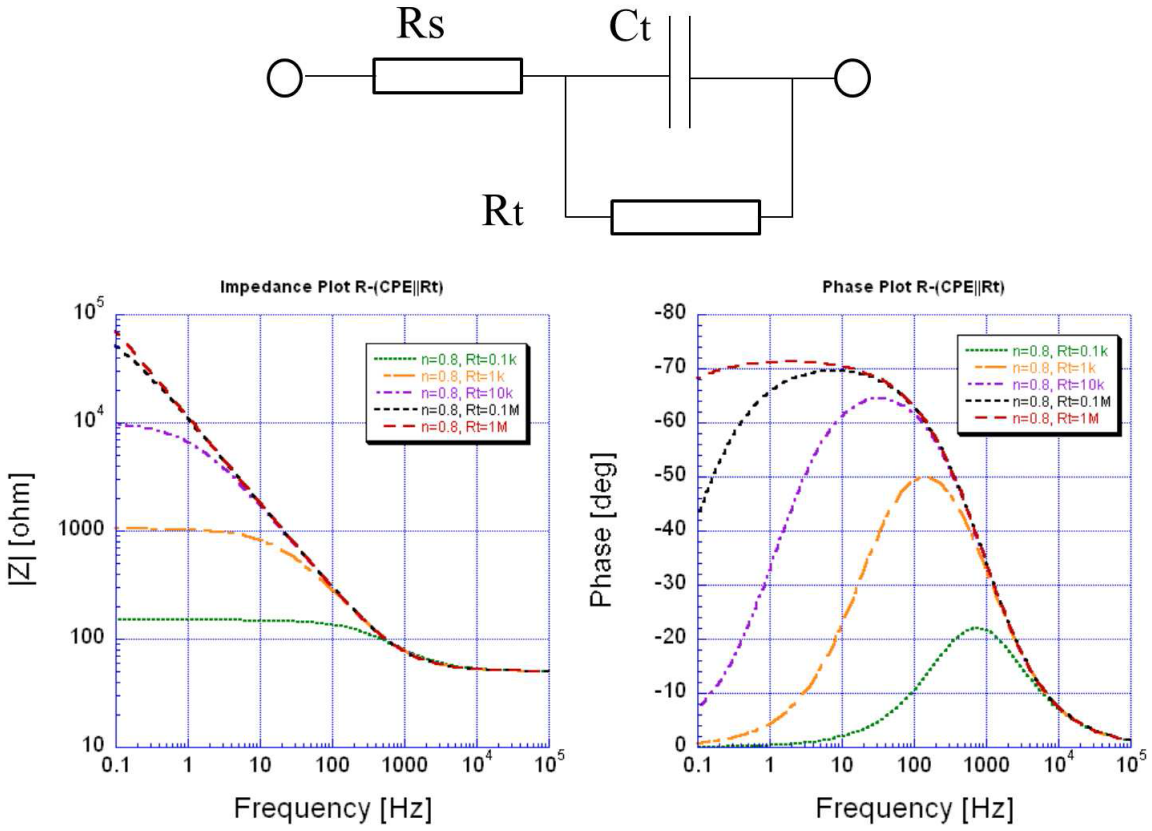


Fig. 9.2: Modelled impedance spectra of a simple electrode interface, showing the effect of varying charge transfer resistance on the electrode interface[5]

With lower n values, the frequency dependent part of the impedance spectrum are less steep (reduced gradient) and the cut off frequency shifts to the right at higher frequencies with the solution resistance dominating at this region (the impedance value levels off at the solution resistance value of 50 Ω). The phase spectrum shows clearly the effect of surface roughness on the interface behaviour. At low frequencies, the phase starts at -90^0 for the ideal capacitor case (n =1). The starting phase value is lower for lower values of n.

The plateau seen at higher frequencies is delayed and is less defined as the cut off frequency has shifted to the right and the frequency at which the phase value reaches 0^0 is higher for lower values of n.

The model is extended to include the charge transfer resistance in parallel. This resistance provides a current path at low frequencies where the capacitive impedance is very high. As it can be seen from the impedance spectra in Fig. 9.2, the resistance R_t dominates at low frequencies where the total impedance levels at the value of R_t before the capacitive effect takes over as frequency increases and converges to the series resistance (R_s). The impedance spectra are relatively unaffected for high charge transfer resistance, as the current avoids travelling through this high resistance path. Lower values of the charge transfer resistance attract the current to travel through the resistive path and hence the charge transfer resistance dominates the impedance spectra at low frequencies. These effects are further articulated in the phase spectra. At low frequencies and for low charge transfer resistance, the phase tends to a perfectly resistive value (0^0) allowing the resistive path to dominate. The capacitive effect becomes more apparent at mid-frequencies before the phase returns again to zero at high frequencies allowing the series resistance to dominate. The effect of high charge transfer resistance is less pronounced at low frequencies as the current shuns away from travelling through this highly resistive path and is hence obliged to travel through capacitive path. The values of R_t are selected to illustrate the various effect of R_t on the system's behaviour ranging from considerable influence for low values to negligible effect for high values.

As a final component, the Warburg impedance (Z_w) is added to the circuit model in series with the charge transfer resistance. This series combination is justified by the diffusion processes limiting the amount of charge transfer possible at a time. The Warburg impedance is a frequency dependent diffusion element with a constant phase of -45^0. The value of the charge transfer resistance is chosen to be $1000\,\Omega$ as the Warburg diffusion resistance can only be of significance if the reaction rate is large enough. The value of n was set to 0.8 for a more practical electrode/electrolyte interface. Fig. 9.3 illustrates the effect of varying the Warburg impedance on the impedance and phase spectra. Normally

the resistive path dominates at low frequencies whilst the capacitive path dominates at high frequencies. However, for values of the Warburg impedance higher than the capacitive branch, the effect observed on the spectra is negligible as the current is less inclined to travel through this highly resistive path. This blocks the effect of the charge transfer resistance and the capacitive path becomes the prominent element with a phase closer to -90^0C. On the other hand, for lower values of the Z_w the steady level observed when only a charge transfer resistance is used (Fig. 9.2) is substituted by a steady gradient demonstrating the frequency dependency of the Z_w at low frequencies. As we move on to smaller values of Z_w, the curve becomes dominated by the charge transfer resistance (R_t) with a phase close to zero as can be seen from the phase plot in Fig. 9.3. As Z_w raises the phase tends towards -45^0 which is the native phase of Z_w. As the frequency increases, the capacitive path dominates allowing the value of the impedance to tend towards and level off at the solution resistance R_s.

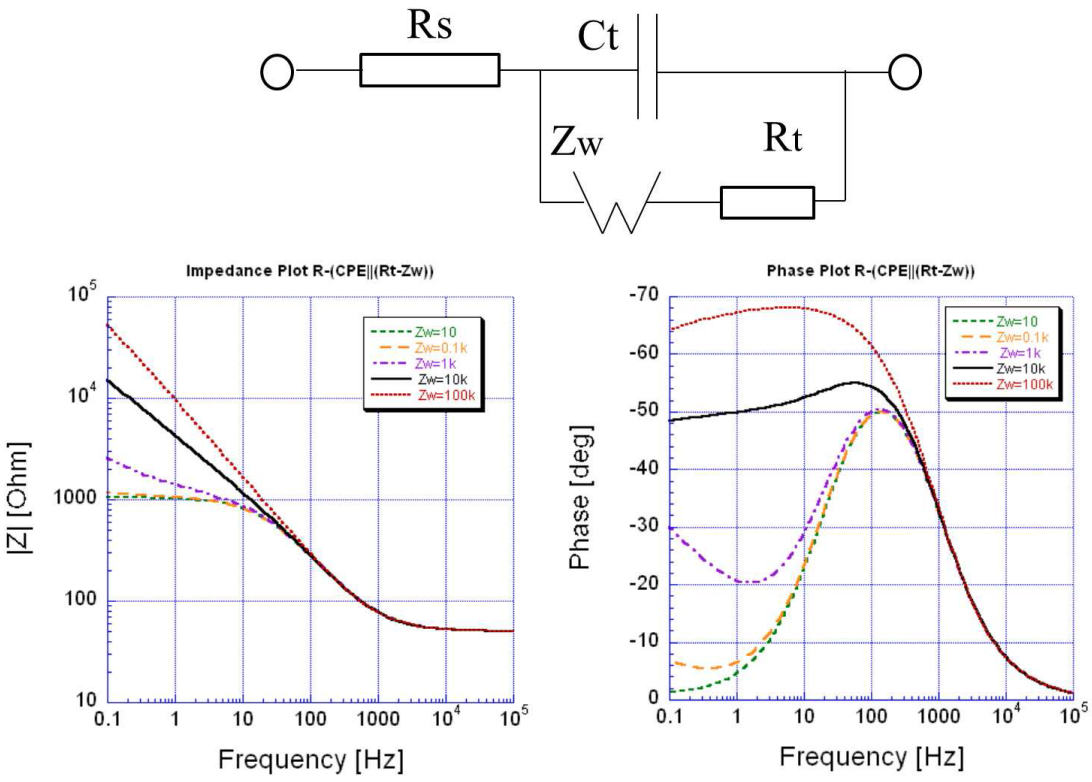


Fig. 9.3: Modelled Impedance spectra of a simple electrode interface, showing the effect of varying the Warburg impedance on the electrode interface[5]

9.4. Analysing the impedance measurements

The EIS was performed on the SPNI devices as discussed earlier. Impedance and phase spectra were obtained for devices before and after rolling. The data presented in this section is for devices from two different batches (batch 1 and 2) containing 8 devices each[50]. Fig. 9.4 shows the impedance spectra prior and post rolling for two different SPNI electrodes. As it can be seen, the impedance spectra post rolling have a similar behaviour to the spectra prior rolling. The spectra have high impedance at low frequency which decreases in almost linear fashion as frequency increases until about 3KHz where the two curves diverge slightly. This suggests that the interfaces on the rolled and unrolled samples have a capacitive behaviour which can be confirmed by analysing the corresponding phase spectra shown in Fig. 9.5.

For the unrolled electrodes, the phase starts at about -70^0 and increases to reach -50^0 at 1KHz frequency. It then decreases as frequency increases until it reaches -70^0 at 10KHz. The phase picks up again to -50^0 at 100KHz. The rolled sample phase appears to behave in an opposite manner where its value ranging from -35^0 to -49^0 suggesting that this interface is not an ideal capacitor but incorporates other elements as such as resistors and the Warburg impedance as demonstrated in the modelling section above. The impedance and phase spectrum of the device prior and post rolling confirms that the electrodes are still functioning and the rolling strain did not cause mechanical failure of the SPNI wiring. Fig. 9.4 also shows a slight increase in the impedance of the sample after rolling, where the impedance was at $286\,K\Omega$ prior rolling and increased to $362\,K\Omega$ post rolling. The mean measured impedance at 1KHz post rolling was $433\,K\Omega$.

Rolling the devices transforms the channels from 2D open roof channels into 3D channels with a closed roof. The microelectrodes become housed in a closed channel that is only accessible from channel ends. This therefore affects the path of the current flow and leads to an increase in the solution resistance. Other factors affecting solution resistance include ionic concentration, types of ions and temperature. The important determining factor

[50] This is the current device yield per wafer. Hence, each batch will have 8 devices in total that have been processed on the same carrier wafer.

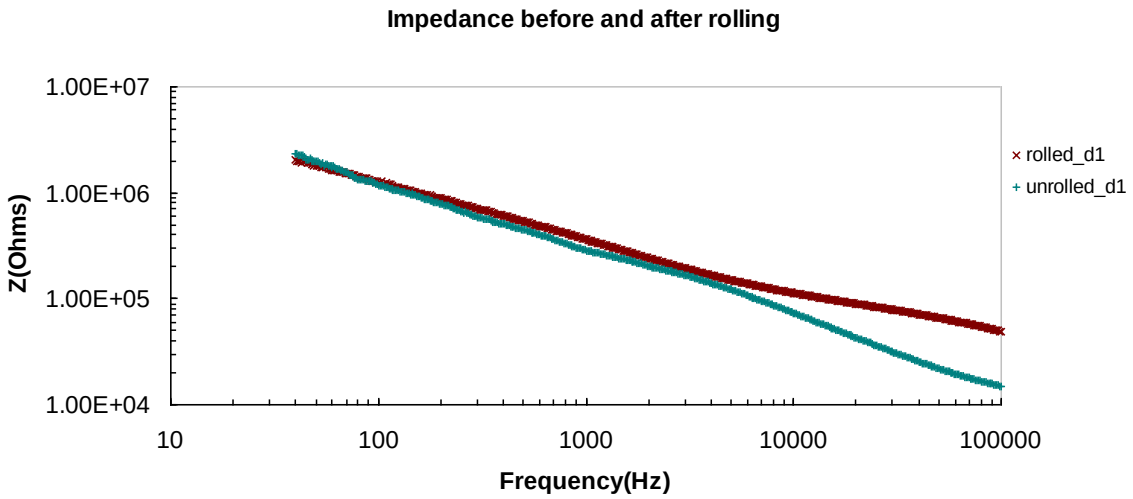


Fig. 9.4: Impedance spectra for an electrode from an SPNI device belonging to batch1 before and after rolling (batch 1 contains 8 devices in total). The frequency ranges is 10Hz to100KHz as it allows electrode-electrolyte interface characterisation in addition to containing the frequency range relevant for nerve signal recordings

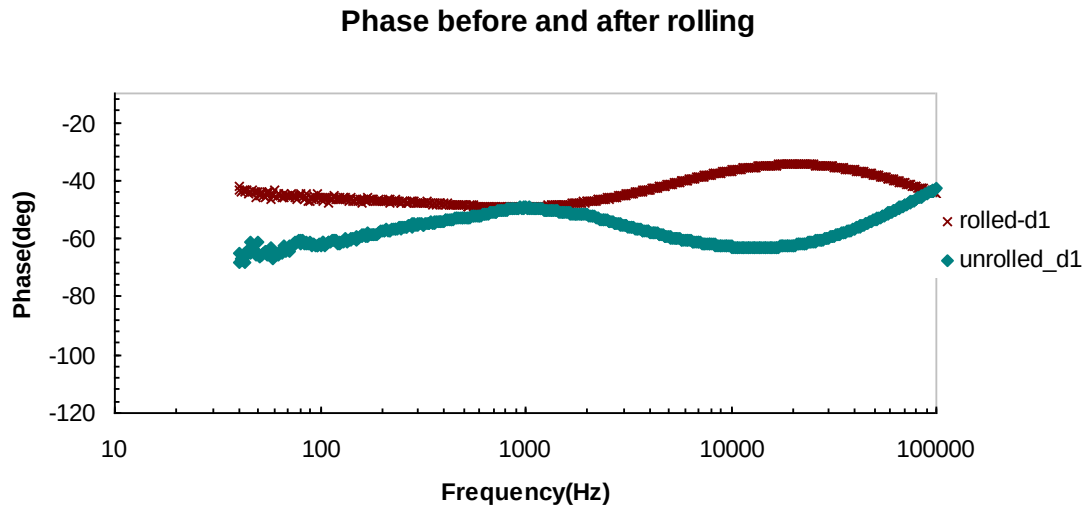


Fig. 9.5: Phase spectra for an electrode from an SPNI device belonging to batch1 before and after rolling. (batch 1 contains 8 devices in total). The frequency ranges is 10Hz to100KHz as it allows electrode-electrolyte interface characterisation in addition to containing the frequency range relevant for nerve signal recordings

which is being altered during rolling is the geometry of the area in which current is carried. In a bounded area with area A and length l carrying a uniform current, the resistance is defined as:

$$R_s = \rho \frac{l}{A} \qquad \text{(Equ. 9.2)}$$

ρ is the solution resistivity. As can be deduced from the equation above the solution resistance is inversely proportional to the area bounding the current. During rolling the area (A) is decreased, and consequently leading to an increase in R_s.

The reciprocal of ρ (κ) is more commonly used where κ is the conductivity of the solution. The relationship with solution resistance becomes:

$$R_s = \frac{1}{\kappa}.\frac{l}{A} \qquad \text{(Equ. 9.3)}$$

κ can be calculated from the specific ion conductances and used in turn to calculate the solution resistance. However this can be very complicated and hence the resistance R_s is normally calculated by a form a model fitting into the measured data. If the frequency range was increased to include higher frequencies, the solution resistance R_s for both the rolled and the unrolled devices could have been deduced from the corresponding impedance spectra. For future measurements a wider frequency range will be used.

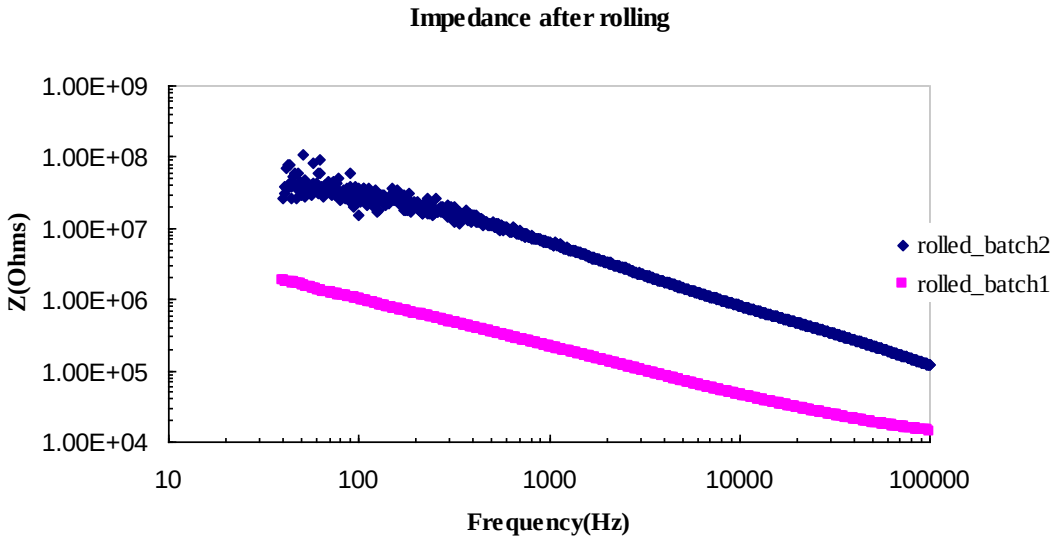


Fig. 9.6: Impedance spectra for a rolled device from batch 1 and rolled device from batch 2. (each batch contains 8 devices in total)

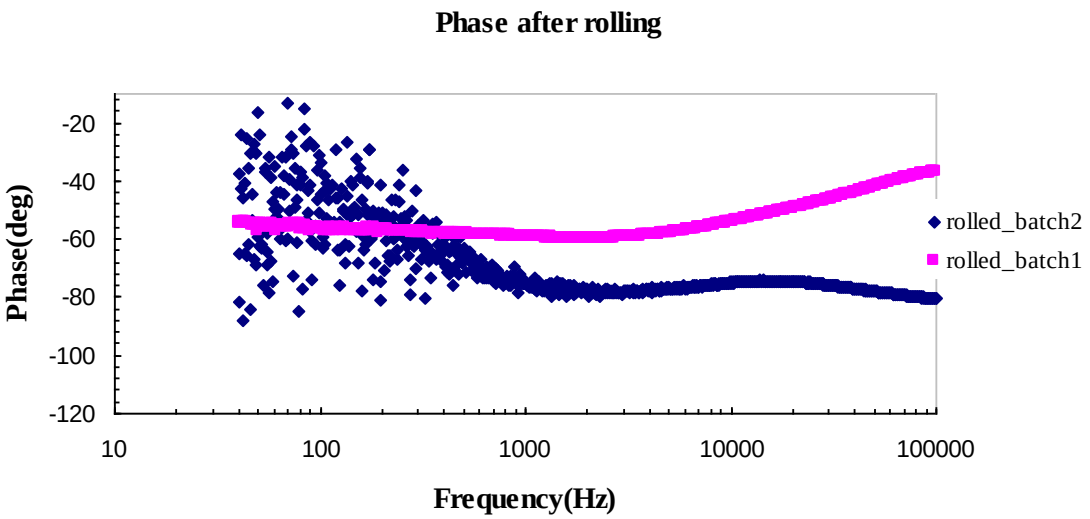


Fig. 9.7: Phase spectra for a rolled device from batch 1 and rolled device from batch 2.

(each batch contains 8 devices in total)

The impedance and phase spectra of two electrodes from two different SPNI device batches were measured and the data is presented in Fig. 9.6 and Fig. 9.7. As it can be seen from the impedance spectra, the two electrode interfaces have a similar behaviour where the impedances decrease almost linearly as frequency raises suggesting a capacitive interface. The phase spectra of two electrodes validate this suggestion; the phase of the electrode from batch1 decreases slightly from -55^0 to -60^0 with the increase in frequency and picks up at about 3000Kz to level at -40^0 by 100 KHz. The phase of the electrode from batch2 has a more capacitive behaviour where the phase is roughly between -90 and -80^0 after the scattering at low frequency settles down. However, an important point to note is that the recorded impedance of the electrode from batch 2 is significantly higher than the impedance of the electrode from batch1, where there is a difference of over $2M\Omega$ between the two spectra. For example at 1KHz the impedance of batch1 electrode is about $250\,K\Omega$ while it is over $5\,M\Omega$ for the batch2 electrode. Although this could be attributed to differences in the quality of the evaporated gold film between the two batches, it is more likely related to the de-scuming process of the electrodes; devices in batch 2 did not undergo any de-scuming[51] to remove any remaining polyimide residues at

[51] The descuming step was purposefully skipped in the fabrication process of devices in batch2 to see if it has any effect on the impedance of the micro-electrodes in this batch.

the electrode sites while devices from batch1 had been de-scumed. The residues left at the microelectrode sites following development of the channel layer can vary between the microelectrode sites belonging to the same batch and across different batches. Missing the descuming step in the fabrication process of SPNI devices can lead to impedance variation across different devices and different batches, and can therefore affect the repeatability of the fabrication process. Consequently, de-scuming the devices to clear any residues covering the microelectrodes sites is important to guarantee microelectrode site exposure. This can potentially decrease microelectrode site impedance which is beneficial for improving signal-to-noise ratio associated with thermal noise (please refer to Equ.4.4 in chapter 4). In brief, besides improving the fabrication process repeatability, it is essential to de-scum the SPNI devices to potentially obtain lower microelectrode impedances that can have better signal sensitivity (i.e. better signal-to-noise ratio).

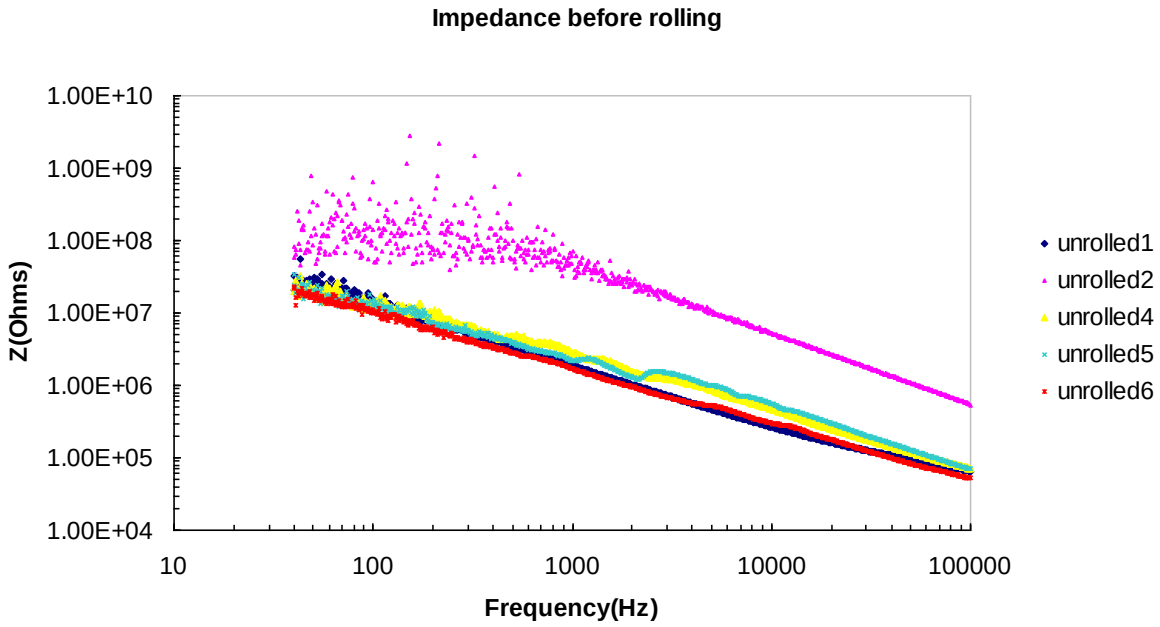


Fig. 9.8: Impedance spectra for 5 different microelectrodes from batch 2 prior rolling.

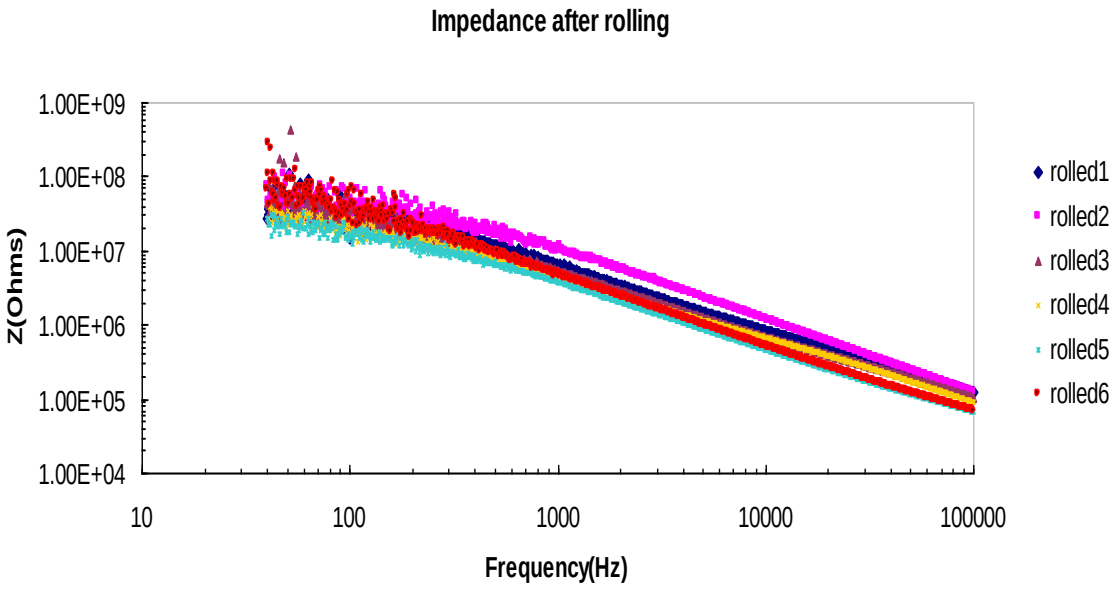


Fig. 9.9: Impedance spectra for 6 different microelectrodes from different SPNI devices taken from batch 2 post rolling

The impedance spectra for 6 more devices from batch 2 were measured for different electrodes prior and post rolling and the results are presented in Fig. 9.8 and Fig. 9.9. From plotted data, the unrolled microelectrodes appear to have similar impedance behaviour apart from the microelectrode labelled unrolled 2 whose impedance spectrum seems to be shifted up significantly. The rest of the electrodes have a mean impedance of about 2.1MΩ at 1KHz with a range of 1.7 to 2.86M Ω which is slightly higher than the values reported for similar electrodes [59]. Rolling the devices increases this mean value as well as the individual impedance for each electrode as shown in Fig. 9.9. In other words, based on the plotted data, the mean value for the rolled samples increases to 5MΩ at 1KHz with an impedance range of 3MΩ to over 6MΩ at 1KHz. The rolled samples exhibit similar impedance pattern across the 6 micro-electrodes. Although, the impedance spectrum of microelectrode 2 is closer to the rest of the spectra it is still at the top of the range.

These measured SPNI devices manifest the right expected behaviour, however the impedances measured are considered high compared to impedances recorded in other comparable devices detailed in earlier studies[61]. This again could be due to the absence of the de-scuming step in the fabrication process of this batch (batch2) which leaves the

microelectrode sites covered with a very thin layer (or residues) of polyimide. Consequently, an increase in the recorded impedance is observed. On the other hand, by referring to the mean and individual impedance shifts between the unrolled and the rolled samples, factors other than skipping the de-scuming step could be contributing to the increase in the impedance particularly after rolling.

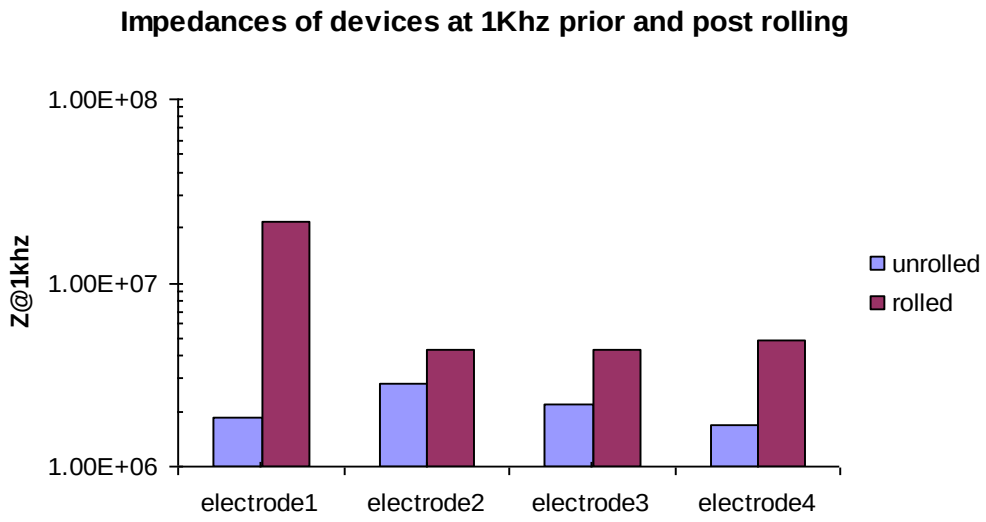


Fig. 9.10: Impedances of various electrodes from batch2 at 1Khz prior and post rolling (batch 2 contains 8 SPNI devices in total)

To illustrate this better, the impedances at 1KHz of 4 microelectrodes from different SPNI devices (taken from batch2) were plotted against each other prior and post rolling. The results are presented in Fig. 9.10. As can be seen from this figure, the impedances at 1KHz are higher in the rolled samples than in the unrolled samples. Again this increase in impedance post rolling is due to the confinement of the electrode sites in the rolled samples as opposed to the unrolled samples where the electrode sites sit halfway a 2D open micro-channel. The degree of the impedance shift after rolling varies. The measured impedances in Fig. 9.10 are for SPNI devices taken from batch2 which did not undergo the de-scuming process. This explains the variation in impedance shift observed post rolling (which is illustrated graphically in Fig. 9.10). Skipping the de-scuming process during the fabrication of the SPNI devices can leave the micro-electrode sites covered by a thin layer of polyimide or polymeric residues which could not be cleared during the

development of the device channel layer. This results in higher micro-electrode impedances, impedance variation across the SPNI microelectrodes and different impedance shifts across the SPNI micro-electrodes post rolling. Therefore, it is important to perform the de-scuming process during the fabrication of the SPNI devices to guarantee device reproducibility and lower microelectrode impedance.

The phases of the 6 electrodes from batch2 are also plotted before and after rolling and the results are presented in Fig. 9.11 and Fig. 9.12 . At first glance, there seems to be a fair amount of scattering at low frequencies especially in the rolled samples. The unrolled phase spectra appear to be different from each other and have various shape patterns. However, they all seem to have a changing phase in the range of -90^0C to -60^0C which implies that the interface has a strong capacitive element. The rolled phase spectra on the other hand seem to have more coordinated phase pattern. After the scatterings at low frequencies settle down, one can notice that the phase for these electrodes mostly stays in the range of -90^0C to -70^0C. This implies that the interface in these electrodes can also be characterized by a capacitive behaviour.

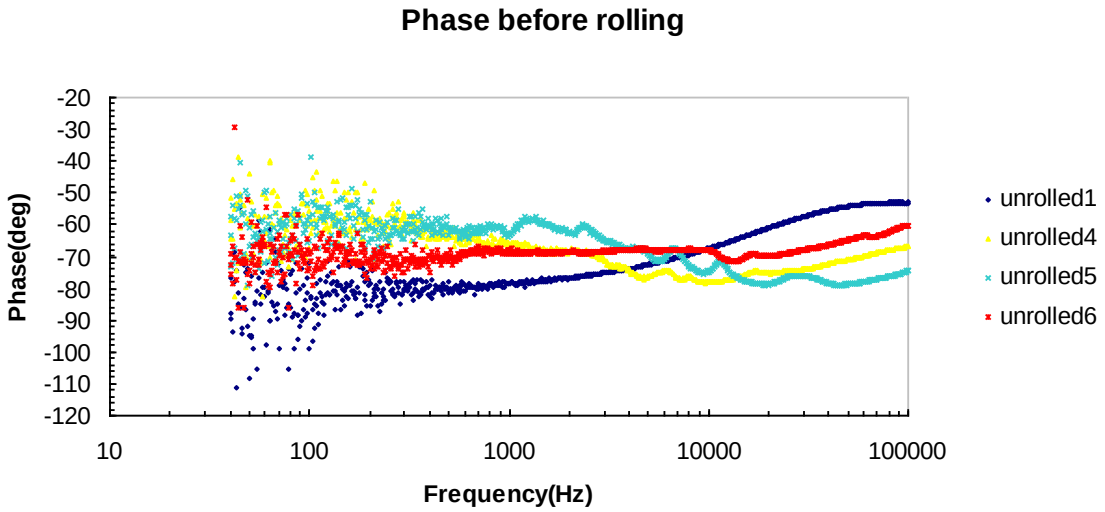


Fig. 9.11: Phase spectra for 5 different microelectrodes from batch2 prior rolling

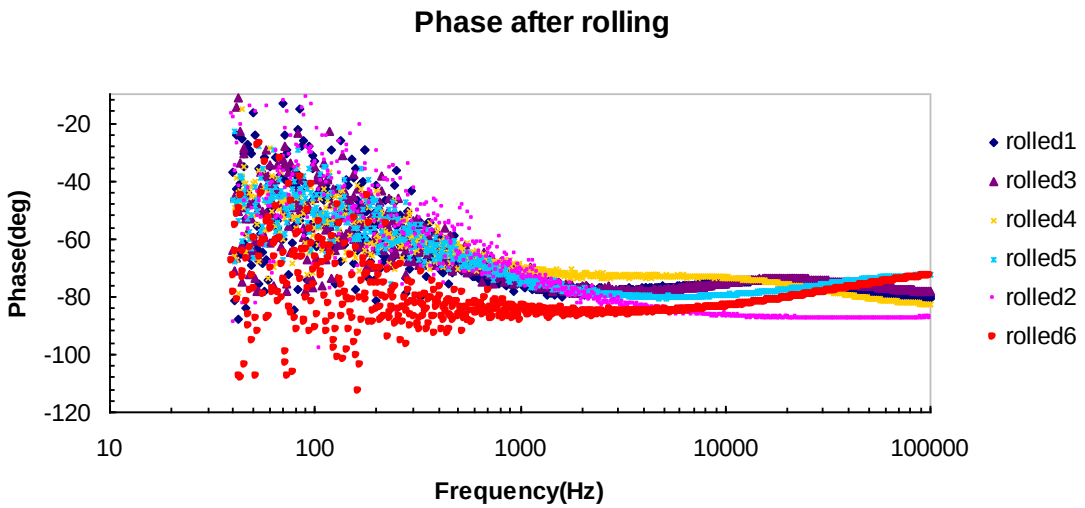


Fig. 9.12: Phase spectra for 6 different microelectrodes from batch2 post rolling

9.5. Chapter summary

Electrochemical Impedance Spectroscopy (EIS) was performed on the fabricated SPNI implants, to access the success of the fabrication process and the intactness of the implant wiring post rolling. EIS was also used to test and validate the incorporation of the Microflex (MFI) technique into the fabricated devices, in addition to characterising the electrode/electrolyte interface of the implants' micro-electrodes. The chapter analysed the data obtained from EIS for the various SPNI devices. This was done by organising the chapter into two main parts; in the first part of the chapter an equivalent circuit model for the electrode/electrolyte interface was derived, whilst the second part analysed the impedance data obtained experimentally (for different SPNI devices) and compared it against the derived equivalent circuit model.

Analysing the impedance and phase spectra of the devices prior and post rolling confirmed that the micro-electrodes are still functioning post rolling and the rolling strains did not cause any mechanical or electrical failure to the wiring of the SPNI devices. The data analysis also confirmed the success of the MFI technique in setting up a reliable mechanical and electrical interconnection between the SPNI devices and the external circuitry.

The impedance and phase spectra exhibit that the electrode/electrolyte interfaces of the SPNI devices have more of capacitive behaviour (non-ideal capacitive behaviour) where the impedances decrease almost linearly as frequency raises to level off at higher frequencies (suggestive of a capacitive interface). The phase spectra confirmed this by having values mostly in the region of -60^0C to -90^0C.

The impedance of the SPNI devices increases slightly post rolling as opposed to prior rolling (20% increase impedance post rolling). Rolling the devices transforms the micro-channels from 2D open roof channels into 3D channels with a closed roof. The microelectrodes become housed in a closed channel that is only accessible from the micro-channel ends. The path of the current flow is therefore affected leading to an increase in the solution resistance.

De-scuming the microelectrodes during the fabrication process of the SPNI devices is very important for device repeatability. Skipping this step can leave behind a thin layer (or residues) covering the micro-electrode sites which can result in impedance variation across the different SPNI devices and across the different processed batches[52]. Hence, de-scuming the devices guarantees microelectrode site exposure, and this can potentially decrease microelectrode impedance which is beneficial for improving signal-to-noise ratio associated with thermal noise (please refer to Equ.4.4 in chapter 4). Therefore, besides improving the repeatability of the SPNI fabrication process, it is essential to de-scum the SPNI devices to potentially obtain lower microelectrode impedances that can yield better signal sensitivity (i.e. better signal-to-noise ratio).

Now that the success of the fabrication process through electrochemical impedance spectroscopy has been confirmed, the next chapter presents the results of testing the SPNI implants in vivo. This includes evaluating axonal regeneration through the SPNI implants and accessing their ability to stimulate and record neural signals.

[52] One batch contains 8 devices processed on the same wafer

10. REGENERATION AND *IN VIVO* RESULTS[53]

10.1. The passive SPNI implants

To evaluate regeneration through the micro-channels with the updated dimensions presented in chapter [5], 24 passive SPNI devices were implanted into the right sciatic nerves of 24 male adult rats[54]. All the implants had the same channel cross-sectional area ($100\ \mu m$ x$100\ \mu m$). 12 out of 24 implants have channel lengths of 2.5mm each while the remaining 12 implants have channel lengths of 4mm each. Fig. 10.1 (Left) shows an optical image of a passive SPNI implant. Each implant has a total of 180 micro-channels and 1.5mm diameter which anatomically matches the sciatic nerve diameter of an adult male rat. The space in the centre of the roll was blocked with a plastic plug to prevent axons from growing into this space and encourage them to grow through the micro-channels instead.

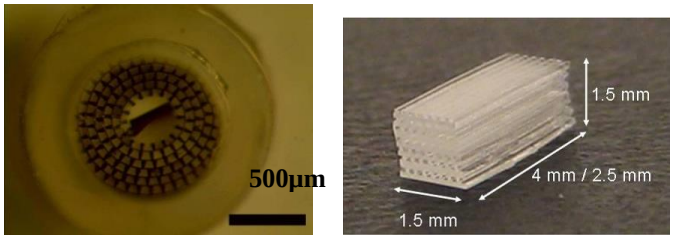


Fig. 10.1: Passive SPNI and PDMS implants. Left- A cross-section of a passive SPNI implant, Right- image of stacked PDMS implants with an illustration its cross-section

To compare the performance of the passive SPNI devices, implants with micro-channel arrays made with stacked PDMS (Polydimethylsiloxane) were also implanted. This implant type was fabricated by Stephanie Lacour at the University of Cambridge as part of the collaborative project mentioned earlier in the introduction chapter of this thesis, which aims to develop neural implants for a peripheral nerve repair. Fig. 10.1(Right)

[53] Chapter based on data reported [65] J. Fitzgerald, *et al.*, "A regenerative microchannel neural interface for recording from and stimulating peripheral nerve axons in vivo," *J Neural Eng,* vol. 9, 2012.

[54] The in vivo experiments on the passive and active SPNI implants were conducted in collaboration with Natalia Lago and Stephan McMahon at department of Neurosience , Kings college London. All experiments were carried out using adult male rats in accordance with United Kingdom Home Office regulations.

illustrates a magnified image of one of those PDMS devices. The implant had an overall height and width of 1.5mmx1.5mm matching the sciatic nerve of diameter an adult male rat. Their micro-channel cross-sectional area was $130\,\mu m$ x$130\,\mu m$, however their transparency was lower (channel spacing of $170\,\mu m$) because of limitations in making channel walls thinner than $100\,\mu m$ and hence each PDMS implant had a total of 24 micro-channels. Attempting to fabricate micro-channel walls thinner than $100\,\mu m$ results in the walls collapsing onto the microchannel space. These passive PDMS implants were fabricated by casting PDMS in moulds prepared specially for this purpose. Every time a layer of PDMS is casted it is stacked on the top of a previously casted PDMS layer (which has 2D micro-channels with an open roof). This creates closed 3D micro-channels and the process is repeated for as many times as is necessary to obtain a micro-channel stack of 1.5mm in height which matches the sciatic nerve diameter. Similar to the passive SPNI devices, two groups of PDMS implants were fabricated with different micro-channel lengths; one group contained implants with micro-channel lengths of 2.5mm each and the other group contained implants with micro-channel lengths of 4mm each. The *in vivo* experiments on the passive SPNI implants were conducted in collaboration with Natalia Lago and Stephan McMahon at the department of Neuroscience, Kings college London. All experiments were carried out using adult male rats in accordance with United Kingdom Home Office regulations.

10.1.1. In vivo implantation of the passive implants

The implants were prepared for implantation by sterilizing them in 70% ethanol for 3 hours and then filling them with saline. The devices were surgically implanted into the right sciatic nerves of adult male rats. To perform these operations, the animals were anaesthetized using a mixture of intraperitoneal medetomidine (0.5mg/kg) and ketamine (60mg/kg). The right sciatic nerve was then exposed at the thigh and freed from the surrounding tissues from sciatic notch (near the hip bone) to the knee. The exposed nerve trunk was transacted at mid-thigh, and two nerve stumps were fixed and sutured into the ends of the SPNI silicone guide with nylon stitches (using 10-0 suture size which is the

smallest and is normally used in the most delicate surgeries). The wound was closed up in layers and the animals were left to recover and allow time for axonal regeneration.

10.1.2. Explantation of the passive implants and preparation for histological assessment

The implants were checked for axonal regeneration at two time intervals, namely 4 weeks post-implantation and 12 weeks post-implantation. The 4 weeks post implantation check point was chosen to be the earliest time point for accessing regeneration through the implants as it can take longer for the neural tissue to grow through arrays of micro-channels as opposed to growing through hollow tubes (such as hollow silicone tubes). Allowing more time, permits more axons to grow through the micro-channels, and hence the 12 weeks post implantation check point was selected as the next time point to ensure sufficient time was given to achieve good re-innervation through the implant micro-channels. At both time intervals, the sciatic nerves were surgically explanted by first sedating the animals with pentobarbital general anaesthesia, and then trans-cardially perfusing them with 0.9% saline solution followed by 4% paraformaldehyde in 0.1M phosphate buffer (BP). This is called fixation and it is done to rapidly and uniformly preserve tissue in a living-like state. The skin was opened and the implants with the corresponding sections of the sciatic nerves attached to them on either end were harvested (Fig. 10.2). As it was difficult to assess regeneration

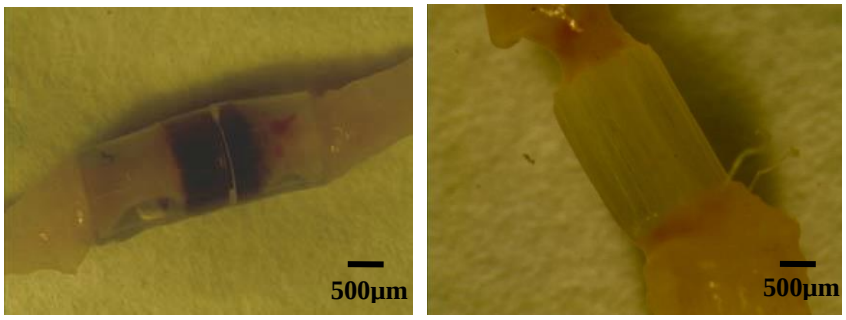


Fig. 10.2:Explanted nerve with implants. Left- an explanted passive SPNI device with the two sciatic nerve stumps. Right- an explanted passive PDMS device with the two sciatic nerve stumps

through the centre of the passive SPNI devices without crashing its content, histological assessment of axonal regeneration was done by examining the nerve emerging immediately on the distal side of the rolled device. Each assembly consisting of the explanted device and its attached nerve section was dismantled by removing the silicone tubes, cutting the nerve stump at the distal end of the micro-channel array, and then pulling the array longitudinally off the proximal nerve stump.

Transverse resin embedded semi-thin sections (0.5 µm thick) and cryo-sections (10 µm thick) were prepared for examination under light microscopy and electron microscopy. The resin embedded semi-thin sections of the regenerated tissue would have been enough for exploring the content of the micro-channels, however cryo-sections were also prepared as they provide a good system for visualizing fine details of the cell. More details on the preparation of these two section types were reported in [62].

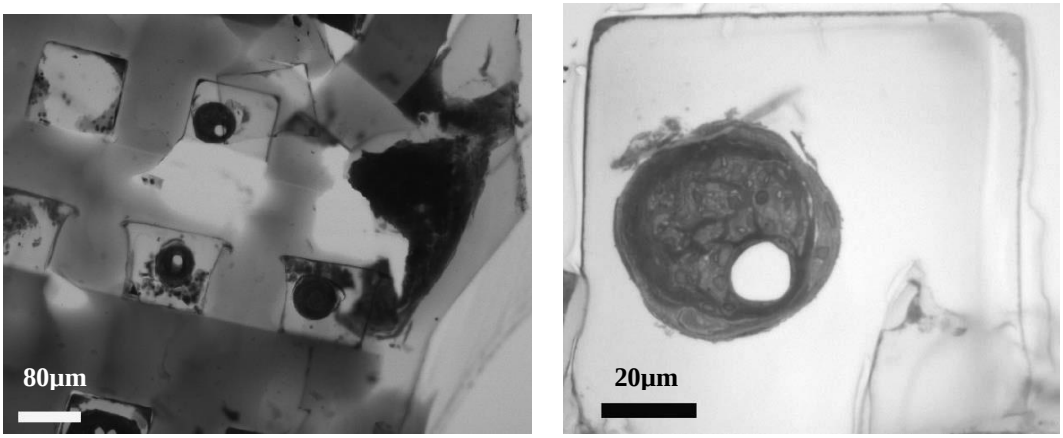


Fig. 10.3: Optical micrograph through the centre of a PDMS implant at 12 weeks post-implantation; Left- an optical micrograph through the centre of a PDMS device shows no axonal regeneration through the micro-channels at any time point post-implantation (4 weeks and 12 weeks). Right- a Zoom into the content of one of the PDMS micro-channels reveals absence of neural tissue; the channels are mainly filled with connective fibrous tissue.

Images of the resin-embedded semi-thin sections of the tissue occupying the micro-channels were obtained at x63 magnification with an AxioCam MRm Zeiss camera. The number of myelinated axons that have regenerated through each micro-channel was recorded. The cryo-sections were imaged with a Leica laser scanning confocal microscope at x63 magnification. The number of myelinated axons that have regenerated

through each micro-channel, the number of micro-channels which supported axonal growth and the total number of myelinated axons were recorded.

10.1.3. Regeneration results through the passive SPNI implants

The histological assessment of the PDMS devices showed no axonal regeneration through the micro-channels at any time point. Fig. 10.3 shows the content of micro-channels through a cross-section taken at the centre of one of the PDMS implants. As it can be seen, channels illustrated in this figure were almost empty and contained only connective tissue and blood vessels occasionally. However no regenerated axons were found in any of the PDMS micro-channels even at 12 weeks post-implantation. The suspected reason behind this was the low transparency[55] of the PDMS device, which meant that the space available for axonal growth was not high enough resulting in the failure of the implant to support any regeneration.

On the other hand, regeneration through the passive SPNI rolled implants was a different story. At 4 weeks post-implantation, there was some axonal regeneration through the PSPI devices but this was not at a significant level (Fig. 10.4). Out of 12 implanted devices, only 4 of the 2.5mm long devices supported axonal regeneration distally, whereas no axonal regeneration was found on the distal part of the 4mm devices. This indicated that axons are growing through the micro-channels of the PI rolled implants but a longer implantation period might be needed to allow significant levels of regeneration. This was confirmed by evaluating axonal growth through the channels after 12 weeks post-implantation where all the implants were found to support a good degree of regeneration on their distal part. This suggested that an implantation period of about 3 months is required for the active implants before stimulation or recording is attempted through these implants.

[55] Transparency is defined as the ratio of the open area occupied by air over the total cross-section (which is air +polymer). Transparency T(%) can be expressed as: $T(\%) = \frac{w}{S+w}$ where w is the channel (air) and S is the spacing between the channels (i.e the width of the channel wall)

Fig. 10.5 shows regeneration on the distal part of 8 passive SPNI implants (4 out of 8 implants have a 2.5mm long micro-channels whilst the other 4 implants have a 4mm long micro-channels). Close up examination of the content of some of the micro-channels is also illustrated. Clusters of regenerated axons (light grey colour) separated by connective tissue can be seen in the Fig. 10.5 (Bottom). The myelinated axons are distinguishable by their dense contour representing the myelin. Blood vessels appear as white dots within the dark regenerated tissue or as white circles depending on image resolution. Quantitatively, the total number of regenerated myelinated axons found at the distal part of the 2.5 mm passive SPNI devices 12 weeks post-implantation ranged from 2612 to 15582 per implant (with a mean value over 8000 total myelinated fibres per implant).

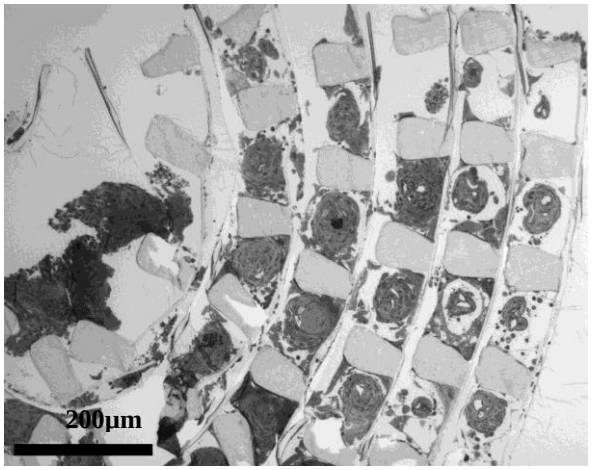


Fig. 10.4: An optical micrograph of regeneration through the distal end of a 2.5mm long passive SPNI implant at 4 weeks post-implantation. Regeneration through the passive implants is not significant at this time point (where only 4 out of 12 animals implanted with the 2.5mm long passive SPNI implants had axons on the distal end of the device, while no axons were seen distally to the 4mm long SPNI devices.

Fig. 10.6 shows the number of myelinated axons that have regenerated through a 2.5 mm long implant and a 4mm long implant at 12 weeks post-implantation. The number of myelinated axons in an intact nerve is also shown for comparison purposes. As can be seen from the figure, the average number of myelinated axons in an intact male rat sciatic nerve is around 7200 which is between the average values for the 2.5mm long implant and the 4mm long implant. The mean number of axons that have regenerated through the 2.5mm devices (8000) is slightly higher than the number found in an intact male sciatic

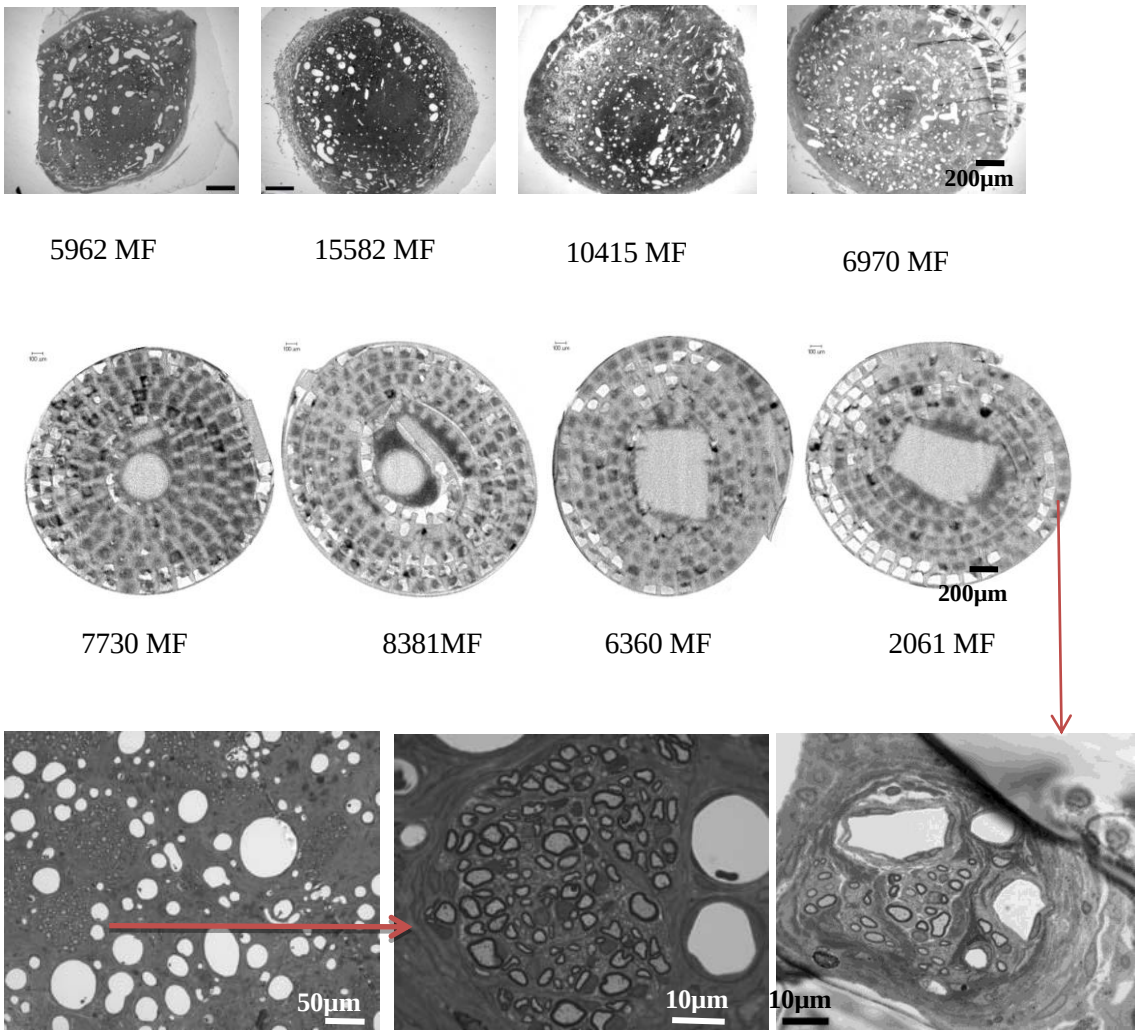


Fig. 10.5: Axonal regeneration through different passive SPNI devices at 12 weeks post-implantation. (MF in the figure stands for regenerating Myelinated Fibres). All animals had regenerated axons on the distal end of the implant at 12 weeks post- implantation. The top set of images show regeneration at the distal end of 4 of the 2.5mm long passive SPNI devices (the number of myelinated fibres that have regenerated through the micro-channels of each implant is also shown. The middle row set of images show regeneration at the distal end of 4 of the 4mm long passive SPNI devices along with the number of myelinated fibres that have regenerated through micro-channels of each implant. The bottom set presents transmission electron microscopy images of transverse semi-thin sections of nerves that have regenerated through SPNI micro-channels; the blood vessels appear as white (almost) circular shapes. The images clearly show the myelinated fibres (with the dark contoured shapes) and the unmyelinated fibres

nerve. Axons branch as the regenerating fibres leave the implanted device and this is likely to bias the counts in the SPNI implants upwards relative to the intra-device counts. However, even with this branching effect, axonal regeneration through these implants is substantially sufficient for selective stimulation and recording from as many regenerated

nerve fibres as possible. This is important because if axons do not sufficiently regenerate through the device, the proportion of proximal fibres that the interface can communicate with is reduced.

Furthermore, regenerated axon diameter distribution within the implants seemed to have shifted to the left in comparison to that found in intact sciatic nerve where it is centred around $5\,\mu m$. However, there was no significant difference between repaired sciatic nerves with micro-channel implants and sciatic nerves at a similar time-point after sectioning and suturing the stumps either directly or onto a standard silicone tube implant [62, 82]. This showed that the micro-channels did not influence the size of the regenerated axons. Vascularisation needed to sustain the regenerating neural tissue was also evident through examination of the channel contents which commonly showed the presence of 1 to 2 longitudinal blood vessels per channel. A fibrous tissue sheath was produced as a reaction to the inner walls of the micro-channels and surrounded all the regenerated mini-nerves. These sheaths which occupied the periphery of the micro-channels had a mean thickness of 25μm. This might severely limit the space available for axonal regeneration if the micro-channels had been 50 μm x50 μm or less in cross-section. Hence increasing the cross-sectional area of the micro-channels to a 100 μm x100 μm would leave plenty of space for the fibres to regenerate even with the formation a fibrous tissue sheath on the boundary of each micro-channel, as proved by regeneration results presented earlier in this section.

In comparison to the PDMS implants and to regeneration results through PI implants with smaller micro-channel cross section[56], the optimising the SPNI device dimensions seems to have a great impact on regeneration through the micro-channels. The main dimensional parameters that mainly influence regeneration through the device micro-channels include the cross-sectional area of the micro-channels and their symmetry in addition to the transparency of the implants. By optimising these parameters, the space available for regeneration through the implant is maximised allowing for an improvement in axonal outgrowth through the implant's micro-channels. Furthermore, regeneration results through the passive SPNI implants have also shown that axons can regenerate

[56] Discussed in chapter 4

successfully through 4mm long micro-channels. This is because blood vessels also grow with the regenerating axons through the implant's micro-channels which is essential for the provision of oxygen and nutrients to the regenerating tissue.

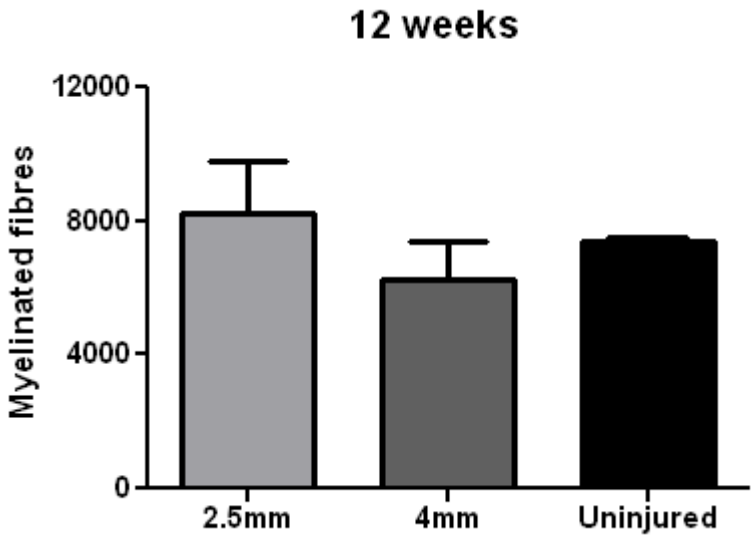


Fig. 10.6: average number of myelinated axons that have regenerated through a 2.5 mm long implant and 4mm long implant at 12 weeks post-implantation. The number of myelinated axons in an intact nerve is also shown for comparison purposes.

Now that regeneration has been accessed through the passive SPNI implants, the remainder of this chapter will assess the ability of the active SPNI implants to stimulate and record neural activity. A histological evaluation of axonal outgrowth through these active implants will also be presented.

10.2. Assessment of the active SPNI implants[57]

To investigate the electrophysiology of the regenerated tissue and evaluate axonal regeneration, 6 active SPNI devices (shown in Fig. 10.7) were implanted in the sciatic nerves of adult male rats. The implanted devices have a diameter that matches the sciatic nerve diameter of an adult rat (1.5mm) and consist of a total of 180 micro-channels with

[57] The work presented in this section is reported in [65] J. Fitzgerald, *et al.*, "A regenerative microchannel neural interface for recording from and stimulating peripheral nerve axons in vivo," *J Neural Eng*, vol. 9, 2012.

20 microelectrodes spread across the middle rolls. The hole at the centre of the roll was blocked with a plastic plug to deter axons from regenerating into it and encourage them to regenerate through the micro-channels instead.

For performance evaluation of the active SPNI implants, the study also explored the use of a passive micro-channel implant constructed with silicone (Sylgard 184, Dow Corning), which served as a useful comparison. The fabrication and the electrophysiology of the silicone implants were carried out by James Fitzgerald at the University of Cambridge. The implants were made by casting silicone on a grid of nylon filaments[62, 65]. Pulling out the filament after curing the silicone, leaves behind an array of channels.

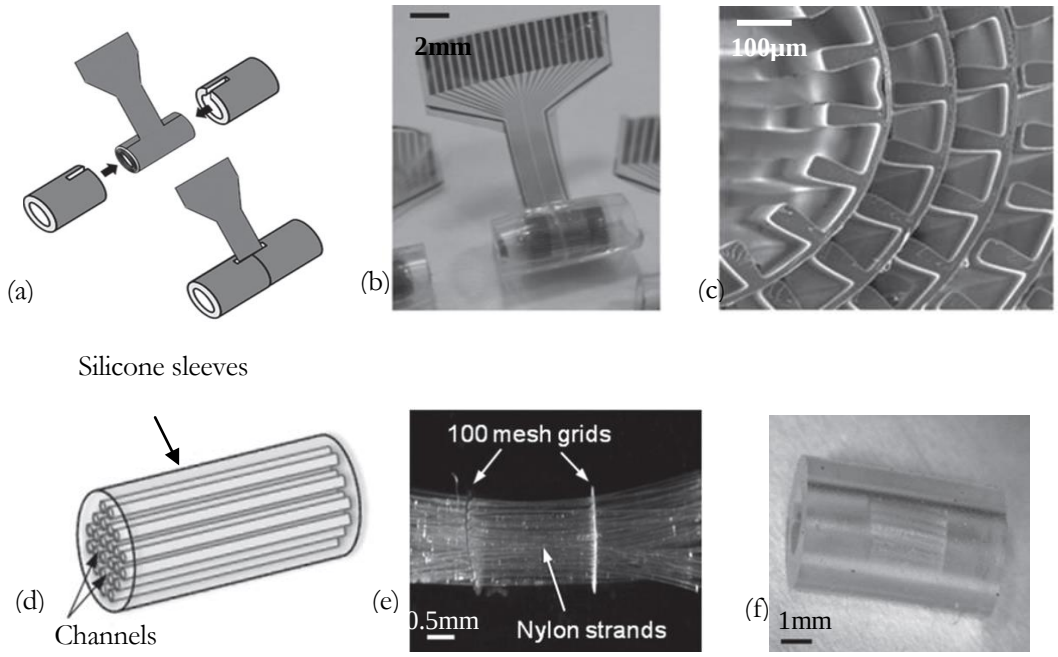


Fig. 10.7: (a-c) SPNI implants (a) A simplified schematic illustrating the application of the silicone tubes on either end of the rolled SPNI structure to prevent it from unravelling and to provide attachments for stitching the nerve stumps. (b) A complete device with the micro-channel rolls bearing the electrodes inserted into the silicone tube. (c) SEM of the end of the rolled channel bundle showing how each channel is roofed by the next layer of the roll. The hole down the centre of the implant was blocked using plastic plug before implantation. (d-f)Silicone implants (d) A schematic of a silicone cylinder containing 24 parallel 130 μm diameter micro-channels. (e) Nylon filaments fed through two aligned electron microscopy grids form a coherent bundle for casting in silicone. (f) Silicone cylinder with filaments pulled out, trimmed to 2.5mm length, and inserted into a silicone tube [65].

The array was trimmed to 2.5 mm long and pushed into the centre of a silicone tube that is 6.5 mm in length and 1.5 mm in inner diameter, thus leaving 2 mm of the tube either end as a sleeve to suture the nerve stumps into (Fig. 10.7). These implants had a channel cross-section of 90μm to 130μm in diameter and hence a transparency (the proportion of the cross section of the device that is open channel rather than silicone substrate) of only 14% as opposed to 67% transparency for the SPNI devices. The in vivo experiments on the active SPNI implants were conducted in collaboration with Natalia Lago and Stephan McMahon at department of Neuroscience, Kings college London. All experiments were carried out using adult male rats in accordance with United Kingdom Home Office regulations.

10.2.1. Implantation of the active SPNI devices

For implantation, the devices were sterilized by soaking in 70% ethanol for 3 hours and then filled with isotonic saline. Surgery was conducted under general anaesthesia with sterile precautions. A mixture of intraperitoneal medetomidine (0.5mg/kg) and ketamine (60mg/kg) was used for the general anaesthesia. The right sciatic nerves of adult male rats were exposed, freed from the surrounding tissue and transacted at mid-thigh level. The nerve stumps were sutured into the ends of the polymeric implant with 9/0 nylon sutures (Ethicon). The strip bearing the wiring and the connection pads was led out through muscular layer and placed subcutaneously. The wound was closed in layers and the animals were allowed to recover. A total of 6 SPNI (with embedded microelectrodes) and 8 silicone devices were implanted and left for 3 months to allow sufficient time for regeneration through the micro-channels.

10.2.2. Explantation of the active SPNI implants and the experimental set up for electrophysiology

At the end of the three months implantation period, the animals were re-anaesthetized with intraperitoneal (i.p.) urethane (1.25 g/kg). The skin was incised the polyimide strip bearing connection pads of the SPNI device was brought out whilst the rest of the implant

and the sciatic nerve were left embedded deep in the muscle. To create electrical connections to the electrodes, the back of the strip was first glued with cyanoacrylate glue to a metal bar, placed just above the wound, for mechanical support. Electrical contact was then made with the individual contact pads using a micromanipulator controlled needle[58] (see Fig. 10.8). The reference electrode was established with a needle inserted into the contra-lateral hindlimb. Stimulation and recording from each micro-channel were conducted via this connection set up. An isolated constant current stimulator (Digitimer) was attached between the micromanipulator-controlled needle electrode and the reference electrode to deliver 50 μs cathodic stimulus pulses into the intended micro-channel. Concentric electrodes (Clark Electromedical Instruments, Reading, UK) inserted into *tibialis anterior* (*t.a.*) and *gastrocnemius* (*gastroc.*) muscles were used to record the electromyogram (EMG) response illustrating the activation of motor units for these muscles. The concentric electrodes were connected to a DC amplifier with high pass filters set at 300 Hz and low pass filters set at 3 kHz. The stimulator output current was gradually increased from zero while recording EMG responses. The threshold current for motor unit activation was also recorded. For recording experiments, a square wave constant current pulse (500 μs, 1–10 mA) was applied through a pair of needle electrodes inserted into hindpaw digits to generate afferent action potentials which can be detected by the embedded microelectrodes of the SPNI implant [63].

Similarly for the silicone implants, after three months of implantation, the skin was reopened at the original incision and dissection through the muscle layers was carried out to expose the implant, the connective tissue sheath formed around it was also opened and the nerve was freed proximally. The side of the channel was exposed by cutting a window in the silicone tubing of the implant; an ultrafine tungsten microelectrode with a 0.2 mm shaft tapering to a 1 μm tip (Microprobe Inc.) was transversely guided with a micromanipulator into the array at its halfway point. The electrode was connected to NeuroLog NL100AK headstage amplifier (Digitimer, UK). The ultra-small diameter of the central electrode enabled it to pass through the channel walls of the silicone implant

[58] Using this connection set-up was a temporary measure. Work was being carried out at this stage to incorporate Microflex interconnection (ball bonding) into the SPNI implants as this would allow stimulation and simultaneous recordings from the 20 available micro-electrodes of the implant, however because of project time scales we had to resort to a temporary more primitive solution.

without deforming the channel structure or significantly compressing its contents. A fall in the amplifier noise was used an indication for channel entry. Two similar electrodes were used as reference electrodes; they were connected together and mounted onto another micromanipulator in a way that allows their tips to be 3.5mm apart. The micromanipulator was used to push the tips into the nerve just proximal and distal to the implant. A pair of silver wire hook electrodes attached to the nerve proximal to the implant was connected to an isolated stimulator unit [63].This was used to stimulate the

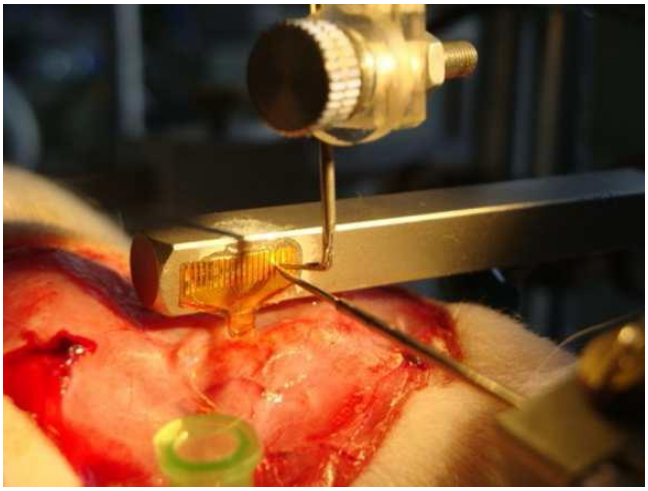


Fig. 10.8: connection set up to gain access to the individual micro-electrodes of the SPNI devices. The microelectrodes are connected to external circuitry to test their ability to stimulate and record from the regenerated tissue in the micro-channels. The contact pad strip is glued onto a metal par positioned just above the wound for mechanical support and the connections with the microelectrodes are made individually with a micromanipulator controlled needle.

sciatic nerve proximal to the silicone implant with a 1mA, 50 μs current pulses at 10Hz and record both compound and single fibre action potentials from the channel via the central electrode. For stimulation through the channel, an isolated constant current stimulator (Digitimer) was attached between the central and end electrodes and used to deliver 50 μs cathodic stimulus pulses into the target microchannel. The stimulator output current was slowly increased from zero while recording the EMG responses for the activation of the ipsilateral *t.a.* motor units (and noting the threshold current for the activation of these motor units [63].

10.2.3. Impedance of the active SPNI devices *in vivo*

To assess the integrity of the gold wiring of the SPNIs after implantation for three months, the impedance of each of the 20 embedded microelectrodes in each device was measured at 1 KHz. Almost 3% (4 electrodes) of the 120 electrodes failed completely as they were found to be open circuits. The impedances of the 97% (116 out of 120) working electrodes are illustrated in Fig. 10.9. 75% (92 electrodes) of these have impedances up to $2.5\,M\Omega$ which is considered within a typical impedance range. The mean impedance value comes to $1.24\,M\Omega$. The remaining electrodes with impedances higher than $2.5\,M\Omega$ were considered to have a degree of degradation or micro-fabrication defects. This could be caused, for instance, by underdevelopment of the thick photosensitive polyimide which might leave a thin film encapsulating the electrode site. The variance seen in the higher

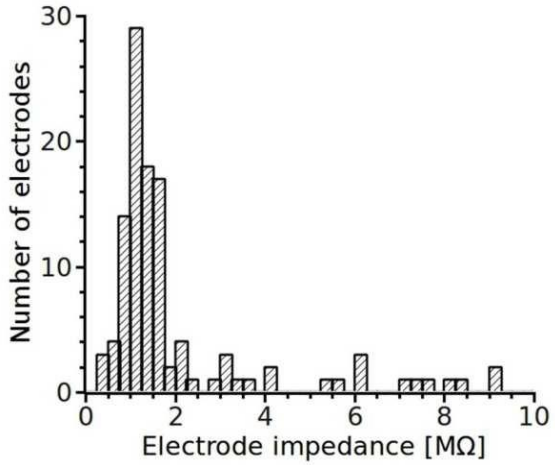


Fig. 10.9: Impedances of microelectrodes at 1 kHz *in vivo* after 3 months implantation[65]

range of impedance distribution could be attributed to variation in the ability of the different electrodes to withstand combined effects of rolling and the subsequent period of implantation for three months. Prior to implantation, some electrodes had a mean impedance of $420\,K\Omega$ at 1 kHz with a phase of around 60^0. Therefore, the impedance measured in *vivo* for 75% electrodes falling in the range of up to $2.5\,M\Omega$ was much higher than that of plane unrolled electrodes. This difference can be explained by the fact

that *in vivo* the test current does not only have to cross electrode/electrolyte interface but also the tissue occupying the micro-channels before reaching the low resistance volume conductor surrounding the microelectrode site. As a result, the measured impedance of electrode/electrolyte interface increases.

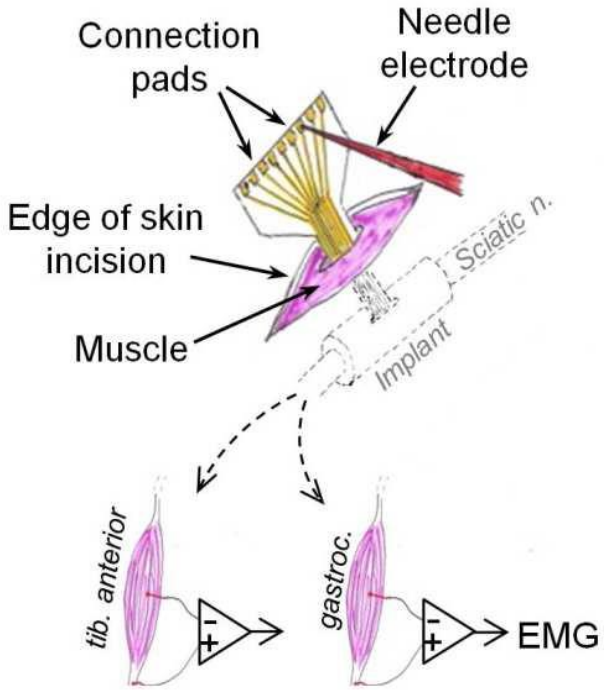


Fig. 10.10: Experimental set-up to investigate the ability of the SPNI to stimulate and elicit EMG responses[65]

10.2.4. Stimulation in SPNI devices

The ability of the SPNI devices to stimulate muscle activity (EMG responses) in the concerned animals was investigated by consecutively applying constant current stimulus pulses to each functioning micro-electrode in each of the 6 implanted SPNI devices. The experimental set-up used is shown in Fig. 10.10 (Top). The EMG responses were concurrently recorded in the tibia anterior (*t.a.*) and its antagonist gastrocenemius (*gastroc.*) muscle via concentric electrodes as mentioned in section [10.2.2] of this chapter. Muscle activity (EMG) was elicited in 5 out of 6 animals. 37 of the 116 functioning electrodes (32%) produced activity in the *t.a.* when stimulated, with 28 of

these electrodes activating more than one *t.a.* motor unit. EMG responses in the *gastroc.* were elicited through 48 micro-electrode channels (41%) with 24 channels activating more than one unit. Fig. 10.11 illustrates quantized EMG changes with increasing stimulus current delivered through the SPNI microelectrode residing in a micro-channel with good regeneration. The micro-channel was particularly chosen as it could activate motor units for both the *t.a.* and the *gastroc.* muscles. The figure clearly shows that more motor units in both *t.a.* and *gastro.* muscles were recruited (activated) with increasing stimulus current. In this particular experiment four motor units in *t.a.* and three motor units in *gastroc.* were recruited.

The EMG responses were initiated using stimulus currents that are low compared to those normally required in an unbounded volume conductor. These currents were however several times higher than those required for the silicone implants. The mean stimulus current for the polyimide micro-channels was $26.2\,\mu A$ as opposed to $4.29\,\mu A$ for the silicone devices. The value of the stimulus current for the silicone implants agreed with that predicted from in vitro data which was $4\,\mu A$ [64-65] . This is because the channels in this implant had perfectly sealed micro-channels whilst this was not guaranteed in the SPNI devices as shown in Fig. 10.7 c. The gaps between the tops of channel walls and the roof (back of the substrate in the next concentric roll) indicate an imperfection in the sealing of the channels which would allow current to spill out of the channel into adjacent channels. This increases the stimulus current required to reach the threshold for EMG response generation.

The study also revealed that current spill over, in few cases, was high enough to result in cross-talk between adjacent channels. This is evidenced by the EMG response having the same morphology and latency indicating that the same motor unit could be activated from neighbouring channels. A total of 104 distinct motor units were observed over both muscles and all six implants. Around 71% of these motor units could only be stimulated from a single channel while the remaining 29% could be activated from more than one micro-channel (more precisely, around 16% of the units can be triggered from two adjacent channels and around 13% from three or more adjacent channels).

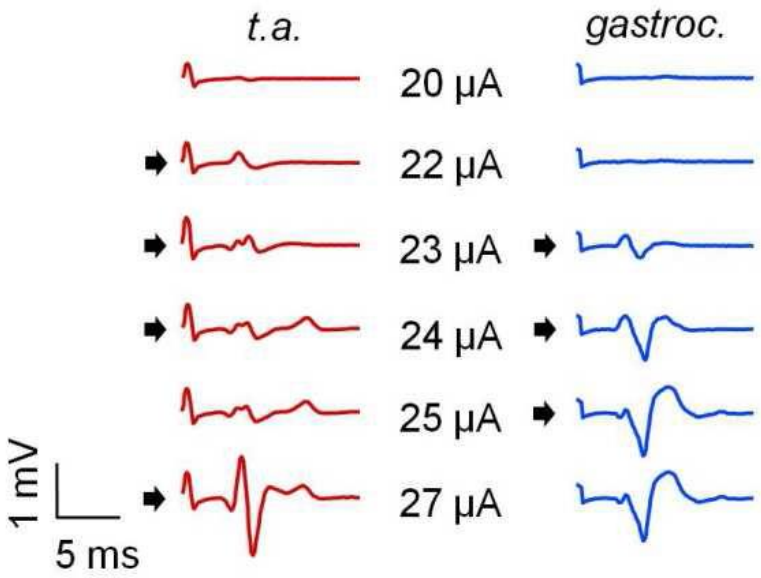


Fig. 10.11: The EMG response elicited in Tibia Anterior (*t.a.*) and its antagonist (*Gastroc.*) as the stimulation current delivered through the SPNI micro-electrode in a micro-channel innervating both muscles is increased. Four motor units in *t.a.* and three in *gastroc* were recruited. Arrows indicate the traces where new motor units are added (compare with the trace immediately above) [65]

Addressing the imperfection in the channel sealing is important for preventing current spill-over to the neighbouring channels and hence reducing the stimulation current requirement of the SPNI devices in addition to preventing cross-talk between SPNI channels. Therefore to maximise the benefits of axonal micro-channel confinement, the SPNI needs to have completely sealed channels. The roof of the micro-channel array needs to be closed via an appropriate fabrication step, in addition to the previous steps of the device. One way to do this is by preparing an appropriate sealing layer and then bonding it prior to rolling onto the device channels using a suitable bonding mechanism. Investigating the various approaches to optimise the seal of the SPNI channels is being carried out by my colleague Richard Barrett and progress to date has been reported in [17]. One approach is to fabricate a thin PDMS layer which can then be laminated onto the 2D open polyimide channels using isopropanol (IPA) as a bonding intermediate. Details of the fabrication steps and the bonding mechanism are reported in [17].

10.2.5. Recording in the active SPNI devices

The ability of the SPNI devices to record from the axons that have regenerated through its micro-channels was investigated. Constant square wave current pulses of 500 μs, 1–10 mA were applied through a pair of needle electrodes inserted across individual digits of the hindpaw to generate afferent action potentials. The stimulating needle electrodes were applied to nerves distal to the implant, while recording from the embedded microelectrodes within the micro-channels. Channels which generated clear EMG responses during stimulation were examined as they were likely to host many regenerated axons. It was chosen to do stimulation this way instead of using natural tactile stimuli (such as touching) because the generated potentials were smaller than those generated by stimulation with proprioceptive afferents, and hence could easily be lost in the background noise and difficult to distinguish from noise if tactile stimulation was used. As can be seen from Fig. 10.12, the recorded signal can be picked up with confidence and its authentic nature is made apparent as it is similar in each consecutive trace while the noise changes. This was enabled by electrical stimulation which allowed the recorded signal to be precisely time-locked. In the eight channels examined in this way, action potentials were recorded proving that axons could regenerate into these most distal sensory nerves and that implant has the ability to record from these axons.

Fig. 10.12 illustrates a common example of this where an early large compound action potential (CAP) is observed followed by smaller signal several milliseconds later. The conduction velocities of the recorded action potentials could be estimated by measuring the conduction distance from the digit stimulating electrodes to the implant and the latency which is the time from the onset of stimulus to the recording of the signal. The first group of elicited action potentials, indicated by the double arrow in Fig. 10.12, had conduction velocities of 5.6-11.3 ms^{-1}. Typically, conduction velocity of a myelineted axon is proportion to fibre diameter with a proportionality of 6 ms^{-1} per μm. This implies that the largest fibres are around 1.9 μm in diameter. The second group of action potentials (denoted by asterisk in Fig. 10.12), with slower conduction velocity of 2.2 ms^{-1} indicate that the fibres in this group could well be unmyelinated axons.

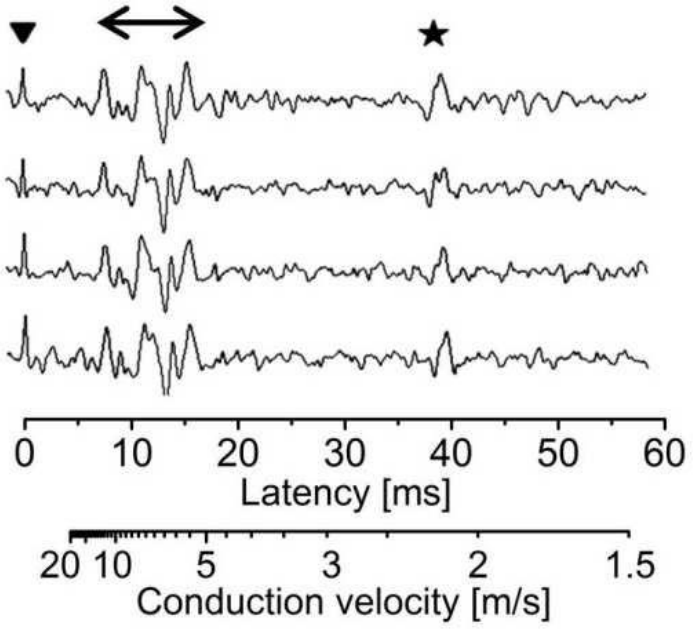


Fig. 10.12: Recording through the SPNI- signals recorded through embedded microelectrodes in the SPNI following distal stimulation of afferent fibres via needle electrodes inserted into the animal's hindpaw[65]

Axon diameters were measured histologically and were found to be close to 60% of those in normal rat sciatic nerve. It had already been shown through previous *in vitro* work that signal amplitude (A) varied as a function of axon diameter (*d)* and this relationship was expressed as $A \alpha d^{1.6}$. This implies that if the diameters of the axons regenerating through the channels grew to ultimately reach those in normal uninjured rat sciatic nerve, then a doubling of the recorded signal could realistically be achieved. Another example is with regenerating human proprioceptive afferents which in a similar implant could give signals of up to $\approx 1.1mV$ when they achieve or approach their normal diameter range of up to 20μm.

In addition to restoring electrical connectivity, muscle reinnervation is also essential for preventing muscle atrophy. This was established by extracting the *t.a.* muscles from each animal and weighting them after the electrophysiological testing had been completed. The ratios of masses for these muscles relative to the intact muscle masses (reinnervated/intact) were computed and a mean of 0.3 was reported for the animals with implants as opposed to a mean ratio of 0.18 that was reported for the six control animals with no re-innervation. The significant difference between the two ratios tells us that

although re-innervated muscle masses were less than their contra-lateral normally innervated counterparts, the degree of atrophy in those re-innervated muscles was substantially smaller when compared to non reinnervated control muscles, indicating that axons regenerating through implants had prevented muscle atrophy to a degree and had partially preserved muscle mass.

10.2.6. Histological analysis of regenerated tissue

Initially, it was unfeasible to make a histological assessment of the regenerated tissue, through the centre of the PI rolled device as it could not be sectioned without damaging its contents. Nevertheless, the study was able to examine the nerves emerging immediately distal to the rolled implants. This showed clusters of axons separated by connective tissue suggesting that each cluster or bundle was an extension of a mini-fascicle that had regenerated through the micro-channel. An example of one of these clusters of axons is shown in Fig. 10.13 (Top). Quantitatively, the total number of regenerated myelinated axons seen at the distal end was in the range of 1317 to 9380 in the different devices with a mean value of 6244, which was in agreement with mean value reported for the 4mm long passive SPNI implants presented earlier. The study also analysed the silicone type implant which was found to have far less regenerated axons compared to the SPNI devices despite the later having much longer channels (the silicone implants were 2.5mm long whilst the SPNI implants were 4mm long). The total number of myelinated axons per device in the silicone type implant was in the range of 1517 to 2734 giving a mean value of 2059 which was far less than mean value found in the SPNI implants. The improvement in regeneration through the SPNI devices could be attributed to device transparency. The silicone implants had 15% transparency whist the SPNI implants had 67% transparency meaning that more cross-sectional space is available for axonal regeneration in the SPNI devices compared to the silicone implants.

For a qualitative analysis of the regenerated tissue within the SPNI micro-channels, micro-computed tomography was used. This imaging technique is currently being

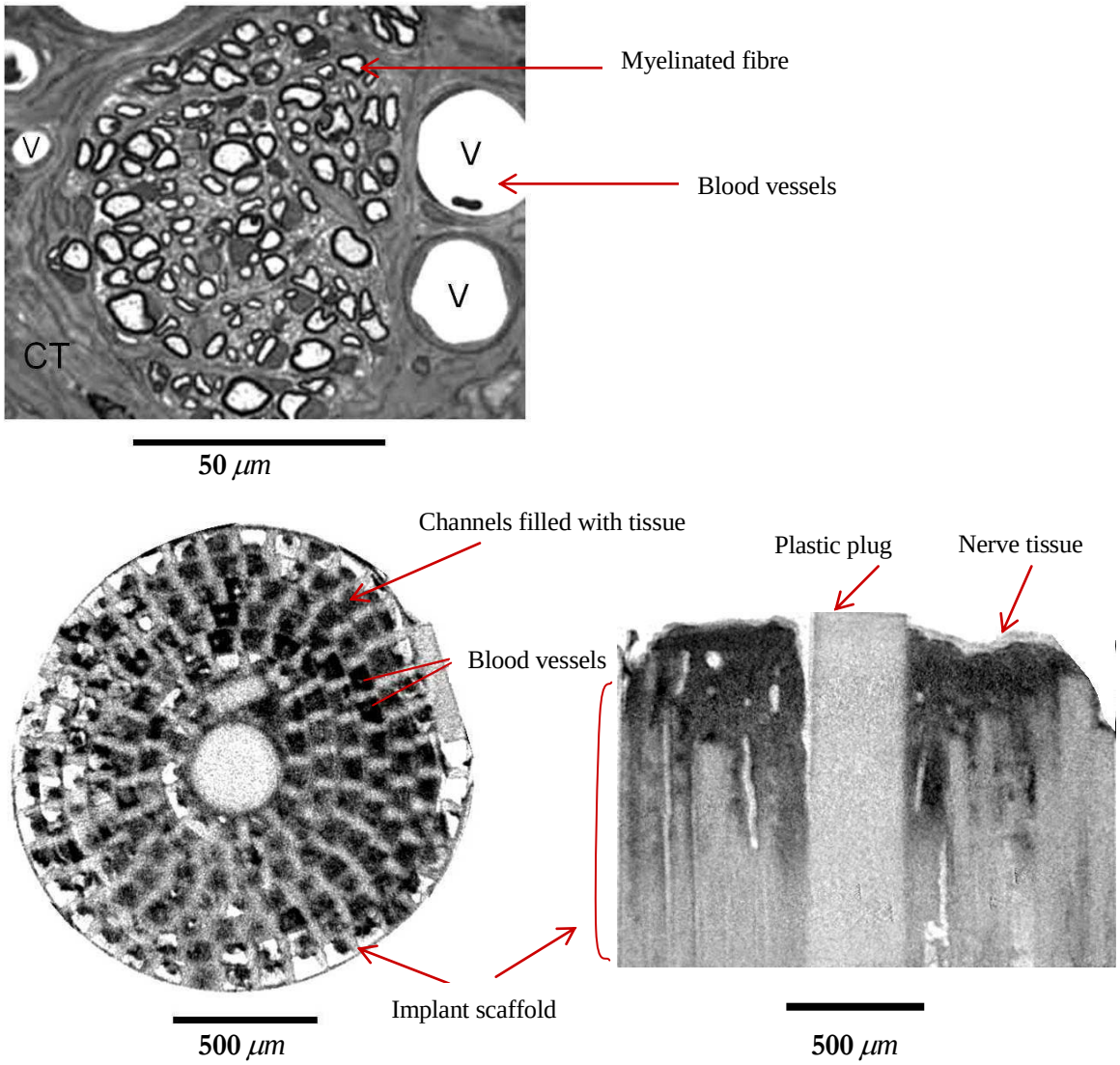


Fig. 10.13: Top- Clusters of axons surrounded by connective tissue (CT) and blood vessels (V) that have regenerate and grew through the SPNI (bar 50 μm) Bottom Right- Transverse Micro-computed tomography of SPNI device showing the implant scaffold in light grey, regenerated tissue in dark grey (Osmium stained) and vascularisation (as small white circles) through the micro-channel array (bar 500 μm)[65], Bottom Left-Equivalent vertical section through the SPNI device showing the implant scaffold in light grey with regenerated tissue in dark grey (osmium stained) and blood vessels as narrow white lines (bar 500 μm)[83].

optimised to enable examination of the SPNI channel content without the need to section device. It works by treating the explanted devices containing the regenerated tissue with osmium tetroxide which makes the myelin radio dense. This increases the x-ray attenuation of the neural tissue to a great extent. A high resolution x-ray micro-computed

tomography with reconstruction software is then used to produce horizontal cross-sectional layers through the rolled implant[83]. An example of one of the cross-sectional images that were obtained from a treated SPNI implant is illustrated in Fig. 10.13 (Bottom). The regenerated tissue is dark, whilst the polymeric channel walls and the plastic plug blocking the centre of the device are grey. Blood vessels appear as white dots within the dark regenerated tissue and this is seen in a number of channels. Empty channels are white as seen around the periphery of the roll. As the micro-computed tomography method is still under development, the resolution is not high enough to view individual myelin rings. However, from the images, 70 % could be given as an estimate for the number of channels containing regenerated axons which lends an approximate mean of about 50 myelinated axons per innervated micro-channel.

10.3. Chapter Summary

This chapter discussed the *in vivo* results for implanting the SPNI devices which have been fabricated according to design specifications detailed in chapter [5]. The first part of the chapter presented the findings for implanting the passive SPNI devices. 24 passive implants were fabricated in total; half of these had a 2.5 micro-channel length whilst the remaining half had a channel length of 4mm. Each passive implant had ($100\ \mu m$ x$100\ \mu m$) microchannel cross-sectional area, 180 micro-channels and 1.5mm implant diameter. The performance of these implants was evaluated against another implant prototype, namely passive PDMS implants, with similar device parameters apart from transparency which was much lower compared to that of the passive SPNI implants. After implanting the passive devices into adult male rats, regeneration was evaluated at 4 weeks post-implantation and at 12 weeks post-implantation. The histological assessment of the passive PDMS devices showed no axonal regeneration through the microchannels at any time point post implantation. The microchannels appeared mostly empty and contained only connective tissue and occasionally blood vessels. This was attributed to the low transparency of the PDMS implants (40%) limiting the space available for axons to regenerate.

In contrast regeneration through the passive SPNI devices was successful. At 4 weeks post-implantation regeneration through the passive SPNI devices was low where only a third (4 out 12 devices) of the 2.5 mm long devices had regenerated axons distal to the implant and no regeneration was detected through the micro-channels of the 4mm long devices. At 12 weeks post implantation, all the SPNI implants (both the 2.5mm long and the 4mm long implants) were found to support a good degree of regeneration on their distal part. This suggested that an implantation period of about 3months was required to allow sufficient time for regeneration through the SPNI devices before stimulation or recording was attempted through the microelectrodes of these implants. The micro-channel content resembled a mini-fascicle containing regenerated axons separated by connective tissue. Vascularisation needed to sustain the regenerating neural tissue was also evident through examination of the micro-channel contents which commonly showed the presence of 1 to 2 blood vessels per channel.

The remainder part of the chapter presented and discussed the findings for implanting active SPNI devices. The *in vivo* experiments on the active SPNI implants demonstrated that:

- The embedded micro-electrodes of the SPNI implants were able to record action potentials from the regenerating nerve fibres
- The SPNI embedded micro-electrodes were able to stimulate EMG responses through the axons that have regenerated through the SPNI micro-channels.
- The SPNI implant reduces the current required to stimulate the *t.a.* and *gastroc.* muscles, when compared to volume conductor.

Stimulation of the regenerated nerve fibres through the SPNI embedded microelectrodes triggered activity (EMG responses) in the *t.a*, and its antagonist *gastroc*. muscles demonstrating that the regenerated axons inside the implant microchannels had re-innervated motor units for these two muscles. This was evidenced by the ability to produce small quantized EMG increments as the stimulus current was slowly increased. the mean stimulus current for the SPNI implants was $26.2\,\mu A$ which is very low compared to those typically required in an unbounded volume conductor, but is several times higher than that recorded for the silicone implants ($4.29\,\mu A$). The reason behind this

increase is likely to be imperfections in channel sealing which gradually allowed current spill-over into the adjacent channels, and hence, more current is needed to reach threshold. In the minority of cases the spill-over was sufficient to cause cross-task between channels (30% of the motor units could be activated from more than one micro-channel). Therefore, addressing the imperfections in the channel sealing is important in future developments of SPNI devices as this will prevent current spill-over to the neighbouring channels, reduce stimulus current requirements and eliminate cross-talk between the channels.

Afferent action potentials triggered by electrical stimulation of the individual digits of the animal's hind-paw were recorded inside the SPNI channels via the embedded micro-electrodes. Recordings of robust action potentials with various sizes and latencies were obtained and a distinction between the signals originating from myelinated and those originating from unmyelinated fibres was possible. This demonstrates that the SPNI devices are able to record neural signals reliably and provide sufficient amplification to allow extracellular recording from different types of nerve fibres.

The histological assessment of the implanted devices revealed that the active SPNI devices had far more regenerated axons than their counterpart silicone implants. The difference was mainly attributed to the SPNI devices having greater transparency compared to the silicone implants. The 100 μm side square micro-channels seem to have successfully supported good regeneration as opposed to devices with smaller channel cross-sectional area reported in earlier studies[62]. Axons appeared to grow in bundles separated by connective tissue suggesting that each bundle is an extension of a mini-fascicle regenerating through the implant. Micro-computed tomography of the SPNI implants suggested that 70% of the channels contained regenerated axons giving an approximate mean of about 50 myelinated axons per innervated channel. This imaging technology is still under development and will definitely be beneficial for assessing the tissue content of future generations of the SPNI implants.

The SPNI implants demonstrated good durability with 97% of electrodes surviving the fabrication process and remaining functional in a harsh physiological medium for 3

months' implantation. Whilst 3% failure rate is promising, further enhancements will be made in the fabrication process of the SPNI implants to reduce the failure/degradation rate to zero as devices reaching clinical application in humans may need to survive for decades.

The work presented in this chapter demonstrated that the SPNI device provides a promising prototype for a novel peripheral neural interface. The 100 μm side 4mm long micro-channel arrays supported significant regeneration bridging the proximal and the distal parts of the severed nerve. Communication was established through the embedded microelectrodes which were able to stimulate and record from the regenerated tissue reliably. The channel confinement of the axons reduced the current threshold required for stimulation and provided sufficient amplification for signals to be recorded. Each micro-channel hosted a small group of axons which can potentially allow spatial selectivity when stimulating or recording within the interfaced nerve. This can provide sufficient resolution for most complex applications such as fine control of artificial limbs.

11. CONCLUSION AND FUTURE WORK

Peripheral neural interfaces are devices that couple the nervous system to electronic circuitry to control assistive technologies such as muscle stimulators or prosthetics that compensate for loss of function due to injury. They work by capturing and/or stimulating the action potentials via implanted electrodes.

Recording from peripheral axons is complicated by the extremely small amplitude of the extracellular neural signal and the concentration of current flow at nodes of Ranvier in myelinated axons. A recording electrode needs to be in close proximity to a node in order to record an optimal signal. The extracellular neural signals are in the order of tens of microvolts and are often submerged in electrical noise *in vivo.* Activity from surrounding musculature (EMG) which may be several hundred microvolts are the main source of electrical noise. Hence, a considerable improvement in the signal to noise ratio (SNR) is important if reliable recordings are to be made *in vivo* in the awake freely moving animal or patient.

My thesis presents the Spiral Peripheral Neural Interface (SPNI), a novel regenerative type implant which can potentially provide a solution for the key issues faced when developing a peripheral neural interface to restore lost function in nerve-injured patients. The implant has a 3D structure consisting of concentric rolls of micro-channel arrays which carry embedded micro-electrodes positioned halfway the channel length to stimulate and record neural signals from the axons that had been allowed to regenerate through its micro-channels.

Housing the regenerated axons in micro-channels produces amplified extracellular signals that are independent of proximity to a node of Ranvier. The microchannel confinement of the axons greatly increases extracellular impedance and hence the transmembrane currents flowing during a propagating action potential generate an amplified extracellular voltage which improves the Signal to Noise Ratio (SNR) of the recordings. Furthermore,

channel confinement prevents the trans-membrane currents leaving the nodes of Ranvier from spreading out in the extracellular space and forces them to flow longitudinally along the channel parallel to the axon. Consequently, the recorded signal becomes independent of proximity to the nodes. This means that a recording electrode does not have to be placed close to a node of Ranvier in the channel housing the axon.

Axon stimulation also benefits from the increased extracellular impedance afforded by micro-channel confinement of the axons. With higher extracellular impedance, less stimulus current is needed to reach the threshold required for generating an action potential in an adjacent axon. The micro-channel isolates the delivered stimulus current and allows it to only affect axons housed in that particular channel providing spatial selectivity for stimulation as well as recording.

The SPNI implants were designed taking into account experimental considerations relating to the micro-channel dimensional parameters that would maximise regeneration through the rolled devices. The implant were fabricated using polyimides which provide the flexibility and the durability needed to mechanically support regenerating axons and provide regeneration guidance through the channels. The SPNI structure consisted of four layers; the substrate layer which carried the patterned gold layer constituting the microelectrode sites of the implant, the metal wiring and the connection pads of the device. The metal layer was fabricated by thermally evaporating gold and a thin adhesion layer of chromium. This layer was then passivated by a thin insulation layer made using a photo-sensitive polyimide. Finally the micro-channel layer was fabricated on the top of the insulation layer using another type of photo-sensitive polyimide. All the layers were fabricated using planar micro-fabrication. Special care was taken to fabricate the thick micro-channel layer. This involved using a very slow ramping temperature during the pre-baking stage of the layer to enable solvent to be evenly dried out so that bubble formation and shrinkage of the layer was avoided. After patterning the channel layer and curing the wafer, we obtained a two dimensional sheet containing the four stated layers which were then rolled to form the three dimensional structure of the implant with closed micro-channel arrays. The electrodes were exposed

at the bottom of each channel to enable intimate contact with the axons that will regenerate through the implant.

The design of the device was configured such that the metal wiring is placed at the neutral place. This was done by developing a stress model to calculate the neutral plane and then varying the substrate thickness to find where the neutral plane corresponds to the top of the substrate (as the metal layer will always be placed at the top of the substrate). At first, the initial stress model was derived and analysed taking into account the effect of the young's modulus of the different materials. This model suggested a substrate thickness of 35 µm for placing the metal layer at the neutral plane of the structure. However, it was realised that this stress model does not accurately describe the strains in the rolled structure. It was found by re-calculating the stress model[59] based on the elastic theory of bending that the neutral plane will always almost reside halfway the substrate. This indicated that the metal wiring was under compressive strains rather than tensile strains in the rolled structure. The corrected stress model illustrated that thinner substrates are preferable to thicker substrates as less compressive strains will be present in the rolled structure.

The Microflex technology was incorporated into the fabrication of the SPNI implants as a reliable method to connect the implants to external circuitry. The process involved optimising the hole size and the thickness of the substrate layer that were compatible with the MFI technique. It was found that the size of the via hole should not be less than 45µmx45µm and the thickness of the polyimide substrate layer should be no more than 20µm. Given a suitable hole size it was possible to ball bond samples with substrate thicknesses of less than 20µm, but as the thickness approaches 20µm, ball bonding became very challenging. Substrate thicknesses above this value make it difficult for the ball to reach the bonding target underneath (gold printed alumina) through the via hole.

To access whether the metal wiring in the SPNI devices had successfully survived the fabrication process and the rolling, the impedance and phase spectra of different fabricated devices were recorded prior and post rolling using an impedance analyser

[59] Please refer to section [5.4.5] chapter 5 for details regarding stress model calculation

setup. The spectra of the different devices were analysed and compared against modelling data representing an equivalent circuit model for the electrode-electrolyte interface. It was found that:

- The devices generally possessed an interface with capacitive element
- The rolling of the SPNI devices increased the impedance of the devices as rolling the devices transformed the channels from 2D open roof channels into 3D channels with a closed roof. The microelectrodes became housed in 3D closed channels that were only accessible from their ends. This, therefore, affected the path of the current flow and led to an increase in the solution resistance which resulted in an increase in the impedance of the electrode/ electrolyte interface.
- The impedance ranges recorded from two batches of SPNI devices differed significantly. Impedances recorded from batch1 devices which had undergone the descum process, had a mean impedance of $433\,K\Omega$ at 1KHz post rolling. These values were in accordance with impedances reported for similar electrodes. However, batch2 devices which did not undergo the descum process ended up with much higher impedances and presented a mean value of $5\mathrm{M}\Omega$ at 1KHz after rolling. This showed the effect residues can have on the microelectrode impedance and the importance of the descuming process for the fabrication of the SPNI implants.

The fabricated SPNI devices were tested *in vivo* by implanting them in animals for three months. This was done to evaluate regeneration through the micro-channels of the implants and test if the implants were able to stimulate and record neural signals from the regenerated axons reliably[60]. The findings from these experiments demonstrated that regeneration through micro-channels with a cross-section of $100\,\mu m$ x$100\,\mu m$ and a length of 4mm was very successful after three months of implantation as the reported numbers of myelinated axons that had grown through the channels were similar to those found in uninjured nerve. It was noted that axons should be allowed to regenerate for about three months before attempting to stimulate or record signals through the

[60] The experiments were conducted in collaboration with King college London Neuroscience.

microelectrodes of the implants; as this period ensures that enough time is given for axonal regeneration through the channels.

The experiments also proved that SPNI implants were able to successfully stimulate and record extracellular signals through the embedded microelectrodes. Stimulating the regenerated nerve fibres generated EMG responses distally demonstrating that axons passing through the micro-channels had re-innervated distal muscles and could efficiently propagate action potentials. Furthermore, channel confinement of the axons had reduced the current threshold required for stimulation through the SPNI implants in comparison to unlimited volume conductor. However, the SPNI current threshold was higher than that reported for a similar implant made of silicone. It was likely that imperfect channel sealing was the reason as this would allow current to leak out of the channel and hence increase the amount of current required for stimulation. Future development of the SPNI devices will include a fabrication step to ensure the micro-channels are completely sealed.

The SPNI devices were able to record neural signals reliably and provide sufficient amplification to allow extracellular recording from different types of nerve fibres. Afferent action potentials triggered by electrical stimulation of the individual digits of the animal's hind-paw were recorded inside the SPNI channels via the embedded micro-electrodes. The SPNI implant was able to capture robust action potentials with various sizes and latencies allowing a possible distinction between the signals originating from myelinated and unmyelinated fibres.

11.1. Future work

The main motivation behind neural interfaces is to capture and/or stimulate action potentials via implanted electrodes in order to re-establish lost functional connectivity. They are intended for long term use to control assistive technologies such as muscle stimulators or prosthetics in case of an amputation due to an injury. However providing fine control to these assistive technologies is a sophisticated and a highly complex

application as it requires a neural interface that can reliably and efficiently interface with high density of nerve fibres (a large peripheral nerve contains several thousands of axons). This is a complex task considering the required number of connections and the necessary signal processing. It is expected that high resolution interfaces will improve selectivity and will eventually provide a means to restore function to nerve-injured patients. However, the design of durable and reliable peripheral nerve interfaces with sufficient resolution, selectivity, and multiplexing capacity for applications such as prosthetic limb control remains a challenge. The majority of peripheral neural interfaces fall into one of the following categories: cuffs, penetrating electrodes and regenerative sieve electrodes which have been discussed earlier in a dedicated review chapter. Cuffs can effectively stimulate a whole nerve, but achieving detailed spatial selectivity within the nerve is difficult as the electrode sites are only in contact with the epineurium (the surface of the nerve). Penetrating electrodes, on the other hand, do not have a fixed interface with their target axons as time post implantation evolves. This is because of fibrous tissue sheath forming around the contact sites pushing them away from their target neural tissue which affects the reliability of the recording and/or stimulation over time and hence compromising selectivity. In addition, penetrating electrodes are not necessarily designed to match the anatomy of the peripheral nerve and hence obtaining resolution throughout the nerve cross-section might be impracticable. The regenerative sieve implants normally have fixed interfaces with the neural tissue that had grown through their holes, however, a high resolution interface is not feasible with this interface type because of limitations with the number of electrode sites that can be used (related to limitations with lead out wiring). The extremely small size of the extracellular signals and their dependence on proximity to a node of Ranvier in the three implant types just explained complicates further the task of obtaining an interface with sufficient selectivity.

The SPNI implant offers a promising prototype for a high resolution device that can potentially meet the information transfer requirements of the most sophisticated applications such as driving limb prostheses and controlling denervated limb muscles via implanted stimulators. Confinement in an insulated microchannel provides spatial selectivity for stimulation and recording. If we consider the nerve to be divided into small groups containing few axons and each group passes through a microchannel, a large

enough insulated micro-channel array might provide sufficient resolution and selectivity. From the histological assessment of regeneration through the SPNI microchannels, the mean number of myelinated fibres in each innervated microchannel was estimated to be 50. Spatial selectivity in an insulated micro-channel interface will be simply governed by the number of channels into which the axons from the nerve are distributed. Hence to maximise selectivity within future SPN implants, further work needs to be done to enable axons to grow through much narrower microchannels. In addition to producing larger recordable signals[10, 84], narrower channels would have space for fewer axons potentially improving selectivity.

The SPNI channels have a $100\,\mu m$ x$100\,\mu m$ cross-sectional area as this seems to offer sufficient microchannel space for good regeneration through the implants. Any smaller cross-sectional area results in poor or no regeneration through the implants[62]. This is because of fibrous sheath formation around the periphery of the micro-channels which limits the room available for axons to regenerate through the channels. The sheath is produced as a foreign body reaction to the inner walls of the micro-channels and is nearly a universal host response to the surface of artificial implants[85]. *In vitro*, where there is no fibrous sheath formation, axons can grow through far narrower microchannels[84]. It would be advantageous to be able to modulate the foreign body response *in vivo* to reduce the extent of fibrous tissue deposition, which might permit a reduction in microchannel calibre without compromising axon growth. The cells constantly probe their surroundings for tensile strength. Encountering surfaces (like artificial implants) that do not have the softness typically displayed by biological tissue can trigger a foreign body reaction. Minimizing this mechanical mismatch may be used in combination with bio-chemical strategies to prevent foreign body reaction. Our research group will work collaboratively on two approaches to minimise the mechanical mismatch between microchannel surfaces of the SPNI implant and the biological tissues that come into contact with these surfaces; the two approaches involve:

- Coating the surface of the microchannels with soft gels that have well controlled mechanical properties
- Nano-structuring and etching the inner surface of the microchannels during the fabrication of the SPNI implants to build polymeric nanopillars. The nanopillars

can bend under the probing force making the surface seem softer to cells than the plain polyimide surface.

Bio-chemical approaches that might be investigated include the use of growth factors and anti-scaring drugs. It is hoped that a combination of the bio-chemical and bio-mechanical approaches will minimise or prevent fibrosis allowing regeneration through much narrower microchannels which can significantly improve the spatial selectivity of the SPNI implants.

12. APPENDICES

A.1 Masks used to fabricate the SPNI devices

1. SPNI devices 1: used in in-vivo studies

Total width of connection pad region: 1cm

SPNI length: 4cm

SPNI micro-channel length: 4mm

SPNI micro-channel width: 100 μm

Metal track width: 50 μm

Micro-electrode site dimension: 30 μm x100 μm

Contact pad dimensions: 400 μm x1000 μm

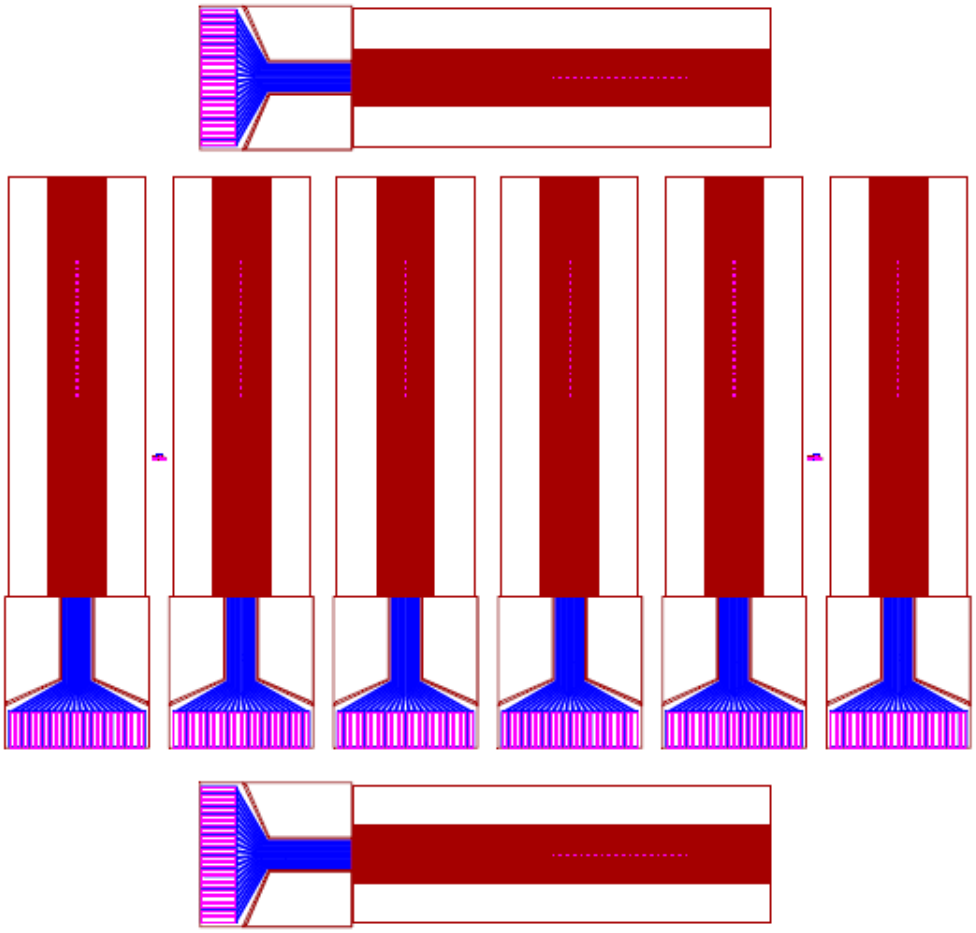


Fig. 12.1: the overall SPNI photpmask layout with the overlapping layers. This layout can produce 8 SPNI devices per wafer.

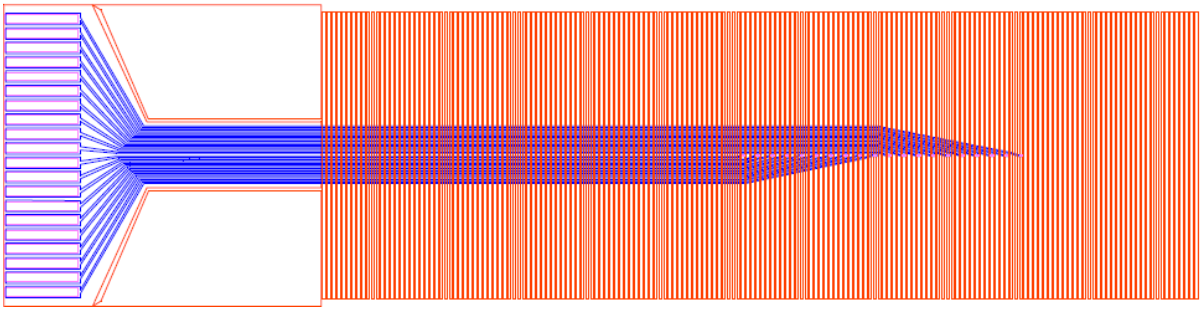


Fig. 12.2: The photomask design for one SPNI device with its overlapping layers.

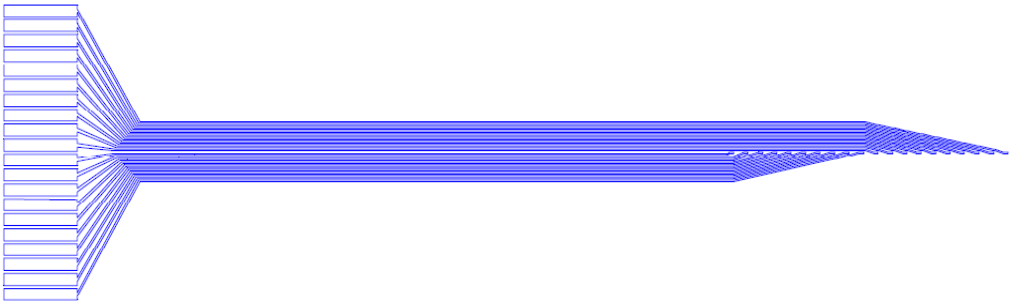


Fig. 12.3: the photomask footprint for the metallisation layer consisting of the microelectrodes, the metal tracks and the connection pads



Fig. 12.4: the photomask for the insulation layer; insulating the metal tracks whilst exposing the microelectrode sites and the connection pads

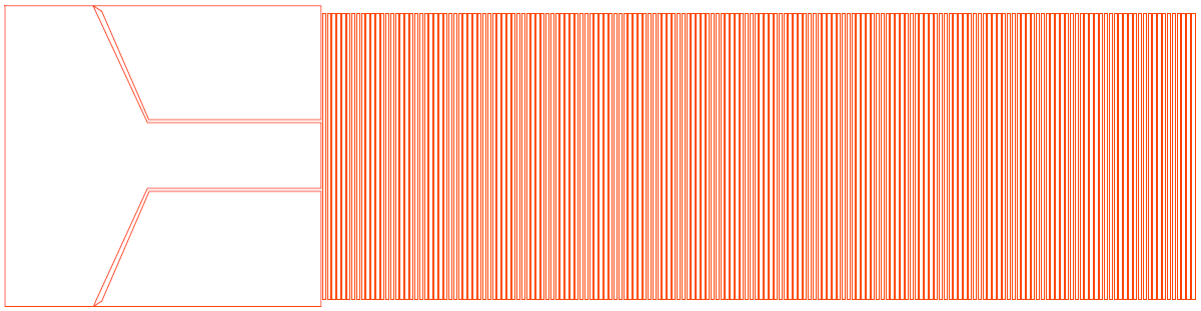


Fig. 12.5: The photomask for the micro-channel layer, the channels in these devices have to be cut down into 4mm long micro-channels

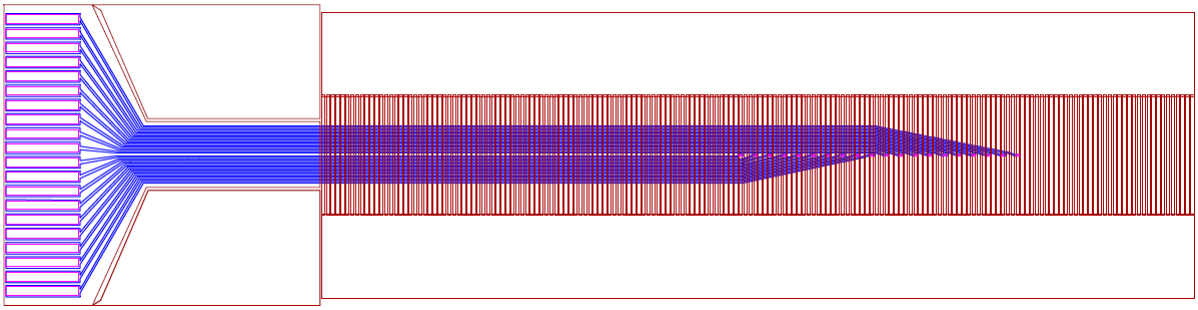


Fig. 12.6: The photomask design for one SPNI device with its overlapping layers, the microchannels are designed to have the right length in this mask (4mm). Hence, the micro-channel length is defined photolithographically, eliminating the need to cut the micro-channels down to the right length. However, as the substrate is still made out of non-photo-definable pyralin 2611, I still need to cut around the foot print of the devices to separate them. Making the substrate with the photo-sensitive Durimide 7020 (as is done when incorporating the Microflex interconnection technique MFI, see next Appendix)

2. SPNI device dimensions: Incorporating Microflex Technology (MFI)

Total width of connection pad region: 1cm

SPNI length: 4cm

SPNI micro-channel length: 4mm

SPNI micro-channel width: 100 μm

Metal track width: 50 μm

Micro-electrode site dimension: 30 μm x100 μm

Contact pad dimensions: 400 μm x1000 μm

Contact pad separation: 100 μm

Microflex interconnection Via hole range: 35-70 μm square

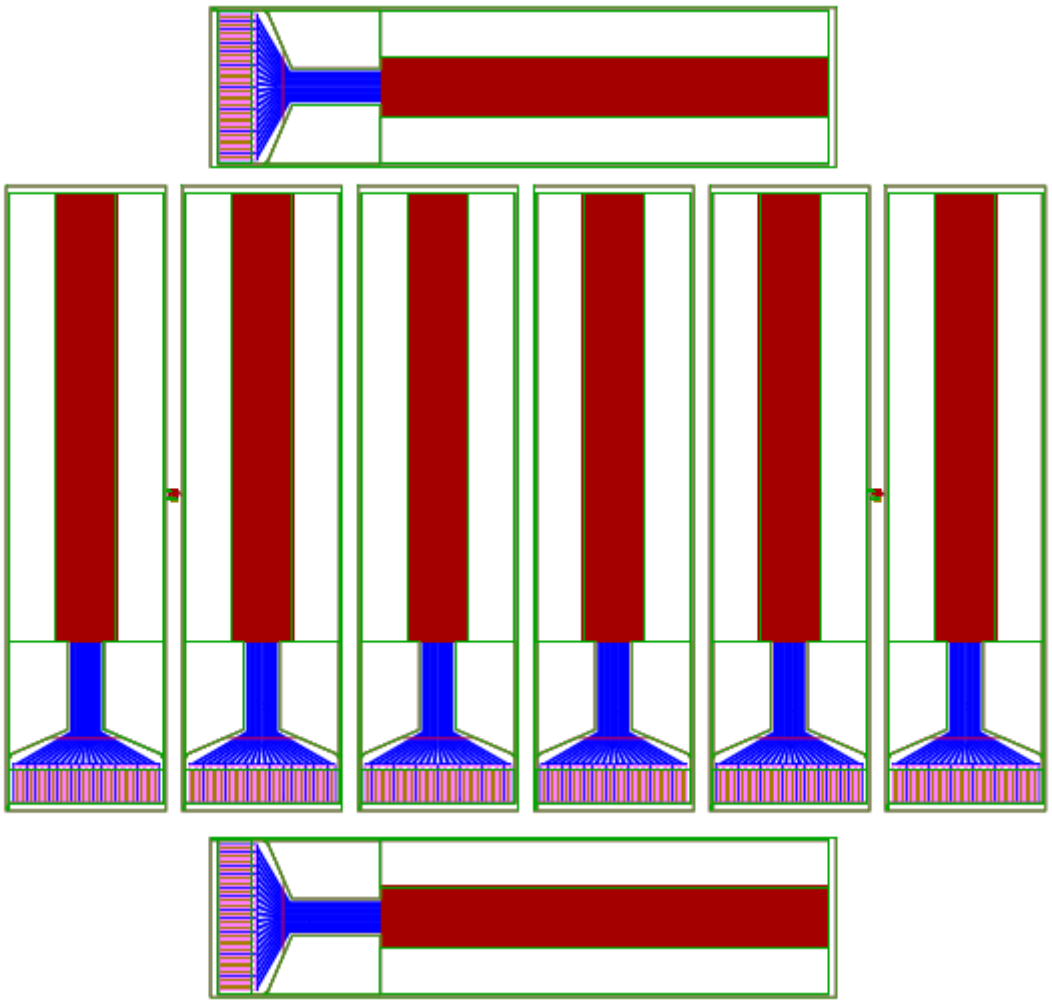


Fig. 12.7: the overall SPNI photpmask layout with the overlapping layers. This layout can produce 8 SPNI devices per wafer.

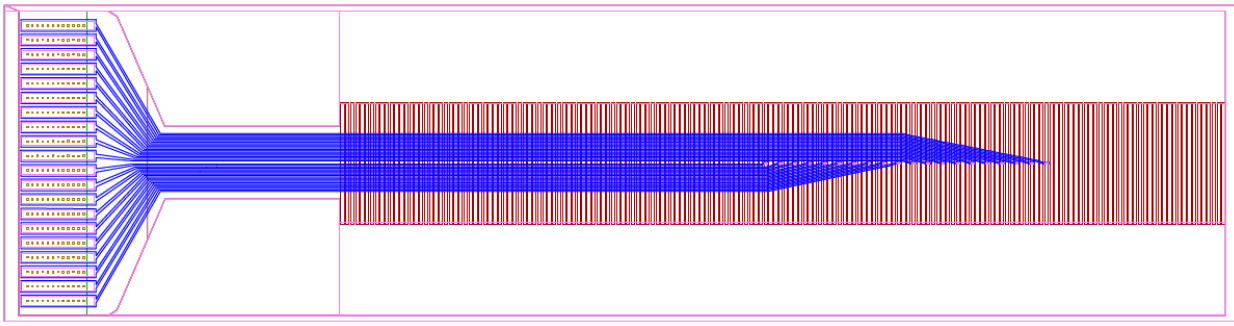


Fig. 12.8: The photomask design for one SPNI device with its overlapping layers. This design incorporates the Microflex interconnection technique MFI by designing the substrate to have via holes for MFI.

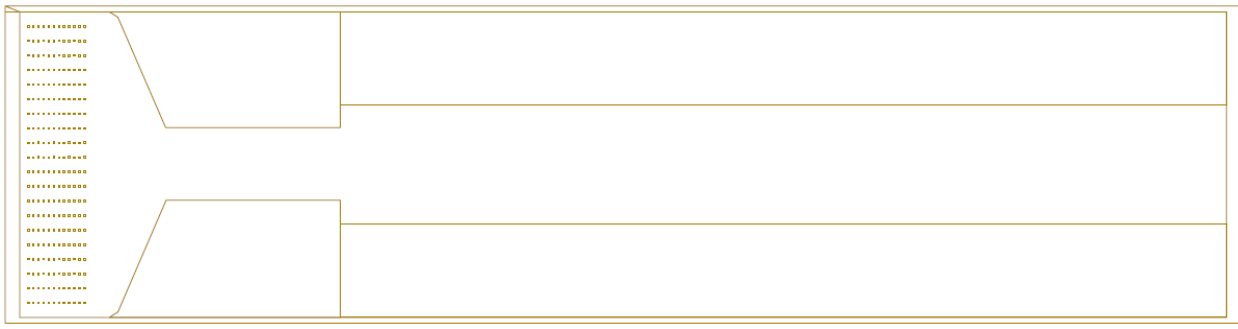


Fig. 12.9: The photomask design for the 1st layer of the photo-definable substrate with the via holes for MFI. This layer will enable ball bonding through the connection pads of the SPNI. The substrate will be made out of photo-definable Durimide7020, allowing the device foot print to be patterned and separated into individual devices photolithographically.

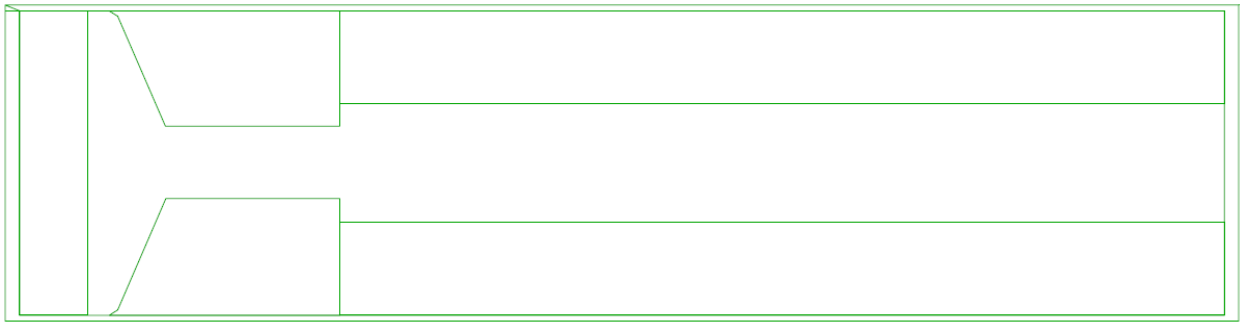


Fig. 12.10: The photomask design for the 2nd layer of the photo-definable substrate. This layer sets the substrate thickness to the right level so that the metal layer of the SPNI device stays intact during rolling.

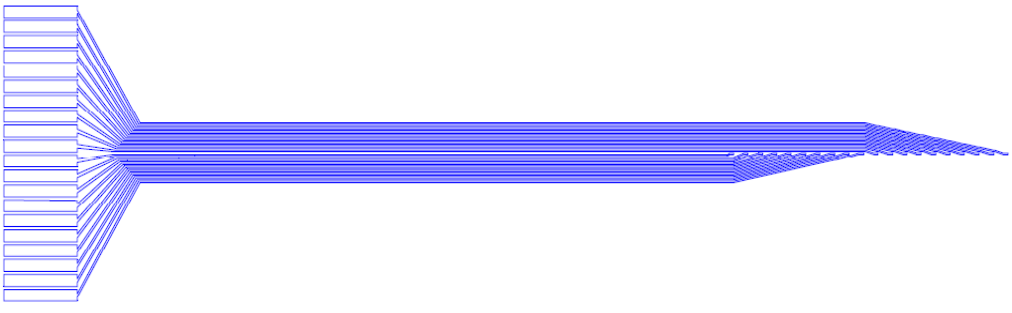


Fig. 12.11: the photomask footprint for the metallisation layer consisting of the microelectrodes, the metal tracks and the connection pads.



Fig. 12.12: hotomask for the insulation layer; insulating the metal tracks whilst exposing the microelectrode sites and the connection pads. This layer is also shaped on the device footprint to allowing the individual device prints to be defined and separated photolithographically

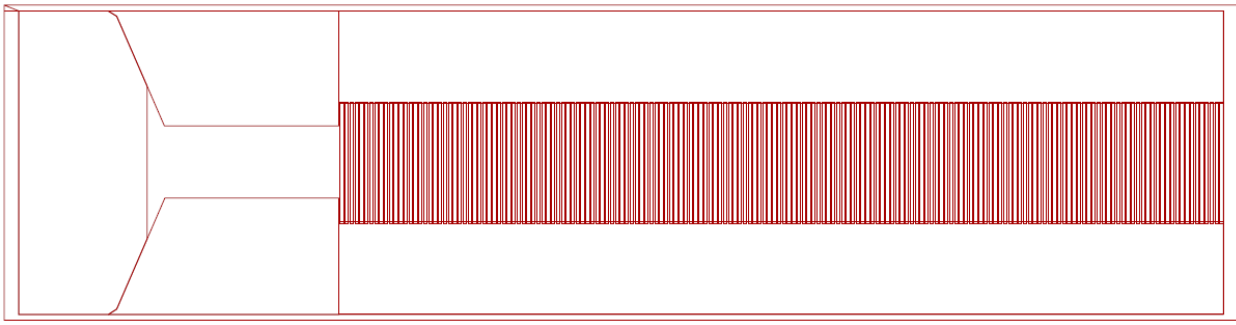


Fig. 12.13: The photomask for the micro-channel layer. The micro-channels are designed to have the right length in this mask (4mm). Hence, the micro-channel length is defined photolithographically, eliminating the need to cut the micro-channels down to the right length (4mm). The substrate will be made out of photo-definable Durimide7020, allowing the device foot print to be patterned and separated into individual devices photolithographically.

A.2 Photos for some of the chrome-on-glass masks used in the fabrication the SPNI devices

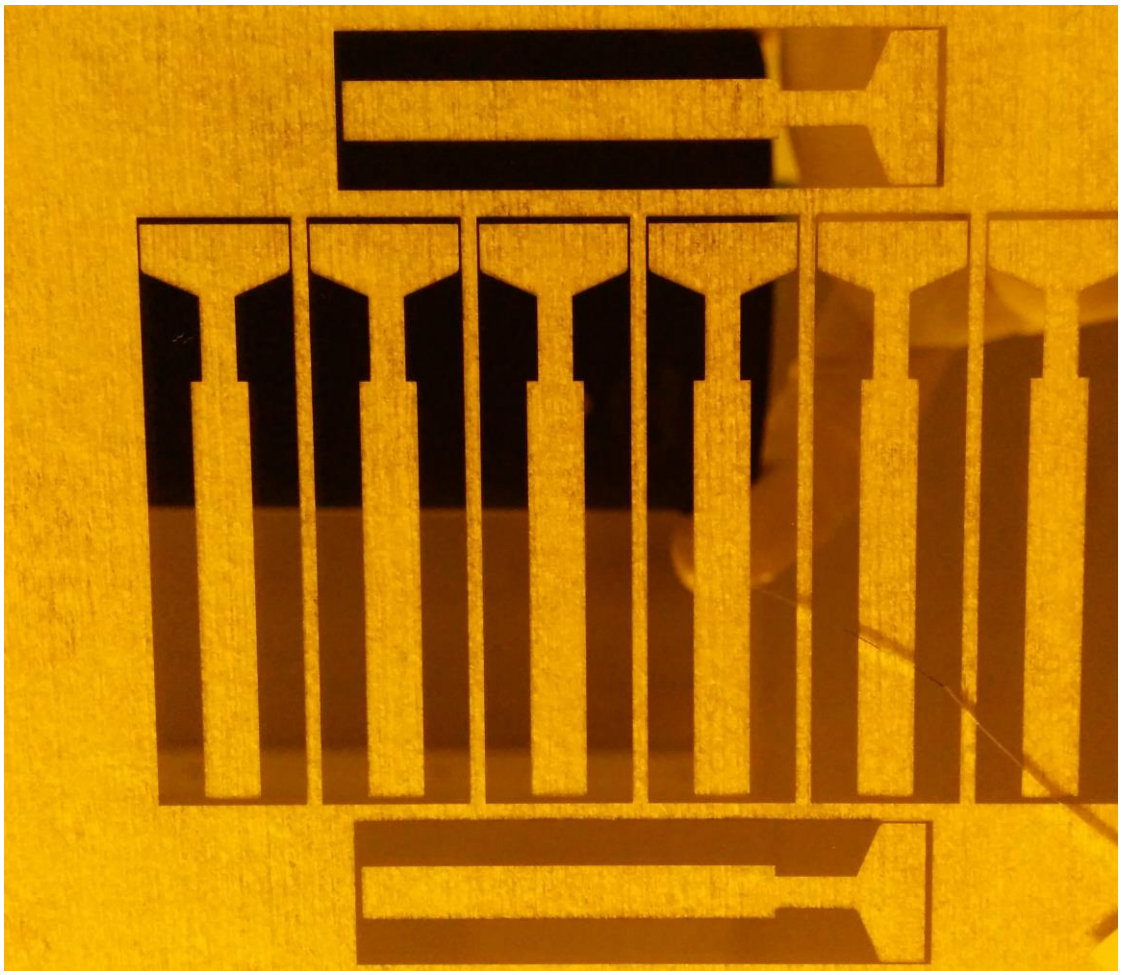


Fig. 12.14: the chrome-on-glass mask used in fabricating the photosensitive substrate layer of the SPNI devices

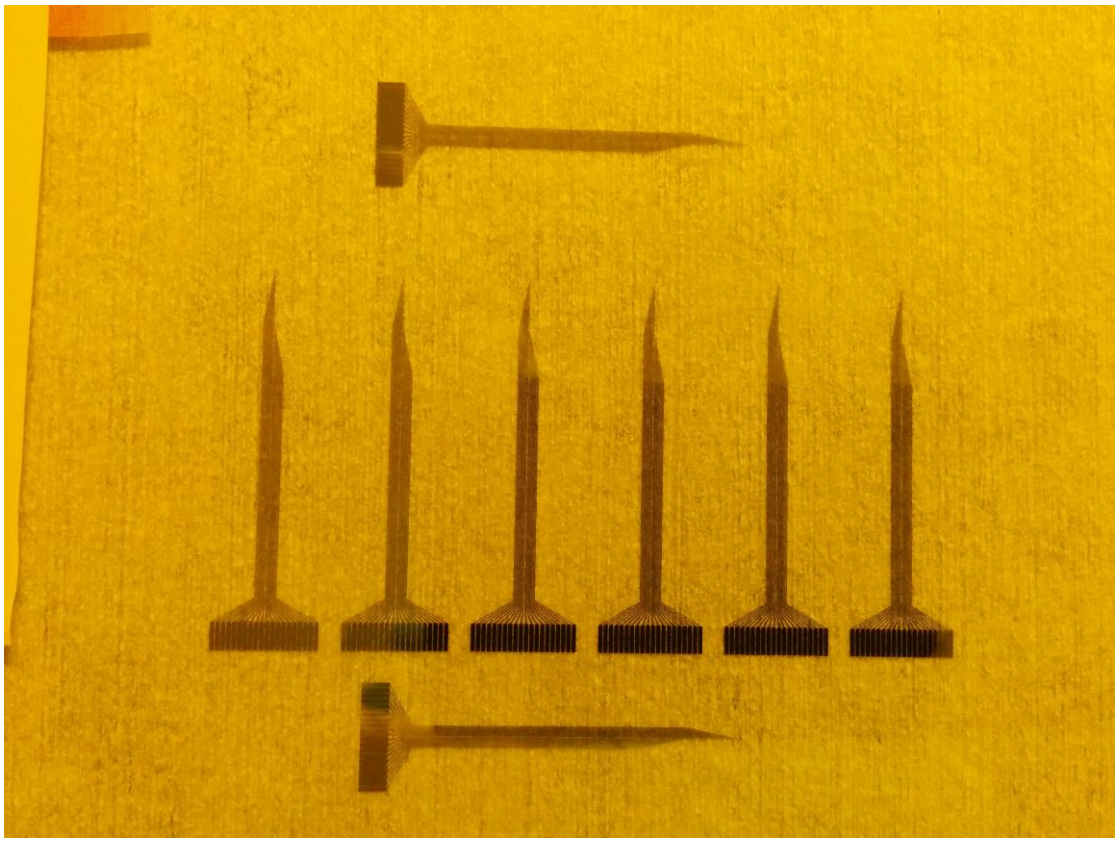


Fig. 12.15: the chrome-on-glass mask used in fabricating the metallisation layer of the SPNI devices

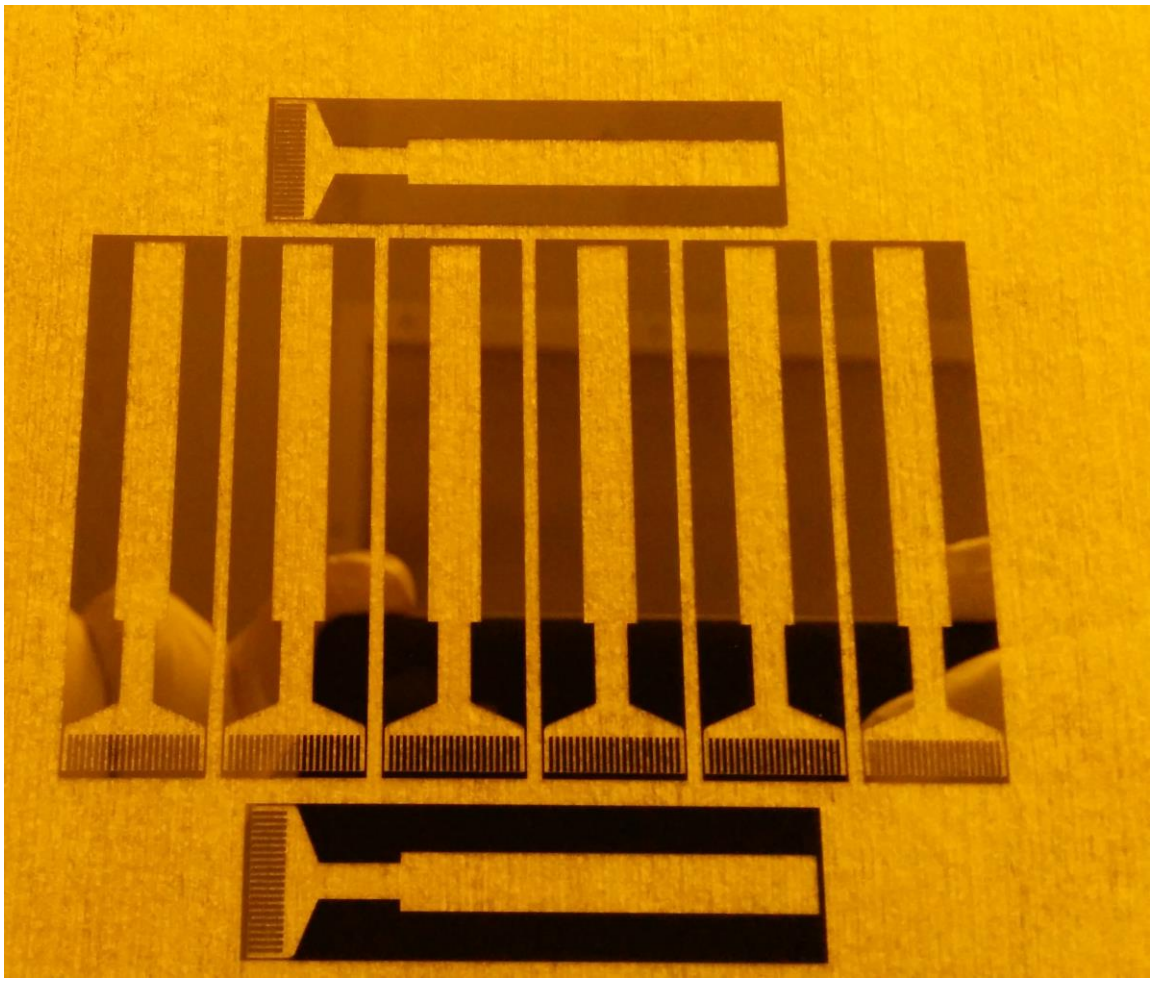


Fig. 12.16: the chrome-on-glass mask used in fabricating the insulation layer of the SPNI devices

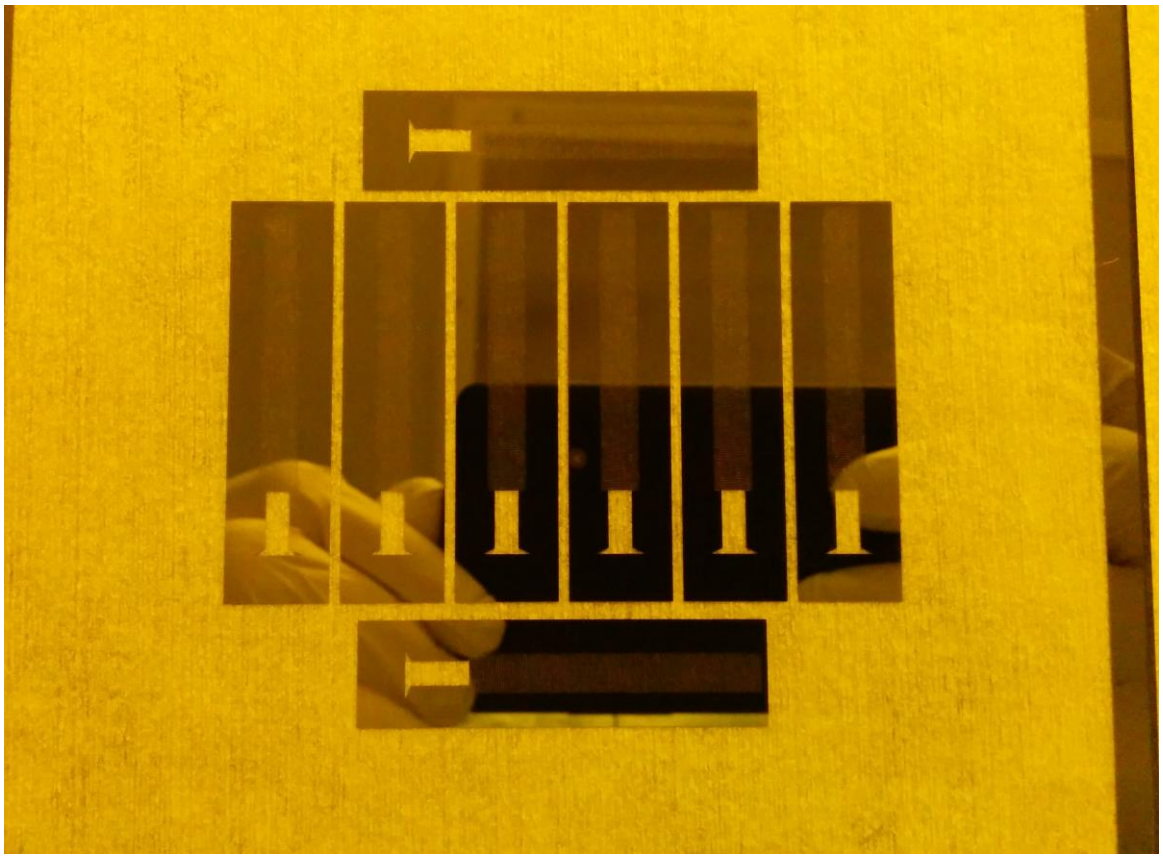


Fig. 12.17: e chrome-on-glass mask used in fabricating the microchannel layer of the SPNI devices

A.3 SPNI fabrication process- step by step summary

Process steps for the pyralin 2611 substrate

1. Clean the carrier wafer by immersing in acetone and then isopropanol (the wafers have been cleaned previously with Piranha solution in addition to undergoing a10 minute oxygen plasma clean).
2. Bake the wafer at 150^{o}C for dehydration (for 10 minutes)
3. Spin the PI 2611 at 500 rpm for 10 seconds to spread out the material and then at 1500 RPM for 60seconds to give a 12 μm thick substrate after full cure.
4. Fully cure the wafer in a programmable furnace at 200^{o}C for 30 minutes, then at 350^{o}C for 60 minutes in a nitrogen environment. The first part of the curing

process was done with a ramp rate of 4 ^{o}C/minute to raise the temperature from room temperature to 200 ^{o}C, whilst the second part of the curing process used a ramp rate of 2.5 ^{o}C/minute to elevate the temperature from 200 ^{o}C to 350 ^{o}C.

5. Leave the wafer in the furnace to cool down overnight.
6. To make the substrate layer thicker, repeat steps from 2 to 5.

Process steps patterning the metallisation layer of the SPNI devices

1. After evaporating a chromium and a gold layer on the fully cured substrate layer, clean the wafer with acetone and isopropanol
2. Bake the wafer at 120 ^{o}C for 1 minute.
3. Dispense enough S1813 photoresist on the centre of the wafer and spin the wafer at 500RPM for 5 seconds and then at 2000RPM for 20 seconds. This is to make a 2 μm thick layer
4. bake the sample for 2 minutes at 120 ^{o}C.
5. with the canon mask aligher, align and expose the sample for 10 seconds (using the photomask designed for patterning the SPNI metal layer)
6. develop the sample in MF319 for 2 minutes to create an image that will be transferred onto the metal layer
7. Rinse the sample wafer with Deionised water
8. The unwanted metal regions are etched away by placing the wafer in a gold etchant for 50 seconds, and then in a chrome etchant for 5-10 seconds. The wafer is then rinsed with de-ionized water to stop the wet etching process and is dried with a nitrogen gun.
9. After this, the photoresist layer is removed by immersing the wafer in acetone and then isopronanol, the result is a patterned metal layer electrode sites, metal tracks and contact pads.

Process steps for the insulation layer

A $3\mu m$ thick insulation layer was fabricated using Durimide PSPI7505. The process steps for this layer are as follows:

10. Spin coat PSPI7505 at 3500 RPM spin speed for 45 seconds.
11. Softbake the layer on hotplate at 70 ^{0}C for 5 minutes then increase the temperature to 95 ^{0}C and bake the sample at this temperature for another 5 minutes.
12. Leave the wafer to cool down for at least 20 minutes before exposure.
13. Expose the layer using the photomask designed specifically for the insulation layer taking care to align the insulation layer to the underlying metal layer (for active devices).
14. Using a programmable hotplate, post bake the wafer at 95 ^{0}C for 2-3 minutes, and then leave to cool down for few minutes.
15. Develop the layer using combination of developer/rinsing solvent (HTR D-2 and RER600). This is done by placing the wafer in the developer for 1 minute and then in a mixture of developer/solvent (with a 50/50 ratio) for 10 seconds. The wafer is then placed in the RER 600 solvent for about 1minutes.
16. Repeated step 6 until a clear pattern is seen
17. The sample wafer is then rinsed with d-ionised water and dried with a nitrogen gun
18. To de-sensitize the insulation layer, bake the sample wafer on a programmable hotplate at 150^{0}C for 30minutes.

Process steps for the micro-channel layer

1. Clean the wafer with acetone and isopropanol
2. Bake the wafer at 150^{o}C for few minutes for dehydration
3. Spin coat Durimide7020 (the photosensitive polyimide7020) at 270 RPM spin speed for 60 seconds
4. Soft-bake the layer on hotplate at temperature ramp up rate of 0.3^{0}C/minute starting from 30 ^{0}C until 95 ^{0}C. Leave the sample to bake at 95 ^{0}C for another 10 minutes

5. take the wafer off the programmable hotplate and leave it to cool down for an hour or more before exposure
6. Expose the layer with UV light in the wavelength range of 380 to 400nm using a Canon mask aligner. The UV light is shined through chrome glass masks (designed specifically for the micro-channel layer) after aligning the micro-channel layer to the underlying insulation layer (for active devices).
7. Post bake the wafer at 95 ^{0}C for 2-3 minutes, and then leave to cool down for few minutes
8. Develop the layer using combination of developer/rinsing solvent (HTR D-2 and RER600). This is done by placing the wafer in the developer for 1 minute and then in a mixture of developer/solvent (with a 50/50 ratio) for 20 seconds. The wafer is then placed in the RER 600 solvent for about 2minutes.
9. Step 8 needs to be repeated until a clear pattern is evolves, and for the 100µm thick channel layer this can take more than 20 repetitions. The beaker containing the wafers needs to be constantly shacked to aid pattern development. An ultrasonic bath may be used at a suitable setting to speed up the process. The solvents might need to be changed for fresh ones few times.
10. The wafer is rinsed with d-ionised water and dried with a nitrogen gun once a clear pattern has developed.
11. The processed sample wafer is then fully cured in a programmable furnace at 200^{o}C for 30 minutes, then at 350^{o}C for 60 minutes in a nitrogen environment. The first part of the curing process was done with a ramp rate of 4 ^{o}C/minute to raise the temperature from room temperature to 200 ^{o}C, whilst the second part of the curing process used a ramp rate of 2.5 ^{o}C/minute to elevate the temperature from 200 ^{o}C to 350 ^{o}C.
12. Leave the wafer in the furnace to cool down overnight

13. BIBLIOGRAPHY

[1] X. Navarro and E. Verdú, "Cell transplants and artificial guides for nerve repair," in *Brain Damage and Repair*, T. Herdegen and J. D. García, Eds., ed: Kluwer Academic Publishing, 2004, pp. 451–471.

[2] X. Navarro, *et al.*, "A critical review of interfaces with the peripheral nervous system for the control of neuro-prostheses and hybrid bionic systems," *Journal of Peripheral Nervous System*, vol. 10, pp. 229–258, 2005.

[3] M. Lotze, *et al.*, "Activation of cortical and cerebellar motor areas during executed and imagined hand movements: An fmri study," *Journal of Cognitive Neuroscience*, vol. 11, pp. 491-501, 1999.

[4] L. R. Hochberg, *et al.*, "Neuronal ensemble control of prosthetic devices by a human with tetraplegia," *Nature*, vol. 442, pp. 164-171, 2006.

[5] A. Frommhold, "Nanotexturisation of Gold Surfaces and its Application to Neural Implants," Ph.D., The University of Birmingham, 2010.

[6] F. Spelman, "The past, present, and future of cochlear prostheses," *IEEE Engineering in Medicine and Biology Magazine*, vol. 18, pp. 27–33, 1999.

[7] G. Dagnelie and R. W. Massof, "Toward an artificial eye," *IEEE Spectrum*, vol. 33, pp. 20-29, 1996.

[8] R. Stein, *et al.*, "Principles underlying new methods for chronic neural recording.," *The Canadian Journal of Neurological Sciences*, vol. 2, pp. 235-44, 1975.

[9] X. Navarro, *et al.*, "Stimulation and recording from regenerated peripheral nerves through polyimide sieve electrodes," *Journal of Peripheral Nervous System*, vol. 3, pp. 91-101, 1998.

[10] J. FitzGerald, *et al.*, "Microchannels as Axonal Amplifiers," *IEEE transactions on biomedical Engineering*, vol. 55, pp. 1136-1146, 2008.

[11] K. Horch and G. Dhillon, Eds., *Neuroprosthetics : Theory and Practice (Series on Bioengineering and Biomedical Engineering, Vol. 2)*. Singapore: World Scientific Publishing Co. Ptc. Ltd., 2004, p.^pp. Pages.

[12] C. Krebs, *et al.*, *Neuroscience* USA: Lippinott Williams and Wilkins, 2012.

[13] J. Malmivuo and R. Plonsey, *Bioelectromagnetism*. Oxford: Oxford University Press, 1995.

[14] C. G. Boeree. 16/05). *The Neuron* *http://webspace.ship.edu/cgboer/theneuron.html*

[15] I. B. Levitan, *The Neuron*. Oxford: Oxford Univ. Press, 1997.

[16] Unknown. 25/05/2014). *Anatomy and Physiology*. Available: https://www.studyblue.com/notes/note/n/lab-13-14/deck/6226124

[17] R. Barrett, "Novel Processing Routes for Neural Interfaces," Ph.D., The University of Birmingham, 2013.

[18] J. P. F. Spratley, "Mechanical Design of an Injectable Microsensor for Neural Connection within the Motor Cortex of the Human Brain," Ph.D., The University of Birmingham, 2008.

[19] X. Navarro, *et al.*, "A critical review of interfaces with the peripheral nervous system for the control of neuroprostheses and hybrid bionic systems," *Journal of Peripheral Nervous System* pp. 229–258 2005.

[20] M. Wieler, *et al.*, "Walkaid: An Improved Functional Electrical Stimulator for Correcting Foot-Drop," in *IFES*, Proc. 1st Ann Conf

[21] P. Taylor, *et al.*, "Clinical use of the Odstock dropped foot stimulator: its effect on the speed and effort of walking.," *Archives of Physical Medicine and Rehabilitation*, vol. 80, pp. 1577–1583, 1999.

[22] N. Bhadra, *et al.*, "Implanted stimulators for restoration of function in spinal cord injury," *Medical Engineering & Physics*, vol. 23, pp. 19–28, 2001.

[23] R. Kobetic, *et al.*, "Implanted functional electrical stimulation system for mobility in paraplegia: a follow-up case report," *IEEE Transactions on Rehabilitation Engineering* vol. 7, pp. 390–398, 1999.

[24] H. Onishi, *et al.*, "Relationship between EMG signals and force in human vastus lateralis muscle using multiple bipolar wire electrodes," *Journal of Electromyography and Kinesiology*, vol. 10, pp. 59–67, 2000.

[25] J. Mortimer and N. Bhadra, "Peripheral Nerve and Muscle Stimulation," in *Neuroprosthetics: Theory and Practice*, K. Horch and G. Dillon, Eds., ed New Jersey: World Scientific 2004.

[26] X. Navarro, *et al.*, "A critical review of interfaces with the peripheral nervous system for the control of neuroprostheses and hybrid bionic systems," *J. Peripheral Nervous Syst.*, vol. 10, pp. 229–258, 2005.

[27] G. Brindley, "The first 500 patients with sacral anterior root stimulator implants: general description," *Paraplegia*, vol. 32, pp. 795–805, 1994.

[28] J. K. Chapin and Karen A. Maxon, Eds., *Neural prostheses for restoration of sensory and motor function*. Washington D.C.: CRC Press, 2001, p.^pp. Pages.

[29] K. Yoshida, *et al.*, "Intrafascicular electrodes for stimulations and recording from mudpuppy spinal roots," *Journal of Neuroscience Methods*, vol. 96, pp. 47–55, 2000.

[30] G. T. A. Kovacs, "Technology Development For A Chronic Neural Interface," Ph.D., Stanford University, , 1990.

[31] J. Wolpaw, *et al.*, "BCI Meeting 2005--workshop on signals and recording methods," *IEEE Transactions On Neural Systems and Rehabilitation Engineering*, vol. 14, pp. 138–141, 2006.

[32] H. Berger, "Über das Elektrenkephalogramm des Menschen," *European Archives of Psychiatry and Clinical Neuroscience*, vol. 87, pp. 527–570, 1929.

[33] (2006, *The Waisman Laboratory for Brain Imaging and Behaviour. Neuroimaging facilities.* http://brainimaging.waisman.wisc.edu/neuroimaging.html.

[34] J. Huggins, "Direct brain interface based on event detection in ecog. ," in *NIH Neural Prosthesis Workshop*, University of Michigan 2000.

[35] A. Cukiert, *et al.*, "Results of surgery in patients with bilateral independent temporal lobe spiking (bitls) with normal mri or bilateral mesial temporal sclerosis (mts) investigated with bilateral subdural grids," *Arq Neuropsiquiatr*, vol. 58, pp. 1009-1013, 2000.

[36] K. Drake, *et al.*, "Performance of planar multisite microprobes in recording extracellular single-unit intracortical activity," *IEEE Trans Biomed Eng* vol. 35, pp. 719–732, 1988.

[37] J. Hetke, *et al.*, "Silicon ribbon cables for chronically implantable microelectrode arrays," *IEEE Trans Biomed Eng*, vol. 41, pp. 314–321, 1994.

[38] D. Kipke, *et al.*, "Silicon-substrate intracortical microelectrode arrays for long-term recording of neuronal spike activity in cerebral cortex," *IEEE Tran Rehabil Eng* vol. 11, pp. 151–155, 2003.

[39] Q. Bai, *et al.*, "A high-yield microassembly structure for threedimensional microelectrode arrays," *IEEE Transactions on Biomedical Engineering,* vol. 47, pp. 281–289, 2000.

[40] K. Najafi and J. Hetke, "Strength characterization of silicon microprobes in neurophysiological tissues," *IEEE Transactions on Biomedical Engineering*, vol. 37, pp. 474–481, 1990.

[41] K. C. Cheung, "Implantable microscale neural interfaces," *Biomed microdevices,* vol. 9, pp. 923-938, 2007.

[42] W. L. C. Rutten, "Selective electrical interfaces with the nervous system," *Annu. Rev. Biomed. Eng,* vol. 4, pp. 407–452, 2002.

[43] W. L. C. Rutten, *et al.*, "Sensitivity and selectivity of intraneural stimulation using a silicon electrode array,," *IEEE Trans. Biomed. Eng,* vol. 38, pp. 192–198, 1991.

[44] W. L. C. Rutten, *et al.*, "3D neuroelectronic interface devices for neuromuscular control: Design studies and realisation steps," *Biosens. Bioelectron,* vol. 10, pp. 141–153, 1995.

[45] M. S. Malagodi, *et al.*, "An intrafascicular electrode for recording of action potentials in peripheral nerves," *Ann. Biomed. Eng.,* vol. 17, pp. 397–410, 1989.

[46] A. Branner and R. A. Norman, "A multielectrode array for intrafascicular recording and stimulation in sciatic nerve of cats," *Brain Res. Bull.,* vol. 51, pp. 293–306, 2000.

[47] K.Warwick, *et al.*, "The application of implant technology for cybernetic systems," *Arch. Neurol.*, vol. 60, pp. 1369–1373, 2003.

[48] T. E. Lefurge, *et al.*, "Chronically implanted intrafascicular recording electrodes," *Ann. Biomed. Eng.*, vol. 19, pp. 197–207, 1991.

[49] W. M. Grill and J. T. Mortimer, "Stability of the input-output properties of chronically implanted multiple contact nerve cuff stimulating electrodes," *IEEE Trans. Rehabil. Eng.*, vol. 6, pp. 364–373, 1998.

[50] A. Branner, *et al.*, "Long-term stimulation and recording with a penetrating microelectrode array in cat sciatic nerve," *IEEE Trans. Biomed. Eng.*, vol. 51, pp. 146–57, 2004.

[51] P. Heiduschka and S. Thanos, "Implantable bioelectric interfaces for lost nerve functions," *Prog. Neurobiol.*, vol. 55, pp. 433–61, 1998.

[52] H. S. Neto, *et al.*, "Estimation of the number and size of human flexor digiti minimi muscle motor units using histological methods," *Muscle Nerve*, vol. 21, pp. 112–114, 1998.

[53] A. Ramachandran, *et al.*, "Design, in vitro and in vivo assessment of a multichannel sieve electrode with integrated multiplexer," *J. Neural Eng.*, vol. 3, pp. 114–124, 2006.

[54] L. Wallman, *et al.*, "Perforated silicon nerve chips with doped registration electrodes, in vitro performance and in vivo operation," *IEEE Trans. Biomed. Eng.*, vol. 46, pp. 1065–1074, 1999.

[55] A. F. Mensinger, *et al.*, "Chronic recording of regenerating VIIIth nerve axons with a sieve electrode," *J. Neurophysiol.*, vol. 83, pp. 611–615, 2000.

[56] D. R. McNeal, "Analysis of a model for excitation of myelinated nerve," *IEEE Trans. Biomed. Eng.*, vol. BME-23, pp. 329–337, 1976.

[57] A. Huxley and R. Stampfli, "Evidence for saltatory conduction in peripheral myelinated nerve fibres," *J. Physiol.*, vol. 108, pp. 315–339, 1949.

[58] G. E. Loeb, *et al.*, "Analysis and microelectronic design of tubular electrode arrays intended for chronic, multiple single-unit recording from captured nerve fibres," *Med. Biol. Eng. Comput.*, vol. 15, pp. 195–201, 1977.

[59] A. L. Hodgkin and A. F. Huxley, "A quantitative description of membrane current and its application to conduction and excitation in nerve," *J. Physiol.*, vol. 117, pp. 500–544, 1952.

[60] H. B. Hiscoe, "Distribution of nodes and incisures in normal and regenerated nerve fibres," *Anatom. Record*, vol. 99, pp. 447–475, 1947.

[61] S. Lacour, *et al.*, "Polyimide micro-channel arrays for peripheral nerve regenerative implants," *Sensors and Actuators: A Physical*, vol. 147, pp. 456–463, 2008.

[62] S. Lacour, *et al.*, "Long micro-channel electrode arrays; a novel type of regenerative peripheral nerve interface," *IEEE Trans on Neur. Sys and Rehab Eng.*, vol. 17, pp. 454–460, 2009.

[63] Y. Sun, *et al.*, "Assessment of the biocompatibility of photosensitive polyimide for implantable medical device use," *Journal of Biomedical Material Research A*, vol. 90, pp. 648-55, 2008.

[64] J. J. FitzGerald, *et al.*, "Microchannel electrodes for recording and stimulation: in vitro evaluation " *IEEE Trans. Biomed. Eng.*, vol. 56, pp. 1524–1534, 2009.

[65] J. Fitzgerald, *et al.*, "A regenerative microchannel neural interface for recording from and stimulating peripheral nerve axons in vivo," *J Neural Eng*, vol. 9, 2012.

[66] G. James and S. P. Timoshenko, *Mechanics of Materials*, 4th ed. Boston: PWS publishing company a devision of international Thomson publishing, 1997.

[67] J.-H. Kim, *et al.*, "Development of thin gold film tensile testing by floating specimen on water surface," *ECS Transactions*, vol. 50, pp. 235–239, 2013.

[68] D. Pashley, "A study of the deformation and fracture of single-crystal gold films of high strength inside an electron microscope," *Proceedings of the Royal Society of London.Series A. Mathematical and Physical Sciences*, vol. 255, pp. 218–231, 1960.

[69] S. Benmerah, *et al.*, "Design and fabrication of neural implants with thick microchannels based on flexible polymeric materials," presented at the 31st Annual Int IEEE EMBS Conference, 2009.

[70] M. Madou, *The handbook of micro-fabrication: Fundamentals of microfabrication* New York: CRC Press LLC, 1997.

[71] E. M. Fujifilm. *Technical Product Information: Photosensitive Polyimide Precursors*. Available: www.fujifilm-ffem.com

[72] (2013, *Theory And Application of Photoresists, Developers, Solvents and Etchants revised 2013, Website: http://www.microchemicals.com/downloads/application_notes.html*.

[73] T. Stieglitz, *et al.*, ""Microflex"—A New Assembling Technique for Interconnects," *Journal of Intelligent Material Systems and structures*, vol. 11, pp. 417-25, 2000.

[74] T. Stieglitz, *et al.*, "Implantable Biomedical Microsystems for Neural Prostheses; Flexible, Polyimide-Based, and Modular," *IEEE Engineering in Medicine and Biology Magazine*, vol. 24, pp. 58-65, 2005.

[75] C. Henle, *et al.*, "First long term in vivo study on subdurally implanted micro-ecog, manufactured with a novel laser technology," *Biomed Microdevices*, vol. 13, pp. 59–68, 2011.

[76] M. Schuettler, *et al.*, "Interconnection technologies for laser-patterned electrode arrays. ," presented at the 30th Annual Int IEEE EMBS Conference, 2008.

[77] J. W. Balde, "The effectiveness of silicone gels for corrosion prevention of silicon circuits: the final report of the IEEE Computer Society Computer Packaging Committee Special Task Force " *IEEE Transactions*, vol. 14, pp. 352-365, 1991.

[78] H. Beutel, *et al.*, "Versatile microflex-based interconnection technique," presented at the Smart Structures and Materials: Smart Electronics and MEMS, 1998.

[79] G. G. Harman, *Wire bonding in microelectronics: materials, processes, reliability, and yield* vol. 21. New York: McGraw-Hill, 1997.

[80] C. Jeschke, *et al.*, "A telemetry platform for implantable devices providing inductive energy supply and a bi-directional data link," presented at the 4th European Conference of the International Federation for Medical and Biological Engineering, 2009.

[81] B. Ulgut, "Basics of Electro-chemical Impedance Spectroscopy: Application Notes," Warminster, USA.

[82] P. Wehling, *et al.*, "The influence of bacterial collagenase on regeneration of severed rat sciatic nerves," *Acta Neurochir (Wien)*, vol. 119, 1992.

[83] C. P. Watling, *et al.*, "Novel use of X-ray micro computed tomography to image rat sciatic nerve and integration into scaffold " *Journal of Neuroscience Methods*, vol. 188, pp. 39-44, 2010.

[84] P. A. Wieringa, *et al.*, "In vitro verification of a 3-D regenerative neural interface design: examination of neurite growth and electrical properties within a bifurcating microchannel structure," *Proceedings of IEEE*, vol. 98, pp. 389-397, 2010.

[85] J. M. Anderson, *et al.*, "Foreign Body reaction to biomaterials," *Seminars in Immunology*, vol. 20, pp. 86-100, 2008.